PHYSICAL SALT ATTACK ON CONCRETE: MECHANISMS, INFLUENTIAL FACTORS AND MITIGATION

by

Mohamed Ramadan Yousef Sakr

A Thesis Submitted to the Faculty of Graduate Studies of
the University of Manitoba
in partial fulfillment of the requirements for the degree of

Doctor of Philosophy

Department of Civil Engineering
University of Manitoba
Winnipeg

July 2020

ABSTRACT

Physical salt attack (PSA) is a key damage mechanism of concrete serving in salt-rich media under certain environments; yet, there is still lack of essential knowledge in the technical literature regarding different aspects of PSA. This thesis applied the response surface method to assess the influence of perspective- and performance-based parameters on PSA of 52 concrete mixtures. Also, the research program considered additional parameters that may alter the kinetics of PSA in service by adopting a holistic testing approach of concurrently exposing concrete to PSA and carbonation, simulating elements serving in heavy traffic and industrial zones. In addition, several surface treatments of concrete were tested/developed (nanocomposites) for mitigating PSA and also tested under salt-frost scaling to generalize their applicability.

The results suggested limiting the water-to-binder ratio and binder content to a maximum and minimum of 0.40 and 400 kg/m^3, respectively, regardless of the binder type. With extended curing, the use of fly ash or slag was beneficial at dosages below 25 and 30%, respectively, for binary binders and 35% for ternary blends combining both. Blended binders (28 to 35% replacement) comprising silica fume (≥ 8%) were capable of resisting severe PSA conditions.

Mutual PSA and carbonation escalated the rate of surface scaling compared to single PSA. The wicking factor of concrete informatively captured the trends of damage for single and combined modes. Thermal, mineralogical, and microscopy analyses elucidated the coexistence of complex degradation processes in concrete subjected to combined PSA and carbonation, which was fundamentally different from salt crystallization in case of single PSA.

Epoxy, ethyl silicate, and acrylic emulsion coatings protected concrete from PSA. Colloidal nano-silica (50% concentration) minimized PSA and salt-frost scaling. Silane mixed with 5% nano-clay or nano-silica mitigated PSA and salt-frost scaling damage of sound and pre-cracked concrete, with relatively better performance for nano-clay. Methyl-methacrylate/nanocomposites, at 5% dosage, were efficient at resisting PSA, but failed against salt-frost scaling.

The synoptic outcomes from this thesis can be used as a basis for updating stipulations on PSA in the current ACI 201.2R document with limits on mixture design variables and suitable surface treatments for concrete protection against PSA.

CO-AUTHORSHIP

This thesis has been prepared following the regulations of integrated-article format stipulated by the Faculty of Graduate Studies at the University of Manitoba. Substantial parts of this thesis were either published/accepted in or submitted for publication to peer-reviewed technical journals and international conferences, as shown below:

Journal Papers

1. **Sakr, M.R.,** and Bassuoni, M.T. "Performance of Concrete under Physical Salt Attack Combined with Carbonation," *Cement and Concrete Research*. (Submitted in July 2020, Under Review)
2. **Sakr, M.R.,** and Bassuoni, M.T. "Modeling of Parameters Affecting Physical Salt Attack of Concrete," *ACI Materials Journal.* (Submitted in May 2020, Under Review)
3. **Sakr, M.R.,** and Bassuoni, M.T. "Silane and Methyl-methacrylate based Nanocomposites as Coatings for Concrete Exposed to Salt Solutions and Cyclic Environments," *Cement and Concrete Composites.* (Submitted in Mar. 2020, Under Review)
4. **Sakr, M.R.,** Bassuoni, M.T., Hooton, D., Drimalas, T., Haynes, H., and Folliard, K.J. "Physical Salt Attack on Concrete: Mechanisms, Influential Factors, and Protection," *ACI Materials Journal*. (Accepted in Jun. 2020, In-press)
5. **Sakr, M.R.,** and Bassuoni, M.T. "Effect of Nano-Based Coatings on Concrete under Aggravated Exposures", *Journal of Materials in Civil Engineering*, Vol. 32, No. 10, 04020284.
6. **Sakr, M.R.,** Bassuoni, M.T., and Ghazy, A. "Durability of Concrete Superficially Treated with Nano-silica and Silane/Nano-clay Coatings," *Transportation Research Record*. (Accepted in June. 2020, In-press)
7. **Sakr, M.R.,** and Bassuoni, M.T. "Effect of Coatings on Concrete Resistance to Physical Salt Attack," *ACI Materials Journal*, Vol. 116, No. 6, 2019, pp. 255-267.

Conference Proceedings

1. **Sakr, M.R.** and Bassuoni, M.T. "Surface Treatments for Concrete Under Physical Salt Attack," *6th International Conference on Durability of Concrete Structures* (ICDCS), Leeds, UK, July 2018.

Dedication

This work is dedicated to those who care and give; those who bring joy to life; my parents Ramadan and Magda, my siblings, and my little family; and my late grandfather Mohamed Emam.

Acknowledgments

First and foremost, all praises, thanks, and gratitude to Allah who bestowed upon me guidance, strength, and persistence to complete this work.

Now, I would like to express my deep sense of gratitude and profound respect to my advisor Dr. Mohamed Bassuoni, who has helped and encouraged me throughout all stages of this research with great patience and immense care. I am mainly attributing the quality of this work to his compassion, knowledge, and endless enthusiasm, without holding back any tiny amount of effort.

My sincere thanks to my colleagues for their support throughout all work stages, especially Ahmed Ghazy, Ahmed Yasien, Ahmed Azzam, and Moustafa Abuzeid. Also, the valuable assistance and technical support of the McQuade Heavy Structures Laboratory staff, Dr. Chad Klowak, Mr. Samuel Abraha, Mr. Brendan Pachal, and Mr. Syed Mohit, during the design and implementation of experiments are greatly acknowledged.

I highly appreciate the financial support from Natural Sciences and Engineering Research Council of Canada, University of Manitoba Graduate Fellowship, and City of Winnipeg. The IKO Construction Materials Testing Facility and Manitoba Institute for Materials at the University of Manitoba in which these experiments were conducted have been instrumental to this research.

I express my deepest gratitude to my parents for their moral support and inspiration throughout my entire life. I am grateful for their endless love, patience, encouragement, and prayers. Also, I acknowledge my brothers and sister for their emotional and spiritual support throughout my journey to finish this work.

I must express my appreciation to Marwa, my wonderful and patient wife, who supported me with all love and life, and stood with me side by side in persuading my path. I also express my gratitude to Sama and Sara, my little daughters and spontaneous motivators for a better future for us all.

Last but not least, I would like to thank all my family and friends for their continuous support and advice throughout all work stages.

TABLE OF CONTENTS

LIST OF TABLES

LIST OF FIGURES

NOTATIONS

A	Absorption
AAP	Average actual-to-predicted ratio
AE	Acrylic emulsion
ANOVA	Analysis of Variance
B	Binder content
C	Concentration of the solution at temperature *T*
C_3A	Tricalcium aluminate
$Ca(NO_3)_2$	Calcium nitrate
$Ca(NO_3)_2.2H_2O$	Calcium nitrate hydrate
$Ca(NO_3)_2.4H_2O$	Calcium nitrate hydrate
$Ca(OH)_2$	Calcium hydroxide (portlandite)
Ca/Si	Calcium-to-silicate ratio
Ca^{2+}	Calcium ions
$CaCl_2$	Calcium chloride
$CaCO_3$	Calcium carbonate (calcite)
CH	Calcium hydroxide (portlandite)
CO_2	Carbon dioxide
COV	Coefficient of variation
C_s	Saturation concentration of the solution at temperature *T*
C-S-H	Calcium-silicate-hydrate
D	Desorption
DSC	Differential scanning calorimetry

E_d	Dynamic modulus of elasticity
EDX	Energy dispersive X-ray analysis
EP	Epoxy
ES	Ethyl silicate
ESEM	Environmental scanning electron microscopy
F/T	Freezing and thawing
FA	Fly ash
f_c	Compressive strength
FCCD	Face-centered composite design
F_{cr}	Critical *F*-value
FI	Full immersion
f_{st}	Splitting tensile strength
f_{st}* E_d	Mechanical capacity
GU	General use portland cement
H^+	Hydrogen ions
H_2CO_3	Carbonic acid
H_2O	Water
HCO_3^-	Bicarbonate ions
HMMA	High molecular weight methacrylate
HRWRA	High-range water reducing admixture
HS	High sulfate-resistant cement
ITZ	Interfacial transition zone
MAPE	Mean absolute percentage error
$MgSO_4$	Magnesium sulfate

$MgSO_4.6H_2O$	Hexahydrate
$MgSO_4.7H_2O$	Epsomite
m_i	Initial mass
MIP	Mercury intrusion porosimetry
ML	Mass loss
MMA	Methyl methacrylate
MNC	MMA/nano-clay composite
MNS	MMA/nano-silica composite
m_t	Mass at time *t*
Na	Sodium
Na_2CO_3	Sodium carbonate (natrite)
$Na_2CO_3.10H_2O$	Natron
$Na_2CO_3.H_2O$	Thermonatrite
Na_2SO_4	Sodium sulfate (thenardite)
$Na_2SO_4.10H_2O$	Mirabilite
NaCl	Sodium chloride (halite)
$NaNO_3$	Sodium nitrate
NC	Nano-clay
NIST	National Institute of Standards and Technology
NS	Nano-silica
Θ	Contact angle
OPC	Ordinary portland cement
P	Crystallization pressure
P	Total porosity

P*A/D	Wicking factor
PCA	Portland Cement Association
PI	Partial immersion
PLC	Portland limestone cement
P_{micro}	Proportion of micropores
PSA	Physical salt attack
R	Ideal gas constant
R	Pearson's correlation coefficient
RCPT	Rapid chloride penetration test
RH	Relative humidity
RSM	Response surface method
S	Sulfur
S	Silane
SCMs	Supplementary cementitious materials
SEM	Scanning electron microscopy
SF	Silica fume
SG	Slag
Si/Al	Silicate-to-aluminate ratio
SNC	Silane/nano-clay composite
SNS	Silane/nano-silica composite
SO_4^-	Sulfate ions
SS	Sodium sulfate
SS	Sodium silicate
T	Temperature

t	time
TEM	Transmission electron microscopy
TEOS	Tetraethylorthosilicate
TNS	Time-to-notable scaling
TSA	Thaumasite sulfate attack
UPV	Ultrasonic pulse velocity
v	Molar volume of the solid salt
w/b	Water-to-binder ratio
w/c	Water-to-cement ratio
W/D	Wetting and drying
XRD	X-ray diffraction
y	Experimental values
$\hat{y}$	Predicted values
α	Significance level
β_i	Linear regression coefficient
β_{ii}	Quadratic regression coefficient
β_{ij}	Interaction regression coefficient
ϵ	Model random error
ϕ_{thd}	Threshold pore diameter

CHAPTER 1: INTRODUCTION

1.1 Overview

Concrete elements may experience premature failure before reaching the target service life due to exposure to harsh service conditions. Thus, huge expenditures are being directed towards repair and maintenance of concrete structures as a result of durability issues, targeting the restoration of the required level of functionality (Lindvall 2001). Physical salt attack (abbreviated as PSA) is a deterioration mechanism that has been recognized as a key cause of concrete damage in salt-rich media (e.g. soil, groundwater, or seawater). PSA gained considerable attention among researchers and practitioners due to the numerous litigations raised by residential homeowners in Southern and Northern California against the builders because damage was occurring within a short period after construction (Haynes and Bassuoni 2011).

Physical salt attack occurs due to the existence of salts in the exposure environment under a range of ambient conditions (cyclic temperature and relative humidity) leading to progressive scaling and flaking of concrete surface, similar in appearance to that caused by freezing/thawing cycles, disrupting its performance (Bassuoni and Rahman 2016). In most field cases, PSA is commonly observed in elements subjected to wicking action, which refers to continuous supply of salt solution and simultaneous evaporation through the drying/evaporative front leading to salt crystallization [e.g. partially embedded elements such as basement walls, piers, abutments, etc., and structures with one side contacting wet soil and the other exposed to air such as tunnel linings] (Haynes et al. 1996; Scherer 2004; Liu et al. 2017). The relationship between evaporation and supply rates determines the location of crystallization, and consequently level of damage. A higher evaporation rate

with respect to solution uptake results in formation of sub-florescence beneath the surface layer of concrete, which is the stimulating mechanism for superficial scaling when developed in sufficient amounts. The severity of damage increases for higher salt concentrations or more salt build-up. Moreover, PSA is not limited to a particular salt; several brines were reported to cause PSA of concrete, such as sodium sulfate, sodium carbonate, and sodium chloride, in order of aggression (Haynes et al. 2008, 2010).

Unlike chemical deterioration mechanisms, the damage of PSA is mainly physical in nature, i.e. limited or no chemical alteration of hydration products is involved (Folliard and Sandberg 1994; Flatt 2002). For instance, in the classical form of external sulfate attack, sulfates from the surrounding environment penetrate through concrete and react with the hydration products to produce gypsum, ettringite, or brucite (depending on the cation type bound with sulfate), resulting in multiple damage manifestations such as expansion, cracking, spalling, softening and decalcification of calcium-silicate-hydrate [C-S-H] (Neville 2004). On contrary, in the case of PSA, same salt compounds (e.g. sodium sulfate) crystallize in the near-surface pores of concrete producing deleterious crystallization pressure to concrete (Haynes et al. 2008; Lee and Kurtis 2017). Flatt (2002) theoretically reported that developed pressures can reach 10-20 MPa for highly supersaturated salt solutions, which is far greater than the tensile strength of normal and even high-performance concrete.

Historically, PSA was confused with chemical attacks caused by sulfate salts. For instance, in the long-term field study (16 years) commenced by Portland Cement Association (PCA) on sulfate resistance of concrete specimens partially embedded in sulfate-rich soil (equivalent to 10% anhydrous sodium sulfate) located in California, damage was initially misidentified as chemical sulfate attack (Stark 1989) and later was

attributed to PSA since damage was localized above soil level with no signs of chemical attack existed above or below ground (Stark 2002). This past confusion of PSA with chemical attacks caused by sulfate salts led to late recognition of PSA as a distinct deterioration mechanism in the latest edition of ACI (American Concrete Institute) -201.2R (2016) [*Guide to Durable Concrete*].

1.2 Need for Research

There is still lack of essential knowledge in the technical literature and current standards regarding PSA on concrete. While the effect of some mixture design parameters [e.g. water-to-binder ratio (*w/b*)] on PSA of concrete has been established in literature (Drimalas 2007; Bassuoni and Rahman 2016), the impact of other parameters (e.g. binder content) still needs to be determined. In addition, conflicting data exists regarding the behavior of concrete containing supplementary cementitious materials (SCMs) under PSA, which may be linked to variations in mixture designs, curing conditions and/or testing protocols. This contradiction spots the need for conducting thorough research to give a better understanding of the actual behavior of concrete containing SCMs under PSA and determine the optimum amounts of SCMs at which concrete performs best, while applying uniform testing conditions to provide a consistent basis of comparison.

The key properties of concrete relevant to PSA are the mechanical, transport, and pore structure characteristics. Higher tensile capacity of a porous material increases its ability to withstand developed crystallization pressures (Scherer 2004). However, this effect is not quantified for cement-based materials. Transport properties and pore structure features determine the rates of solution supply and evaporation, which are crucial for the process of PSA. A few studies considered the effect of pore structure features on the vulnerability of concrete to PSA (Bassuoni and Rahman 2016; Lee and Kurtis 2017). Thus,

a wide range of concrete mixtures needs to be uniformly tested to determine the dominant performance metrics affecting PSA of concrete. Such datasets will require the use of statistical models capable of accommodating various sources of uncertainty in predicting the performance of concrete under PSA. In the prequalification stage of a construction project, such models can effectively assist in selecting optimum concrete mixtures proposed for PSA exposures, to avoid potential durability risks and associated costly rehabilitations.

In addition, the current practice of studying PSA involves exposing specimens to a salt solution combined with cyclic conditions that provoke salt crystallization. Nevertheless, in real field conditions, the damage of concrete structures often occurs due to a multitude of mechanisms (chemical and/or physical) acting in a synergistic manner. There is dearth of information on the interaction between PSA and carbonation in concrete, which maybe encountered in field cases such as tunnel linings (Long et al. 2011) and partially embedded elements in industrial zones (Yoshida et al. 2010). There is still need for research in this direction to elucidate possible mechanisms of concrete damage due to combined effects of PSA and carbonation.

Furthermore, procedures and techniques for protection and repair of concrete damage induced by PSA are not adequately addressed. Common methods for improving the durability of concrete, such as using SCMs, were proven unsatisfactory to protect concrete subjected to PSA stimulating conditions (Nehdi et al. 2014; Zhutovsky and Hooton 2017a). Accordingly, ACI 201.2R (2016) stated that "*specific recommendations cannot be made to prevent physical salt attack*." Thus, research was directed to enhance the properties of concrete outer layer by surface treatments to minimize the ingress of salt solutions into concrete. However, there is just one laboratory study (Suleiman et al. 2014)

in this direction with mild testing conditions, which was insufficient to conclusively judge the performance of coatings. Consequently, further research on the applicability of various surface treatments to protect concrete under severe PSA conditions is required, considering different qualities of the substrate and implementation of innovative measures such as nano-based coatings. Fundamental knowledge from this thesis can be applied towards improving current guidance, recommendations, and specifications for developing durable concrete mixtures suitable for application against PSA, and selecting suitable surface treatments to protect concrete from PSA damage.

1.3 Objectives of Research

To respond to the aforementioned research needs, the fundamental theme of this work is to improve the current level of knowledge on the mechanisms, influential factors, and mitigation of PSA on concrete to minimize the risk of premature deterioration. The specific objectives of this thesis are to:

- Investigate the influence of perspective-based (e.g. binder content and SCMs) and performance-based (e.g. mechanical, transport, and pore structure features) parameters on the resistance of concrete to PSA under uniform testing conditions.
- Develop statistical models to link the damage by PSA to perspective- and performance-based parameters of concrete, complemented with numerical optimization to identify criteria for resilient concrete mixtures under PSA.
- Implement an integrated testing approach on concrete that considers concomitant damaging mechanisms with PSA such as carbonation and capture the difference in performance and failure mechanisms, if any, from single PSA.
- Identify effective surface treatments and develop polymeric nanocomposites to protect concrete elements affected by PSA taking into consideration the effect of

concrete substrate quality and application of suitable testing conditions to give reliable conclusions on these treatments.

1.4 Scope of Research

To achieve the objectives mentioned above, the scope of work shall involve:

- Experimental design of a wide range of concrete mixtures (52) using the response surface method (RSM) to evaluate the effect of prescriptive parameters [*w/b*, binder content, and dosages of SCMs] on concrete resistance to PSA.
- Determination of performance parameters (tensile strength, dynamic modulus of elasticity, absorption, desorption, apparent total porosity, proportion of micropores, and threshold pore diameter) for 52 mixtures to link with damage due to PSA.
- Modeling of PSA damage in terms of prescriptive- and performance-based parameters of concrete, which may provide an assistive design tool for selecting concrete mixtures for this exposure, followed by optimization to identify resilient concrete mixtures under PSA.
- Investigation of damage mechanisms by combined carbonation and PSA of concrete made with different *w/b*, cement, and binder types, applying a long-term holistic testing regime (1 year) based on realistic ambient conditions in locations with previous history of PSA field cases.
- Evaluation of the suitability of seven commercial surface treatments having different functions (surface coatings, hydrophobic agents, surface pore blockers, and multifunctional treatments) for protection of concrete made with various *w/b* against severe conditions stimulating PSA.

- Assessing the potential of colloidal nano-silica at different solid particles concentration to act as a pore blocker (surface treatment) for concrete and testing its ability to resist PSA on concrete with different qualities.
- Enhancing the performance of polymeric resins by addition of nanoparticles (nano-silica and nano-clay) to synthesize polymeric nanocomposites capable of providing adequate protection for concrete under PSA. Also, those composites are to be tested under salt-frost scaling to verify the conclusions on their applicability in the field.

1.5 Original Contributions

The current Ph.D. thesis targets researching different aspects concerning PSA on concrete that are not yet investigated in the technical literature. The outcome of this work will contribute to the scientific and engineering communities as follows:

- Developing a large and comprehensive database on the durability of a wide range of concrete mixtures to PSA and identifying the suitability/unsuitability of those mixtures under conditions stimulating PSA based on key mixture design parameters (*w/b*, type of binder, SCMs).
- Modeling the mass loss and time to notable scaling due to PSA in terms of prescriptive- and performance-based parameters to provide an assistive design tool for selecting concrete mixtures resistant to this exposure.
- Proposing a classification for the resistance of concrete to PSA with corresponding ranges for the mechanical capacity and wicking factor (performance criteria), which allow the design of resilient concrete mixtures to PSA without being restricted to specific mixtures.
- Implementing a 'holistic' (rather than a 'reductionist') testing approach for evaluating PSA on concrete, which progresses from single to dual damage

mechanisms, and developing innovative testing techniques capable of identifying the synergistic effects of PSA and carbonation, with determination of potential durability risks under real field exposure.

- Revealing the mechanism of concrete damage by combined PSA and carbonation, compared to single PSA, and identifying potential performance improvement and risks.
- Analyzing the mechanisms of success or failure of different surface coatings in minimizing/eliminating the damage of concrete subjected to PSA, putting forward a basis for initial selection of efficient coatings capable of protecting concrete from surface scaling by PSA.
- Data compiled from this thesis and results of modeling and experimental work will be used as a basis for updating the current ACI 201.2R (2016) document with specific guidelines on the mixture design aspects to produce durable concrete against single PSA or combined with carbonation, in addition to protective coatings.

1.6 Structure of the Thesis

This thesis consists of eight chapters, as described below:

- CHAPTER 1, the introduction, provides a brief overview on PSA and the problem statement motivating this research. Research objectives, scope of work, and contribution of thesis are also addressed.
- CHAPTER 2 provides a comprehensive literature review on the current understanding of PSA, including occurrence, mechanisms, laboratory tests, and influential factors. In addition, the current repair/protection techniques and code recommendations, if any, for PSA on concrete are discussed.

- CHAPTER 3 experimentally and statistically investigates a wide range of concrete mixtures to determine the effect of prescriptive and performance parameters on the resistance of concrete to PSA and link those factors to damage level of concrete.
- CHAPTER 4 includes laboratory-simulated regime to mimic concurrent exposure of concrete to PSA and carbonation, considering the effects of *w/b*, cement type and incorporation of SCMs.
- CHAPTER 5 focuses on the application of seven commercial surface treatments on concrete under severe conditions provoking PSA and discusses the attributes of failed and succeeded coatings.
- CHAPTER 6 tests the suitability of water-based colloidal nano-silica and synthesized silane/nano-clay composites at different concentrations of nanoparticles for concrete protection against PSA. Also, the applicability of coatings was verified through testing under salt-frost scaling.
- CHAPTER 7 tries to improve the performance of failed coatings (silane and methyl-methacrylate) in Chapter 5 by mixing nanoparticles (nano-clay and nano-silica) into the polymeric resins. Coatings were also verified against salt-frost scaling.
- CHAPTER 8 presents a summary of the major findings and significant conclusions of this thesis, as well as some remarks on recommendations for future study.

CHAPTER 2: LITERATURE REVIEW

The topic of physical salt attack (PSA), also known as salt weathering or salt hydration distress, has been a subject of extensive research on stones and rocks for a relatively long time (Doehne 2002). Also, PSA was recognized under a range of environments as a potential cause of concrete deterioration that leads to progressive scaling and flaking of concrete surfaces (Haynes and Bassuoni 2011). PSA occurrence is due to the presence of certain salts, notably sodium sulfate, in the exposure environment, while the ambient conditions (temperature and relative humidity) are favorable for salt crystallization. Damage is observed on the evaporative surfaces of concrete in contact with salt-rich media (e.g. soil, groundwater or seawater), such as the exposed portions of basement walls, abutments, piers, slabs on grade, tunnels, etc. (Figs. 2.1, 2.2). Sodium sulfate, carbonate, and chloride, in order of aggression, have been reported to cause PSA (Rodriguez-Navarro and Doehne 1999; Haynes and Bassuoni 2011).

(a) (b)

Figure 2.1: Example of PSA occurring in basement walls due to sodium sulfate from: (a) outside (courtesy of Harvey Haynes, California, USA), and (b) inside (courtesy of Robert L. Day, Alberta, Canada).

Figure 2.2: Walls in a service tunnel showing efflorescence and scaling of concrete involving sodium chloride (courtesy of Robert L. Day, Alberta, Canada).

The damage from PSA is mainly physical in nature, i.e. limited or no chemical alteration of hydration products is involved (Folliard and Sandberg 1994; Flatt 2002). In the classical form of external sulfate attack, sulfates from the surrounding environment enter concrete as a solution to react with the hydration products. The cation type bound with the anion of sulfate determines the mechanisms and complexity of chemical interactions. These chemical reactions might produce gypsum, ettringite, thaumasite, or brucite, resulting in multiple damage manifestations such as expansion, cracking, spalling, softening and decalcification of calcium-silicate-hydrate [C-S-H] (Neville 2004). In the case of specific environments conducive to PSA, compounds from these same sulfate salts crystallize in the near-surface pores producing deleterious pressure to concrete. Flatt (2002) reported that the value of this pressure can reach 10-20 MPa, which is far greater than the tensile strength of normal and even high-performance concrete. However, it must be recognized that both chemical and physical attack may result from the same exposure to external sources of sulfates; therefore, they do not necessarily occur in isolation from each other. In case of efflorescence depositing on the surface or minor surface scaling, PSA can be only of aesthetic concern. However, in severe PSA cases, significant spalling of concrete

cover occurs causing a reduction of the effective cross-section and provoke corrosion of steel reinforcement, which in turn would compromise the structural capacity of concrete.

2.1 PSA Occurrence

PSA as a deterioration mechanism in concrete has only recently appeared as a distinct deterioration mechanism in the latest edition of ACI-201.2R (2016) (*Guide to Durable Concrete*). This late recognition of PSA is likely the result of confusion of PSA with chemical sulfate attack as both mechanisms result from external sulfate exposure. Part of that was from the field studies commenced in 1982 by Portland Cement Association (PCA) on sulfate resistance of concrete, where concrete specimens were partially embedded in sulfate-rich soil (10% sodium sulfate) located in Sacramento, California. In a report issued by PCA in 1989, the distress in specimens was misidentified as chemical sulfate attack (Stark 1989); however, a subsequent report in 2002 indicated that specimens' distress was mainly located only above the level of sulfate-saturated sand which was not characteristic of chemical attack, with only minor damage below ground level. Stark (2002) attributed the main cause of damage to PSA, and it was stated that the physical damage was far more prominent than that resulting from chemical attack.

Earlier examples of PSA were reported in Hansen (1968), Price and Peterson (1968), and Hamilton and Handegord (1968). Hansen (1968) mentioned the experiments performed by the National Bureau of Standards in 1913 in which salt solutions evaporated through the walls of mortar pipes. This study showed porous mortar could be damaged by the mechanical force exerted by salt crystallization. This damage was observed in areas above the waterline of partially immersed elements in salt-bearing water or soils. Price and Peterson (1968) recognized PSA as part of the sulfate durability problem in western Canada back in the 1920s. An example is their investigation of a conduit constructed in 1914,

located about 100 miles southeast of Calgary, Canada. They reported a severely destructive process in some localized areas for example, at the junction of the conduit roof slabs and breast walls. Weathering and sulfate attack combined to produce severely disruptive forces such that with time, weathering weakened the concrete making it vulnerable to a more rapid transfer of water and an accelerated rate of sulfate attack. In comparison, conduit elements beneath the earth fill were in good condition. Inspection of concrete in a wide variety of structures and exposures revealed that the most extensive damage by weathering occurred in a moist environment, especially in parts situated in fluctuating water level or exposed to mist and spray.

Hamilton and Handegord (1968) reported the rapid penetration of sulfate salts through concrete footings in many house basements in Saskatoon, Canada, where salt deposits became evident on the inside surfaces in a relatively short period. The entry of moisture apparently occurred upward through the unprotected footings. Also, inspection of a service tunnel in Saskatoon which had been buried in soils of moderate to high sulfate content for 45 years showed that on the inside of the tunnel, the floor and the lower portion of the walls had significant spalling. In most areas, less than 12 mm of concrete had been lost, but in few locations, as much as 25-50 mm of concrete had been lost. The manifestations of damage indicated a typical appearance of PSA.

Tuthill (1978) showed a photograph of significant deterioration to a concrete cut-off wall at an earthen canal. The concrete wall that was underground was intact, but above ground, the exposure to sulfate solutions caused concrete spalling as salt crystals developed in the concrete pores when moisture evaporated. Reading (1982) showed examples of structural elements in a dam (Montana, USA) that were attacked only by physical activity of sodium sulfate. Tests showed that chemical sulfate attack was not evident. St John

(1982) reported that apart from chemical attack on tunnel arches by sulfur gases in coal smoke, severe exfoliation of concrete linings along the walls of three railway tunnels in New Zealand was found 0.25-1.5 m above ballast level and around construction joints. The author described the damage to be unusual and the characteristic feature was a coating of fine, silky, acicular crystals of sodium sulfate on the affected locations. It was concluded that groundwater was drawn up the walls while natural ventilation in tunnels caused groundwater evaporation, which led to deposition of sodium sulfate that resulted in scaling of concrete. It can be deduced from the previous description that PSA was the primary cause of attack; however, lack of characterization techniques and the appearance of this unusual form of deterioration at that time made it difficult to determine the underlying damage mechanism.

Novak and Colville (1989) reported on salt depositions forming on several deteriorated concrete slabs of 20-30 years old residential homes in Southern California. White efflorescence was found on the concrete surface; also, severe long and wide cracks were found on the surface filled with white salt deposits. Mineralogical analysis showed the absence of ordinary indicators of sulfate attack such as gypsum, ettringite, or thaumasite while thenardite and/or mirabilite were present in the majority of samples. In addition, minor amounts of sodium carbonate, nitrate, or chloride phases deposited with sodium sulfates were also observed in some cases. The slabs had no vapor retarders which allowed salt solutions to rise by capillary action into concrete. As water evaporated, salts crystallized and exerted pressure on pore walls resulting in cracking and damage of concrete. Moreover, the authors outlined that conversion between salt phases (e.g. thenardite to mirabilite) might have been a factor in escalating the damage process.

Similarly, Haynes (2002) reported PSA damage of low-specified strength, high water-to-binder ratio (*w/b*) concrete foundations and slabs in hundreds of residential homes in Southern and Northern California due to sodium sulfate salt existing in soil. White deposits of sodium sulfate were found on foundation walls in contact with soil and below floor finishes with no signs of chemical alteration of the hydration products from external sulfate attack (the cements used had low C_3A contents). Many homeowners brought their cases to court against the builders as the damage was happening within a short period after construction. These legal cases brought considerable attention from researchers and practitioners to PSA (e.g. Haynes 2002; Haynes et al. 2008, 2010).

Yoshida et al. (2010) reported on the wide distribution of degradation cases in residential concrete foundations by PSA in Japan. Surface scaling or even collapse of floor post footings due to sodium sulfate crystallization was found. The height of the deterioration on concrete above ground level reached about 300 mm; however, concrete under ground was sound. Some other cases were reported in China, especially in railway tunnels. Long et al. (2011) found that damage of concrete linings of approximately 40-year-old railway tunnels was due to combined chemical and physical sulfate attack. Also, Liu et al. (2017) concluded that the detached parts from tunnel linings in China were due to crystallization of sodium sulfate.

PSA has been observed on concrete in various locations worldwide typically in arid environments where concrete elements exist in salt-rich media (e.g. soil, groundwater or seawater). In Australia, the damage is called salt damp where salts rise through the concrete foundations, and seasonal cycles between summer (drying) and winter (wetting) cause deposition of salts resulting in concrete damage (Neville 2004). Soils in parts of the Canadian Prairie Provinces are sulfate-laden, and structures constructed in these

environments have been attacked by PSA (Florinsky et al. 2000). Similarly, cases of PSA were reported in the saline Sabkha soils in the Arabian region (Rasheeduzzafar et al. 1986; Bates 2010).

2.2 Mechanisms of PSA

There are different hypotheses on the mechanisms of damage induced by salts in porous media; namely: hydration pressure, thermal expansion, and crystallization pressure.

2.2.1 Hydration Pressure

The hydration pressure hypothesis states that during the process of salt hydration, expansion of the crystal lattice occurs with incorporation of additional water molecules. Damage occurs when the larger crystals exert pressure on the pore walls of concrete. For instance, there is about 314% increase in solid volume when the anhydrous sodium sulfate (thenardite, Na_2SO_4) converts to the hydrous form (mirabilite, $Na_2SO_4.10H_2O$). However, it has been argued by Thaulow and Sahu (2004) that this hypothesis does not account for the volume of the water in the original system, which if considered, the net calculation would show a reduction in the total volume. For the example of Na_2SO_4, the reduction is about 5.6% volume decrease. Moreover, this mechanism assumes solid-state hydration of anhydrous salts that absorb moisture, which is technically flawed because of the different crystal structure of the hydrous salt and its anhydrous companion. For example, thenardite is orthorhombic in crystal structure, whereas mirabilite is monoclinic, which cannot occur just by hydration. Using environmental scanning electron microscopy (ESEM), Rodriguez-Navarro et al. (2000) found that conversion between the un-hydrated and hydrated salts occurs via through-solution process, meaning that thenardite crystals dissolve in solution followed by mirabilite crystallization and vice-versa. In addition, this hypothesis fails to

explain why anhydrous salts such as halite (NaCl) can cause PSA damage (Rodriguez-Navarro and Doehne 1999).

2.2.2 Thermal Expansion

This hypothesis was proposed to explain the PSA damage of stones in hot desert climates based on the argument that salts (enclosed in the pores) with higher thermal coefficients of expansion than the host material expand much more than the surrounding system causing pressure on the pore walls which can consequently cause disruption (Bland and Rolls 1998). Johannessen et al. (1982) found experimentally that the thermal expansion pressure of NaCl could break the quartz crystals from the surrounding matrix in sandstone rock when subjected to a temperature change of 50°C. Thus, for damage to occur, the salt and its host porous material would have to be exposed to severe temperature fluctuations. However, it is less realistic to consider this mechanism as the primary cause for salt damage when the temperature fluctuations are not as large. Moreover, the scaling and exfoliation damage caused by this effect is marginal when compared with that of other mechanisms due to the minimal volumetric expansions of salts at regular temperatures (Bland and Rolls 1998). Considering the compositional and microstructural differences between concrete and rocks (e.g. sandstone), this hypothesis does not likely explain the damage induced by PSA on concrete, especially when it is exposed to normal temperature and RH ranges (no extreme changes).

2.2.3 Crystallization Pressure

This mechanism has been widely accepted by the scientific community as the most significant route by which salts cause damage in concrete (Flatt 2002; Thaulow and Sahu 2004; Steiger 2005; Bassuoni and Rahman 2016). When salt crystals grow inside confined pore space, crystallization pressure will be exerted on the pore walls, and if this value

exceeds the host material's tensile capacity, damage occurs (Scherer 2004). In field cases, PSA damage occurs when an evaporative surface exists such as concrete elements being in contact with soil on one side while the other is exposed to air (e.g. tunnels and slabs-on-grade). The process of salt damage when concrete comes in contact with a salt-laden source can be described, as shown in Fig. 2.3.

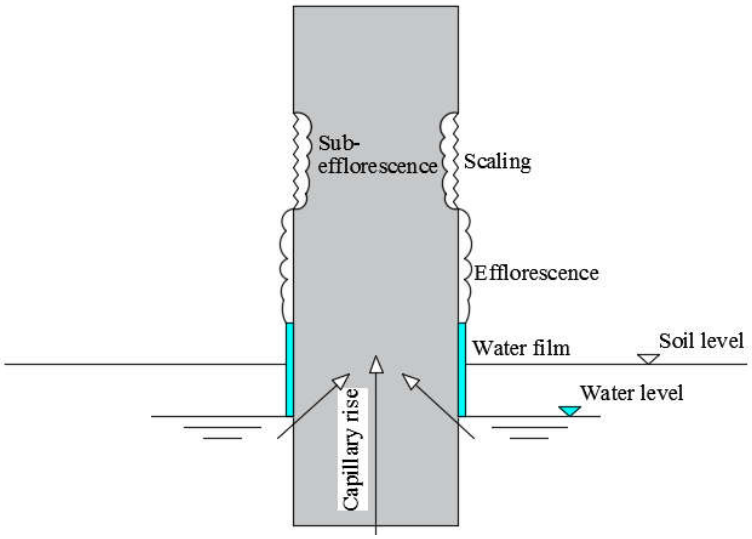

Figure 2.3: Schematic of capillary rise and evaporation from a partially embedded concrete element in wet soil.

The salt solution is drawn into the element by capillary action. The relation between the evaporation rate and capillary flux determines the condition and location of crystallization. In concrete, the evaporation rate is a function of the relative humidity of the air, while the capillary flux is a function of the volume, connectivity and size distribution of the capillary pore structure. Close to the ground level, the rate of solution supply by capillary rise exceeds the rate of evaporation, which leads to the formation of a liquid film on the surface with no crystals. Higher up the surface, the rate of capillary rise becomes slower and the solution becomes supersaturated on the surface resulting in efflorescence. When the evaporative flux exceeds capillary flux, the crystals form below the surface of the element (sub-florescence) and cause progressive surface scaling due to the resulting

high supersaturation ratio of salt solution, which is essential for damage as highlighted by Correns (1949):

$$P = \frac{RT}{v} \ln \frac{C}{C_s} \quad \text{Eq. (2.1)}$$

where, P is the crystallization pressure, R is the ideal gas constant, v the molar volume of the solid salt, C is the concentration of the solution at temperature T, C_s is saturation concentration of the solution at temperature T, and C/C_s is defined as the supersaturation ratio.

2.3 Testing

Experimental procedures to evaluate PSA on concrete vary significantly due to application of different methods and environmental conditions, making the comparison of the outcomes of these tests difficult. In this section, the various methods used to simulate salt damage in concrete are discussed, noting that these tests have been mostly performed using sodium sulfate due to its aggressiveness which made it the rational choice for accelerated protocols (Rodriguez-Navarro and Doehne 1999). In general, tests that cause salt damage of concrete are various and can be classified into full immersion, wetting and drying, and partial immersion methods. Tables 2.1 and 2.2 summarizes the exposure conditions adopted in various laboratory and field studies reported in the literature.

2.3.1 Full Immersion Tests

This type of test method depends on immersing test specimens in a salt solution and subjecting them to thermal cycles, which results in PSA during or after immersion. Folliard and Sandberg (1994) tested specimens completely immersed in 30% by mass sodium sulfate solution and concurrently subjected to cooling from 30°C to 5°C to promote high supersaturation, followed by crystallization of mirabilite. Subsequently, the fully immersed specimens were warmed back to 30°C. This thermal cycle was then repeated every 24 h

and the applied cooling and heating rates were about 4 and 2.5°C/h, respectively. These exposure conditions were sufficiently severe to cause complete disintegration for concrete cubes (*w/b* of 0.50) after 30 cycles. Recently, similar exposure conditions were applied recently in Zhutovsky and Hooton (2017a, b) where specimens experienced surface scaling and mass loss over all surfaces; for example, the mass loss values were 20% and 75% for specimens made with *w/b* of 0.35 and 0.50, respectively (Zhutovsky and Hooton 2017b).

2.3.2 Wetting and Drying Tests

Goudie (1993) submerged mortar specimens in five saturated salt solutions (Table 2.1). The test procedure started by drying specimens to constant mass at 25°C/40% RH, followed by full immersion for 24 h in the corresponding salt solutions. Subsequently, the specimens were exposed to 25 daily cycles of six different exposures, which simulated daily field observations of ground surface temperature and RH at six arid geographic locations. Under these conditions, mortar specimens experienced PSA, which was quantified by measuring the mass loss at the end of the cycles. Goudie and Viles (1995) reapplied the previous test procedure, but with increasing the number of exposure cycles to 100 to obtain more distinctive features of damage. The main advantage of this work was using field environmental conditions for the exposure cycles.

Haynes (2005) applied tests that simulated ASTM C88 (2013) sulfate soundness test for aggregates and found that oven-dried thenardite forms a hard mass as opposed to air-dried thenardite, which forms a fluffy mass, and the oven-dried thenardite does not dissolve readily when re-exposed to solution. Also, increasing temperatures caused damage by thermal expansion of the oven-dried thenardite. Bassuoni and Nehdi (2009) exposed prismatic concrete specimens with *w/b* of 0.38 to a wetting-drying exposure in which each cycle consisted of 4 days of full immersion in a 5% sodium sulfate solution and 3 days of

drying in a hot environment of 45°C/35% RH. This exposure continued for 104 cycles that lasted up to 24 months. Micro-analysis after 24 months elucidated that the wetting-drying exposure caused combined deterioration i.e. salt crystallization and chemical sulfate attack such that sodium sulfate crystallized near-in the exposed surfaces of specimens resulting

Table 2.1: Summary of laboratory PSA exposures of concrete reported in the literature

Source	Type	Test*	Exposure Conditions	Duration	Salt Solution
Folliard and Sandberg (1994); Zhutovsky and Hooton (2017 a,b)	Lab	FI	Cooling from 30°C to 5°C at a rate of 4°C/h, and heating to 30°C at a rate of 2.5°C/h	30 cycles, 24 h each	30% Na_2SO_4
Goudie (1993)	Lab	W/D	Wadi Digla (35-72°C/58-84% RH) and Negev (10-4°C/30-100% RH)	25 cycles, 24 h each	Saturated: Na_2SO_4, NaCl, $NaNO_3$, Na_2CO_3, $MgSO_4$
Bassuoni and Nehdi (2009)	Lab	W/D	Full immersion for 4 days followed by 3 days of drying at 45°C/35%RH	24 months (104 cycles)	5% Na_2SO_4
Benavente et al. (2007)	Lab	PI	Capillary stage for 12 h at 40°C/80%RH followed by precipitation stage for 12 h at 10°C/70%RH	15 cycles, 24 h each	14% Na_2SO_4
Bassuoni and Nehdi (2009)	Lab	PI	4 days of partial immersion while the upper portions were exposed to drying under 22±2°C/55±5% RH. Then, the entire specimens were dried at 45°C/35% RH for 3 days	24 months (104 cycles)	5% Na_2SO_4
Haynes et al. (2008, 2010)	Lab	PI	Most severe: 2 weeks at 20°C/82% RH followed by 2 weeks at 40°C/31% RH	19 months (19 cycles)	5% Na_2SO_4, 5% Na_2CO_3, 5% NaCl
Hartell et al. (2011)	Lab	PI	Stored under ambient conditions	24 months	5% Na_2SO_4
Nehdi et al. (2014); Suleiman et al. (2014)	Lab	PI	One week at 20°C/82% RH followed by one week at 40°C/31% RH	6 months (12 cycles)	5% Na_2SO_4
Bassuoni and Rahman (2016)	Lab	PI	8 h hot/dry stage (40±2°C/35±5% RH) followed by 16 h temperate/humid stage (20±2°C/90±5% RH).	4 months (120 cycles)	10% Na_2SO_4
Obla and O'Neill (2017)	Lab	PI	12 to 15 months at lab environment. Then, one week at 21-24°C/44-72% RH followed by one week at 37-38°C/21-34% RH	27 months	10% Na_2SO_4
Chen et al. (2017)	Lab	PI	The drying portion of samples was kept at 35±1°C/50±5% RH	9 months	10% Na_2SO_4
Lee and Kurtis (2017)	Lab	PI	Specimens were kept at 23±2°C/35±3% RH	65 d	15%, 30% $Ca(NO_3)_2$ 15% Na_2SO_4

* FI: full immersion, W/D: wetting and drying, and PI: partial immersion.

in micro-cracking that facilitated further ingress of solution deep inside specimens, developing chemical sulfate attack products (Bassuoni and Nehdi 2009). The current authors believe that the low *w/b* of the concretes, the mass loss due to salt crystallization was not sufficiently severe to conclusively evaluate the resistance of concrete to PSA from this exposure. Moreover, the long period of exposure might have led to the development of chemical sulfate attack, which may mask PSA, if any.

2.3.3 Partial Immersion Tests

Although the full immersion tests have been used by many researchers to accelerate the attack, the tests have been considered, by others to be less realistic in simulating the natural salt damage that occurs in porous materials such as rock (Goudie 1986; Benavente et al. 2001) and partially embedded concrete (Bassuoni and Nehdi 2009). Continuous partial immersion of specimens has been used as a more representative method of salt damage of concrete in the field, albeit much more slowly and harder to quantify the level of damage. This method allows the wicking effect to occur where the salt solutions migrate through the capillary pores of the samples to the evaporative zone to crystallize. An early application of this exposure was done by Portland Cement Association (PCA) in 1921-1927 where 0.25 m diameter and 0.60 m long cylinders were partially immersed in sulfate soils (Wilson and Cleve 1928), and mixtures with *w/b* higher than 0.45 were severely damaged after 7 years. A recent example for this protocol is the outdoor sulfate exposure in Austin, Texas (Fig. 2.4) where soil trenches were excavated and backfilled with soil of known sulfate salt concentration; specimen sizes of 75×75×300 mm were partially submerged in sodium sulfate soils for up to 18 months and signs of PSA damage were only observed above the soil level (Drimalas 2007). Samples were also placed in calcium and magnesium sulfate, but these conditions did not show any physical damage. Mixtures with

supplementary cementitious materials (SCMs) (20 and 40% Class C fly ash, 20% Class F fly ash) showed more physical damage than the same mixtures without SCMs. In addition, the 0.40 *w/b* mixtures showed less damage than the 0.70 *w/b* mixtures. The *w/b* effect would be more noticeable with mixtures with SCMs compared to the control mixtures.

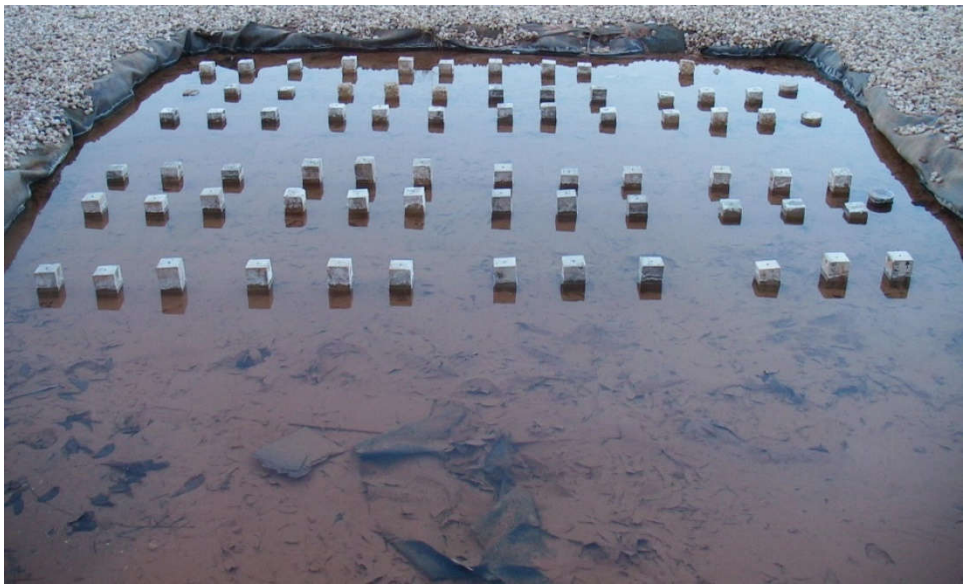

Figure 2.4: Outdoor sulfate exposure site at the University of Texas at Austin containing ~ 5% calcium sulfate, 5% sodium sulfate and 5% magnesium sulfate. [Notes: This picture shows the sodium sulfate trench which has dimensions of 4.5×6 m, and the concrete prisms have dimensions of 75×75×300 mm]

Studies that implemented partial immersion protocols used various environmental conditions. Ferraris et al. (2006) reported on a test developed at NIST where half of the specimen was partially immersed in sulfate solution and exposed to temperature and RH controlled conditions with a film of paraffin oil placed on top of the solution reservoir to avoid evaporation. Constant exposure conditions were tested; specifically, (25±2°C/80±5% RH) and (25±2°C/30±5% RH). It was concluded that the selection of low relative humidity (e.g. 30%) and a temperature below 32.4°C is advisable to accelerate the damage. In Haynes et al. (2008, 2010), cylindrical concrete specimens (75×150 mm) with *w/b* of 0.65 were partially immersed in 5% sodium sulfate, 5% sodium carbonate and 5%

sodium chloride solutions in the laboratory. The exposed parts of specimens were subjected to different ambient conditions. Several environmental conditions were tested including steady-state and cyclic ones based on the different Na_2SO_4-H_2O, Na_2CO_3-H_2O, and NaCl systems. The test program lasted for 3.1 years, divided into two phases [Phase I (1.1–1.5 years) and Phase 2 (up to 3.1 years)]. For the three steady conditions tested, the temperature and RH were 20°C/82%, 20°C/54%, 40°C/74% in Phase I and then changed in Phase II to 20°C/82%, 20°C/32%, and 40°C/31%, respectively. Cyclic exposures involved changing temperature and RH every two weeks during each phase. Moreover, it was reported that surface scaling notably increased under cyclic temperature and RH compared to steady-state conditions with the most severe ambient conditions cycling between 20°C/82% RH and 40°C/31% RH.

Nehdi et al. (2014) applied similar test conditions as in Haynes et al. (2008, 2010), but subjected specimens to one week cycles at 20°C/82% RH followed by one week at 40°C/31% RH. The test continued for six months; however, the maximum mass loss for concrete made with *w/b* of 0.60 was only about 3% indicating the need to conduct the test for more cycles to obtain reliable conclusions regarding the performance of concretes exposed to PSA. Bassuoni and Rahman (2016) proposed a partial immersion test applying more severe exposure conditions to give results on the resistance of concrete to PSA within four months. In this test, one-third of the concrete cylinders' heights were immersed in 10% sodium sulfate solution. The top portion of the specimens was exposed to cyclic temperature and humidity, while the immersed bottom portion was only exposed to cyclic temperature changes. Each cycle continued for 24 h and consisted of two stages: 8 h warm/dry stage (40±2°C/35±5% RH) followed by 16 h temperate/humid stage (20±2°C/90±5% RH). These conditions were selected based on the phase diagram of

sodium sulfate to cause repetitive crystallization of thenardite in the hot/dry environment and mirabilite in the wet/damp room temperature environment. The test results showed considerable scaling within four months; the mass loss value ranged between 7% to 16% and 21% to 25% after 120 cycles for specimens made with *w/b* of 0.40 and 0.50, respectively.

In general, partial immersion tests are representative of PSA on concrete as it occurs in the field. This type of exposure results in a visual appearance of the damage comparable to the damage of full-scale elements (e.g. foundation walls, tunnels, basement walls, or abutments partially immersed in or in contact with salt-containing soils or groundwater). Also, with the appropriate test conditions, the resistance of concrete to PSA can be judged in a relatively short period of time (4 months).

2.4 Indicators for Assessing PSA on Concrete

Visual assessment is one of the common methods to evaluate PSA on concrete. To give a visual rating, a scale has to be used from previous studies (Bassuoni and Rahman 2016) or developed, such as the pictorial rating shown in Figure 2.5. This visual assessment is similar to salt scaling distress for concrete exposed to de-icing chemicals, as described in ASTM C672 (2012). This method is helpful when there is a significant difference in the level of damage among specimens. However, in the case of comparable deterioration levels of the concrete surface, visual assessment does not provide quantitative performance among concrete mixtures, and thus other physical indicators should be applied to capture variations in performance.

Table 2.2: Summary of field studies on PSA of concrete reported in the literature

Source	Type	Test*	Exposure Conditions or Reported Findings	Duration	Salt Solution
Price and Peterson (1968)	Field investigation	--	A conduit constructed in 1914 was reported to be severely damaged by weathering and sulfate attack in parts above the earth fill while buried elements were in good condition	--	Na_2SO_4
Hamilton and Handegord (1968)	Field investigation	--	Rapid penetration of sulfate salts through concrete footings in many house basements in Saskatoon, Canada. Also, a service tunnel in Saskatoon buried in soils of moderate to high sulfate content for 45 years showed significant spalling of the floor and the lower portion of the walls.	--	Na_2SO_4
Tuthill (1978)	Field investigation	--	PSA of a cut-off wall at an earthen canal; the underground concrete wall was intact, while the above ground part suffered severe scaling.	--	Na_2SO_4
Reading (1982)	Field investigation	--	Structural elements in a dam (Montana, USA) that were attacked only by physical activity of sodium sulfate.	--	Na_2SO_4
St John (1982)	Field investigation	--	Severe exfoliation of concrete linings along the walls of three railway tunnels in New Zealand.	--	Na_2SO_4
Novak and Colville (1989)	Field investigation	--	Reported on salt depositions forming on several deteriorated concrete slabs of 20-30 years old residential homes in Southern California.	--	Na_2SO_4
Haynes et al. (1996)	Field investigation	--	PSA damage of concrete foundations and slabs in hundreds of residential homes in Southern and Northern California due to sodium sulfate salt existing in soil.	--	Na_2SO_4
Yoshida et al. (2010)	Field investigation	--	Wide distribution of degradation cases of residential concrete foundations by PSA in Japan.	--	Na_2SO_4
Long et al. (2011)	Field investigation	--	Damage of concrete linings of about 40-year-old railway tunnels	--	Na_2SO_4
Irassar et al. (1996)	Field study	PI in soil + W/D	Weather conditions at site: an annual rainfall of 900 mm, highest temperature of 34°C in summer and lowest of 0°C in winter. Specimens were exposed to about 15 to 20 cycles of wetting and drying per year.	5 years	1% Na_2SO_4
PCA study (Stark 2002)	Field study	PI in soil + W/D	Specimens were half buried and submerged with tap water. Then, specimens were allowed to air dry and submerging was repeated after a drying state was reached. Conditions were 7.2-38°C/10-65% RH. Rainfall ranged from trace to 24 mm. Number of wetting and drying cycles was estimated at 10 to 12 per year.	16 years	6.5% Na_2SO_4

* W/D: wetting and drying, and PI: partial immersion.

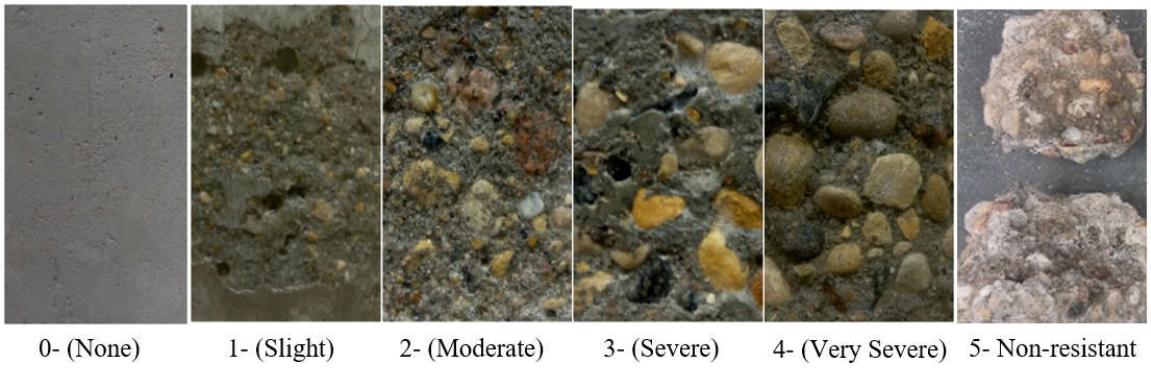

Figure 2.5: Proposed visual ratings for PSA on concrete.

Mass loss expresses the amount of scaled material from the specimens as a result of salt crystallization relative to their initial masses. For tests running for short periods of time (less than 6 months) and/or for mixtures resistant to chemical attack, mass change is a satisfactory and sensitive indicator of PSA damage (Zhutovsky and Hooton 2017a,b + others). However, this parameter might not be appropriate to assess PSA damage when the test is conducted for long durations (one year and beyond) where the concrete mixtures tested are not resistant to chemical attack. Under such conditions, chemical attack might also affect specimens, especially in the immersed portion, resulting in mass loss of concrete (Hartell et al. 2011).

Ferraris et al. (2006) and Obla and O'Neill (2017) applied a scaling distance indicator along with mass loss to characterize the damage of specimens exposed to PSA for long testing duration. For partially immersed specimens, scaling due to PSA occurs near the solution surface and progresses upwards with time and level of damage. Thus, the scaling distance was measured as the vertical distance along the exposed specimen surface between the solution level and the uppermost point to which the scaling front had progressed. Although this procedure could be beneficial to evaluate and compare damage levels for moderate deterioration, it is not possible to be applied in cases of severe damage

as the entire top proportion of the specimens would continually lose mass, and even the height of specimens might be shortened.

The validity of ultrasonic pulse velocity (UPV) and fundamental resonant frequency to assess the resistance of concrete to PSA was studied by Zhutovsky and Hooton (2017b). The UPV durability factor was calculated as a ratio of the squared pulse velocity of the deteriorated specimen relative to the initial conditions. However, no correlation could be established between UPV and the level of damage induced by PSA, since proper contact of transducers with specimen surfaces could not be achieved due to scaling. Moreover, PSA causes disruption to the near surface zone only while the elastic modulus of the core does not significantly decrease leading to poor correlation with the surface damage, as expressed by mass loss. Comparatively, the durability factor based on fundamental resonant frequency (the ratio of the squared frequency of specimen at deteriorated and initial conditions) showed a decreasing trend as PSA progressed; however, the reductions were not proportional to the observed damage. Fundamental resonant frequency is affected by the actual size and mass of the specimen which changes significantly due to PSA; while the calculations were based on the assumption of constant mass and dimensions of the specimen during testing.

For short-term and aggressive PSA exposures, visual ratings combined with mass loss are appropriate to be applied as indicators of the damage level. Although, some visual ratings were previously developed, no description for each level was given; also, there is no corresponding classification for mass loss. Thus, based on analyzing data from the studies summarized in Table 2.1, Table 2.3 presents combined visual rating and mass loss metrics, which are proposed to classify the resistance of concrete to PSA.

Table 2.3: Proposed classification for the resistance of concrete to PSA

Visual Rating*	Description**	Mass Loss (g/m^2)***
0	No scaling	0
1	**Slight scaling**: most surface mortar remaining	≤ 800
2	**Moderate scaling**: with some surface mortar remaining and coarse aggregate starts to appear	>800 to 1500
3	**Severe scaling**: surface mortar is mostly removed, and most coarse aggregate is exposed	>1500 to 2500
4	**Very severe scaling**: deep loss of mortar between coarse aggregate particles and some aggregate is dislodged	> 2500 to 5000
5	**Non-resistant**: loss of significant depth of concrete mortar and coarse aggregate, and/or fracture	> 5000

*The pictorial scheme of damage is shown in Figure 2.5.
** Visual damage in zones of capillary rise in both large-scale concrete elements and laboratory concrete specimens.
***Mass loss of concrete specimens per unit surface area of zone of capillary rise.

2.5 Factors Affecting PSA on Concrete

2.5.1 Parameters Related to Mixture Design

2.5.1.1 Type of cement and water-to-binder ratio (w/b)

Unlike the case of chemical attack, cement type was found to have an insignificant influence on the performance of concrete exposed to PSA. For example, Drimalas (2007) reported that the mixtures partially embedded in sodium sulfate soils and made with ASTM C150 Type I, Type II, or Type V cements did not experience a noticeable difference in PSA damage over 18 months. Also, Lowe (2011) investigated PSA on 100×200 mm cylinders and larger 0.0038 m^3 sized specimens made from various cement types in the outdoor sulfate exposure site in Austin, Texas. It was found that the cement type did not make a difference between mixtures with respect to PSA damage.

Water-to-binder ratio (*w/b*) is an important parameter that influences many aspects of concrete durability including PSA. Lower *w/b* was found to improve the resistance of concrete to PSA (ACI 201.2R 2016; Lee and Kurtis 2017). Bassuoni and Rahman (2016)

reported that decreasing *w/b* from 0.50 to 0.40 notably reduced the mass loss experienced by concrete due to PSA. Zhutovsky and Hooton (2017a) showed much lower mass loss of Type V portland cement mixtures as *w/b* was reduced from 0.50 to 0.45 and 0.40; however, a 0.35 *w/b* mixture performed the same as that made of *w/b* of 0.40. This effect was attributed to the reduced penetrability of concrete. It was indicated that lower *w/b* resulted in concrete with less porosity and reduced pore connectivity, which led to slower rate of solution ingress and lower solution uptake and thus, discounted the volume of crystallizing salt within the surface pores and consequently surface scaling. Reduction of *w/b* below a specific value [e.g. 0.40 in Zhutovsky and Hooton 2017a] could minimize the surface scaling due to PSA. Further reduction of *w/b* may not cause further decrease in mass loss since the absorption and desorption ratios obtained at the higher *w/b* were sufficient to minimize the damage.

In some lab studies (e.g Bassuoni and Rahman 2016), the early-age results may seem to favor systems with high *w/b*, because of the larger pore space available for the deposition of salts and crystallization growth. However, results from (Drimalas 2007; Clement 2009; Lowe 2011; Aguayo 2016) consistently reported that the permeability effect governs the performance of concrete specimens placed in field conditions and subjected to PSA, with the rate of attack increases with the *w/b* of the concrete. Nehdi et al. (2014) reported the same conclusion after partially immersing concretes with *w/b* of 0.30, 0.45, and 0.60 in 5% Na_2SO_4. The highest mass loss was experienced by specimens made with *w/b* of 0.60, followed by those with *w/b* of 0.45. Regarding concrete cylinders made with *w/b* of 0.30, no mass loss was experienced. However, it should be noted that for longer and more severe exposures, concrete with *w/b* of 0.30 may experience some mass loss (Sakr et al. 2019). Figure 2.6 shows an example for the effect of reducing *w/b* on concrete exposed

to PSA conditions for 120 cycles (each cycle consisted of 8 h at 40±2°C/35±5% RH followed by 16 h at 20±2°C/90±5% RH) (Sakr et al. 2019). Thus, reducing the *w/b* will provide better resistance of concrete to PSA and keeping this value below 0.40 is advisable.

(a) (b) (c) (d)

Figure 2.6: PSA damage of concrete cylinders (75×150 mm) made with *w/b* of: (a) 0.60, (b) 0.50, (c) 0.40, and (d) 0.35 exposed to 120 cycles, where each cycle consisted of 8 h at 40±2°C/35±5% RH followed by 16 h at 20±2°C/90±5% RH (Sakr et al. 2019).

2.5.1.2 Supplementary cementitious materials (SCMs)

Regarding the influence of SCMs (e.g. fly ash, slag, and silica fume) on PSA of concrete, there is a discrepancy in the data reported. Nehdi et al. (2014) investigated the effect of replacing cement with different SCMs on concrete under PSA (Table 2.1). Concretes made from ordinary portland cement (OPC) with 8% silica fume, OPC with 25% Class F fly ash, and OPC with 8% metakaolin were tested after 24 h and 28 days of moist curing. At the same *w/b*, addition of SCMs was found to escalate surface scaling of specimens. However, the reported values of mass loss were small without significant variation in the results. For instance, after 6 months, concrete made with *w/b* of 0.45 had mass losses of approximately 0.5%, 1%, and 0.8% for replacement of 8% silica fume, 25% Class F fly ash, and 8% metakaolin, respectively, compared to 0.2% for reference concrete without SCMs. This

makes it difficult to differentiate or categorize the resistance of concrete mixtures according to any rating (e.g. Table 2.3). The authors argued that SCMs refine the pore structure of concrete and increase the capillary rise of solution resulting in higher surface scaling than concretes containing plain OPC. However, no explanation was given why certain types of SCMs (e.g. silica fume) performed better than others (e.g. fly ash and metakaolin). Moreover, for these exposure conditions, the test needed to be conducted for longer periods to obtain a clearer trend in the results. Increasing the period of moist curing reduced the amount of PSA damage (Fig. 5 of Nehdi et al. 2014).

Under the same PSA exposure, Suleiman and Nehdi (2017) tested replacement of OPC with 5%, 10%, 15%, and 20% fly ash, metakaolin, or silica fume in concrete with *w/b* of 0.60. Similar to Nehdi et al. (2014), the reported mass loss values were small due to the mild exposure conditions and thus classification of concrete damage is difficult. However, the trend showed that for all SCMs, the higher replacement ratios caused more deterioration and the same performance of SCMs was found as in Nehdi et al. (2014), i.e. silica fume performed better than metakaolin followed by fly ash.

Zhutovsky and Hooton (2017a) studied the influence of replacing high sulfate-resistant portland cement (Type HS) with Class F fly ash (20% and 40%) on PSA of mortars at *w/b* of 0.40. Specimens were moist cured for 3 days and then seal cured before being fully submerged in 30% sodium sulfate solution subjected to a thermal cycling exposure at 28 days (Table 2.1). Mixtures containing fly ash exhibited significantly higher mass losses compared to the reference mixture (i.e. without fly ash) and those with 20% fly ash showed slightly lower mass loss than mortars with 40% fly ash up to 50 cycles, in agreement with the trends reported by Suleiman and Nehdi (2017). However, the trend reversed afterward such that mass loss of 20% fly ash mortar was slightly higher for the remaining 50 cycles.

The mass loss of the 0.40 *w/b* fly ash mixtures was less than that of the 0.45 reference mixture after 100 cycles. Conversely, the long-term PCA studies (16 years) (Table 2.2) reported inferior performance for field concrete containing 40% Class F fly ash compared to those made with 20% fly ash throughout the entire 16 years of testing (Stark 2002). Using 20% fly ash led to some improvement relative to reference concrete, especially when combined with lower *w/b* (0.39). Also, Lowe (2011) reported that addition of 30% Class F fly ash in 0.0189 m^3 specimens led to the PSA damage as shown in Fig. 2.7. Moreover, Najjar et al. (2017) reported that two-staged concrete specimens incorporating fly ash at dosages of 30% and 50% cured at 56 days exhibited significant surface scaling in PSA exposure.

Figure 2.7: PSA on large 0.0189 m^3 buckets of 0.50 *w/b* concrete: (a) Type V cement with 30% Class F fly ash, and (b) Type V Cement without fly ash. [Note: These samples were placed half submerged in soil in the 5% sodium sulfate trench, Fig. 2.4]

Comparatively, Bassuoni and Rahman (2016) reported that incorporating 30% Class F fly ash into concrete mixtures with *w/b* of 0.40 significantly improved its resistance to PSA in terms of less mass loss with respect to reference concrete (i.e. without fly ash). Irassar et al. (1996) reported that field concrete with *w/b* of 0.52 (Table 2.2) containing

20% Class F fly ash experienced mass loss slightly lower than that of mixtures made with OPC after five years of exposure while concrete with 40% Class F fly ash had considerably higher mass loss with respect to the reference concrete. Folliard and Sandberg (1994) reported that concrete with a *w/b* of 0.30 containing 30% slag cement was highly resistant to accelerated, full submersion testing in sodium sulfate solution, cycled between 5 and 40ºC.

Regarding mortar specimens (*w/b* of 0.40) comprising slag, Zhutovsky and Hooton (2017a) found that their initial mass loss was similar to that of the reference mixtures without slag. However, the rate of mass loss of the sulfate-resistant cement reference mixture exceeded that of mixtures with slag at later stages, with higher cumulative mass loss. The differences between the mortars with 45% and 65% slag were small. On contrary, Irassar et al. (1996) found that mixtures made with *w/b* of 0.52 and with a high replacement ratio of SCMs (40% fine natural pozzolan or 80% slag) were more vulnerable to PSA, hypothesized as due to excessive pore refinement. Moreover, PCA studies reported inferior performance of field concrete containing 40 or 65% slag with the 65% replacement ratio being the worst (Stark 2002). Obla and O'Neill (2017) compared the scaling heights between mixtures made with plain cements (e.g. Types I, II, and V) and those containing fly ash (15%, 20%, 30%) or slag (25%, 35%, 50%) at various *w/b* (0.40, 0.45, 0.50, 0.60). It was stated that fly ash and slag did not improve the concrete resistance to PSA, but they did not result in poorer performance either. However, it should be noted that this conclusion was reached by comparing mixtures that were not made with similar *w/b*.

Tiburzi (2018) investigated the effect of interground limestone addition (3.2% to 21%) in combination with various SCMs on concrete (*w/b* of 0.45) resistance to PSA by partially submerging specimens in sulfate-bearing soil (Na_2SO_4) of a water-soluble sulfate

content greater than 2% by mass of soil, which corresponds to the most severe exposure class (S3) in ACI 318 (2019). It was found that incorporating 21% interground limestone with relatively high amounts of SCMs (35% slag cement, 20% Class C fly ash + 5% silica fume, 40% Class C fly ash) led to a lower degree of degradation. Limestone had a profound impact on the microstructure of the hardened system such that the total volume of the accessible porosity was shown to increase but the average pore size decreased with respect to the Type I cement control system. Similar effects have been observed before in portland-limestone cement (PLC) systems with lower limestone contents, and its impact on the resistance to PSA has been shown to depend on the *w/b*.

Nadelman (2016) showed that high *w/b* (0.60) PLC mixtures exhibited an inferior resistance to PSA due to the increased crystallization pressure that can develop in pores, while no detriment to the performance was observed for companion mixtures at 0.40 *w/b*. In contrast to the higher *w/b* systems, the 0.40 *w/b* PLC mixtures showed secondary sorptivity values lower than the control counterpart. Accordingly, greater driving forces for salt crystallization might be required in low *w/b* limestone-containing systems, attributed to the reduced capillary rise due to the refined and discontinuous pore structure, which would increase the resistance to the attack. Nevertheless, more research is still needed to substantiate this hypothesis.

It is notable that there is contradiction in the reported data regarding the influence of SCMs on PSA of concrete. These variations in results might be attributed to differences in testing methods, curing and exposure conditions, materials types, and replacement ratios. As well, many studies did not quantify the characteristics of the pore structure of concrete exposed to PSA (Nehdi et al. 2014; Obla and O'Neill 2017). The safe SCMs replacement levels at which concrete performs better are still uncertain; however, increasing the moist

curing period should improve performance, but limited data are available on this aspect. The maximum replacement ratio tested for fly ash was 40% with no data available on the performance of higher volumes of fly ash. Further research is still needed to provide better understanding of the behavior of concretes containing SCMs under conditions provoking PSA, considering the curing aspect.

2.5.1.3 Air entrainment

Incorporating air bubbles in the concrete matrix through the use of air-entraining admixtures is another parameter affecting the features of pore structure and thus the damage level to PSA. Drimalas (2007) cast mortar samples with and without air-entraining admixtures and noted that mortars that were air-entrained failed shortly after the non-air-entrained samples in PSA full immersion tests. Folliard and Sandberg (1994), and more recently Bassuoni and Nehdi (2009), reported that air-entraining bubbles in concrete could provide host locations for salt crystals formation and growth, thus initially relieving the generated pressures and delay the concrete damage compared to non-air-entrained concrete. However, this delaying effect diminishes when these bubbles are eventually infilled with salt crystals and or/reaction products. At this stage, crystallization pressure induces rapid micro-cracking and scaling of the cementitious matrix in a manner similar to non-air-entrained concrete (Yang et al. 2016).

2.5.1.4 Features of pore structure

A key parameter associated with PSA damage of porous materials, including concrete, is the porosity as it influences the movement of salt solutions within the material. The pore system in cement-based materials consists of four types of pores. These are: (a) gel pores, 0.5–10 nm; (b) capillary pores, which are mesopores and micropores with average diameters from 10 to 10000 nm; (c) macropores due to deliberately entrained air, 10–

100μm; and (d) macropores due to inadequate compaction [>10μm]. There can also be micro-cracks at aggregate–mortar interfacial zone (ITZ). The gel pores do not influence the concrete adversely through its porosity, while capillary pores and other larger pores/fissures are responsible for transport properties of concrete (Mehta and Monteiro 2014).

A few studies considered the effect of pore structure characteristics, determined by mercury intrusion porosimetry (MIP) on the vulnerability of concrete to PSA. For instance, Bassuoni and Rahman (2016) reported that addition of fly ash to concrete led to higher resistance to PSA. However, when nanosilica was incorporated in the mixture, concrete was more vulnerable to higher crystallization pressure and surface scaling due to excessive refinement of the pore structure. Also, Bassuoni and Nehdi (2009) showed that specific combinations of quaternary binders produced concretes with large proportions of micro-pores (≤ 0.1 μm), and they were extremely vulnerable to PSA. In both studies, the samples were taken from the first 0 to 15 mm, which included many pieces from the first 0-5 mm, where the first sub-florescence zone forms, reflecting the surface and curing effects. Although the salt solution may take longer time to penetrate through refined pore structure, the damage process is significant upon supersaturating micro-pores. This conforms to theoretical studies that predict more PSA damage to occur in porous materials, including concrete, having higher proportions of micro-pores (Folliard and Sandberg 1994; Scherer 1999). Scherer showed mathematically that crystallization pressure is inversely proportional to the pore radius i.e. the crystallization pressure developed in micro-pores is greater than that developed in macro-pores indicating higher vulnerability to PSA (Scherer 1999).

The results of the aforementioned studies should be interpreted with caution considering that the pore structure of concrete/mortar was determined by MIP, which is known to have multiple limitations including different pore shapes other than the assumed cylindrical shape in MIP calculations, and the ink-bottle effect, that results in simultaneous filling of both large and small pores beyond the threshold diameter (Diamond 2000). Hence, it appears that there is still need to conduct more research on a wide range of concrete mixtures using various characterization techniques to identify either a specific range for micro-pores, pore size distribution, or combined parameters that determine vulnerability of concrete to PSA.

2.5.2 Parameters Related to Exposure Conditions

2.5.2.1 Type of salt

The properties of salt solutions have an impact on the crystallization pattern and degree of damage of porous materials. While some salts tend to crystallize on the surface of a porous material (efflorescence) causing little or no damage, others crystallize within the pores below the surface (sub-florescence) leading to significant damage (Rodriguez-Navarro et al. 1996). For example, Haynes et al. (2008, 2010) studied PSA on concrete (*w/b* of 0.65) exposed to three different brine solutions at 5% concentration: sodium sulfate, sodium carbonate, and sodium chloride. Each set of specimens was partially submerged in the corresponding solution under the same exposure environments. Sodium sulfate was found to cause the most aggressive damage followed by sodium carbonate, while sodium chloride had little effect on surface scaling. A saturated solution of sodium carbonate has a vapor pressure of 2.148 kPa at 20^{o}C (Wolf 1966), which is comparable to that of sodium sulfate. However, its viscosity (2.6 cP) (Davis and Kulwiec 1969) at saturation is higher than the

viscosity of saturated sodium sulfate solution (1.834 cP), which might explain the greater tendency of damage associated with sodium sulfate due to easier capillary rise.

In another study (Aye and Oguchi 2011), magnesium sulfate was reported to have low potential to cause PSA compared to sodium sulfate. This might be due to the low degree of supersaturation that magnesium sulfate experiences because of phase changes between epsomite ($MgSO_4.7H_2O$) and hexahydrate ($MgSO_4.6H_2O$). Moreover, at 20^oC, the viscosities of saturated sodium and magnesium sulfates are 1.834 cP and 7.270 cP, respectively, which alludes to the slower transport of magnesium sulfate through the processes of wicking and evaporation resulting in PSA (Aye and Oguchi 2011).

At 23°C/35% RH, Lee and Kurtis (2017) compared PSA damage caused by calcium nitrate and sodium sulfate at concentration of 15%. The damage pattern of mortar (25.4×25.4×254 mm) was different. In the case of sodium sulfate, surface efflorescence covered the specimens' faces to their top without damage. Comparatively, specimens tested in the calcium nitrate solution showed minimal efflorescence; however, they experienced cracking and spalling. Optical microscopy showed deposition of needle-like structures within the cracks and glassy and amorphous deposits on the surface. Needle-like crystals were thought first to exert pressures that opened the cracks and then imbibed moisture which changed them into the glassy deposits. XRD analysis showed that these crystalline precipitates were calcium nitrate hydrate [$Ca(NO_3)_2.2H_2O$ and $Ca(NO_3)_2.4H_2O$]. Further microstructural analysis is still needed to verify this behavior of calcium nitrate salts. It should also be noted that while calcium nitrate was able to cause PSA damage, the authors are not aware of any calcium nitrate field exposures.

2.5.2.2 Ambient conditions

The conditions of the surrounding environment constitute an important factor in the salt crystallization process as they govern the rate of evaporation. It was stated by Sperling and Cooke (1985) that rapid evaporation, which is caused by RH reduction, temperature increase, or both lead to the generation of high crystallization pressure. At the same ambient temperature, the degree of damage caused by sodium sulfate was found to differ considerably with varied humidity conditions (Rodriguez-Navarro and Doehne 1999). For example, when RH is decreased, the evaporation of solution proceeds faster such that salt crystallizes beneath the surface causing more damage, whereas the capillary rise remains constant as it depends on constant properties of the salt and the porous media (e.g. surface tension and pore radius). Thus, reducing RH leads to higher supersaturation ratios. Also, the temperature can influence the rate of evaporation and dictates which salt phase will crystallize. The hydrate phase of sodium sulfate (mirabilite, $Na_2SO_4.10H_2O$), for example, is stable below 32.4°C when in contact with a saturated solution of Na_2SO_4 or when relative humidity is higher than 71% at 20°C. If RH reduces below 71% at 20°C or temperature is 32.4°C or higher at any humidity, mirabilite will be transformed to anhydrous sodium sulfate (thenardite, Na_2SO_4) [Fig. 2.8a]. Repeated conversion between thenardite and mirabilite was reported to escalate the damage as it increases the supersaturation ratio sodium sulfate solution leading to higher crystallization pressure as highlighted by Eq. 2.1 (Rodriguez-Navarro and Doehne 1999). Sodium carbonate has a similar behaviour to sodium sulfate, i.e. depending on the ambient conditions (temperature and RH), the salt can hydrate or dehydrate [Fig. 2.8b]. For instance, changing the conditions from 40°C/31% RH to 20°C/82% RH would cause the salt to convert from thermonatrite ($Na_2CO_3.H_2O$) to natron ($Na_2CO_3.10H_2O$).

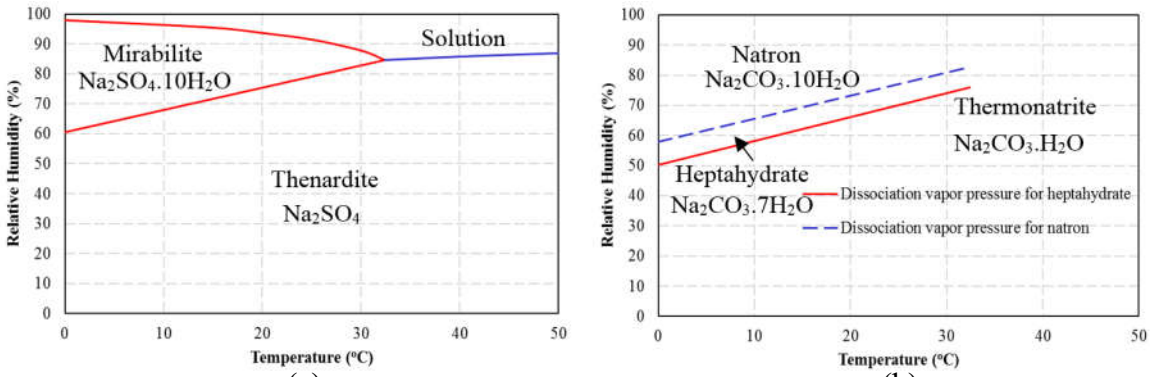

Figure 2.8: Phase diagrams of: (a) sodium sulfate (after Flatt 2002), and (b) sodium carbonate (after Goudie and Viles 1997).

2.6 Protection against PSA Damage

Other than using good quality concrete, procedures and strategies for protection and repair of concrete damage induced by PSA are not widely addressed in the literature. In the PCA field study (Stark 2002), four sealers and coatings were tested: linseed oil, epoxy, alkylalkoxysilane and a proprietary blend of silane, siloxanes, stearates, and aluminum compounds in a blended solvent. In general, the concrete beams coated with linseed oil had better performance than those without a sealer at *w/b* of 0.49 and 0.39 (visual ratings of 4.3 and 1.9, respectively for beams coated with linseed oil, and of 5 and 3.7, respectively for uncoated concrete). At *w/b* of 0.71, beams with epoxy coatings provided performance comparable to those without treatment while at *w/b* of 0.49 and 0.39, epoxy provided performance similar to the linseed oil sealer. Regarding silicon-based sealers, after nine years of exposure, beams treated with alkylalkoxysilane or the proprietary blend had superior performance (visual ratings of 1.3 and 2, respectively) compared to the beams with no surface treatment (visual rating of 4.2); noting that, visual rating of 1 is the best and of 5 is the worst. However, the reasons for these differences in performance were not

explained, but it is expected that sealers were keeping the sodium sulfate out of the concrete.

Haynes (2012) conducted tests on coatings using the test method reported by Haynes et al. (2008), where 5% sodium sulfate solution was used to partially submerge concrete cores while ambient environmental conditions changed from 40ºC/31% RH to 20ºC/82% RH. For these tests the environments cycled every 3 days (a full cycle in 6 days). Cores from field concrete having a design strength of 20.5 MPa (*w/b* ratio was unknown but likely around 0.70) were exposed to ten cycles, which resulted in scaling damage above the solution level. Subsequently, the cores were cleaned with water, dried, and coated using various products: asphaltic emulsion, sodium silicate, lithium silicate, latex paint, latex polymer modified mortar, and acrylic emulsion (with some portland cement and sand), and epoxy. The specimens were then exposed to an additional ten cycles. Major distress occurred in most of the specimens. The successful coatings were acrylic emulsion and epoxy, where the coatings remained intact, and the concrete did not show any scaling. Haynes has since recommended the acrylic emulsion product for repair of numerous foundations affected by PSA because the coating is vapor permeable, UV resistant, has a stucco appearance, and is paintable. Foundation stem walls were repaired by water-blasting the concrete surfaces, chipping scaled areas deeper by a depth of 3 mm, parge coating the concrete surfaces with polymer modified mortar to fill in depressed areas and bug-holes, and applying two coats of acrylic emulsion (as recommended by the manufacturer). The stem walls were coated from 125 mm below soil level to the top of the stem wall, usually 125 mm above soil level. For one project, where concrete masonry units were severely attacked by PSA (sodium sulfate), he followed the performance of the repair for 6 years. The repair performed well without any evidence of reoccurrence of PSA.

Suleiman et al. (2014) studied some surface treatment materials to determine their resistance to PSA conditions. Four materials were tested, namely: silane (water repellent), epoxy (membrane coating), bitumen modified polyurethane (waterproof membrane) and water-based solid acrylic polymer resin (surface sealer). Cylinders (100×200 mm) were coated (while leaving the bottom part uncoated to allow for salt ingress into concrete), partially immersed in a 5% Na_2SO_4 solution and subjected to cyclic temperature and relative humidity as described in Table 2.1. Epoxy and silane were reported to be effective at protecting concrete under PSA conditions because epoxy forms a barrier on the surface of concrete that makes salt penetration difficult while silane performs a hydrophobic function. Regarding the bitumen coating, when it was applied to high-quality concrete (*w/b* of 0.40), similar protection as with epoxy was achieved. However, for concretes with *w/b* of 0.50, the coating detached as when high porosity concrete with higher water content is coated at early-age, water molecules may entrap between the bitumen coating layer and the substrate, leading to emulsification of the bitumen and its stripping, unlike epoxy which has better adhesion (Price 1989). The acrylic-based coating was not adequate in resisting conditions stimulating PSA as the coating exhibited slightly less damage than uncoated concrete. Suleiman et al. (2014) attributed this for the complete failure of the coating after two months of exposure which is consistent with data of Moreira et al. (2006) that showed poor performance of water-based acrylic resin under capillary absorption compared with other types of surface treatment materials. It is also possible that acrylic only partially fills concrete surface pores allowing the salt solution to crystallize in the remaining spaces and thus damaging the acrylic layer. Also, acrylics are relatively brittle materials which might not withstand crystallization pressures. The authors did not provide an explanation regarding the cause of coating failure, but it can be postulated that the coating used,

although effective at decreasing the absorption process, did not significantly reduce the rate of evaporation, as found by Sakr et al. (2019). Nevertheless, it should be mentioned that the test conditions applied in Suleiman et al. (2014) were not sufficiently severe to conclusively judge the suitability of these coatings as the maximum reported mass loss for uncoated specimens was less than 3%.

2.7 Code and Guidelines Provisions for PSA

The topic of PSA has not been explicitly discussed in various guidelines and codes for concrete. However, guidance to low *w/b* mixtures for sulfate exposures also applies to PSA. For example, it was briefly referred to in the previous version of ACI 201.2R (2008) (*Guide to Durable Concrete*). In the latest version (ACI 201.2R 2016), a new chapter was added to address PSA as a separate damage mechanism for concrete. Although ACI 201.2R (2016) gives recommendations for mitigating the damage of concrete from mechanisms such as corrosion, freezing-thawing, etc., it states that "specific recommendations cannot be made to prevent physical salt attack" because of the lack of full understanding of the factors affecting the deterioration of concrete due to PSA. However, the document highlights some findings from the PCA long-term study (Stark 2002) which demonstrated that reducing *w/b* produced concretes with better performance under PSA and for the maturity of the mixtures studied while adding SCMs to concrete had a negative effect relative to plain portland cement concrete. Also, the ACI 201.2R (2016) document recommends applying measures (e.g. capillary breaks or protective coatings) to isolate the concrete from the surrounding media when PSA is likely to occur; however, no generic specifications of these coatings (e.g. silane, epoxy, etc.) are provided since research in this area is limited. In addition, codes such as ACI 301 (2016), ACI 318 (2019), and ACI 350 (2006) do not explicitly mention any specific requirements regarding PSA of concrete.

The Canadian standard, CSA A23.1 (2019), states that when structures are only partially immersed or in contact with only one side with sulfate water or soils, continual evaporation can build up a high concentration of sulfates within concrete. Thus, severe sulfate attack can occur even where the sulfate content is not initially high. Although it is not mentioned directly, this statement is referring to PSA from sulfate salts. Also, it should be noted that the previous statement has existed in the Canadian standard since the 1942 edition (CSA A23.1 1942). However, no distinction is made between chemical and physical sulfate attack and the same recommendations (e.g. lower *w/b*, and the inclusion of SCMs) were given for both cases although the effect of cement type was found to be insignificant in case of PSA and the addition of some SCMs may lead to inferior performance of PSA-exposed elements. In spite of this, no cases of PSA damage have been reported in Canada where low *w/b* concrete made with Type V or SCMs was used. Moreover, this note was mentioned for sulfates only, whereas PSA on concrete may potentially occur when other types of salt exist (e.g. in the case of the tunnel that appears to be damaged by sodium chloride as shown in Fig. 2.2); however, reported occurrences in the latter case are uncommon. If concrete is exposed to sulfates, both PSA and chemical attack may occur together; therefore, the mixture design selected should mutually mitigate both aspects.

Saudi building code, SBC 304 (2018) briefly states that "concrete structures susceptible to salt weathering shall be protected by applying an appropriate barrier coating." Other codes such as European standard (BS EN 206 2013) and Australian Standard (AS 3600 2018) do not address this durability issue of concrete. However, in the Building Research Establishment (BRE) special digest 1 (2005), crystallization of salts (e.g. sulfates and chlorides) was mentioned as a cause for concrete degradation, especially

where concrete of high permeability is partly buried in wet sulfate or chloride bearing ground and partly exposed to air. It was mentioned that applying measures to mitigate chemical sulfate attack (e.g. $w/b \leq 0.50$ and SCMs) should be reasonable to protect concrete against physical degradation due to salt crystallization. However, these measures may not be sufficient in extreme cases, as discussed in this review.

CHAPTER 3: MODELING OF PARAMETERS AFFECTING PHYSICAL SALT ATTACK OF CONCRETE

3.1 Introduction

The resistance of concrete to physical salt attack (PSA) depends on its mixture design parameters, which may be used to establish prescriptive limits [e.g. maximum water-to-binder ratio (*w/b*) and minimum binder content (*B*)]. These parameters, however, affect the resistance of concrete to PSA to different extents. For example, unnoticeable variation in PSA resistance was reported for concrete made with various cement types (I, II, or V) and partially embedded in soil rich in sodium sulfate (Drimalas 2007). Comparatively, reducing *w/b* significantly decreased the mass loss of concrete due to PSA, as highlighted by ACI 201.2R (*Guide to Durable Concrete*) based on the results of long-term field studies by Portland Cement Association (PCA) (Stark 2002; ACI 201.2R 2016).

Nevertheless, the effect of other prescriptive parameters (e.g. *B*) on PSA of concrete has not been fully established in the literature. Also, conflicting data was reported regarding the behavior of concrete containing supplementary cementitious materials (SCMs) under PSA. Zhutovsky and Hooton (2017a) reported that mortars made with 20 and 40% Class F fly ash and cured for 28 days, which were fully submerged in 30% Na_2SO_4 with thermal cycling, had inferior resistance to PSA with 20% fly ash causing slightly higher mass loss than 40%. Conversely, in field studies by PCA (Stark 2002) [16 years] and Irassar et al. (1996) [5 years], incorporating 20% Class F fly ash in concrete partially embedded in sodium sulfate soils led to some improvement relative to plain concrete, while severe damage occurred for concrete containing 40% fly ash. Bassuoni and Rahman (2016) reported that partially immersed concrete cured for 28 days (including 30% Class F fly ash) in 10% Na_2SO_4 (with dry and humid cycles) had reduced mass loss compared to

reference/plain concrete. Mortars comprising 45 and 65% slag had better resistance to PSA than reference specimens with comparable mass loss obtained for both dosages (Zhutovsky and Hooton 2017a). Conversely, PCA field studies reported inferior performance for concrete containing 40 or 65% slag, with the latter being the worst (Stark 2002). Moreover, Nehdi et al. (2014) stated that concrete made with 8% silica fume experienced higher surface scaling than reference concrete (especially, non-cured concrete); in contrast, Sakr et al. (2019) reported that using 8% silica fume notably enhanced the resistance of concrete to PSA. This discrepancy in trends, even for the same replacement ratio, may be attributed to differences in mixture designs, testing conditions, and/or curing regimes, which warrants further research on the effect of SCMs on PSA of concrete under uniform testing conditions to provide a consistent basis of comparison.

The mixture design of concrete impacts its properties (performance parameters) and in turn, the resistance to PSA. The key properties of concrete relevant to PSA are the mechanical, transport, and pore structure characteristics. Scherer (2004) stated that higher tensile capacity of a porous material increases its ability to withstand developed crystallization pressures. However, this effect was not quantified for cement-based materials. Transport properties determine the rates of solution supply and evaporation, which are crucial in the process of PSA on concrete as they control the crystallization location and level, hence the severity of damage. Pore structure features influence the movement of salt brines within concrete. A few studies considered the effect of pore structure features on the vulnerability of concrete to PSA. For instance, Bassuoni and Rahman (2016) indicated that concrete comprising fly ash and nano-silica was susceptible to PSA due to excessive refinement of pore structure, as higher crystallization pressures develop in finer pores (Scherer 2004). A wide range of concrete mixtures needs to be

uniformly tested to determine the dominant performance metrics affecting PSA of concrete and link them to the level of deterioration. For instance, Zeidan et al. (2016) attempted to relate the mass loss of concrete due to PSA to either absorption, porosity, or proportion of micropores; however, weak correlations were obtained, indicating the need for further research in this direction, perhaps on the basis of combined performance parameters.

3.2 Research Significance

ACI 201.2R (2016) does not provide specific guidelines on the mixture design aspects (e.g. SCMs) to produce durable concrete to PSA, as research is still ongoing in this area, albeit using different testing protocols. Mass loss of various concrete mixtures, using the same PSA test, was linked to prescriptive- and performance-based parameters of concrete. The analysis of trends relied on statistical modeling, followed by optimization to identify resilient concrete mixtures under PSA. Key findings from this chapter may contribute to updating current stipulations on PSA, and the models may provide an assistive design tool for selecting concrete mixtures for this exposure.

3.3 Methodology

3.3.1 Statistical Design and Modeling

The experiments were designed using the response surface method (RSM) based on face-centered composite design (FCCD) to evaluate the effect of five key mixture design (prescriptive) parameters [*w/b*, *B*, and dosages of fly ash (*FA*), slag (*SG*), and silica fume (*SF*)] on concrete resistance to PSA. The total number of mixtures was 52, including 36 for the factorial part, 13 axial points, and one central point (replicated three times to estimate the experimental error and improve the reliability of model predictions) (Montgomery 2014). Table 3.1 shows the coding and levels of design variables. The domain/code of each factor ranged from -1 (minimum) to +1 (maximum) with 0 as the

central point. The *w/b* ranged from 0.40 to 0.60, while *B* varied between 300 to 400 kg/m^3. *FA*, *SG,* and *SF* ranged from 0-40%, 0-50%, and 0-10% by mass of binder, respectively. The responses calculated for each mixture were mass loss due to PSA (*ML*) and the time-to-notable scaling (*TNS*) on surface, which corresponded to *ML* of 3% (analogous to moderate scaling of concrete in the PSA test) (Bassuoni and Rahman 2016). In addition, performance parameters [tensile strength, dynamic modulus of elasticity, absorption, desorption, apparent total porosity, proportion of micropores, and threshold pore diameter] were calculated to link them by regression analysis with *ML* and *TNS*.

Table 3.1: Coded and absolute values for the factors analyzed

Parameter	Level		
	-1	0	1
w/b	0.40	0.50	0.60
***B* (kg/m^3)**	300	350	400
***FA* (%)**	0	20	40
***SG* (%)**	0	25	50
***SF* (%)**	0	5	10

Note: *w/b*: water-to-binder ratio, *FA*: fly ash, *SG*: slag, *SF*: silica fume, *B*: binder content.

3.3.2 Materials and Mixtures

The mixtures investigated in this study were prepared using general use (GU) portland cement, Class F *FA*, Grade 100 *SG*, and *SF*, meeting CAN/CSA-A3001 (2018) specifications. Table 3.2 presents the chemical and physical properties of the binders used. Coarse aggregate was natural gravel with max. size, specific gravity, and absorption of 9.5 mm, 2.65, and 2%, respectively. Well-graded river sand was used as fine aggregate with specific gravity, absorption, and fineness modulus of 2.53, 1.5%, and 2.9, respectively. A polycarboxylic superplasticizer complying with ASTM C494 (2019) was added to achieve a target slump of 75 to 125 mm, if needed. Constituent materials were mixed in a mechanical mixer and were cast according to ASTM C192 (2019), demolded after 24 h, and cured at 22±2ºC and relative humidity [RH] ≥ 95% for 56 days to provide extended duration for the reactivity of *FA* and *SG*, as recommended by CSA A23.1/A23.2 (2019).

The proportions of concrete mixtures along with their corresponding coded values and compressive strength (f_c) [as per ASTM C39 (2018)] are listed in Table 3.3.

Table 3.2: Chemical composition and physical properties of binders

	Cement	Fly ash	Slag	Silica fume
Chemical composition				
SiO_2 (%)	19.2	56.0	33.4	92.0
Al_2O_3 (%)	5.0	23.1	13.4	1.0
Fe_2O_3 (%)	2.33	3.6	0.76	1.0
CaO (%)	63.2	10.8	42.2	0.3
MgO (%)	3.3	1.1	5.3	0.6
SO_3 (%)	3.0	0.2	2.4	0.2
$Na_2O_{eq.}$ (%)	0.12	3.2	0.3	0.2
Physical properties				
Mean particle size, µm	13.15	16.56	14.12	0.15
Specific gravity	3.15	2.12	2.87	2.22
Fineness, m^2/kg	390*	290*	492*	20000*

*Blaine fineness.

3.3.3 Testing

The resistance of concrete to PSA was evaluated using the accelerated partial immersion protocol developed in Bassuoni and Rahman (2016), which showed distinctive trends for the resistance of concrete to PSA in a relatively short duration. In that study, sodium sulfate was selected because it was reported as the most destructive salt that causes PSA compared to other salts (e.g. NaCl and $MgSO_4$). Each specimen was placed in a 50 mm plastic container containing 10% Na_2SO_4 solution. Containers' lids were circularly cut with an opening nearly equal to the cylinder diameter to minimize solution evaporation. The exposed part of specimens (100 mm) was subjected to cyclic conditions provoking repetitive crystallization of thenardite (Na_2SO_4) and mirabilite ($Na_2SO_4.10H_2O$). Exposure continued for 120 days; each cycle (24 h) consisted of two consecutive stages: 8 h dry stage (40±2°C and 35±5% RH) followed by 16 h humid stage (20±2°C and 90±5% RH). Due to continuous uptake and evaporation, the solution was frequently replenished to maintain the

Table 3.3: Proportions of mixtures per cubic meter of concrete

Mixture ID.	Mixture code	Cement (kg)	Water (kg)	FA (kg)	SG (kg)	SF (kg)	Fine/coarse aggregate (kg)	f_c (MPa)
0.6GU-300	1, -1, -1, -1, -1	300	180	0	0	0	650/1200	28.8
0.6GU-400	1, 1, -1, -1, -1	400	240	0	0	0	410/1200	35.8
0.6SF10-300	1, -1, -1, -1, 1	270	180	0	0	30	640/1200	33.8
0.6SF10-400	1, 1, -1, -1, 1	360	240	0	0	40	400/1200	41.2
0.6FA20-300	1, -1, 0, -1, -1	240	180	60	0	0	625/1200	31.6
0.6FA40-300	1, -1, 1, -1, -1	180	180	120	0	0	602/1200	28.8
0.6FA40-400	1, 1, 1, -1, -1	240	240	160	0	0	346/1200	33.9
0.6SG25-300	1, -1, -1, 0, -1	225	180	0	75	0	644/1200	32.0
0.6SG50-300	1, -1, -1, 1, -1	150	180	0	150	0	638/1200	27.1
0.6SG50-400	1, 1, -1, 1, -1	200	240	0	200	0	395/1200	32.9
0.6FA40SF10-300	1, -1, 1, -1, 1	150	180	120	0	30	592/1200	30.7
0.6FA40SF10-400	1, 1, 1, -1, 1	200	240	160	0	40	332/1200	36.7
0.6FA20SG25SF5-350	1, 0, 0, 0, 0	175	210	70	87.5	17.5	489/1200	35.1
0.6SG50SF10-300	1, -1, -1, 1, 1	120	180	0	150	30	628/1200	27.3
0.6SG50SF10-400	1, 1, -1, 1, 1	160	240	0	200	40	381/1200	31.8
0.6FA40SG50-300	1, -1, 1, 1, -1	30	180	120	150	0	590/1200	12.4
0.6FA40SG50-400	1, 1, 1, 1, -1	40	240	160	200	0	330/1200	12.6
0.6FA40SG50SF10-300	1, -1, 1, 1, 1	0	180	120	150	30	580/1200	9.2
0.6FA40SG50SF10-400	1, 1, 1, 1, 1	0	240	160	200	40	316/1200	10.3
0.5GU-350	0, 0, -1, -1, -1	350	175	0	0	0	620/1200	32.1
0.5FA20SF5-350	0, 0, 0, -1, 0	262.5	175	70	0	17.5	587/1200	34.5
0.5FA40SF10-350	0, 0, 1, -1, 1	175	175	140	0	35	553/1200	31.9
0.5SG25SF5-350	0, 0, -1, 0, 0	245	175	0	87.5	17.5	608/1200	36.8
0.5SG50SF10-350	0, 0, -1, 1, 1	140	175	0	175	35	595/1200	33.4
0.5FA20SG25-350	0, 0, 0, 0, -1	192.5	175	70	87.5	0	586/1200	36.0
0.5FA20SG25SF5-300	0, -1, 0, 0, 0	150	150	60	75	15	693/1200	32.4
0.5FA20SG25SF5-350*	0, 0, 0, 0, 0	175	175	70	87.5	17.5	580/1200	37.7
0.5FA20SG25SF5-400	0, 1, 0, 0, 0	200	200	80	100	20	467/1200	40.2
0.5FA20SG25SF10-350	0, 0, 0, 0, 1	157.5	175	70	87.5	35	574/1200	36.0
0.5FA40SG25SF5-350	0, 0, 1, 0, 0	105	175	140	87.5	17.5	522/1200	26.8
0.5FA20SG50SF5-350	0, 0, 0, 1, 0	87.5	175	70	175	17.5	573/1200	24.5
0.4GU-300	-1, -1, -1, -1, -1	300	120	0	0	0	806/1200	39.7
0.4GU-400	-1, 1, -1, -1, -1	400	160	0	0	0	618/1200	45.5
0.4SF10-300	-1, -1, -1, -1, 1	270	120	0	0	30	796/1200	45.9
0.4SF10-400	-1, 1, -1, -1, 1	360	160	0	0	40	604/1200	52.9
0.4FA40-300	-1, -1, 1, -1, -1	180	120	120	0	0	758/1200	38.5
0.4FA20-400	-1, 1, 0, -1, -1	320	160	80	0	0	585/1200	47.2
0.4FA40-400	-1, 1, 1, -1, -1	240	160	160	0	0	554/1200	45.5
0.4SG50-300	-1, -1, -1, 1, -1	150	120	0	150	0	794/1200	37.9
0.4SG25-400	-1, 1, -1, 0, -1	300	160	0	100	0	610/1200	47.5
0.4SG50-400	-1, 1, -1, 1, -1	200	160	0	200	0	602/1200	44.2
0.4FA40SF10-300	-1, -1, 1, -1, 1	150	120	120	0	30	748/1200	42.9
0.4FA40SF10-400	-1, 1, 1, -1, 1	200	160	160	0	40	540/1200	50.3
0.4FA20SG25SF5-350	-1, 0, 0, 0, 0	175	140	70	87.5	17.5	671/1200	47.4
0.4SG50SF10-300	-1, -1, -1, 1, 1	120	120	0	150	30	784/1200	35.2
0.4SG50SF10-400	-1, 1, -1, 1, 1	160	160	0	200	40	588/1200	44.1
0.4FA40SG50-300	-1, -1, 1, 1, -1	30	120	120	150	0	745/1200	16.9
0.4FA40SG50-400	-1, 1, 1, 1, -1	40	160	160	200	0	538/1200	18.1
0.4FA40SG50SF10-300	-1, -1, 1, 1, 1	0	120	120	150	30	736/1200	12.0
0.4FA40SG50SF10-400	-1, 1, 1, 1, 1	0	160	160	200	40	525/1200	14.5

*The central mixture was repeated three times.

Note: f_c: compressive strength.

level to 50 mm. Also, fresh solution was used every 30 cycles. The final *ML* of specimens was calculated relative to the initial mass before exposure along with *TNS* as damage indicators.

The performance parameters were determined after the specified curing period (56 days). Splitting tensile strength (f_{st}) of triplicate cylinders (100×200 mm) was determined as per ASTM C496 (2017). Also, the dynamic modulus of elasticity (E_d) was calculated for triplicate prisms (100×100×350 mm) by determining the transverse resonant frequency (ASTM C215 2019). As PSA significantly depends on the rate of solution supply from the surroundings and the evaporation rate as per the ambient conditions, an absorption/desorption experiment was performed to give an indication of those rates for different mixtures. For absorption, concrete disks (75×50 mm) were dried at 50±2ºC and 40%±5% RH until constant mass (difference in mass in two successive days ≤0.1%). Dry specimens were then immersed in 10% Na_2SO_4 for 48 h. For desorption, specimens were fully immersed in 10% Na_2SO_4 until constant mass followed by drying at the same PSA testing conditions (40±2°C and 35±5% RH) for 48 h. The absorption (A)/desorption (D) percentage at a time (t) was calculated as: $100\times (m_t - m_i)/m_i$, where m_i and m_t are the initial and final masses, respectively.

The features of pore structure [percentage of total porosity (P), proportion of micropores (P_{micro}) [pores < 0.1 μm], and threshold pore diameter (ϕ_{thd})] for specimens were determined after 56 days by mercury intrusion porosimetry (MIP). Small pea-sized chunks (4-7 mm) taken from at least two concrete cylinders of each mixture were used as test samples. Samples were oven dried until constant mass at 45±2°C to reduce the drying shrinkage cracks associated with higher temperatures. By assuming a cylindrical geometry of pores, a mercury contact angle of 130° and surface tension of 485 dynes/cm, the high-

pressure limit (228 MPa) of the equipment used yields a pore radius of about 3 nm, implying intrusion of the smallest size of capillary pores (5 nm).

The mechanism of damage and alteration of hydration compounds were investigated by mineralogical, thermal, and microscopy analyses. The mineral phases within the cementitious matrix were identified by X-ray diffraction (XRD, Cu-Kα) with a scanning rate of 0.5°/min and quantified by differential scanning calorimetry (DSC) with an incremental heating rate of 10°C/min on powder samples extracted from the surface (0-5 mm) of various specimens. The powder samples were prepared from fracture pieces (carefully extracted not to include obvious coarse aggregate), which were pulverized to fine powder passing through sieve #200 (75 μm). The findings from XRD and DSC analyses were supplemented by microanalysis from scanning electron microscopy (SEM) equipped with energy-dispersive X-ray analysis (EDX) on carbon-coated fracture pieces extracted from the affected surface layer of specimens.

3.4 Results

3.4.1 Prescriptive-Based Models

The average experimental *ML* and *TNS* for the mixtures are listed in Table 3.4. The general form of each response model was expressed by:

$$y = \beta_0 + \sum \beta_i x_i + \sum \beta_{ij} x_i x_j + \sum \beta_{ii} x_i x_i + \epsilon \qquad \text{Eq. (3.1)}$$

where, y is the response (*ML* or *TNS*), x represents independent variables, β_0 is a constant for the model intercept, while β_i, β_{ij}, and β_{ii} represent the linear, interaction, and quadratic regression coefficients of the contribution of variables to responses, respectively, with i = 1 to 5; $j<i$ = 2 to 5, and ϵ is the model random error term for uncontrolled factors. The coefficients corresponding to multiple factors were determined by non-linear regression analysis (polynomial function). For each mixture, three values of each response

Table 3.4: Average experimental results of mixtures

Mixture ID.	f_{st} (MPa)	E_d (GPa)	A (%)	D (%)	P (%)	P_{micro} (%)	ϕ_{thd} (µm)	ML (%)	TNS (d)
0.6GU-300	2.7	31.7	8.1	3.6	21.8	31.2	1.20	19.1	34
0.6GU-400	3.2	37.1	6.1	3.0	19.5	35.9	1.00	14.7	45
0.6SF10-300	3.2	37.8	6.6	2.8	17.8	42.8	0.85	13.5	45
0.6SF10-400	3.6	41.5	5.1	2.6	15.5	53.7	0.67	10.8	66
0.6FA20-300	2.8	34.6	7.0	3.2	20.2	37.5	1.08	16.2	40
0.6FA40-300	2.6	30.9	8.4	3.7	22.3	33.5	1.10	18.7	32
0.6FA40-400	3.1	36.6	6.5	3.3	21.8	36.1	1.00	15.8	45
0.6SG25-300	3.0	35.0	7.1	3.2	19.8	40.4	0.95	16.0	43
0.6SG50-300	2.6	31.3	8.6	3.8	24.0	27.7	1.22	19.5	32
0.6SG50-400	3.0	37.2	7.0	3.3	20.7	33.8	1.05	15.7	42
0.6FA40SF10-300	2.9	32.3	7.0	3.5	19.5	40.1	0.95	16.9	42
0.6FA40SF10-400	3.4	39.9	6.1	2.9	17.2	43.7	0.85	13.5	60
0.6FA20SG25SF5-350	3.2	37.5	6.3	3.0	18.5	46.2	0.78	15.1	45
0.6SG50SF10-300	2.5	28.7	9.3	4.2	24.3	23.6	1.32	21.6	30
0.6SG50SF10-400	3.0	35.5	7.4	3.6	21.2	31.4	1.13	16.5	38
0.6FA40SG50-300	1.2	15.0	13.0	6.1	28.8	7.3	2.90	22.1	25
0.6FA40SG50-400	1.5	15.5	11.8	5.8	28.6	8.5	2.68	21.9	25
0.6FA40SG50SF10-300	0.9	10.3	17.8	8.9	30.1	5.1	3.00	23.5	22
0.6FA40SG50SF10-400	1.0	11.9	15.9	7.9	29.5	7.8	2.70	22.6	24
0.5GU-350	3.0	34.6	6.7	3.2	18.5	41.3	0.90	15.4	45
0.5FA20SF5-350	3.2	38.4	6.2	3.0	17.8	49.0	0.65	13.2	52
0.5FA40SF10-350	3.0	36.9	6.5	3.0	18.3	47.7	0.83	14.5	44
0.5SG25SF5-350	3.8	43.9	5.3	2.4	15.2	57.1	0.50	10.9	60
0.5SG50SF10-350	2.7	36.5	7.4	3.2	20.0	39.0	0.90	16.5	38
0.5FA20SG25-350	3.5	41.8	6.1	2.6	17.0	50.5	0.70	12.5	49
0.5FA20SG25SF5-300	3.1	37.6	6.4	2.9	18.6	44.9	0.81	13.7	55
0.5FA20SG25SF5-350	3.5	42.2	5.6	2.5	16.3	53.8	0.60	11.0	64
0.5FA20SG25SF5-350	3.8	43.9	5.7	2.6	16.9	54.8	0.60	11.1	62
0.5FA20SG25SF5-350	3.4	42.0	5.3	2.6	16.5	54.3	0.58	10.0	72
0.5FA20SG25SF5-400	4.0	47.2	4.6	2.2	14.2	61.6	0.40	8.5	80
0.5FA20SG25SF10-350	3.3	41.3	5.5	2.8	16.9	54.0	0.60	10.2	68
0.5FA40SG25SF5-350	2.8	31.4	7.5	3.3	20.1	39.0	1.03	18.4	42
0.5FA20SG50SF5-350	3.0	35.5	7.0	3.1	21.2	32.5	0.10	16.6	45
0.4GU-300	3.8	42.3	5.3	2.5	15.4	56.4	0.55	9.8	70
0.4GU-400	4.6	47.8	4.5	2.1	13.2	64.4	0.35	7.7	82
0.4SF10-300	4.4	46.4	3.9	2.0	11.6	73.2	0.13	7.6	85
0.4SF10-400	5.2	50.9	3.1	1.8	9.3	78.3	0.06	2.8	120
0.4FA40-300	3.7	41.2	5.3	2.5	16.0	59.3	0.50	10.5	66
0.4FA20-400	4.8	50.0	3.8	2.1	12.7	70.4	0.20	6.6	90
0.4FA40-400	4.3	45.9	4.5	2.2	13.8	67.2	0.27	8.0	80
0.4SG50-300	3.7	43.0	5.5	2.7	16.7	54.6	0.48	11.3	65
0.4SG25-400	4.8	50.5	3.7	1.9	12.0	74.6	0.10	6.4	92
0.4SG50-400	4.1	43.6	4.7	2.2	14.5	66.0	0.30	8.8	78
0.4FA40SF10-300	4.2	44.5	4.1	2.3	12.7	70.1	0.20	8.5	80
0.4FA40SF10-400	4.9	47.7	3.4	2.0	11.1	75.1	0.10	4.9	102
0.4FA20SG25SF5-350	4.5	45.3	4.1	2.1	12.2	72.2	0.16	7.8	90
0.4SG50SF10-300	3.5	41.7	5.9	2.9	16.8	55.3	0.57	11.8	60
0.4SG50SF10-400	3.9	42.3	5.2	2.1	14.2	64.7	0.35	9.3	75
0.4FA40SG50-300	1.6	21.5	9.7	4.8	19.4	20.8	1.80	15.4	40
0.4FA40SG50-400	1.5	21.9	8.9	4.5	17.9	22.5	1.65	13.9	42
0.4FA40SG50SF10-300	1.5	15.9	11.4	5.3	21.7	17.1	2.10	17.1	35
0.4FA40SG50SF10-400	1.2	17.3	10.3	5.0	19.3	18.7	1.95	13.5	35

Note: f_{st}: splitting tensile strength, E_d: dynamic modulus of elasticity, A: absorption, D: desorption, P: total porosity, P_{micro}: proportion of micropores, ϕ_{thd}: threshold pore diameter.

were inputted in the database representing the three replicates tested, i.e. modeling was based on 156 points (52 mixtures by 3 replicates). Analysis of variance (ANOVA) was performed to determine the significant variables and interactions for adoption in the modeling equations. Significant factors were defined to have p-value < 0.05, which indicates less than 5% probability (i.e. 95% confidence level) that the null assumption is correct. Accordingly, the models yielded high coefficients of determination (R^2), indicating systematic change of factors with experimentation (Montgomery 2014). Table 3.5 shows the initially derived regression coefficients and corresponding p-values, based on a quadratic model. The best fit responses for repeated analysis after eliminating insignificant factors are given in Eqs. (3.2, 3.3), where predictors are in coded values (i.e. -1 to +1):

$$\sqrt{ML}\,(\%) = 3.4 + 0.55w/b - 0.22B + 0.22FA + 0.35SG - 0.11SF + 0.09FA \cdot SG + 0.11FA \cdot SF + 0.16SG \cdot SF - 0.26B^2 + 0.22FA^2 + 0.3SG^2 \quad \text{Eq. (3.2)}$$

R^2=0.93

$$\log_{10} TNS\,(d) = 1.79 - 0.13w/b + 0.05B - 0.06FA - 0.1SG + 0.02SF - 0.05FA \cdot SG - 0.02FA \cdot SF - 0.04SG \cdot SF + 0.06B^2 - 0.06FA^2 - 0.1SG^2 \quad \text{Eq. (3.3)}$$

R^2=0.92

RSM was used to develop isoresponse surfaces (contour plots) for *ML* and *TNS* based on Eqs. (3.2, 3.3), respectively. Four exemplar graphs were plotted for each response (Figs. 3.1 and 3.2; other examples are in Appendix A: Figs. A.1-A.4), showing the effect of different mix design variables on the performance of concrete under PSA. For all plots, *w/b* was fixed as the abscissa, while the ordinate was assigned to other factors. The statistical models showed that *ML* and *TNS* were significantly influenced by the factors studied (Table 3.5).

Table 3.5: Initial derived coefficients and corresponding *p*-values based on ANOVA

Source	$\sqrt{ML}$ (%)	*p*-value	$\log_{10} TF\ (d)$	*p*-value
Intercept	**3.43**	--	**1.78**	--
w/b	**0.548**	**< 0.0001**	**-0.131**	**< 0.0001**
B	**-0.224**	**< 0.0001**	**0.048**	**< 0.0001**
FA	**0.216**	**0.0001**	**-0.062**	**0.0001**
SG	**0.351**	**< 0.0001**	**-0.096**	**< 0.0001**
SF	**-0.107**	**0.0012**	**0.023**	**0.0035**
w/b*B	0.035	0.215	-0.006	0.499
w/b*FA	-0.022	0.744	-0.004	0.695
w/b*SG	-0.061	0.469	0.002	0.798
w/b*SF	0.028	0.147	-0.024	0.215
FA*B	0.047	0.587	-0.004	0.653
FA*SG	**0.145**	**0.001**	**-0.046**	**< 0.0001**
FA*SF	**0.111**	**0.008**	**-0.022**	**0.022**
SG*B	0.053	0.062	-0.018	0.068
SG*SF	**0.158**	**0.007**	**-0.041**	**0.002**
SF*B	-0.044	0.148	-0.003	0.706
FA*SG*SF	-0.043	0205	0.0006	0.943
w/b^2	-0.102	0.471	0.033	0.137
B^2	**-0.244**	**0.002**	**0.051**	**0.003**
FA^2	**0.307**	**0.037**	**-0.069**	**0.045**
SG^2	**0.389**	**0.010**	**-0.103**	**0.010**
SF^2	-0.027	0.850	-0.009	0.365

Note: bold numbers denote statistical significance

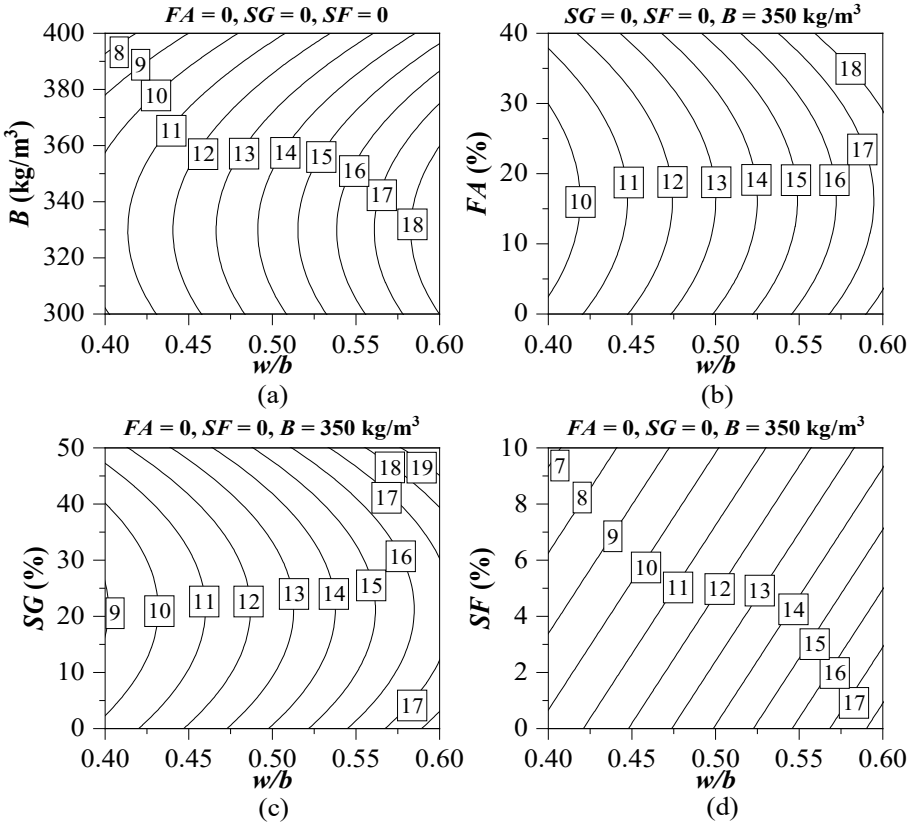

Figure 3.1: Exemplar isoresponse plots showing the effect of *w/b* and: (a) *B*, (b) *FA*, (c) *SG*, and (d) *SF* on mass loss (%) of concrete under PSA.

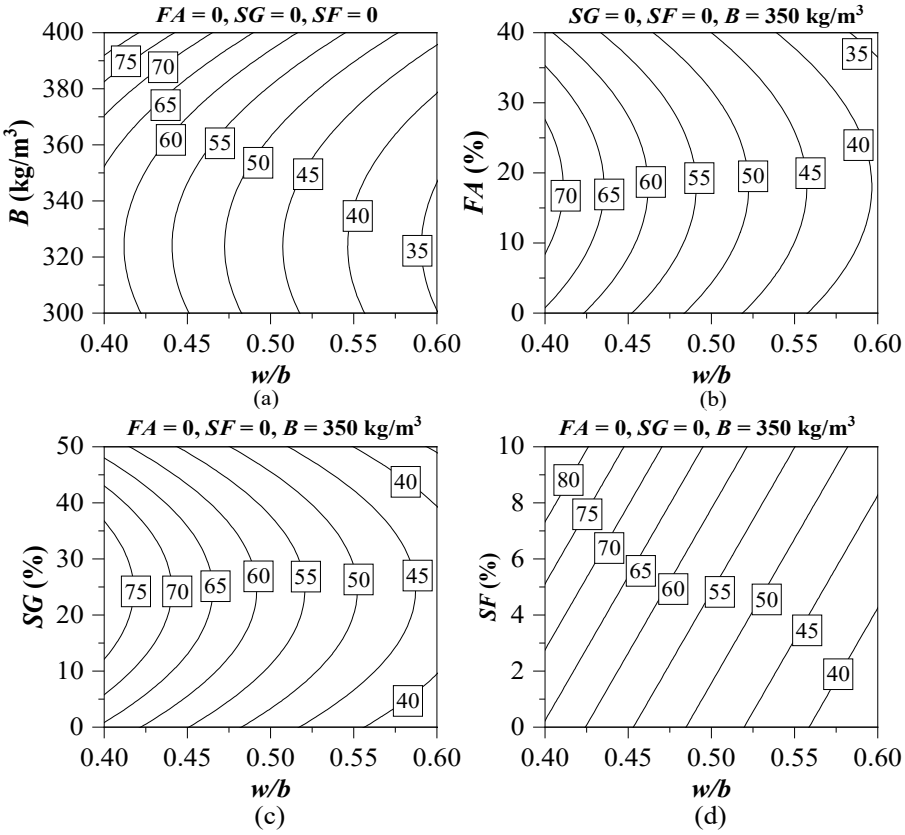

Figure 3.2: Exemplar isoresponse plots showing the effect of *w/b* and: (a) *B*, (b) *FA*, (c) *SG*, and (d) *SF* on time-to-notable scaling (days) of concrete under PSA.

Increasing the *w/b* escalated PSA damage of concrete. For example, concrete made with *B* of 350 kg/m^3 without SCMs in Fig. 3.1a had average *ML* of 14% at *w/b* of 0.50 (corresponding *TNS* of 47 days, Fig. 3.2a) compared to 18.5% for *w/b* of 0.60 (corresponding *TNS* of 36 days, Fig. 3.2a). This influence of *w/b* was also indicated in Fig. 3.3a, which shows exemplar variation of *ML* (Fig. A.5 shows the equivalent graph for *TNS*) with *w/b,* considering the limits of *B*. Regarding the effect of *B*, increasing its amount to approximately 340 kg/m^3 had marginal impact on *ML* and *TNS*; higher *B* relatively improved the resistance of concrete to PSA (Fig. 3.3b). For example, concrete with *w/b* of 0.60 had average *ML* of 18.1% and 18.6% at *B* of 300 and 340 kg/m^3, respectively, whereas using *B* of 400 kg/m^3 at the same *w/b* reduced *ML* of concrete by 22% (Figs 3.1a).

Correspondingly, the average *TNS* was 35, 34, and 47 days at *B* of 300, 340, and 400 kg/m^3, respectively (Fig. 3.2a).

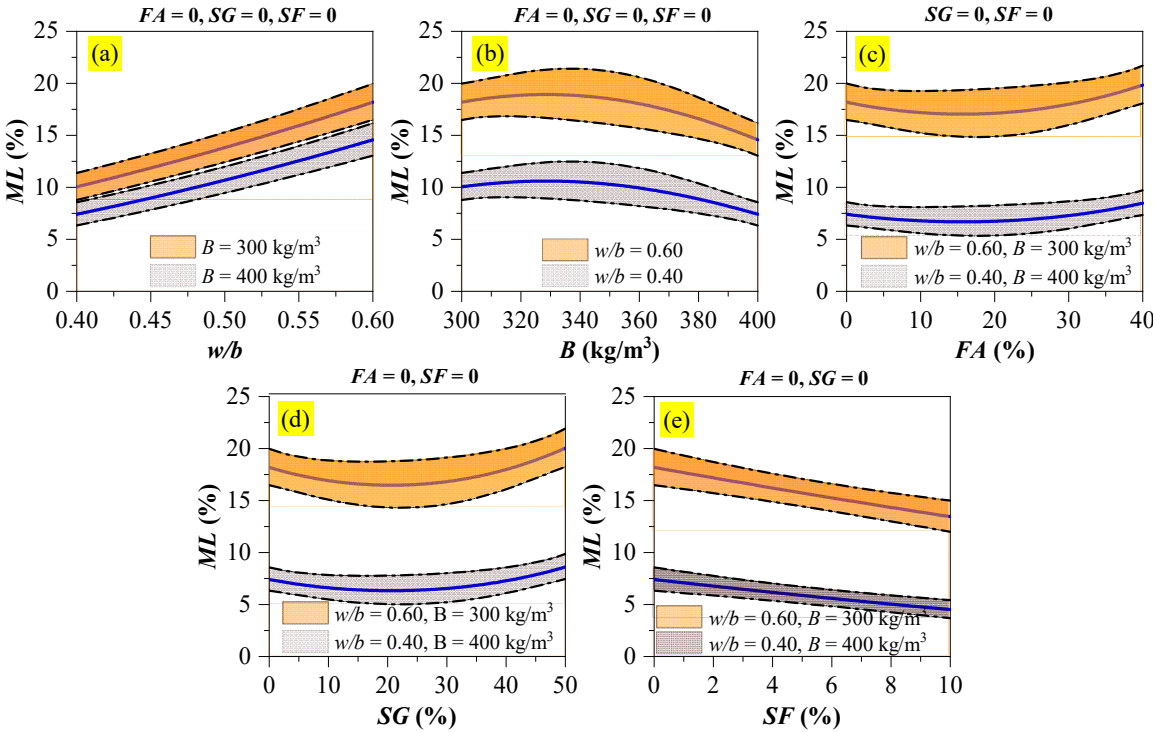

Figure 3.3: Upper and lower bands for the effect of: (a) *w/b*, (b) *B*, (c) *FA*, (d) *SG*, and (e) *SF* on mass loss (%) of concrete under PSA.

At fixed *w/b* and *B*, incorporating *FA* or *SG* in binary binders reduced the scaling of concrete up to specific dosages, beyond which the deterioration level increased (e.g. Figs. 3.1b,c and 3.2b,c at a fixed *B* of 350 kg/m^3). These limits were also notable in the analysis of lower and upper bands, and depended on the combination of *w/b* and *B*. For instance in Figs. 3.3c,d, at *w/b* of 0.60 and *B* of 300 kg/m^3, the minimum *ML* experienced by concrete mixtures comprising 20% *FA* or 25% *SG* was 14.7% and 14.3% (lower bound), respectively, compared to a maximum *ML* of 20% (upper bound) for plain concrete, corresponding to 27 to 29% reduction in *ML* with addition of *FA* and *SG*. However, increasing the dosages of *FA* and *SG* to 40% and 50% respectively led to marginally lower resistance to PSA (maximum *ML* of 21.6% and 21.8%, respectively) than reference

concrete, which was rendered insignificant by ANOVA at a significance level (α) of 0.05, where the *F*-values were 0.38 and 0.51, respectively, compared to a critical threshold (F_{cr}) of 7.7. At *w/b* of 0.40 and *B* of 400 kg/m^3, which represents the lower band of *ML*, the limits of improvement of *FA* and *SG* seemed to increase by 5%, i.e. 25 and 30%, respectively. In addition, a close range of *ML* (7.4 to 9.8%) was obtained for concrete with 40% *FA* and 50% *SG*, which was comparable to the range of *ML* (6.3 to 8.6%) for concrete without SCMs (Figs. 3.3c,d).

Increasing the dosage of *SF* in binary binders was consistently beneficial at decreasing the vulnerability of concrete to PSA (e.g. Figs. 3.1d and 3.2d); however, this effect was distinctive beyond a dosage of 5%. At *w/b* of 0.60 and *B* of 300 kg/m^3, using 5% *SF* decreased *ML* by an average of 14%, compared to reference concrete, while using 10% *SF* further improved the average reduction to 27%. Similar trend was observed for the lower band, where the average reduction in *ML* was 22 and 39% for 5 and 10% *SF*, respectively, compared to plain concrete (Fig. 3.3e).

The interaction effects of SCMs were significant for the ternary case, while insignificant for the quaternary case (Table 3.5); thus, the latter was eliminated from the developed models and analysis. For ternary binders (visual examples are in Fig. A.6), the combination and volume of SCMs determined the resistance of concrete to PSA as indicated for example, by the contour plots in Fig. 3.4 for the worst-case scenario (*w/b* of 0.60 and *B* of 300 kg/m^3). Figures 3.4a,d showed that combining *FA* and *SG* with a total replacement ratio below 40% yielded relatively better *ML* and *TNS* to plain concrete and binary binders comprising 40% *FA* or 50% *SG*. Higher volume of SCMs compromised the resistance to PSA, with maximum damage occurred when 40% *FA* and 50% *SG* were combined. Adding 10% *SF* to any dosage of *FA* reduced the susceptibility of concrete to

PSA, compared to binary binders with *FA*, whereas using higher dosages of *FA* (> 25%) with *SF* reduced the performance compared to binary binders with *SF*. The best performance was obtained for 10% *SF* combined with 10-20% *FA*, where the reduction in *ML* and increase in *TNS* was 27% and 50%, respectively, compared to plain concrete (Figs. 3.4b,e). For mixed *SG* and *SF* (Figs. 3.4c,f), the minimum *ML* and maximum *TNS* were obtained for *SG* dosages below 25% combined with 10% *SF* (23% lower and 44% higher than that of plain concrete, respectively).

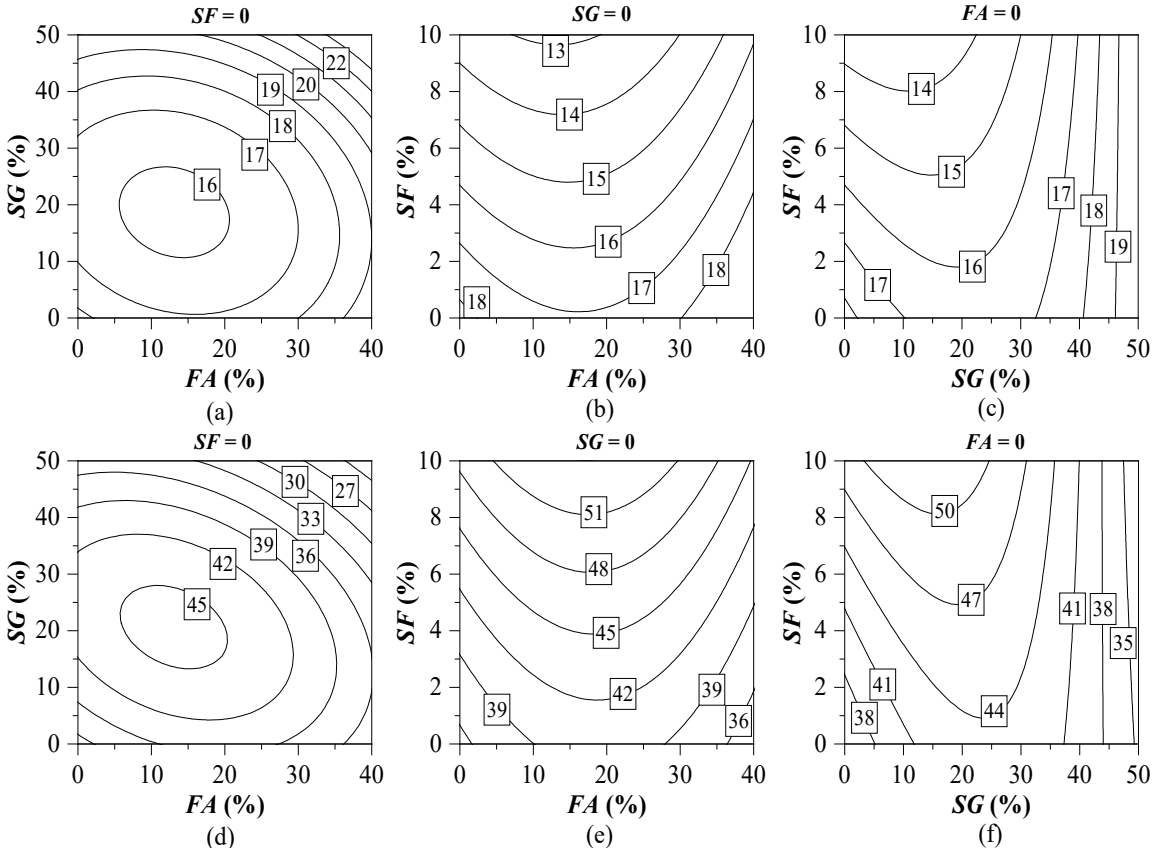

Figure 3.4: Effect of ternary binders on mass loss (%) [a, b, and c], and corresponding time-to-notable scaling (days) [d, e, and f] of concrete at *w/b* of 0.60 and *B* of 300 kg/m^3.

Figure 3.5 shows the condition of exemplar specimens at the end of exposure along with visual rating based on a scale of 0 (no scaling) to 5 (severe scaling without/with fracture), highlighting the effect of mixture design parameters on the resistance of concrete

to PSA. The visual state of specimens complied with model predictions/trends: lower *w/b* and higher *B* enhanced the resistance to PSA; binary binders incorporating 20% *FA* or 25% *SG* improved the visual condition of specimens, while 40% *FA* and 50% *SG* showed similar resistance to PSA; using 10% *SF* notably enhanced the visual appearance of specimens.

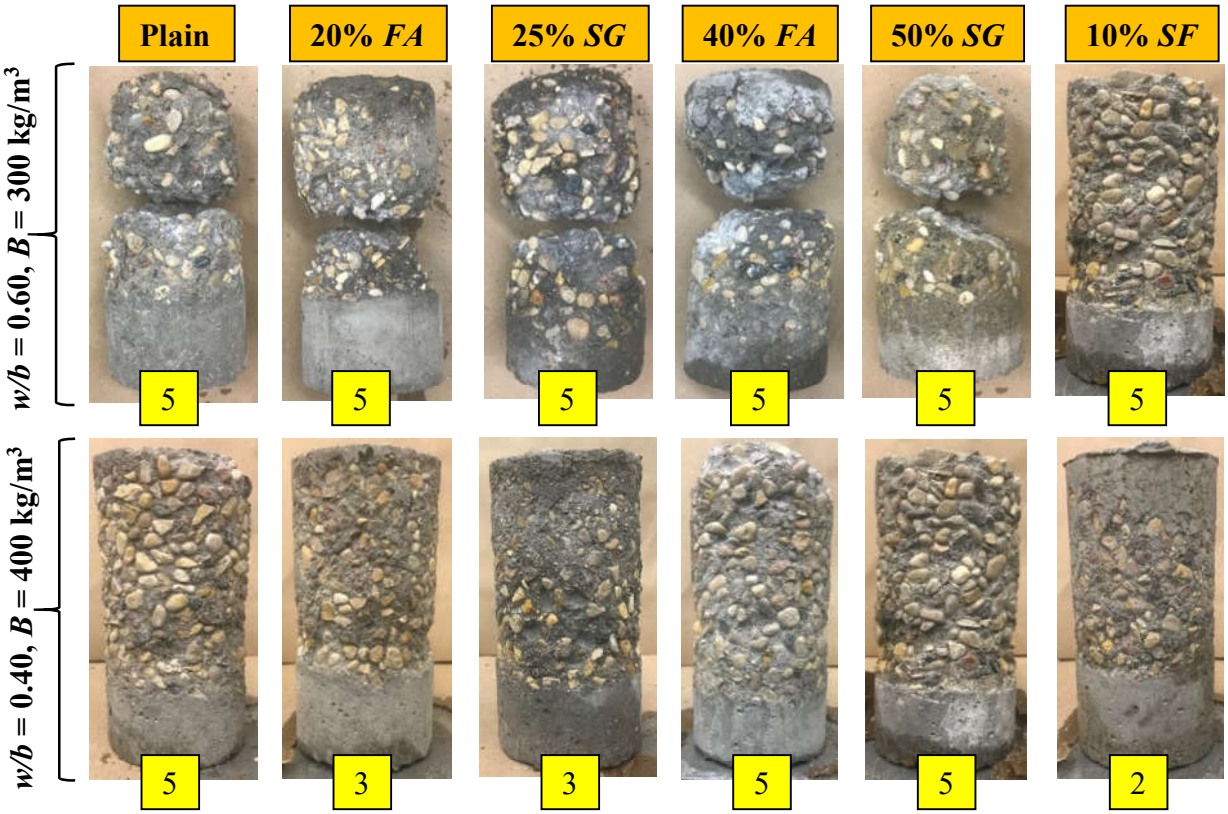

Figure 3.5: Final condition of exemplar specimens made from various binders representing the upper and lower bands, along with visual ratings.

3.4.2 Performance-Based Models

ML and *TNS* were also mapped based on mechanical, transport, and pore structure (performance) properties of concrete (Table 3.4) as the independent parameters. Due to interrelation between some predictors (e.g. correlation between f_{st} and E_d, *A* and *D*), multicollinearity (a phenomenon where one independent variable can be linearly predicted from others variables accurately) would occur in the regression analysis, which increases the standard errors of regression coefficients leading to potential conversion of some key

variables to statistically insignificant (Montgomery 2014). This situation can be resolved by excluding highly correlated factors from the model that provide redundant information. Thus, initial screening of factors was performed to eliminate unessential parameters/redundancies, noting that some combinations among parameters were proposed to further reduce this effect. For this purpose, Pearson's correlation coefficients (R) ranging from -1 to +1, which measure the strength of the relationship between two variables, were calculated; a Pearson's coefficient of at least (±) 0.7 was considered indicative for strong association between the variables ("+" and "-" signs refer to direct and inverse relationships, respectively).

ML and *TNS* of concrete had strong correlation with multiple performance parameters (e.g. f_{st} and A), but they had weak relationships with others (e.g. P_{micro}), as presented in Table 3.6. The equations were then developed using interaction/combined terms that possessed the highest R, expressing mechanical, transport, and pore structure properties of concrete. Accordingly, the terms selected for regression were $f_{st} \cdot E_d$ and $P \cdot A/D$, which had R of -0.92 and 0.95, respectively, with *ML* and R of 0.93 and -0.92 with *TNS*. The former expressed the 'mechanical capacity' of concrete by combining strength and elasticity, while the latter (termed as 'wicking factor') reflected the connectivity and tortuosity of pore structure, which determines the ease of solution transport into or out of concrete by wicking. Subsequently, the database of *ML* and *TNS* was randomly divided into 117 and 39 data points for training/establishing and testing/verifying the models, respectively, to improve the reliability of predicted results. The training and testing datasets were selected to have similar statistical characteristics in terms of min., max., and average values (Table 3.7). The best fit responses for *ML* and *TNS* were given by:

$$ML\ (\%) = 6.12 - 0.03(f_{st} \cdot E_d) + 0.29(P \cdot \frac{A}{D}) \qquad \mathbf{R^2=0.94} \qquad \text{Eq. (3.4)}$$

$$TNS\ (d) = 71.5 + 0.19(f_{st} \cdot E_d) + 1.0(P \cdot \frac{A}{D}) \qquad \mathbf{R^2=0.92} \qquad \text{Eq. (3.5)}$$

Table 3.6: Pearson's correlation coefficients between *ML*/*TNS* and performance parameters

Parameters	*ML* (%)	*TNS* (d)
Individual		
f_{st}	**-0.90**	**0.91**
E_d	**-0.86**	**0.83**
A	**0.91**	**-0.82**
D	**0.90**	**-0.85**
P	**0.93**	**-0.91**
P_{micro}	-0.50	0.48
ϕ_{thd}	0.30	-0.36
Combined		
$f_{st}*E_d$	**-0.92**	**0.93**
$\sqrt{f_{st} * E_d}$	**-0.88**	**0.87**
f_{st}/E_d	-0.25	0.36
A/D	0.32	-0.41
$A*D$	**0.88**	**-0.79**
D/A	-0.36	0.45
$\sqrt{A * D}$	**0.84**	**-0.78**
$P*P_{micro}$	**-0.71**	0.67
$P*\phi_{thd}$	0.59	-0.57
$P*f_{st}$	-0.33	0.30
P/f_{st}	**0.79**	**-0.70**
$P*A/D$	**0.95**	**-0.92**
$P*D/A$	**0.92**	**-0.84**

Note: bold numbers denote significant factors

Table 3.7: Range of training and testing data for *ML* and *TNS*

Model/Property	Training data			Testing data		
	Min.	Max.	Avg.	Min.	Max.	Avg.
***ML* (%)**	2.6	24.2	13.5	2.8	23.9	13.2
***TNS* (d)**	55	120	22	56	120	21

Figure 3.6 shows the factorial plots, which demonstrate the effect of each term in Eqs. (3.4, 3.5) on the obtained responses. The plot highlighted the positive impact of higher mechanical capacity on reducing *ML* and increasing *TNS*. Also, porous concrete with higher transport properties was more vulnerable to PSA. The wicking factor had more significant influence on *ML* and *TNS* than the mechanical capacity of concrete, as depicted in Fig. 3.6; the standardized effect of $(P \cdot A/D)$ and $(f_{st} \cdot E_d)$ was 15.3 and 9.4, respectively, in case of *ML* and was 12.7 and 10.3 in case of *TNS*, compared to a threshold of 1.98. For example, changing $(F_{st} \cdot E_d)$ from 100×10^3 to 200×10^3 MPa^2 (100% increase)

reduced *ML* by 22% and extended *TNS* by 55%, whereas changing $(P \cdot A/D)$ from 20 to 40% (100% increase) increased *ML* by 73% and shortened *TNS* by 60% (Figs. 3.6a,b).

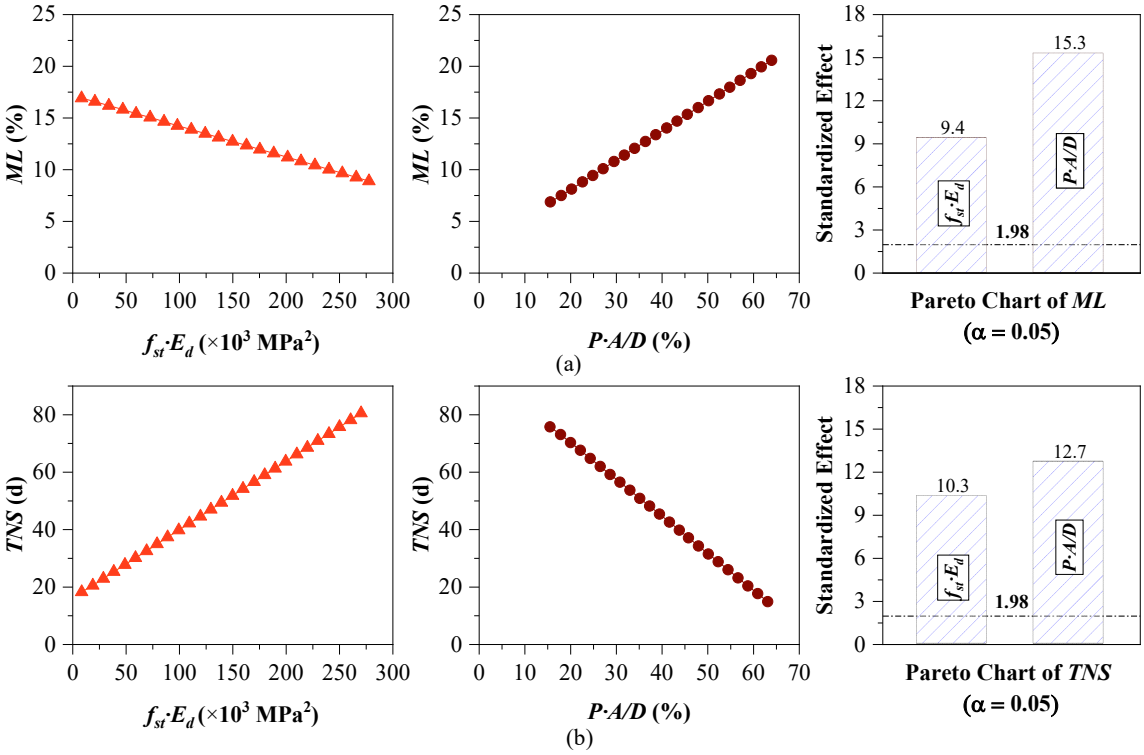

Figure 3.6: Effect of mechanical capacity and wicking factor on: (a) *ML*, and (b) *TNS* of concrete.

At the training stage, the performance of the obtained models was assessed based on the mean absolute percentage error (MAPE) and the average actual-to-predicted ratio (AAP) according to:

$$MAPE = \frac{100}{n}\sum\left|\frac{y-\hat{y}}{y}\right| \quad \text{Eq. (3.6)}$$

$$AAP = \frac{1}{n}\sum\left|\frac{y}{\hat{y}}\right| \quad \text{Eq. (3.7)}$$

where, y and $\hat{y}$ are the experimental and predicted values (*ML* or *TNS*), respectively, and n is the number of data points. The accuracy of developed models was verified by predicting *ML* and *TNS* of specimens from the training data and plotting predictions against experimental results (Fig. 3.7). The models captured the input-output relationships since

the points were mostly located on or slightly deviated from the equity line between the experimental and predicted values. The MAPE, average AAP, and coefficient of variation (COV) of AAP of the training dataset were 5.6%, 1.0, and 6.9%, respectively for *ML*, and 7.2%, 1.0, and 9.5%, respectively, for *TNS*, which indicate reliability of the models. The generalization capacity of *ML* and *TNS* models was verified by the randomly selected 39 testing points, which were excluded from the regression process; hence, the predictive ability of the models for new (unknown) data can be evaluated.

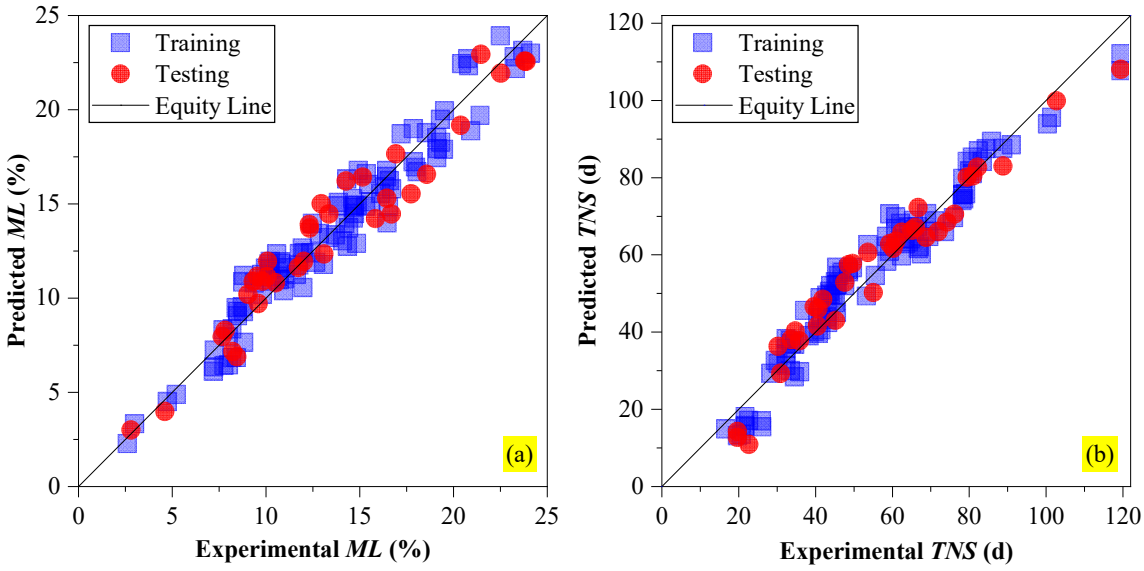

Figure 3.7: Experimental vs. predicted values of: (a) *ML*, and (b) *TNS* models obtained by multiple regression analysis.

Figure 3.7 shows that the predictions for testing points were in good agreement with the experimental data, where testing data points were mostly located on the equity line. The MAPE, average AAP, and COV of AAP of the testing dataset were 6.7%, 0.99, and 7.0%, respectively, for *ML*, and 7.8%, 0.99, and 9.4%, respectively, for *TNS*. Thus, the developed models have robust generalization capacity for predicting *ML* and *TNS* of concrete partially immersed in sodium sulfate solution and exposed to aggravated PSA conditions, similar to those adopted in this study.

3.5 Discussion

3.5.1 Effect of *w/b* and *B*

Generally, the effect of *w/b* complied with the results reported in previous studies (e.g. Bassuoni and Rahman 2016) in terms of the positive impact of *w/b* reduction (from 0.60 to 0.40) on concrete durability to PSA and current recommendations of ACI 201.2R (2016). The resistance of concrete to PSA also improved with increasing *B* from 300 to 400 kg/m^3. Mixtures with low *w/b* and high *B* consistently had their *ML* and *TNS* in the lower band (e.g. Fig. 3.3). XRD analysis on samples extracted from the evaporative front of specimens without SCMs showed more intense peaks of thenardite (Na_2SO_4) in pastes with higher *w/b* and lower *B* (e.g. Fig. 3.8). Thus, massive deposition of sodium sulfate crystals beneath the surface layer (sub-florescence) was responsible for its detachment, as shown by the exemplar SEM images of the inner side of scaled crust from 0.6GU-300 specimens (Fig. 3.9).

Concrete with lower *w/b* and/or higher *B* had better mechanical, transport, and pore structure characteristics (Table 3.4). Considering Eqs. (3.4, 3.5), this improvement had beneficial effect in terms of reducing *ML* and increasing *TNS* of concrete under PSA. Increased tensile strength of concrete, caused by *w/b* reduction and/or *B* increase, led to withstanding the developed crystallization pressures induced by PSA. Also, higher elasticity/stiffness improved the capacity of concrete to resist corresponding strains and/or delayed progression to the failure strain. This is analogous to trends reported by Sakr et al. (2019) on protective coatings, as resins having high tensile strength or elongation capacity protected concrete against PSA through resisting developed tensile stresses and accommodating volumetric expansions due to crystallization. In addition, MIP results (Table 3.4) showed that lower *w/b* and/or higher *B* discounted the porosity of concrete and

densified its microstructure, as shown by lower threshold pore diameters and higher proportion of micropores. This led to reduced absorption/desorption percentages (Table 3.4) of sodium sulfate solution, indicating lower rates of solution uptake and evaporation, which disrupted wicking, decreased build-up of crystallizing salt, and consequently reduced surface scaling of concrete.

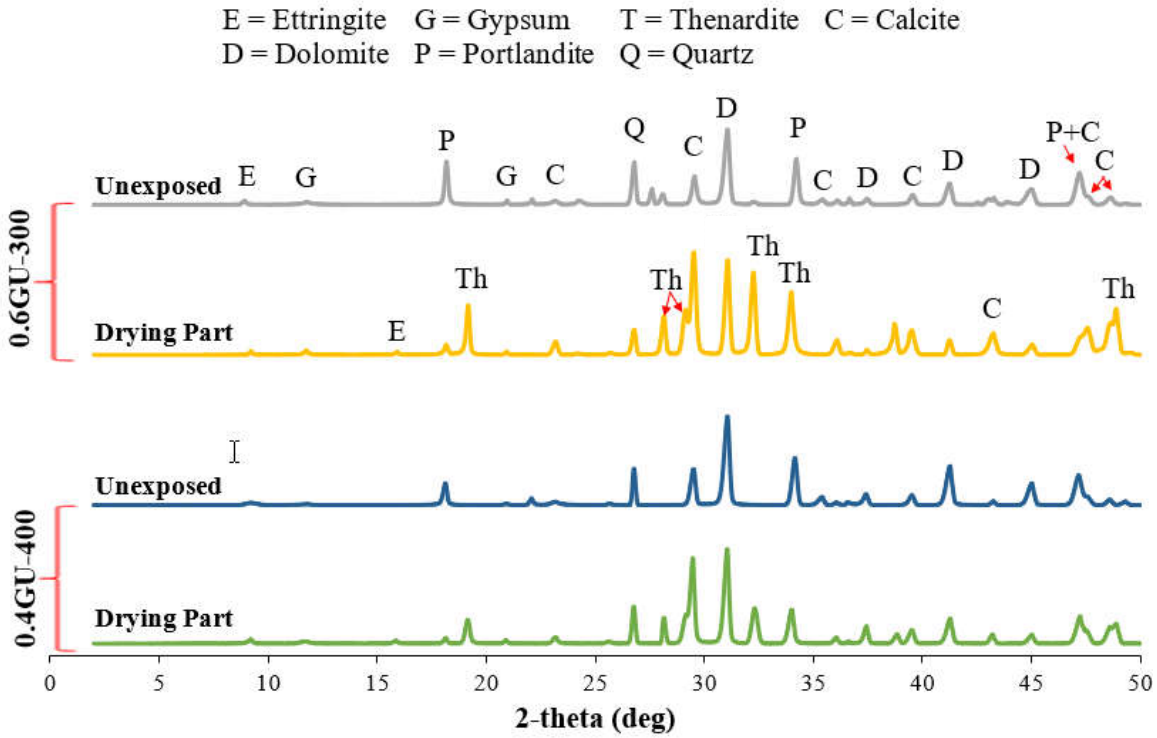

Figure 3.8: Exemplar XRD analysis of unexposed and exposed specimens made with different *w/b* and *B*, without SCMs.

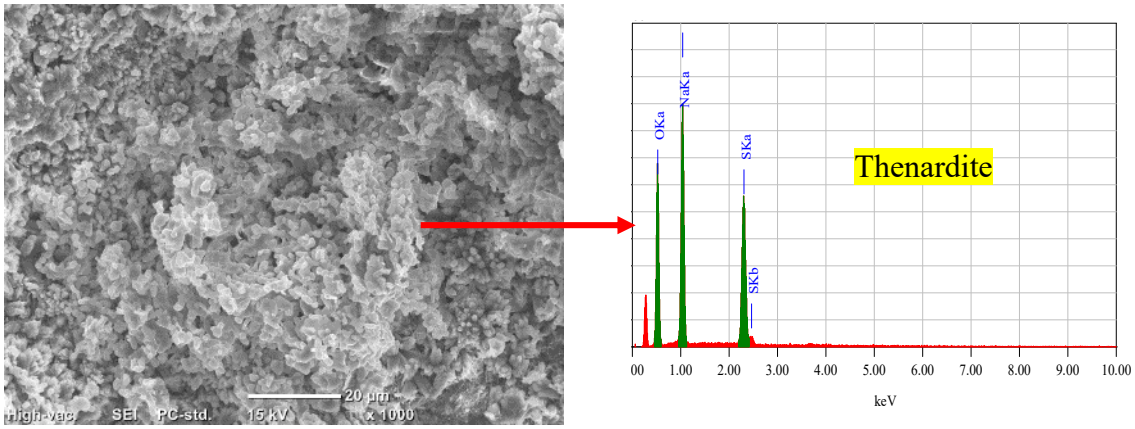

Figure 3.9: SEM and EDX analyses for samples extracted from top parts of 0.6GU-300 specimens showing prevailing crystals of sodium sulfate.

3.5.2 Effect of SCMs

Concrete made with binary binders comprising moderate dosages of *FA* or *SG* showed better resistance to PSA compared to plain concrete without SCMs, which conforms to the trends reported in some previous studies (e.g. Irassar et al. 1996; Stark 2002; Bassuoni and Rahman 2016; Dhole et al. 2019). The alteration of hydration products imparted by *FA* and *SG* at 56 days was studied by DSC on powder samples extracted from the surface layer of cured specimens at *w/b* of 0.60 and *B* of 300 kg/m^3 (Fig. 3.10). The results showed the pozzolanic effect of 20% *FA* and 25% *SG*, with extended curing, at reducing the initial portlandite content by 13% and 19%, respectively, compared to the reference cementitious matrix (GU). Thus, precipitation of secondary calcium silicate hydrate (C-S-H) in the cementitious matrix relatively densified microstructure of hydrated paste and disrupted the connectivity of accessible pores leading to slower solution uptake/evaporation (Table 3.4), and thus less surface damage of concrete from crystallization of salt.

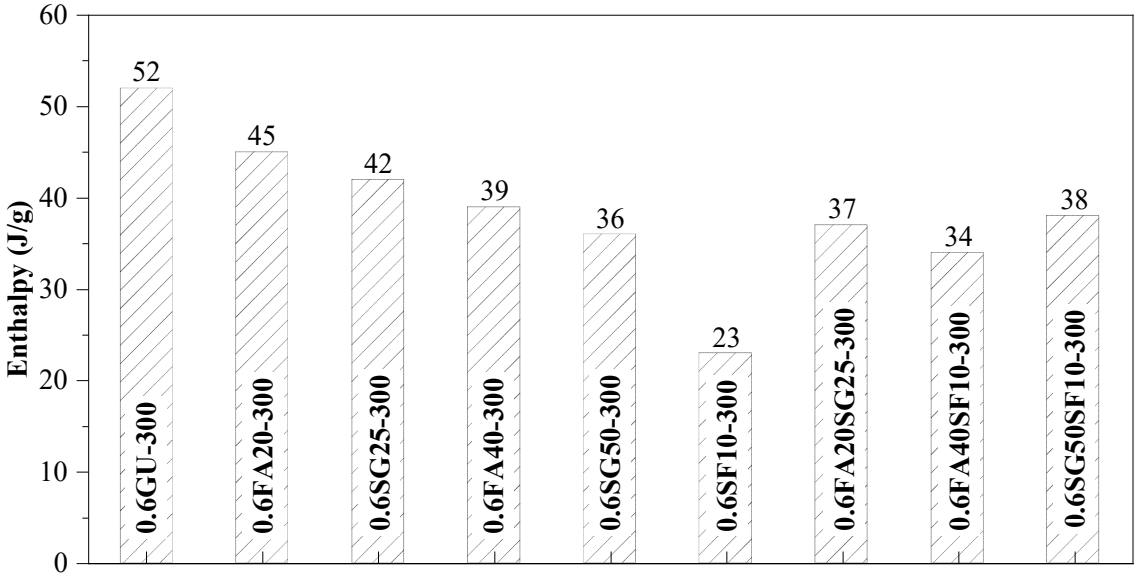

Figure 3.10: Enthalpy of portlandite in specimens made with various binders.

In contrast, higher dosage of *FA* (40%) or *SG* (50%) marginally worsened the resistance of concrete to PSA relative to plain (single binder) concrete, although the curing

period was extended to 56 days. Similarly, ternary binders containing *FA* and *SG* tended to degrade the performance of concrete under PSA as the total replacement ratio increased. DSC analysis showed that increasing the dosage of *FA* and *SG* to 40% and 50% reduced the amount of portlandite in the paste by 13 and 15%, respectively compared to moderate dosages (Fig. 3.10), alluding to considerable proportion of unreacted particles after curing, noting that similar enthalpy was obtained for ternary mixture with 20% *FA* and 25% *SG*. This was confirmed by SEM analysis, which showed abundantly unreacted *FA* and *SG* particles in the matrices of 0.6FA40-300 and 0.6SG50-300 specimens [e.g. Figs. 3.11a,b]. This trend conforms to findings from previous studies, which reported that binders with high-volume *FA* or *SG* comprise large proportions of unreacted particles up to one year of curing acting as a filler (e.g. Bentz 2014; Wang et al. 2014).

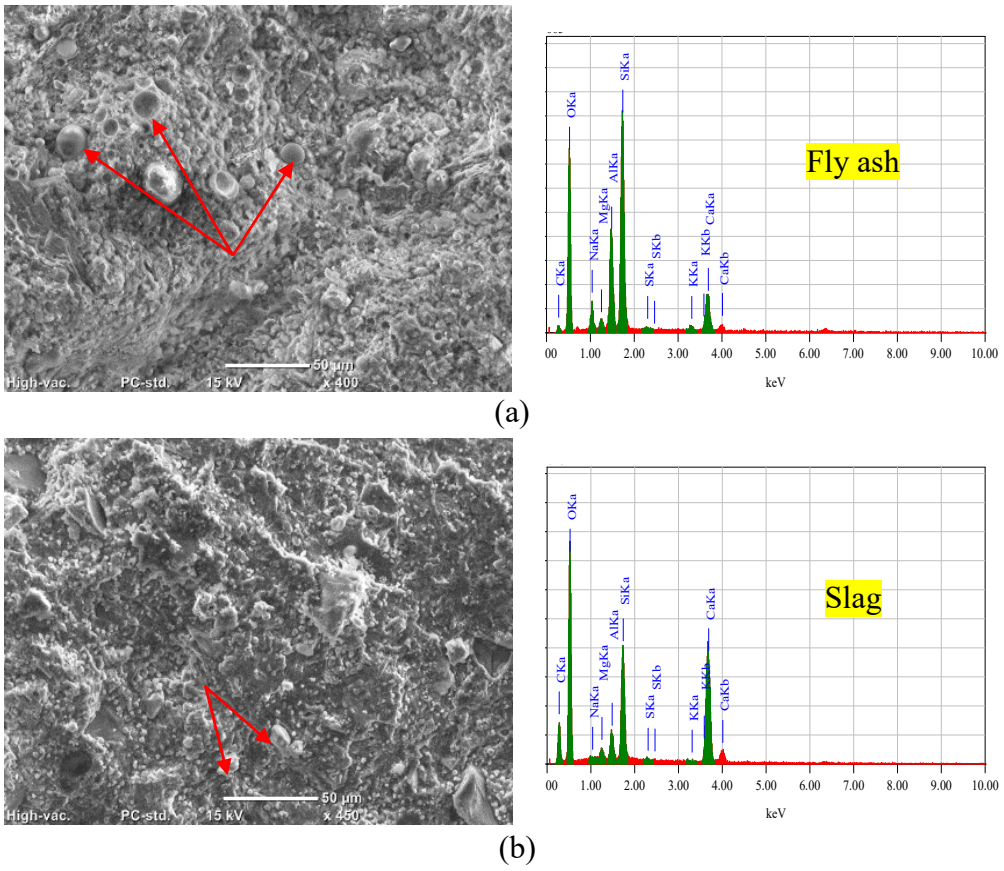

Figure 3.11: SEM and EDX analyses of unexposed specimens made with *w/b* of 0.60, *B* of 300 kg/m^3 and: (a) 40% *FA*, and (b) 50% *SG*.

In the case of PSA, large proportions of unreacted *FA* and *SG* in the surface layer of concrete would be easily dislodged in a manner similar to salt-frost scaling tests (Hasholt et al. 2019). In particular, the aggravated PSA conditions (partial immersion and significant evaporation of the top part during the drying periods) implemented herein did not provide favorable curing conditions for efficient and continual reactivity of either *FA* or *SG* particles in the matrix. Thus, the similar or slightly worse performance of mixtures with high dosages of *FA* and *SG* compared to plain concrete could be linked to their comparable mechanical, transport, and pore structure characteristics (Table 3.4) as well as loose particles in the matrix. This might also explain the inferior resistance to PSA of concrete incorporating high-volume of SCMs obtained in other studies that implemented insufficient curing for 28 days (e.g. Irassar et al. 1996). This trend, however, was dissimilar to that obtained in other studies that used different testing protocols. For example, in Zhutovsky and Hooton (2017a), it was reported that addition of 45 and 65% *SG* reduced the mass loss of mortar under full immersion in 30% Na_2SO_4 while cycling the temperature between 30 and 5°C. The full immersion test protocol likely promoted further curing and development of the hydration/pozzolanic processes due to the constantly high RH and intermittently high temperature portion of the cycle. It should be noted that the results obtained in the current study are based on the partial immersion procedure, which is representative to most PSA cases of concrete encountered in the field.

The incorporation of *SF* in the binder notably enhanced the resistance of concrete to PSA, which is consistent with the data reported in Sakr et al. (2019), except that the binder was made with lower *w/b* (0.35). DSC analysis showed that using 10% *SF* significantly decreased the amount of portlandite by 56% compared to plain concrete (Fig. 3.10), indicating more rapid pozzolanic reactivity than that of *FA* and *SG*, which can be

attributed to the amorphous nature of silicon dioxide and the higher fineness (20,000 m^2/kg) of silica fume. This produced concrete with higher tensile strength and stiffness as well as denser microstructure and consequently lower transport properties, which were effective at minimizing the vulnerability of concrete to PSA. Combining high dosages of *FA* or *SG* with *SF* (ternary binders) reduced this beneficial effect, as reflected by the higher portlandite content in those mixtures, similar to the case of binary binders (Fig. 3.10). Thus, careful selection of *w/b*, *B,* and SCMs types and dosages has to be made to produce concrete resistant to PSA, which can be achieved by optimization of the models developed herein.

3.6 Numerical Optimization

Multi-objective optimization was performed considering combinations of different factors at various levels, while simultaneously satisfying the desired requirements of each response. Each factor/response was assigned one of five goals: none, maximum, minimum, target, or within a specified range. Also, each response was assigned a weight of one to five (least to most important). Goals of all parameters were combined into an overall desirability function that ranges from zero to one (ideal solution) for any given response. The best solution with the highest desirability function and satisfying all target goals was selected, considering the use of practicable mix design combinations, or performance metrics (Montgomery 2014).

Regarding prescriptive parameters, various scenarios were assumed to provide optimum mixture design components. For all scenarios, the weight for both *ML* and *TNS* was selected as five (most important). Table 3.8 summarizes the target goals in the adopted scenarios along with corresponding results. The single binder scenario (I) had a desirability function of 0.77, and it showed that *w/b* and *B* should be at 0.40 and 400 kg/m^3, respectively, which was also valid for other scenarios. For binary binders, the optimum

dosages of *FA* and *SG* were approximately 25 and 30%, respectively (Scenarios II and III). The optimum combinations in Scenarios II and III would possibly lead to *ML* of 6% with *TNS* between 90 to 100 days in the accelerated PSA test. In comparison, using *SF* with dosages ≥ 8% would provide higher resistance to PSA (*ML* of 3% and *TNS* of 120 days, Scenario IV). In case of ternary and quaternary binders, the total volume of SCMs should be limited to 28-35%, comprising ≥ 8% *SF*, to minimize *ML* (about 2.8-3.5%) and maximize *TNS* (above 110 days) [Scenario VI, VII, VIII].

ACI 201.2R (2016) and ACI 318 (2019) limit *w/b* to 0.40 for exposure class S3 (very severe chemical sulfate attack, which is the case of the solution used herein) and allow using blended cements that have a record of sulfate attack resistance; alternately, the expansion criteria of ASTM C1012 (full immersion test) shall be met. Generally, blended binders are expected to comprise *FA* (15-50%), *SG* (<70%), and/or *SF* (5-12%), while keeping cement content between 35-70% (ACI 201.2R 2016). Also, in CSA A23.1/A23.2 (2019), high sulfate-resistant (HS) cement should be used for concrete exposed to S1 (very severe chemical sulfate attack), either plain or blended, meeting stringent expansion limits of CSA A3004-C8 (analogous to ASTM C1012). At *w/b* of 0.40 and *B* of 400 kg/m^3, the optimized dosages of SCMs for blended binders (Table 3.8), which would provide adequate resistance to PSA, fit within permissible dosages for chemical sulfate attack. Besides, many studies reported these dosages to be successful under chemical attack as per ASTM C1012 (e.g. Atahan and Arslan 2016; Holland et al. 2017; Obla and Lobo 2017). In contrast, while higher volumes of SCMs provide adequate resistance to chemical attack (e.g. Kandasamy and Shehata 2014), they tend to increase the vulnerability of concrete to PSA. Thus, the selected combinations of blended binders (Table 3.8), especially the ones comprising *SF*,

should mutually protect concrete against both PSA and chemical attack when they are expected to occur together in the field.

Table 3.8: Selected criteria, goals, and results of the numerical optimization

Criteria	Goal	Result	Criteria	Goal	Result
Scenario I (0.77)			**Scenario V (0.84)**		
w/b	Within 0.40 to 0.60	0.40	***w/b***	Within 0.40 to 0.60	0.40
B	Within 300 to 400 kg/m^3	400 kg/m^3	***B***	Within 300 to 400 kg/m^3	400 kg/m^3
FA	None	0%	***FA***	Within 0 to 40%	15%
SG	None	0%	***SG***	Within 0 to 50%	20%
SF	None	0%	***SF***	None	0%
ML, TNS	Minimize, Maximize	6.9%, 88 d	***ML, TNS***	Minimize, Maximize	5.1%, 106 d
Scenario II (0.82)			**Scenario VI (0.99)**		
w/b	Within 0.40 to 0.60	0.40	***w/b***	Within 0.40 to 0.60	0.40
B	Within 300 to 400 kg/m^3	400 kg/m^3	***B***	Within 300 to 400 kg/m^3	400 kg/m^3
FA	Within 0 to 40%	24.2%	***FA***	Within 0 to 40%	20%
SG	None	0%	***SG***	None	0%
SF	None	0%	***SF***	Within 0 to 10%	≥ 8%
ML, TNS	Minimize, Maximize	6.1%, 94 d	***ML, TNS***	Minimize, Maximize	2.8%, 120 d
Scenario III (0.84)			**Scenario VII (0.97)**		
w/b	Within 0.40 to 0.60	0.40	***w/b***	Within 0.40 to 0.60	0.40
B	Within 300 to 400 kg/m^3	400 kg/m^3	***B***	Within 300 to 400 kg/m^3	400 kg/m^3
FA	None	0%	***FA***	None	0%
SG	Within 0 to 50%	28.5%	***SG***	Within 0 to 50%	22%
SF	None	0%	***SF***	Within 0 to 10%	≥ 8%
ML, TNS	Minimize, Maximize	5.9%, 102 d	***ML, TNS***	Minimize, Maximize	3.5%, 116 d
Scenario IV (0.97)			**Scenario VIII (0.97)**		
w/b	Within 0.40 to 0.60	0.40	***w/b***	Within 0.40 to 0.60	0.40
B	Within 300 to 400 kg/m^3	400 kg/m^3	***B***	Within 300 to 400 kg/m^3	400 kg/m^3
FA,	None	0%	***FA***	Within 0 to 40%	10%
SG	None	0%	***SG***	Within 0 to 50%	15%
SF	Within 0 to 10%	≥ 8%	***SF***	Within 0 to 10%	≥ 8%
ML, TNS	Minimize, Maximize	3.0%, 120 d	***ML, TNS***	Minimize, Maximize	3.4%, 112 d

Note: Values between parentheses are the desirability function.

In addition, optimization was conducted in terms of performance-based parameters to allow for the PSA classification of concrete mixtures made with different variables not implemented in this study such as other *w/b* and/or cementitious materials/dosages (e.g. metakaolin). These binders should still meet the expansion limits mentioned in ACI 318 (2019) in cases of chemical sulfate attack and PSA. The targets for mechanical capacity and wicking factor were in ranges of 7×10^3 to 279×10^3 MPa^2 and 15 to 65%, respectively, to achieve the target *ML* categories. Table 3.9 provides a proposed classification (from highly resistant to none) for the resistance of concrete to PSA with corresponding ranges for the mechanical capacity and wicking factor.

Table 3.9: Proposed classification for the resistance of concrete to PSA

Resistance Classification	**Visual rating***	**Mass loss (%)**	**Mass loss (g/m^2)****	**Mechanical capacity ($\times 10^3$ MPa^2)**	**Wicking factor (%)**
High	0-2	≤ 4	≤ 1500	> 260	< 19
Moderate	3-4	> 4 to 7	> 1500 to 3000	220-260	19-25
Low	5	> 7 to 10	> 3000 to 5000	200-220	25-35
None	5	> 10	> 5000	< 200	> 35

* Visual condition in zones of capillary rise.

**Mass loss of concrete specimens per unit surface area of zone of capillary rise.

CHAPTER 4: PERFORMANCE OF CONCRETE UNDER PHYSICAL SALT ATTACK COMBINED WITH CARBONATION

In Chapter 3, the response surface method, a statistical modeling approach, was used to assess the influence of performance- and prescriptive- based parameters on the performance of 52 concrete mixtures under accelerated physical salt attack (PSA). The current chapter is concerned with the damage of concrete due to dual PSA and carbonation, adopting a combined testing approach where concrete is concurrently investigated under both mechanisms and implementing ambient conditions similar to that in geographic locations with previous cases of PSA.

4.1 Introduction

PSA refers to progressive surface scaling and flaking of concrete by salt crystallization in the near-surface pores of concrete that is in contact with salt-rich media (e.g. soil, groundwater, or seawater) and subjected to ambient conditions favorable for salt crystallization (ACI 201.2R 2016). PSA damage is produced due to growth of salt crystals [e.g. sodium sulfate, carbonate, and chloride, in order of aggression (Haynes et al. 2008, 2010)] inside concrete pores beneath the surface layer (sub-florescence) with sufficient amounts to develop crystallization pressures capable of imposing deleterious action to concrete, without chemical alteration of hydration products in the cementitious matrix (Scherer 2004; Bassuoni and Rahman 2016). Flatt (2002) theoretically estimated that crystallization pressure might reach 10-20 MPa for highly supersaturated solutions, which is far exceeding the tensile capacity of concrete, thus causing superficial scaling. In the field, damage is commonly observed on concrete elements subjected to wicking of salt

solutions and simultaneous evaporation through the drying surfaces/fronts such as basement walls, abutments, piers, slabs on grade, and tunnel linings (Haynes et al. 1996; Haynes and Bassuoni 2011; Long et al. 2011).

While the effect of some mixture design parameters [e.g. water-to-binder ratio (*w/b*)] on PSA has been well established in literature, other factors [e.g. supplementary cementitious materials (SCMs)] are still controversial. Reducing *w/b* has been reported to significantly decrease the mass loss of concrete due to PSA [e.g. Bassuoni and Rahman 2016; Lee and Kurtis 2017]. However, conflicting data were reported regarding the behavior of concrete containing SCMs under PSA. For example, Zhutovsky and Hooton (2017a) reported that mortars cured for 28 days and made with 20 and 40% Class F fly ash had inferior resistance to PSA when fully submerged in 30% sodium sulfate (Na_2SO_4) with thermal cycling. Conversely, long-term field studies by Portland Cement Association (PCA) [16 years] (Stark 2002) and Irassar et al. (1996) [5 years] showed that incorporating 20% Class F fly ash in concrete partially embedded in sodium sulfate soils led to some improvement relative to plain concrete, while severe damage occurred for concrete containing 40% fly ash. Mortars comprising 45 and 65% slag had better resistance to PSA than reference specimens with comparable mass loss obtained for both dosages (Zhutovsky and Hooton 2017a). Conversely, PCA field studies reported inferior performance for concrete containing 40 or 65% slag, with the latter being the worst (Stark 2002). This discrepancy in trends, even for the same replacement ratio, may be attributed to differences in mixture designs, testing conditions, and/or curing regimes.

Nevertheless, previous studies on the mechanisms of surface scaling (e.g. Bassuoni and Rahman 2016) and effect of mixture design parameters on the level of deterioration (e.g. Irassar et al. 1996; Stark 2002; Bassuoni and Rahman 2016; Lee and Kurtis 2017;

Zhutovsky and Hooton 2017a) investigated PSA in isolation from other damage mechanisms. However, in the field, service conditions could provoke a multitude of damage mechanisms (physical or chemical) on concrete elements along with PSA, which may act in a combined or synergistic manner. For instance, carbonation is a chemical deterioration mechanism of concrete with high potential to concurrently occur with PSA in elements serving in heavy traffic and industrial zones, which have high carbon dioxide (CO_2) emissions. Field examples include linings of tunnels in China (Long et al. 2011) and basement walls/piers/abutments in industrialized cities in Japan (Yoshida et al. 2010), where the effect of carbonation on PSA was overlooked. Also, in Mittermayr et al. (2013), the damage of railroad tunnels in Austria was mainly attributed to thaumasite sulfate attack, without analyzing the manifestations of PSA (e.g. surface scaling and efflorescence of sodium sulfate) and potential implications of carbonation on concrete.

To date, there is limited data on the combined effects of PSA and carbonation on the behavior of concrete. Yoshida et al. (2010) compared PSA damage of water cured (56 days) mortar prisms versus conjugate specimens cured in water for 28 days, followed by carbonation curing at 5% CO_2 for 28 days. Single binder specimens were prepared at *w/b* of 0.40, 0.55, and 0.70, whereas binary binder specimens (30% fly ash and 45% slag) were made with *w/b* of 0.55. Prisms were partially immersed in 5% Na_2SO_4 and exposed to wetting and drying for 6 months; each cycle (7 days) involved 8 h partial immersion, followed by 40 h of air drying, 8 h partial immersion, 40 h of air drying, 8 h partial immersion, and lastly 64 h of air drying. Carbonated specimens were reported to scale more than the reference mortar as determined by laser profiling of scaled depth (Yoshida et al. 2010), but without quantification of mass loss or explanation of possible damage mechanisms. Also, the applied exposure conditions were mild to provide definitive trends

since both uncarbonated and carbonated specimens showed minimal damage localized within 20-50 mm above the solution level, which correspond to a mass loss of less than 1% for specimens having similar visual appearance reported in other studies (e.g. Bassuoni and Rahman 2016). Liu et al. (2018) pre-exposed concrete specimens to carbonation for 10-20 days at 20% CO_2 before PSA testing. Specimens were partially immersed in 10% Na_2SO_4 at lab conditions for 240 days, without cyclic temperature and/or relative humidity. However, such testing conditions were reported in Haynes et al. (2008) to cause minimal PSA distress up to three years of exposure and may provoke chemical sulfate attack instead. In addition, the procedure of testing in these studies did not simulate concurrent exposure to both carbonation and PSA as maybe encountered in the field.

Most guidelines and codes (ACI 201.2R 2016; ACI 301 2016; ACI 318 2019; ACI 350 2006; CSA A23.1/A23.2 2019; BS EN 206 2013; AS 3600 2018) for durability of concrete do not explicitly discuss the topic of PSA because of the lack of full understanding of factors affecting the behavior of concrete under such process (e.g. SCMs, pore structure features [Irassar et al. 1996; Bassuoni and Nehdi 2009; Bassuoni and Rahman 2016; Zhutovsky and Hooton 2017a]), mostly due to past confusion of PSA with chemical sulfate attack of concrete (Stark 2002). For example, the most recent version of ACI 201.2R (2016) states that "specific recommendations cannot be made to prevent physical salt attack," but it mentions the use of low *w/b* and application of protective coatings to isolate concrete from the surrounding media without generic specifications of these coatings. American codes such as ACI 301 (2016), ACI 318 (2019), and ACI 350 (2006) do not explicitly mention any specific requirements regarding PSA of concrete. Canadian standard (CSA A23.1/A23.2 2019) does not differentiate between chemical and physical sulfate attacks and give same recommendations [e.g. lower *w/b* and SCMs] for both cases, although the

addition of SCMs, according to some studies (Irassar et al. 1996; Stark 2002; Suleiman and Nehdi 2017), have been reported to cause inferior performance of concrete elements exposed to PSA. Other codes, such as European standard (BS EN 206 2013) and Australian Standard (AS 3600 2018), do not directly address this durability issue of concrete. In addition, none of the aforementioned documents provide direct advice on exposure scenarios involving PSA combined with other damage mechanisms

4.2 Research Significance

At this stage, continual investigation of PSA on concrete isolated from other damage mechanisms (e.g. carbonation), i.e. reductionist approach, may lead to overlooking some important parameters/processes with synergistic effects on concrete. There is dearth of information on the interaction between PSA and carbonation in concrete, which maybe encountered in field cases such as tunnel linings and partially embedded elements in industrial zones. Hence, there is still need for research in this direction to elucidate possible mechanisms of concrete damage due to combined effects of PSA and carbonation. In comparison to a reference (single) PSA exposure, the current study aimed at implementing a holistic testing regime that provoked combined occurrence of PSA and carbonation in concrete, considering environmental conditions in locations with previous cases of PSA. The effect of mixture design parameters (*w/b*, use of limestone materials, and SCMs) was studied under such conditions to provide a consistent basis of comparison. Fundamental knowledge from this study can be applied towards improving current guidance, recommendations, and specifications for developing durable concrete mixtures suitable for applications when combined exposure to PSA and carbonation is expected in the field.

4.3 Experimental Program

4.3.1 Materials and Mixtures

Ten concrete mixtures were prepared using single and binary binders. General use (GU) portland cement, portland limestone cement (PLC), Class F fly ash (FA), and Grade 100 slag (SG) [Table 4.1], were used as the main components of the binders. Single binder mixtures were prepared with GU cement or PLC at various *w/b* (0.40, 0.50, and 0.60) representing different pore structure qualities, while concrete comprising blended binders was made with GU cement at a fixed *w/b* of 0.50, and incorporating fly ash (20% and 40%) or slag (30% and 60%). The total cementitious materials content was kept constant at 400 kg/m^3 for all mixtures.

Table 4.1: Chemical composition and physical properties of binders

	GU cement	PLC	Fly ash	Slag
Chemical composition				
SiO_2 (%)	19.2	18.9	56.0	33.4
Al_2O_3 (%)	5.0	4.4	23.1	13.4
Fe_2O_3 (%)	2.33	3.2	3.6	0.76
CaO (%)	63.2	63.4	10.8	42.2
MgO (%)	3.3	0.7	1.1	5.3
SO_3 (%)	3.0	2.7	0.2	2.4
$Na_2O_{eq.}$ (%)	0.12	0.3	3.2	0.3
$CaCO_3$ (%)	2.4	11.6	-	-
Physical properties				
Mean particle size, µm	13.15	11.81	16.56	14.12
Specific gravity	3.15	3.11	2.12	2.87
Fineness, m^2/kg	390	460	290	492

The fine aggregate was well-graded river sand (refer to Section 3.3.2). Natural siliceous gravel (refer to Section 3.3.2) was used as the coarse aggregate in all mixtures except those made with PLC, where crushed limestone (max. size, specific gravity, and absorption of 9.5 mm, 2.69, and 2.1%, respectively) was used. Procedure for casting and curing was similar to that used in Chapter 3 (refer to Section 3.3.2). Table 4.2 shows the

proportions of concrete mixtures along with their corresponding compressive strength as per ASTM C39 (2018).

Table 4.2: Proportions of concrete mixtures per cubic meter

Mixture ID	Cement (kg)	Fly ash (kg)	Slag (kg)	Water (kg)	Coarse aggregate (kg)	Fine aggregate (kg)	Compressive strength** (MPa)
0.6GU	400	--	--	240	1200	409	33 [0.66]
0.5GU	400	--	--	200	1200	514	38 [0.50]
0.4GU	400	--	--	160	1200	621	45 [0.30]
0.6PLC-L*	400	--	--	240	1200	409	37 [0.35]
0.5PLC-L	400	--	--	200	1200	514	43 [0.40]
0.4PLC-L	400	--	--	160	1200	621	49 [0.25]
0.5GUFA20	320	80	--	200	1200	482	39 [0.34]
0.5GUFA40	240	160	--	200	1200	450	36 [0.50]
0.5GUSG30	280	--	120	200	1200	504	38 [0.42]
0.5GUSG60	160	--	240	200	1200	495	33 [0.68]

*L denotes limestone aggregate.
**Values between brackets are the standard deviations for compressive strength results.

4.3.2 Exposures

Two reference/single exposures of carbonation or PSA alone were implemented, in addition to the dual exposure (PSA and carbonation). For the single carbonation exposure, triplicate specimens (75×150 mm) of each mixture were stored in a carbonation chamber maintained at 20±2ºC and 60±5% RH. CO_2 gas at 10% concentration, which was maintained at this level during exposure, was injected into the chamber with a controlled pressure of 0.15 bar at determined time intervals matching the carbonation periods in the dual exposure (Table 4.3). Carbonation continued for 90 cycles, similar to the combined exposure, at 20±2°C and 60±5% RH during each cycle (4 days) consisting of: 32 h without carbonation (Stages I and II), followed by 16 h of carbonation (Stage III), 24 h without carbonation (Stage IV), and 24 h of carbonation (Stage V). Every eight cycles, a 10 mm disk was sliced out of each specimen and immediately sprayed with 1% phenolphthalein

pH solution indicator to determine the depth of carbonation. Zones where pH dropped below 9 (i.e. carbonated) remained colorless while non-carbonated areas displayed a magenta color. The depth of neutralization of each specimen was calculated as the average of eight readings measured around the disk circumference for the colorless portion.

Table 4.3: Description of all exposures

Stage	Duration (h)	Carbonation			PSA			Combined exposure		
		Temperature (ºC)	RH (%)	CO_2	Temperature (ºC)	RH (%)	CO_2	Temperature (ºC)	RH (%)	CO_2
I	24	20±2	60±5	No	20±2	90±5	No	20±2	90±5	No
II	8	20±2	60±5	No	40±2	35±5	No	40±2	35±5	No
III	16	20±2	60±5	Yes	20±2	60±5	No	20±2	60±5	Yes
IV	24	20±2	60±5	No	5±2	60±5	No	5±2	60±5	No
V	24	20±2	60±5	Yes	20±2	60±5	No	20±2	60±5	Yes

The regime stimulating PSA in both the reference and combined exposures was designed based on multiple factors. Bassouni and Rahman (2016) developed an accelerated partial immersion testing that provided clear assessment for the resistance of concrete to PSA within four months. The current study implemented slower cyclic conditions compared to (Bassouni and Rahman 2016) to provide ample duration (12 months) for capturing the evolution of damage in concrete, while still using similar conditions for wetting-drying to the previous study (Bassouni and Rahman 2016). In addition, the designed exposure considered realistic ambient conditions simulating seasonal variations in geographic locations with history of reported field cases of PSA on concrete [e.g. California, USA (Haynes and Bassuoni 2011) and Adelaide, Australia (Neville 2004)].

Accordingly, in the reference PSA and combined exposures, triplicate specimens (75×150 mm) from each mixture were partially immersed (one-third) in a 50 mm plastic container containing 10% sodium sulfate solution, while the exposed part of specimens (100 mm) was subjected to the cyclic conditions listed in Table 4.3. Besides, specimens in the combined exposure were exposed to CO_2 gas at specific slots during the cycle,

matching the periods of the reference carbonation exposure. The dual exposure lasted for 90 cycles; each cycle (4 days) consisted of: (I) 24 h temperate/humid period (20±2°C and 90±5% RH), (II) 8 h hot/dry period (40±2°C and 35±5% RH), (III) 16 h temperate/moderate period (20±2°C and 60±5% RH) combined with carbonation, (IV) 24 h cold/moderate conditions (5±2°C and 60±5% RH), and (V) 24 h temperate/moderate stage (20±2 °C and 60±5% RH) combined with carbonation. During the single and combined PSA exposures, the salt solution was frequently replenished to maintain the 50 mm level due to continuous uptake and evaporation. Also, fresh solutions were put every eight cycles.

4.3.3 Testing

Following the procedure in Chapter 3 (Section 3.3.3), the penetrability (physical resistance) of the concrete specimens was determined by absorption and desorption ratios after the curing period and every eight cycles of exposure. Test specimens were 75×50 mm disks for the initial absorption/desorption percentages, whereas sliced disks (20 mm above the solution level) from exposed specimens were used to calculate variation in absorption/desorption percentages with time.

During the single and combined PSA exposures, specimens were regularly monitored every eight cycles. Salt deposits and concrete debris were carefully removed from the surface using a nylon brush. Subsequently, specimens were air-dried at lab conditions (20±2°C and 55±5% RH) for 6 h before recording their masses. The mass change of specimens was then determined relative to the initial mass before exposure. At the end of exposure, the surface degradation of specimens was visually assessed and rated based on 0 (no scaling) to 5 (severe scaling) pictorial scale (Bassuoni and Rahman 2016).

The pore structure characteristics were studied for the mixtures, after the curing period and every eight cycles during exposure, by mercury intrusion porosimetry (MIP). The total porosity, absorption, and desorption percentages were used to calculate variation of wicking factor [equals to porosity (%)×absorption (%)/desorption (%)] with time. Chapter 3 statistically showed that the wicking factor reliably projected the ease of solution transport into and out of concrete due to wicking of salt solutions, which is of particular importance in case of PSA.

In addition, the alteration of microstructure in damaged specimens was investigated by mineralogical (XRD with a scanning rate of 0.5°/min), thermal (with an incremental heating rate of 10°C/min), and microscopy (SEM/EDX) analyses (refer to Section 3.3.3).

4.4 Results

4.4.1 Absorption/Desorption of Concrete

The penetrability of all mixtures after curing was evaluated by calculating the mass gain (absorption) and loss (desorption) percentages (Table 4.4), which are representative for the initial processes of solution supply and evaporation (wicking) in PSA of concrete.

Table 4.4: Absorption and desorption values for concrete at 56 days

Specimen	Absorption (%)		Desorption (%)	
0.6GU	7.52	[0.29]	-3.46	[0.15]
0.5GU	6.12	[0.05]	-2.75	[0.12]
0.4GU	4.55	[0.08]	-2.15	[0.10]
0.6PLC-L	6.36	[0.22]	-3.00	[0.14]
0.5PLC-L	5.30	[0.18]	-2.40	[0.10]
0.4PLC-L	3.95	[0.13]	-2.02	[0.06]
0.5GUFA20	5.45	[0.17]	-2.36	[0.16]
0.5GUFA40	6.32	[0.19]	-2.90	[0.07]
0.5GUSG30	5.60	[0.17]	-2.45	[0.10]
0.5GUSG60	7.15	[0.30]	-3.30	[0.18]

Note: values between brackets are the standard deviations.

Decreasing the *w/b* resulted in lower transport properties, complying with the well-documented effect of *w/b* reduction on the penetrability of concrete (Mehta and Monteiro 2014). GU specimens made with *w/b* of 0.60, 0.50, and 0.40 had absorption ratios of 7.52, 6.12, and 4.55%, respectively, with corresponding desorption percentages of -3.46, -2.75, and -2.15%, respectively. The effect of *w/b* on penetrability of concrete was rendered significant by analysis of variance (ANOVA) at a significance level (α) of 0.05, as listed in Table 4.5. The positive effect of *w/b* reduction on the penetrability of concrete was replicated for mixtures prepared with PLC. However, compared to the GU mixtures, conjugate mixtures prepared with PLC consistently showed lower transport properties at all *w/b*. For instance, the absorption and desorption percentages of 0.6PLC-L specimens were 16 and 14% lower than that of 0.6GU specimens, respectively (Table 4.4). ANOVA showed a significant effect for changing the type of cement (Table 4.5); for example, at *w/b* of 0.6, *F*-values of 21 and 16 were obtained for absorption and desorption, respectively compared to a critical threshold (F_{cr}) of 7.7.

At a *w/b* of 0.50, the incorporation of SCMs into concrete affected the transport properties compared to the reference mixture (0.5GU), depending on the type and dosage of SCMs. Concrete comprising 20% fly ash showed moderate reduction in absorption (11%) and desorption (14%), compared to that of the reference concrete without SCMs (Table 4.4). Increasing the dosage of fly ash to 40% tended to increase the transport properties of concrete and yielded slightly higher absorption (4%) and desorption (5%) percentages, relative to plain concrete; however, this effect was found statistically insignificant (Table 4.5). Binary binders incorporating 30% slag showed 8% and 11% lower absorption and desorption percentages, respectively, compared to that of reference

concrete (Table 4.4), but the higher replacement ratio (60%) significantly (Table 4.5) increased these percentages by 17% and 20%, respectively.

Table 4.5: Analysis of variance (ANOVA) for various testing parameters

Parameter	Absorption	Desorption	Carbonation depth	PSA mass loss	Combined PSA mass loss
	F values				
w/b					
0.6GU vs. 0.5GU	45*	28*	518*	150*	109*
0.5GU vs. 0.4GU	536*	29*	6740*	2158*	1201*
Type of cement					
0.6GU vs. 0.6PLC-L	21*	16*	334*	38*	20*
0.5GU vs. 0.5PLC-L	62*	14*	231*	47*	57*
0.4GU vs. 0.4PLC-L	32*	2	--	--	--
SCMs					
0.5GU vs. 0.5GUFA20	29*	7	97*	10*	40*
0.5GUFA20 vs. 0.5GUFA40	6	19*	41*	105*	37*
0.5GU vs. 0.5GUFA40	0.4	2.3	184*	79*	101*
0.5GU vs. 0.5GUSG30	17*	7.3	264*	2.2	79*
0.5GUSG30 vs. 0.5GUSG60	40*	103*	812*	156*	91*
0.5GU vs. 0.5GUSG60	23*	32*	2371*	152*	269*

*Denotes statistical significance.
Note: F_{cr} for all tests equals to 7.7.

4.4.2 Single Carbonation Exposure

The depth of carbonation in different mixtures after 90 cycles of exposure is shown in Fig. 4.1. The carbonation front progressed at high rates within the first 24 to 32 cycles, but the rates decreased afterwards up to the end of exposure (Fig. 4.2). The depth of carbonation in all specimens, except for 0.4GU and 0.4PLC-L, was 2.5 to 5.2 mm after eight cycles, indicating potential neutralization of concrete beyond the sub-florescence zone (2-3 mm) where salts crystallize in cases of PSA damage. The resistance of concrete to carbonation increased as the *w/b* decreased, irrespective of the type of cement. For example, the carbonation depths of 0.6GU and 0.5GU specimens were 15 and 10 mm, respectively. Specimens made with *w/b* of 0.40 did not experience any carbonation, as indicated by the magenta color in the entire cross-section (Fig. 4.1). Compared to GU specimens,

corresponding PLC specimens showed higher carbonation depths at *w/b* of 0.60 and 0.50 by 33 and 40%, respectively, while at *w/b* of 0.40, both GU and PLC specimens showed very high resistance to carbonation. ANOVA (Table 4.5) showed that using limestone materials had a significant effect on carbonation depths at *w/b* of 0.60 and 0.50, as the *F*-values were 334 and 231, respectively compared to F_{cr} of 7.7.

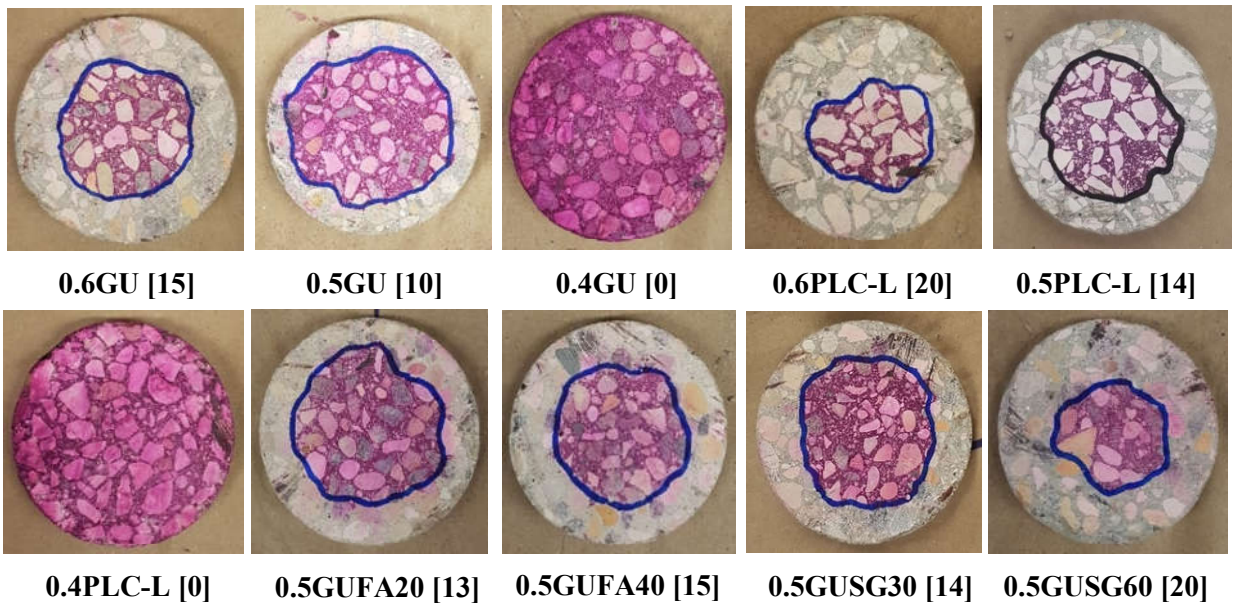

Figure 4.1: Final carbonation depth for all mixtures at the end of single carbonation exposure. (Note: numbers between brackets are carbonation depths in mm)

Mixtures comprising 20% fly ash had 30% higher carbonation depth than that of the reference 0.5GU specimens. The higher dosage of fly ash (40%) significantly increased the vulnerability of concrete to carbonation (Table 4.5), as the 0.5GUFA40 specimens yielded 50% higher carbonation depths than 0.5GU specimens. Comparatively, using slag led to worse resistance of concrete to carbonation relative to fly ash. The carbonation depths of concrete containing 30 and 60% slag were 40 and 100% higher than that of reference specimens (0.5GU), which was rendered significant by ANOVA (Table 4.5).

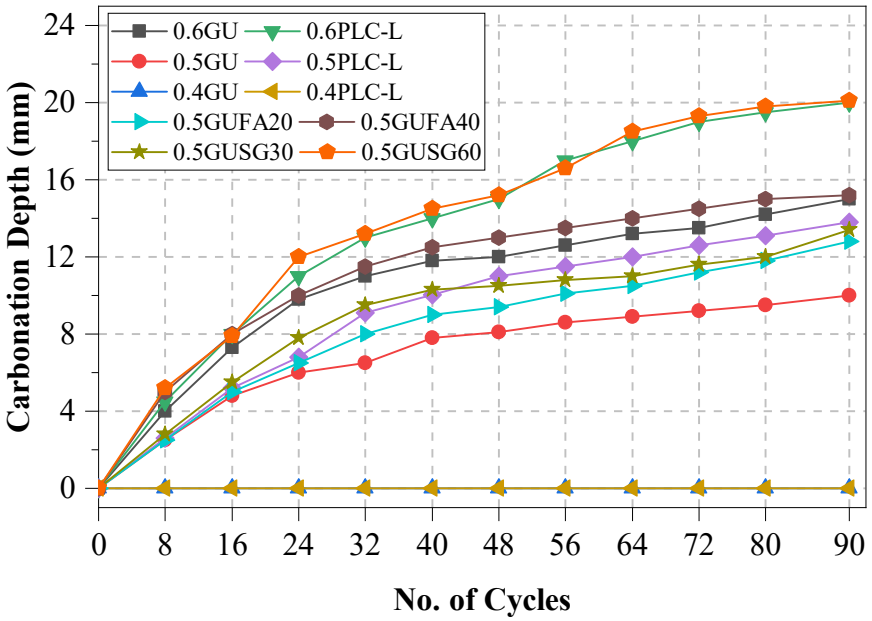

Figure 4.2: Carbonation depth in specimens in the single carbonation exposure.

4.4.3 Single PSA Exposure

Figure 4.3 shows the progression of damage (mass loss) during the single PSA exposure, and Figure 4.4 shows the visual condition of specimens at the end of exposure, along with visual ratings. During the drying portions of the cycle, salt efflorescence deposited on the exposed surface of specimens due to solution uptake and evaporation (wicking). As exposure proceeded, efflorescence accumulated on the exposed portions of specimens, followed by superficial scaling and spalling of concrete just above the solution level propagating upwards. During the first eight cycles, all specimens gained little mass due to solution ingress through the immersed portion. Afterward, specimens started to scale and lose mass at a slow rate up to 32-40 cycles, followed by accelerated mass loss of specimens till the end of exposure.

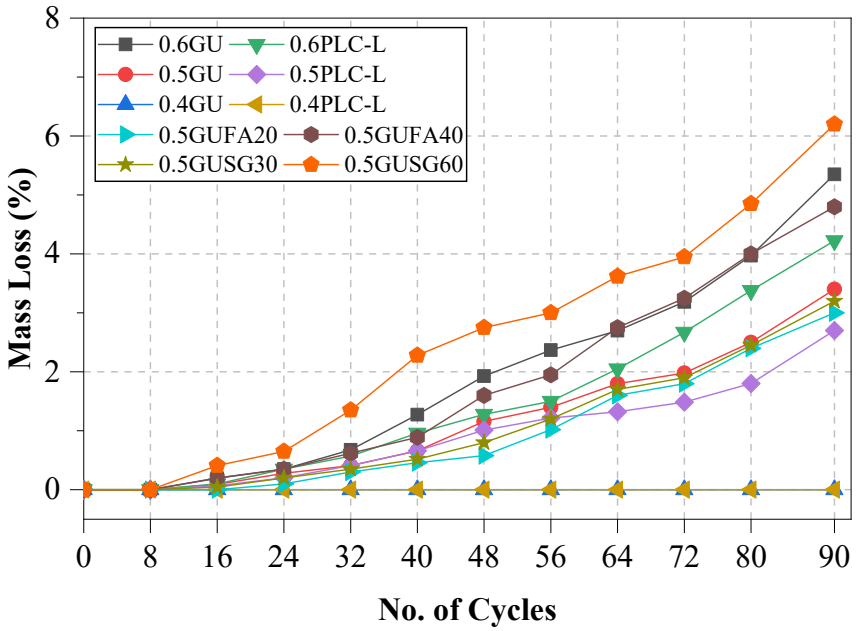

Figure 4.3: Variation of mass loss of specimens during the single PSA exposure.

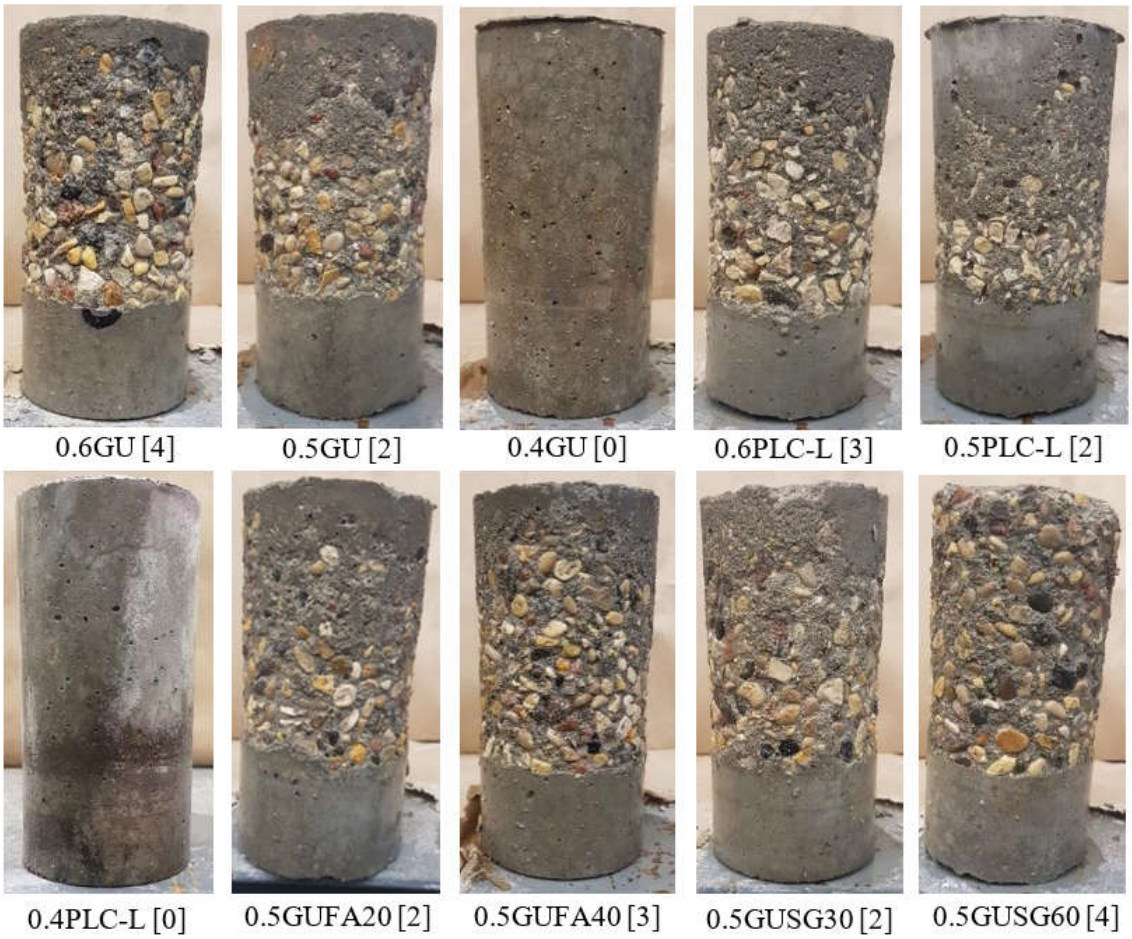

Figure 4.4: Conditions of specimens from various mixtures at the end of single PSA exposure. (Note: numbers between brackets are the visual ratings)

At the same *w/b* (0.50), incorporating 20% fly ash decreased the mass loss by 12% compared to plain concrete, but both had similar visual conditions (visual rating of 2, Fig. 4.4). However, increasing the amount of fly ash to 40% resulted in higher vulnerability (40% increase in mass loss and visual rating of 3) to PSA, relative to the reference concrete [0.5GU], with statistical significance (Table 4.5). Addition of slag to the binder at a replacement ratio of 30% yielded comparable performance under PSA to plain concrete without SCMs (mass loss of 3.2% compared to 3.4% for reference concrete), whereas the higher dosage of slag (60%) significantly escalated PSA damage such that the mass loss of 0.5GUSG60 specimens was 82% higher than that of the reference 0.5GU specimens (Fig. 4.3). ANOVA projected this significant effect with *F*-value of 152 compared to F_{cr} of 7.7 (Table 4.5).

4.4.4 Combined Exposure

The mass loss of specimens exposed to the combined exposure (PSA and carbonation) was determined every eight cycles, as shown in Fig. 4.5. Also, the final condition of specimens, along with the corresponding visual ratings, is presented in Fig. 4.6. Generally, the damage manifested in a manner similar to the single PSA exposure, where salt efflorescence accumulated on the drying portion of specimens followed by surface scaling and spalling. The progression of PSA with carbonation caused more surface scaling and mass loss than the single PSA exposure for the same concrete mixtures. For instance, 0.6GU specimens subjected to the combined exposure had a final mass loss of 7.5% (38% increase), whereas similar specimens exposed to PSA only had a mass loss of 5.4%. In contrast to the single PSA exposure, where the mass loss progressed slowly at the beginning of exposure followed by accelerated rates, the rate of surface deterioration in case of the dual exposure

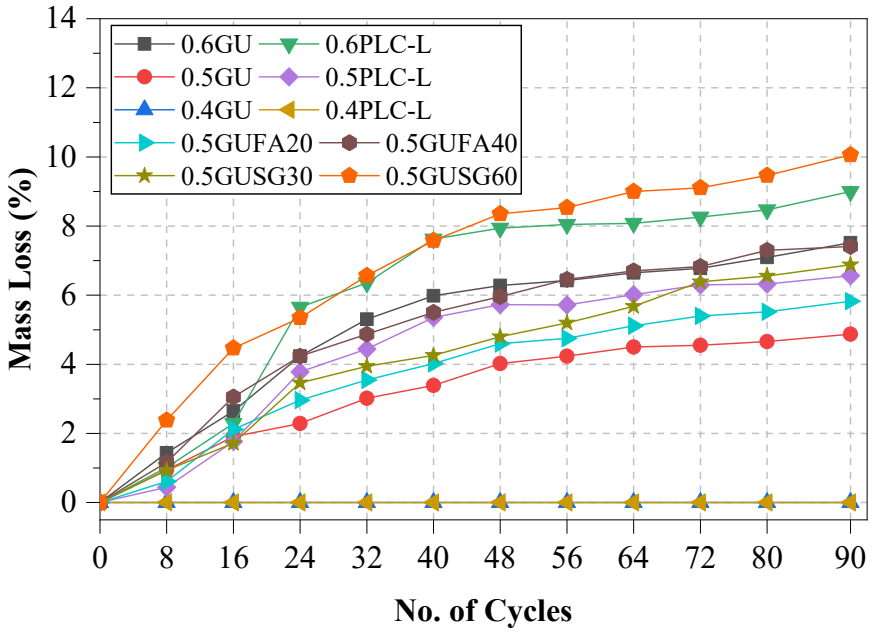

Figure 4.5: Variation of mass loss of specimens during the combined exposure (PSA and carbonation).

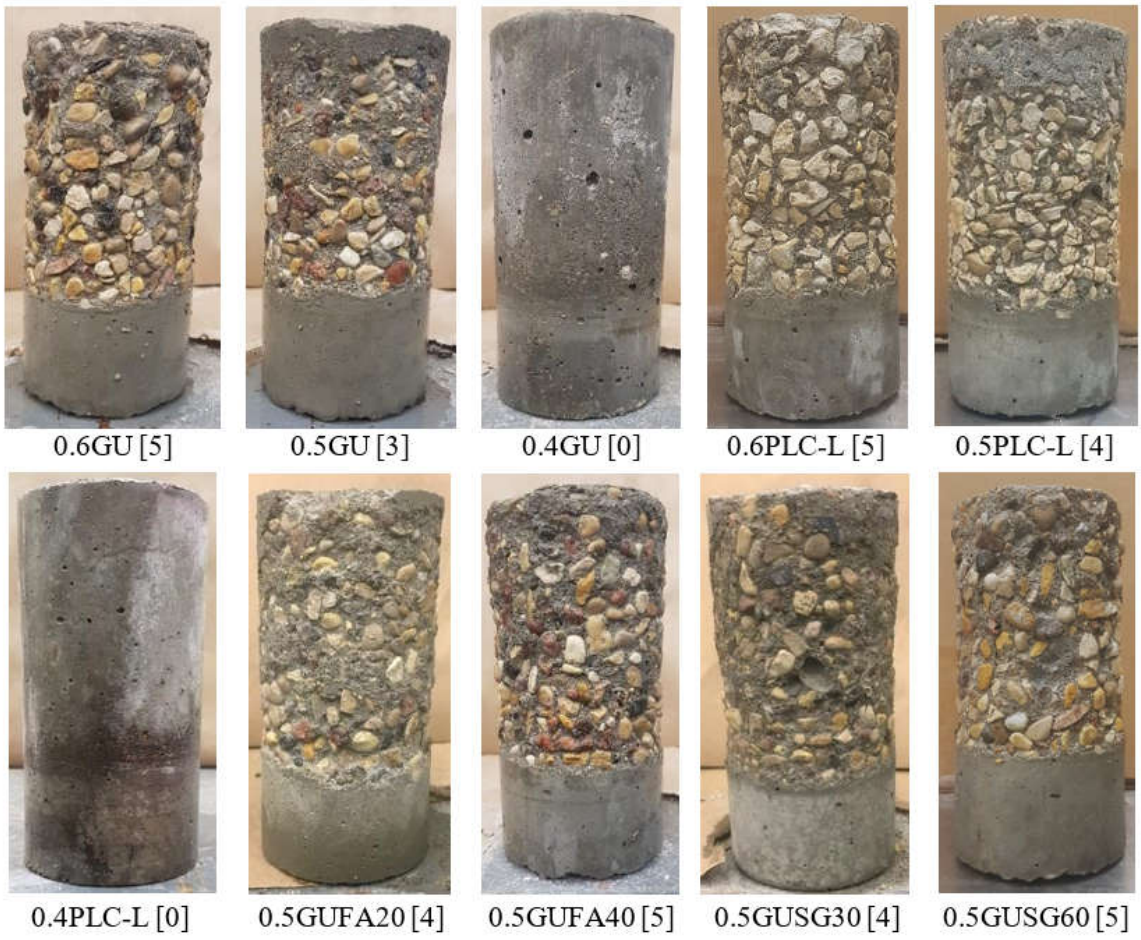

Figure 4.6: Condition of specimens from various mixtures at the end of combined exposure [PSA and carbonation]. (Note: numbers between brackets are the visual ratings)

was high within the first 32 to 40 cycles, and it subsequently reduced till the end of exposure (Figs. 4.3 vs. 4.5). This pattern of damage resembled that of carbonation front advancement in concrete (Fig. 4.2).

Decreasing the *w/b* significantly enhanced the resistance of concrete to the combined exposure. For example, 0.6GU specimens had a final mass loss of 7.5% (visual rating of 5) compared to 4.8% (visual rating of 3) for 0.5GU specimens (i.e. 36% reduction), while GU specimens made with *w/b* of 0.40 did not experience any damage. The positive effect of *w/b* reduction was replicated for PLC specimens. Nevertheless, unlike the case of single PSA, the use of PLC escalated the level of damage in specimens at all *w/b* except for 0.40. The mass loss of PLC specimens was 20% and 35% more than conjugate GU specimens at *w/b* of 0.60 and 0.50, respectively. The effect of changing the cement type was found significant by ANOVA as *F*-values of 20 and 57 were obtained at *w/b* of 0.60 and 0.50, respectively, compared to F_{cr} of 7.7 (Table 4.5).

The effect of SCMs on concrete under the combined damage did not follow the same trend as the case of single PSA. The use of fly ash at both dosages (20 and 40%) tended to increase the susceptibility of concrete to mass loss, with higher dosages causing more damage, as the incorporation of 20 and 40% fly ash into concrete increased the final mass losses by 21 and 52%, respectively, compared to that of the reference specimens without SCMs, with statistical significance (Table 4.5). Similarly, addition of slag to concrete increased the level of damage. For the slag dosage of 30%, the mass loss was 41% higher than that of plain concrete. Increasing the dosage of slag to 60% significantly (Table 4.5) increased the mass loss to 10% compared to 4.8% for the reference 0.5GU specimens.

4.5 Discussion

4.5.1 Mechanisms of Damage

4.5.1.1 Single PSA exposure

In the single PSA exposure, specimens were partially immersed in 10% sodium sulfate solution and subjected to cyclic environmental conditions. Reference 0.5GU specimens were used to elucidate the mechanism of damage in this case, while the effects of other variables are discussed in succeeding sections. XRD and SEM analyses were conducted on samples extracted from the surface zone (0-3 mm) of unexposed and exposed specimens at the end of testing. For unexposed concrete, some traces of hydration ettringite were found along with portlandite peaks (Fig. 4.7). Immersed parts of exposed specimens showed traces of ettringite and gypsum, without damage manifestations of swelling and cracking, indicating limited progress of chemical sulfate attack within the duration of exposure (Fig. 4.7). Comparatively, the drying portion showed a prevailing occurrence of thenardite with some traces of ettringite, which are similar in intensity to those detected in the immersed part. These findings excluded chemical sulfate attack as a cause of damage and substantiated that deposition of intensified salt sub-florescence beneath the surface layer of concrete was the precursor for PSA damage, manifested by surface scaling. In particular, the applied exposure conditions provoked reversible conversion between thenardite (forms during the drying cycles) and mirabilite (forms during the wetting cycle), which resulted in highly supersaturated sodium sulfate solution, and consequently more surface damage (Rodriguez–Navarro and Doehne 1999). Analysis by SEM and EDX on the scaled crust from evaporative surface of specimens verified the formation of massive planes of sodium sulfate crystals beneath this layer (Fig. 4.8), thus exerting high crystallization pressures on the pore walls of concrete, causing surface scaling.

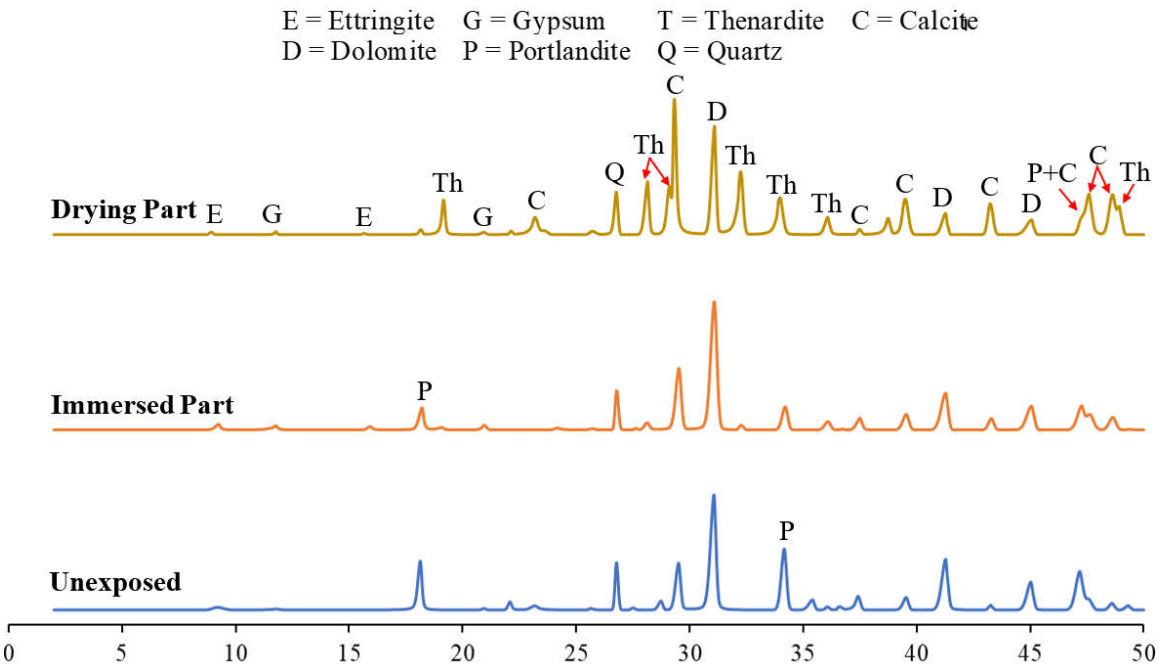

Figure 4.7: XRD analysis of unexposed and exposed 0.5GU specimens to the single PSA exposure.

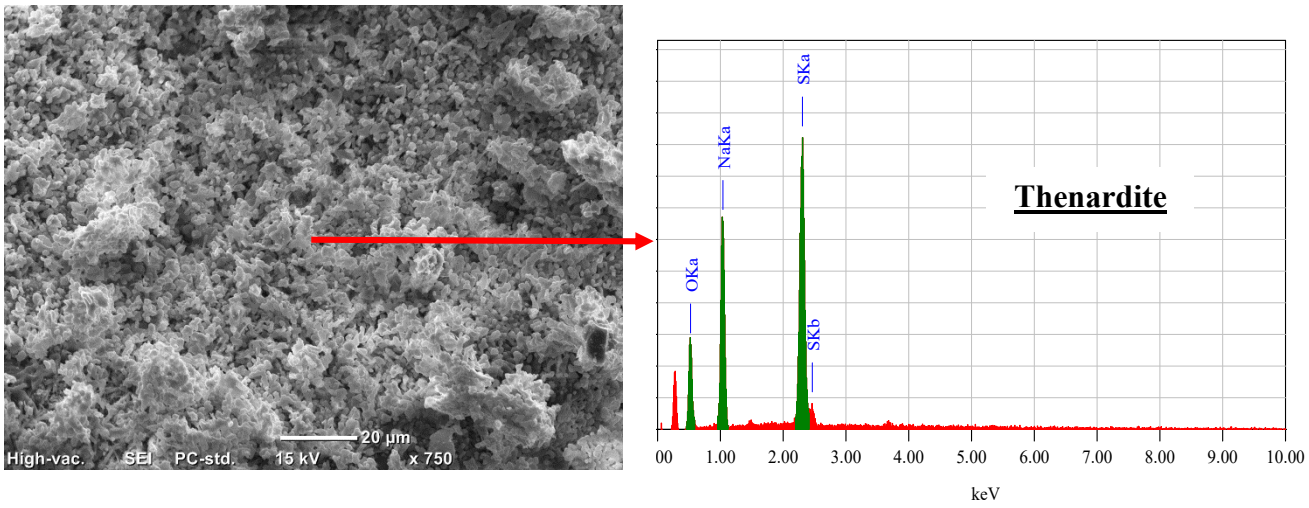

Figure 4.8: SEM and EDX analyses of scaled concrete layer from 0.5GU specimens exposed to the single PSA exposure.

4.5.1.2 Combined carbonation and PSA

To detect the mechanisms and evolution of damage induced by combined PSA and carbonation on concrete, the microstructural features of the drying portion of 0.5GU specimens were regularly analyzed since the onset of dual exposure. Thermal analysis by

DSC, based on the enthalpy concept (integration of heat flow peaks over temperature) that relates the amount of a certain compound to its enthalpy, indicated carbonation of the surface layer (0 to 3 mm) after four cycles of exposure, as shown by the absence of endothermic portlandite peaks within the temperature range of 400-500°C, relative to a portlandite enthalpy of 58 J/g in the unexposed specimens after the curing period (Fig. 4.9). As six cycles elapsed, sodium sulfate crystals were deposited within the exterior crust but without sufficient amounts (enthalpy of 4.6 J/g) to cause PSA, as reflected by the absence of visual signs of damage on surface. By the eighth cycle, abundant amounts of salt crystals (enthalpy of 24.5 J/g) were formed within this layer leading to scaling of portions from the surface layer (0-3 mm) of specimens.

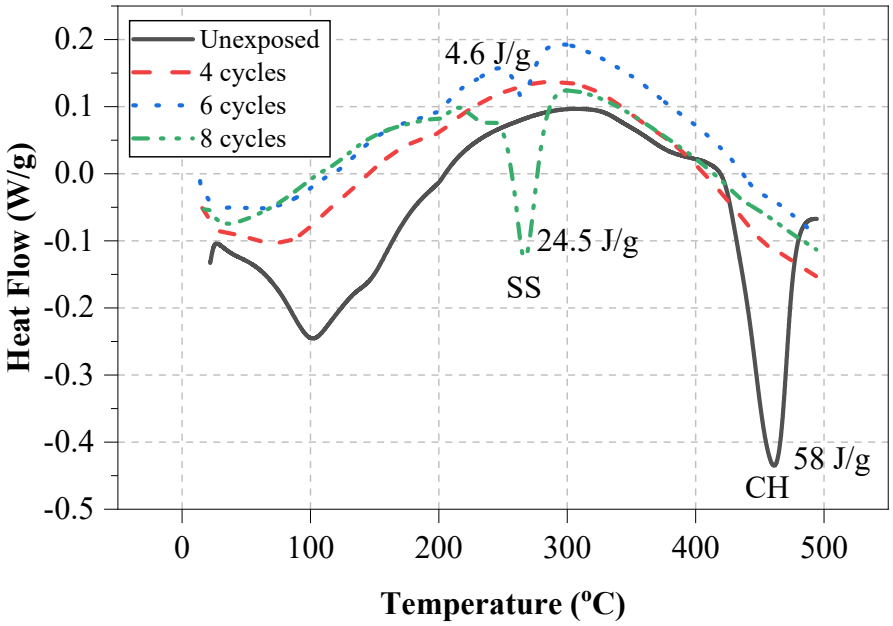

Figure 4.9: DSC curves of 0.5GU specimens (drying portion) exposed to combined PSA and carbonation at different time intervals. (Note: SS = sodium sulfate; CH = calcium hydroxide).

The DSC findings were substantiated by the SEM/EDX analyses on fracture pieces extracted from the surface curst. Fig. 4.10 shows that the process commenced with

formation of prismatic calcite ($CaCO_3$) crystals in the surface layer [also reflected by the carbonation front trends (Fig. 4.2)] after four cycles of exposure due to the reaction of portlandite with CO_2, followed by the deposition of sodium sulfate crystals along with calcite at the sixth cycles, and ended with abundant formation of salt crystals underneath the outer crust leading to its detachment at the eighth cycle. Subsequent scaling of successive layers of concrete proceeded in a similar manner with a life span of 6 to 8 cycles until detachment.

The rate of deterioration of concrete under the combined exposure was escalated, compared to the single PSA exposure, due to the synergistic effects of carbonation with sodium sulfate, although precipitation of calcite, due to carbonation alone, was reported to cause a net increase in volume, block the pore system, and decrease the porosity of concrete (Arandigoyen et al. 2006). This could be linked to the variation of wicking factor with time [Fig. 4.11a], as calculated per the procedures described in the testing section. Carbonation steadily increased the wicking factor since the start of exposure by up to 27% at 48 cycles, which was attributed to the decomposition of C-S-H (Swenson and Sereda 1968; Ngala and Page 1997; Rimmelé et al. 2008) in the surface zone, after the consumption of portlandite (occurred after the fourth cycle). Carbonation of C-S-H starts by initial decalcification where calcium is consumed from the interlayer and defect positions within the silicate chains, followed by decomposition due to consumption of calcium from C-S-H principle layers and formation of amorphous silica (Arandigoyen et al. 2006; Sevelsted and Skibsted 2015), which led to increase in the porosity of concrete that outweighed the effect of calcite precipitation. Thus, the coarsened pore structure of concrete was manifested as higher rates of solution uptake and evaporation, increased build-up of crystallizing salt, and

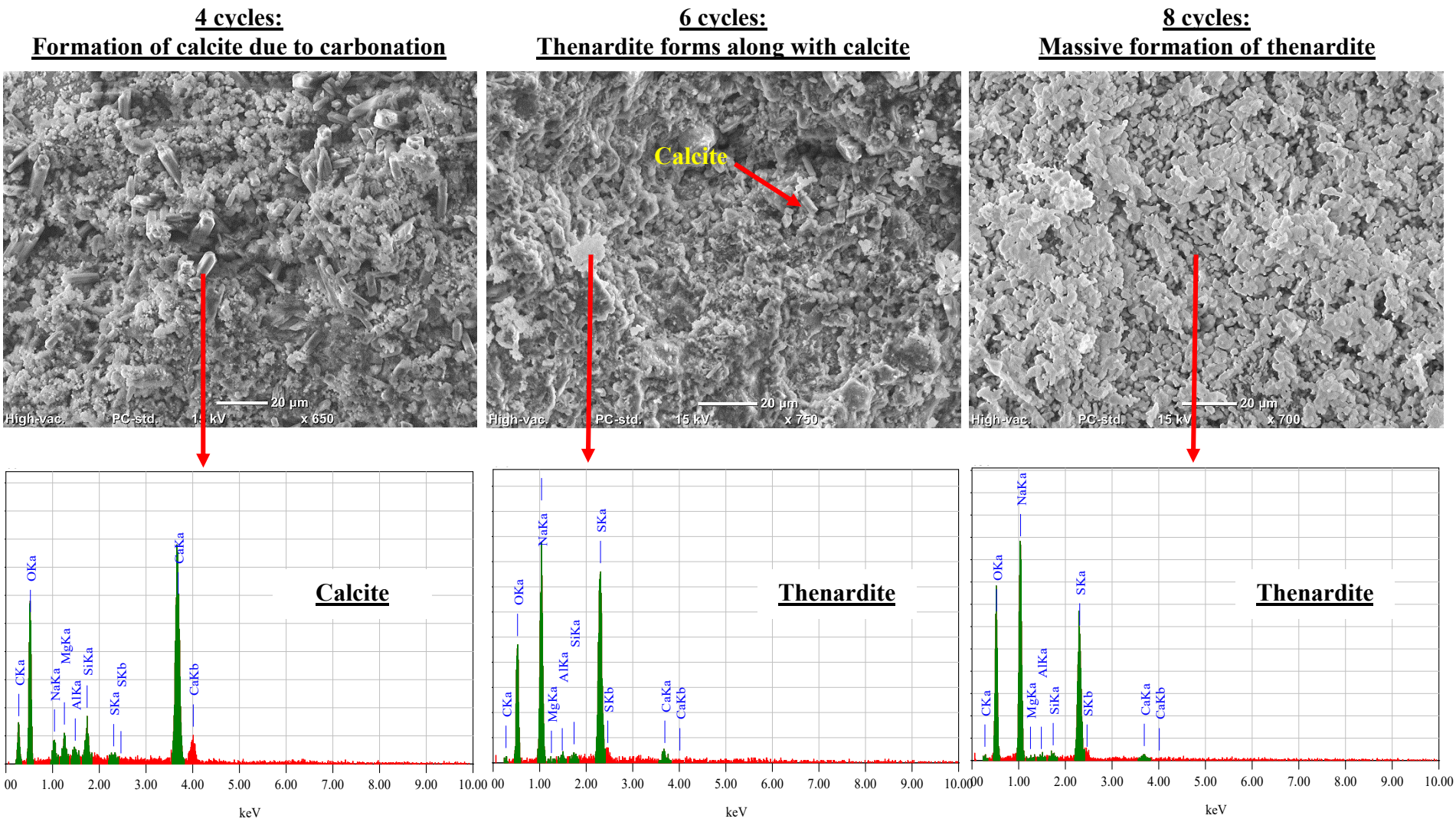

Figure 4.10: SEM and EDX analyses of surface layer (0-3 mm) of 0.5GU specimens showing the alteration of microstructure in the drying portion during the combined exposure.

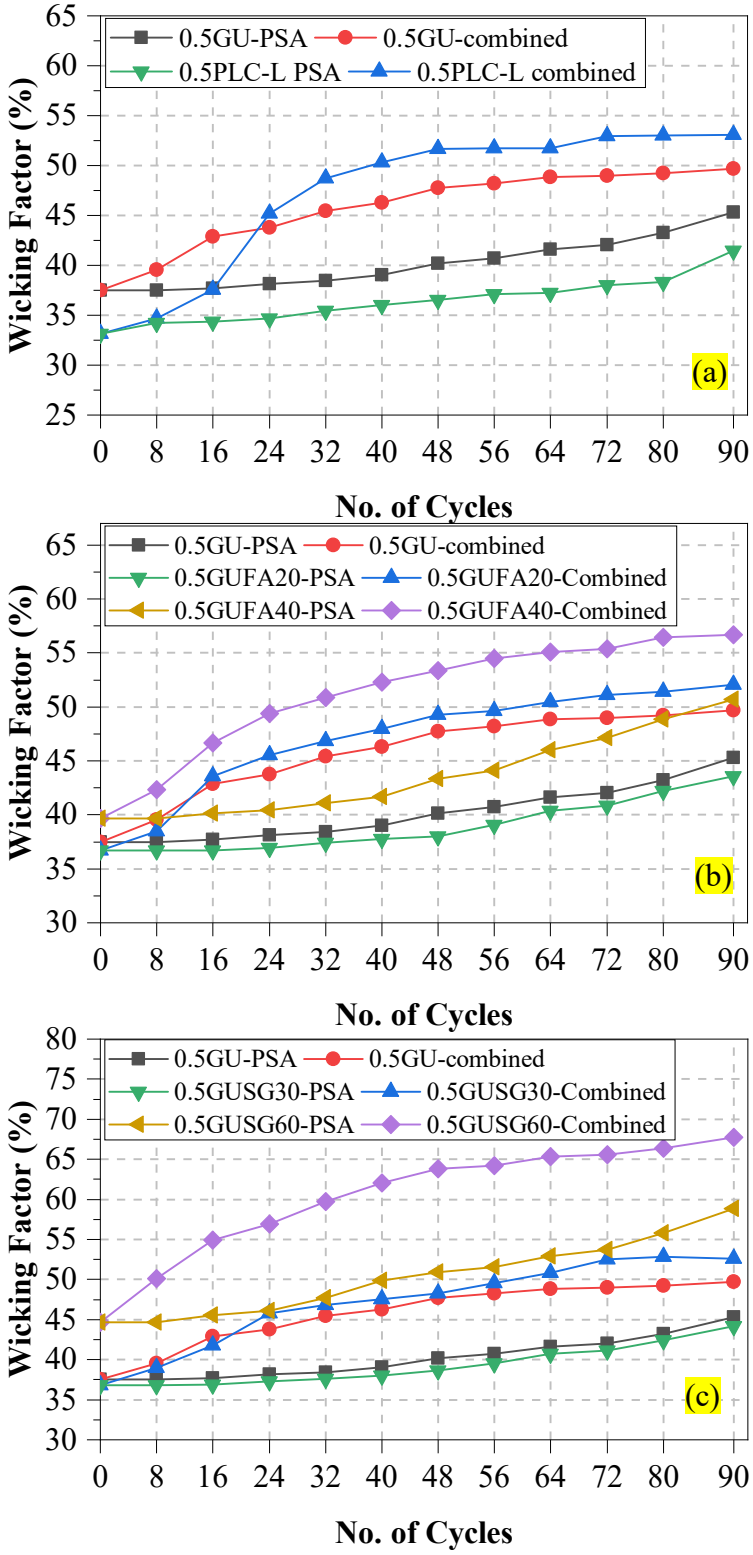

Figure 4.11: Variation of the wicking factor in specimens made from: (a) single, (b) binary/fly ash, and (c) binary/slag binders at *w/b* of 0.50 under different exposures.

consequently elevated surface scaling of concrete. The wicking factor diminished between 48-90 cycles, possibly due to the deposition of abundant calcite crystals after 3 mm from surface forming an inner band of approximately 2-3 mm thickness towards the core of specimens (e.g. Fig. 4.12) that discounted wicking and thus the rate of PSA damage of specimens.

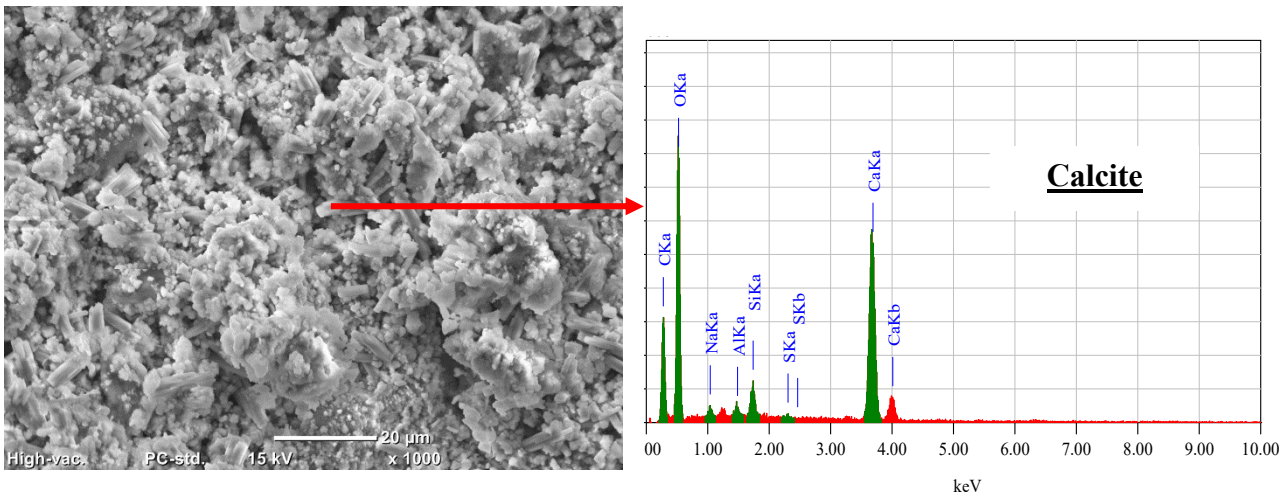

Figure 4.12: SEM and EDX analyses of the inner band [3-5 mm from surface] of 0.5GU specimens (drying portion) at 90 cycles.

In addition, carbonation promoted the formation of other phases that may contribute to the damage process. XRD analysis at an intermediate stage of exposure (32 cycles) showed peaks of natrite (sodium carbonate, Na_2CO_3) salt, in addition to the intense peaks of thenardite, within the surface layer (Fig. 4.13). Na_2CO_3 may form as a reaction product of carbonic acid (formed as CO_2 gas dissolves in pore solution) and sodium sulfate solution, according to:

$$Na_2SO_4 + H_2CO_3 \rightarrow Na_2CO_3 + H_2SO_4 \quad \text{(Eq. 4.1)}$$

Another possible route for the reaction is through dissolution of calcite into calcium and bicarbonate ions after the consumption of portlandite and reduction in pH below 10 (Hekal et al. 2002), which subsequently reacted with sodium sulfate to produce Na_2CO_3:

$$CaCO_3 + HCO_3^- + H^+ + H_2O \rightarrow Ca^{2+} + 2HCO_3^- + H_2O \quad \text{(Eq. 4.2)}$$

$$Na_2SO_4 + HCO_3^- \rightarrow Na_2CO_3 + H^+ + SO_4^- \quad \text{(Eq. 4.3)}$$

According to the phase diagram of sodium carbonate, the cyclic conditions applied herein would promote recurring phase changes between thermonatrite ($Na_2CO_3 \cdot H_2O$) and natron ($Na_2CO_3 \cdot 10H_2O$), which is associated with 255% volume increase. This transformation was reported in (Haynes et al. 2010) to cause moderate PSA damage of concrete.

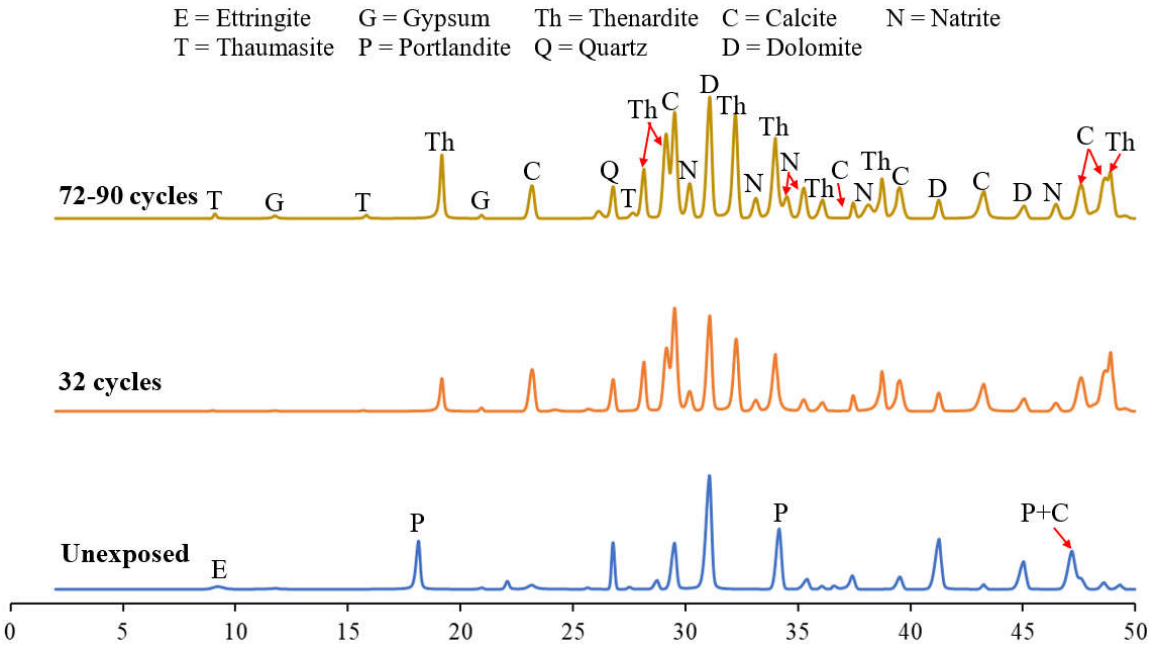

Figure 4.13: XRD analysis of unexposed and exposed (drying portion) 0.5GU specimens to combined exposure.

Within 72-90 cycles, XRD analysis showed incidental formation of thaumasite within the cementitious matrix (Fig. 4.13). Thaumasite was detected beyond the heavily carbonated zone (beyond 5 mm from surface) as its stability may be compromised below pH of 10.5 (Gaze and Crammond 2000). Besides formation of calcite in these locations, the pH of the pore solution might not be affected since the existence of sodium ions and/or formation of sodium hydroxide contribute to maintaining the alkalinity of the matrix. The existence of aluminum peak in the EDX of thaumasite (e.g. Fig. 4.14) suggested that it formed through the indirect route, where ettringite acts as a precursor for thaumasite formation; ettringite first forms and then it reacts with C-S-H and carbonates to form thaumasite, especially during the cold portion of the cycles cycle (5°C) (Rahman and Bassuoni 2014):

$$C_3S_2H_3 + C_6A\bar{S}_3H_{32} + 2CaCO_3 + 4H_2O \rightarrow 2C_3S.\bar{C}\bar{S}H_{15} + C\bar{S}H_2 + AH_3 + 4CH \quad \text{(Eq. 4.4)}$$

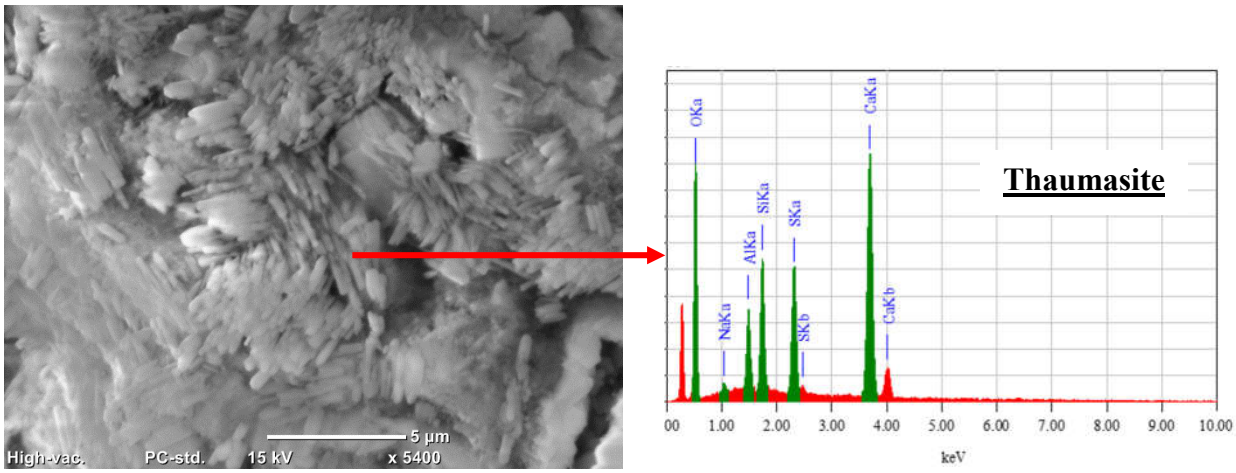

Figure 4.14: Formation of thaumasite at 5 mm from surface in the drying portion of 0.5GU specimens subjected to combined exposure.

EDX elemental spatial distribution maps on 0.5GU specimens (Fig. 4.15) at the end of exposure also reflected this zonation of precipitated phases in the matrix. It showed the abundance of sodium and sulfur in the sub-florescence zone (3 mm), indicating formation of sodium sulfate crystals within the surface crust of specimens. Beyond this zone, the intensity of sodium diminished at 5 mm from surface, while the amount sulfur slightly varied, suggesting the existence of sulfate reaction products (e.g. thaumasite) in deeper regions of specimens. Formation of thaumasite in fissures and voids of concrete does not necessarily deteriorate the matrix unless excessively formed within the microstructure, which is indicative of thaumasite sulfate attack (TSA) that transforms concrete into a mushy and non-cohesive mass (Rahman and Bassuoni 2014). Thus, for extended duration of exposure and/or with other mixture design constituents, TSA may coexist with PSA in concrete.

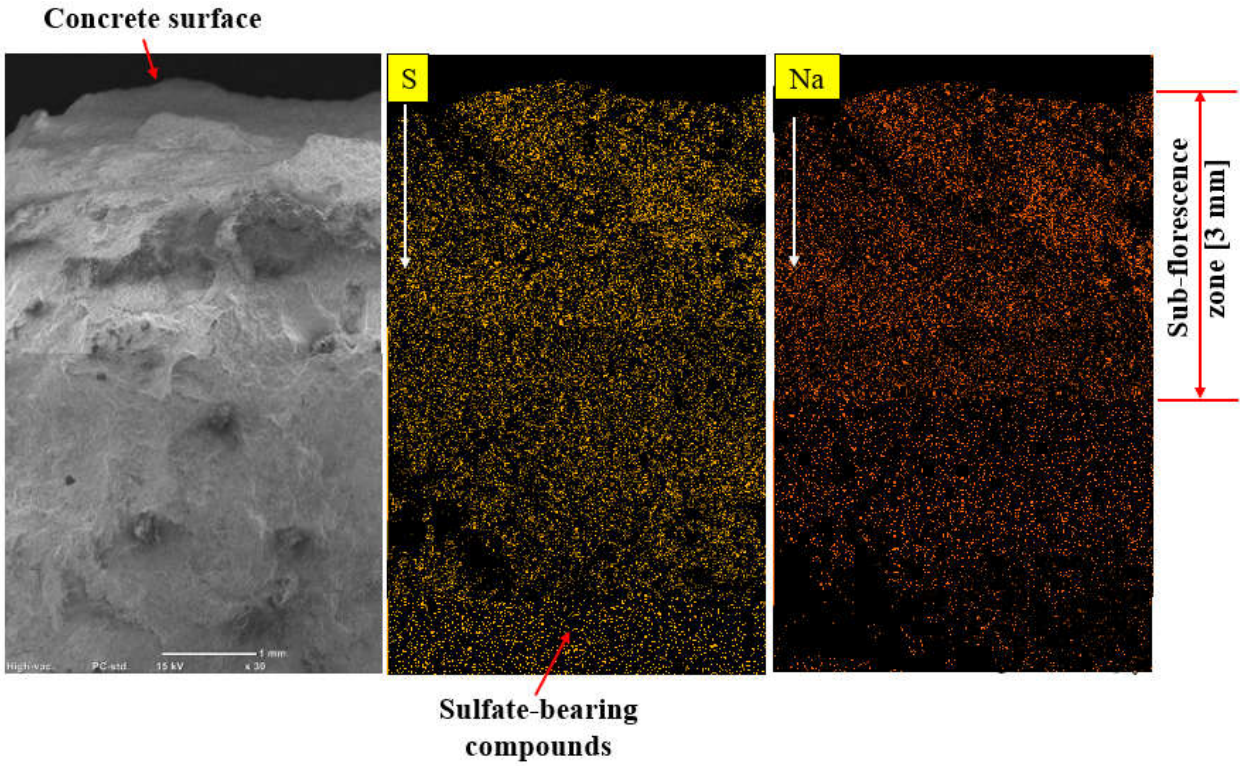

Figure 4.15: Spatial distribution of sodium and sulfur elements in 0.5GU specimens exposed to the combined PSA and carbonation at 90 cycles.

4.5.2 Effect of *w/b*

The *w/b* was a key factor at improving the resistance of concrete to both single and combined PSA exposures, regardless of the cement type (GU or PLC). XRD analysis on powder samples collected from the evaporative front of specimens exposed to combined PSA and carbonation at 90 cycles showed prevailing occurrence of thenardite in 0.6GU specimens with occurrence of natrite and traces of thaumasite, while 0.4GU specimens did not show such compounds (Fig. 4.16).

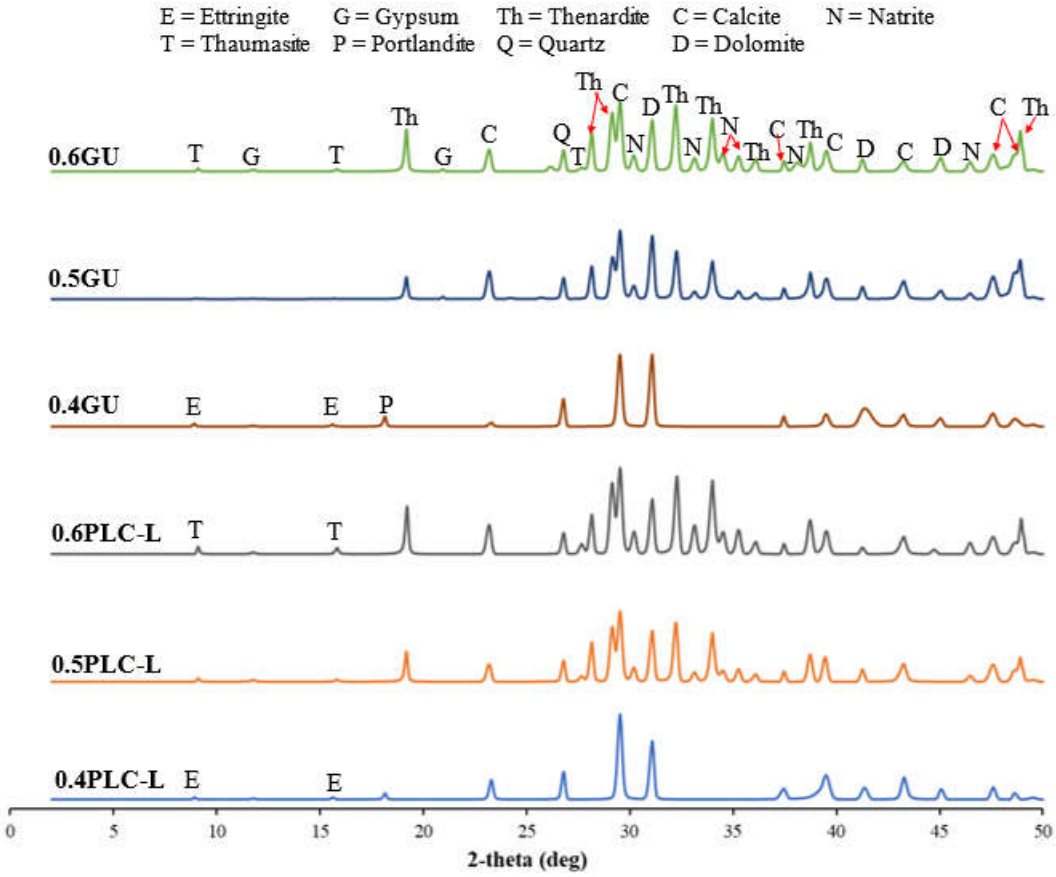

Figure 4.16: XRD analysis of GU and PLC specimens exposed to combined PSA and carbonation.

For example, pore structure characteristics determined by MIP at 56 days showed that GU specimens made with *w/b* of 0.40 had less porosity and connectivity of pores than conjugate 0.6GU specimens since the total porosity and proportion of micropores were

32% less and 79% higher, respectively than that of 0.6GU concrete (Table 4.6). The densification of microstructure caused by *w/b* reduction resulted in lower rates of carbonation (Fig. 4.2) and solution uptake/evaporation (Table 4.4), which disrupted wicking, decreased build-up of crystallizing salt, and consequently reduced surface scaling of concrete. Generally, the effect of *w/b* followed the results of previous studies on single PSA of concrete and current recommendations of ACI 201.2R to reduce *w/b* for producing concretes less vulnerable to environments conducive to PSA (ACI 201.2R 2016; Bassuoni and Rahman 2016).

Table 4.6: Summary of MIP results at 56 days

Mixture ID.	Apparent total porosity (%)	Proportion of micro-pores (<0.1 µm)	Threshold pore diameter (µm)
0.6GU	19.5	35.9	1.00
0.5GU	17.3	47.5	0.80
0.4GU	13.2	64.4	0.35
0.6PLC-L	17.4	40.1	0.85
0.5PLC-L	15.0	54.8	0.67
0.4PLC-L	11.7	71.5	0.17
0.5GUFA20	15.9	51.4	0.62
0.5GUFA40	18.2	44.8	0.81
0.5GUSG30	16.2	48.5	0.69
0.5GUSG60	20.6	37.3	0.93

4.5.3 Effect of Limestone Materials

Specimens prepared with PLC and limestone aggregate showed two distinctive trends in the reference and combined PSA exposures. PLC specimens subjected to the single PSA exposure consistently experienced less mass loss than conjugate GU specimens throughout testing at *w/b* of 0.60 and 0.50. MIP trends (Table 4.6) showed that specimens made with limestone materials had lower porosity and denser microstructure; for example, 0.5PLC-L specimens had 13% less total porosity and 15% higher proportion of micro-pores than that

of 0.5GU specimens. This could be attributed to the physical effects of PLC including its higher fineness (460 m^2/kg) compared to GU cement (390 m^2/kg) due to intergrinding of clinker with limestone powder, which can enhance the hydration process and microstructural development of concrete. Also, PLC contributes a filler effect due to particle packing in the matrix (Marzouki et al. 2013). Accordingly, PLC specimens had lower absorption and desorption percentages (Table 4.4) than that of GU specimens, leading to less solution uptake and evaporation, reduced intensity of crystallized salt, and subsequently decreased surface damage. This was substantiated by comparing the wicking factors of PLC and GU specimens; for example, the initial wicking factor of 0.5PLC-L was 30.4% compared to 37.5% for 0.5GU specimens (i.e., 19% reduction), and it remained consistently lower for 0.5PLC-L specimens throughout the single PSA exposure (Fig. 4.11a)

At *w/b* of 0.40, the effect of cement type was insignificant since no damage occurred in 0.4GU and 0.4PLC-L specimens, indicating the dominant effect of *w/b* reduction at mitigating PSA on concrete. The trends obtained herein for the effect of PLC were in line with that reported by Nadelman and Kurtis (2019) for the low *w/b* (0.40). However, at *w/b* of 0.60, PLC was reported to slightly worsen the resistance of concrete to PSA in conditions promoting crystallization of mirabilite, where specimens fractured suddenly by transverse cracks (Nadelman and Kurtis 2019). Whereas comparable total porosity was obtained for PLC and GU specimens, slightly higher proportion of micropores (< 0.1 μm) existed in PLC specimens, which may increase the crystallization pressure due to inverse proportionality with pore size (Nadelman and Kurtis 2019), as hypothesized by Scherer (2004). In the current study, the PLC specimens at higher *w/b* (0.60 and 0.50) had less porosity and higher proportion of micro-pores, but without excessive refinement,

which was reflected by the consistently lower wicking factor compared to that of GU specimens [Fig. 4.11(a)], which accommodated cyclic conversion between thernadite and mirabilite and in turn less progressive surface scaling with time, without abrupt failure.

In the case of combined exposure, at *w/b* of 0.40, the effect of *w/b* reduction was dominant as no damage occurred for both 0.4GU and 0.4PLC-L specimens. On contrary to the single PSA exposure, specimens made with limestone materials and higher *w/b* (0.60 and 0.50) showed higher level of damage relative to corresponding GU specimens. The use of carbonate-rich constituents in concrete initially showed comparable neutralization depths (Fig. 4.2) and mass loss (Fig. 4.5) to that of GU specimens up to 16-24 cycles, which could be attributed to the densification of microstructure by the filler and packing effects contributed by limestone powder in cement (about 12%) that led to slowing down the ingress of carbon dioxide and sodium sulfate. However, as carbonation progressed beyond this stage, the rate of carbonation of PLC specimens was significantly higher than that in GU specimens till the end of exposure (Fig. 4.2). DSC analysis showed approximately 12% less enthalpy of portlandite in 0.5PLC-L specimens compared to 0.5GU specimens (Fig. 4.17). The dilution effect of limestone powder and in turn reduction of the portlandite content in the matrix led to decreasing the carbonation resistance of concrete by promoting C-S-H decalcification, which facilitated further ingress of CO_2 and sodium sulfate, causing more damage of concrete. The nucleation effect of fine limestone particles promoted rapid precipitation of calcite, thus speeding up portlandite consumption and consequent decalcification of C-S-H. Moreover, the use of limestone aggregates provided an additional source of carbonate ions that accelerated the kinetics of carbonation reactions. All these factors outweighed the initial physical enhancement of the microstructure by PLC, leading to an accelerated rate of damage.

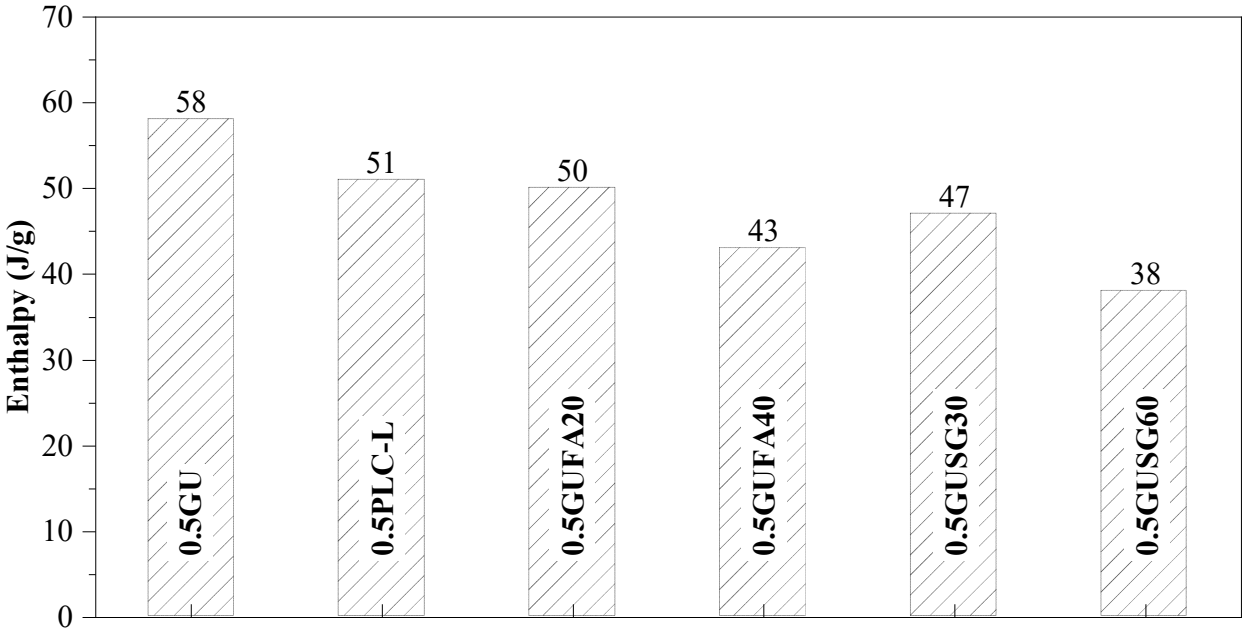

Figure 4.17: Enthalpy of initial portlandite in various binders at 56 days.

In addition, the chemical effects of limestone materials contributed to the damage of PLC specimens. XRD analysis showed that these specimens contained visible peaks of sodium carbonate and thaumasite (Fig. 4.16) since limestone materials provided additional source for carbonate ions that facilitated the formation of these compounds. Correspondingly, SEM images showed the deposition of natrite in some locations underneath the sub-florescence zone and formation of thaumasite in fissures and voids of PLC specimens (e.g. Figs. 4.18 and 4.19). The net effects of limestone materials were captured by the variation of wicking factor in PLC specimens throughout the combined exposure (e.g. Fig. 4.11a). For example, 0.5PLC-L specimens yielded less wicking factor than 0.5GU specimens during the first 16 cycles (densification) of the combined exposure, which was followed by a drastic increase up to 48 cycles (decomposition of C-S-H and more PSA damage); eventually, the wicking factor almost stabilized up to 90 cycles due to abundant deposition of calcite crystals with time in the matrix.

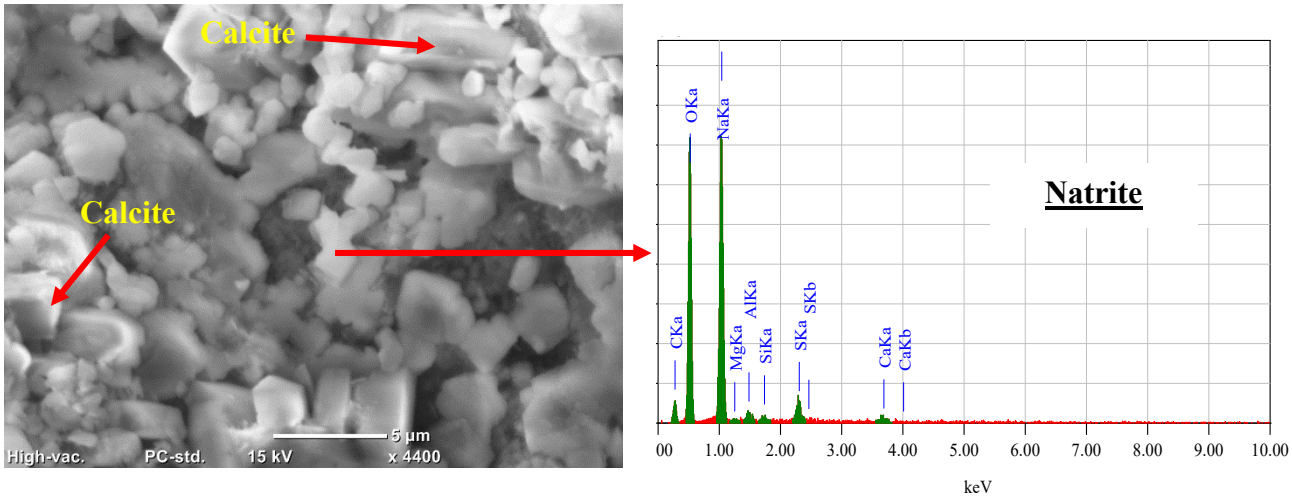

Figure 4.18: Deposition of natrite crystals along with calcite beyond the sub-florescence zone in the drying portion of 0.5PLC-L specimens subjected to the combined exposure.

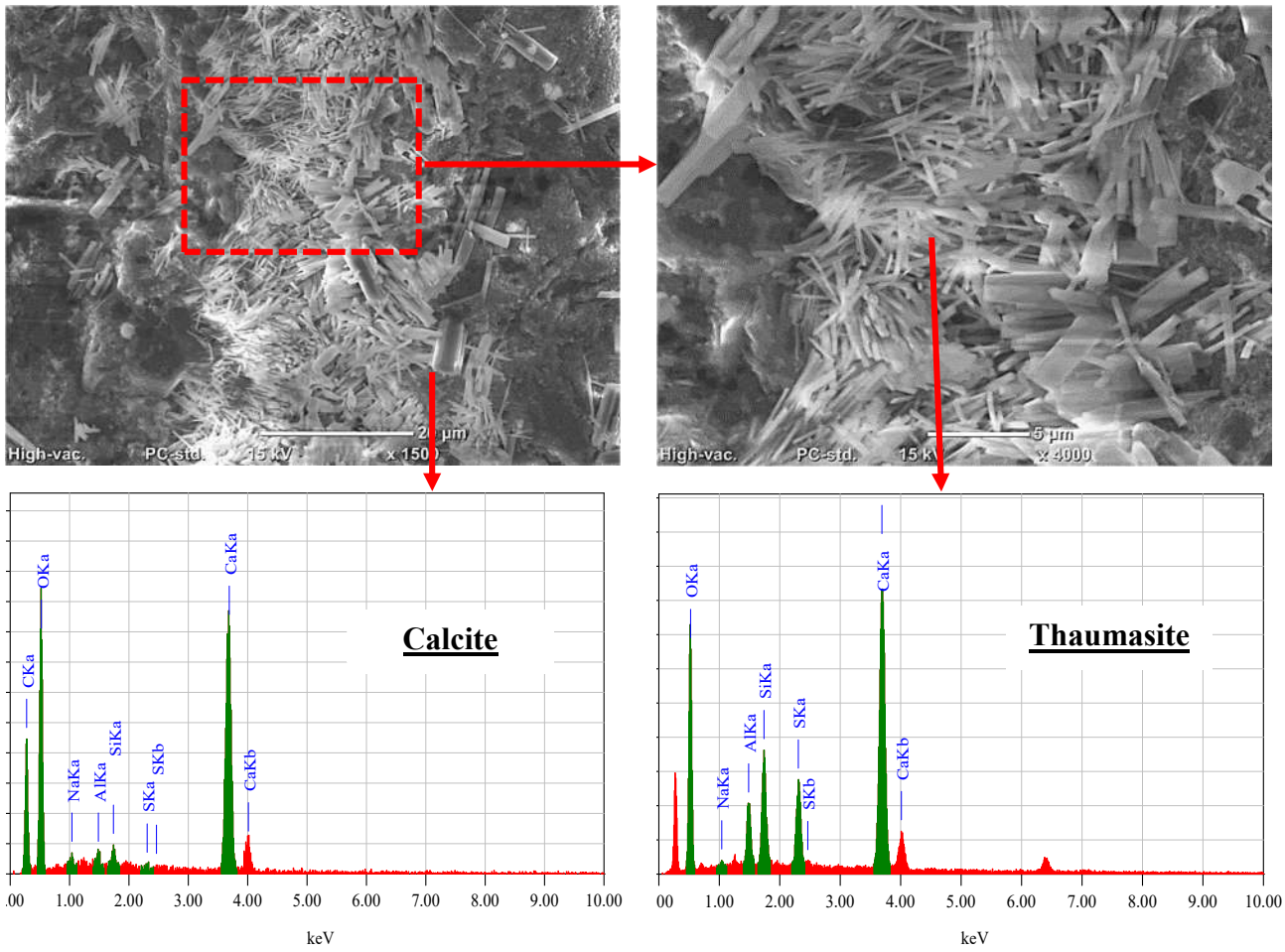

Figure 4.19: Formation of thaumasite along with calcite at 5 mm from surface in the drying portion of 0.5PLC-L specimens subjected to combined exposure.

4.5.4 Effect of SCMs

As mentioned in the Introduction section, the discrepancy in trends regarding the effect of SCMs on PSA of concrete, even for the same replacement ratio, may be attributed to differences in mixture designs, testing conditions, and/or curing regimes (Irassar et al. 1996; Stark 2002; Bassuoni and Rahman 2016; Zhutovsky and Hooton 2017a). In this study, with application of uniform testing conditions, concrete specimens incorporating moderate dosages of SCMs (20% fly ash or 30% slag) and exposed to single PSA showed slight improvement (6 to 12% less final mass losses) compared to reference 0.5GU specimens. The alteration of hydration products imparted by fly ash and slag was studied by DSC analysis on the surface layer of unexposed specimens following the curing period. The results showed reduction of portlandite by 13% and 19% in specimens made with 20% fly ash and 30% slag, respectively, compared to reference specimens without SCMs (Fig. 4.17), indicating pozzolanic reactivity and precipitation of secondary C-S-H in the cementitious matrix. SEM images on the microstructure of specimens containing SCMs (20% fly ash and 30% slag) showed the existence of unreacted fly ash and slag particles after extended curing for 56 days (Figs. 4.20a,b). In the case of PSA, these unreacted loose particles in the surface layer of concrete would be easily dislodged in a manner similar to salt-frost scaling tests (ASTM C672 2012), especially that the implemented exposure conditions (partial immersion and evaporation in the drying periods) did not provide favorable curing conditions for continual reactivity of either fly ash or slag particles in the matrix of drying portion of specimens. For moderate amounts of SCMs, the net effect of pozzolanic reactivity (densification of pore structure) and scaled unreacted particles led to mild enhancement for resistance of concrete to PSA. This was reflected by the wicking factor calculations that yielded slightly lower values for 0.5GUFA20 and 0.5GUSG30

specimens throughout the single PSA exposure compared to that of 0.5GU concrete (Figs. 4.11b,c).

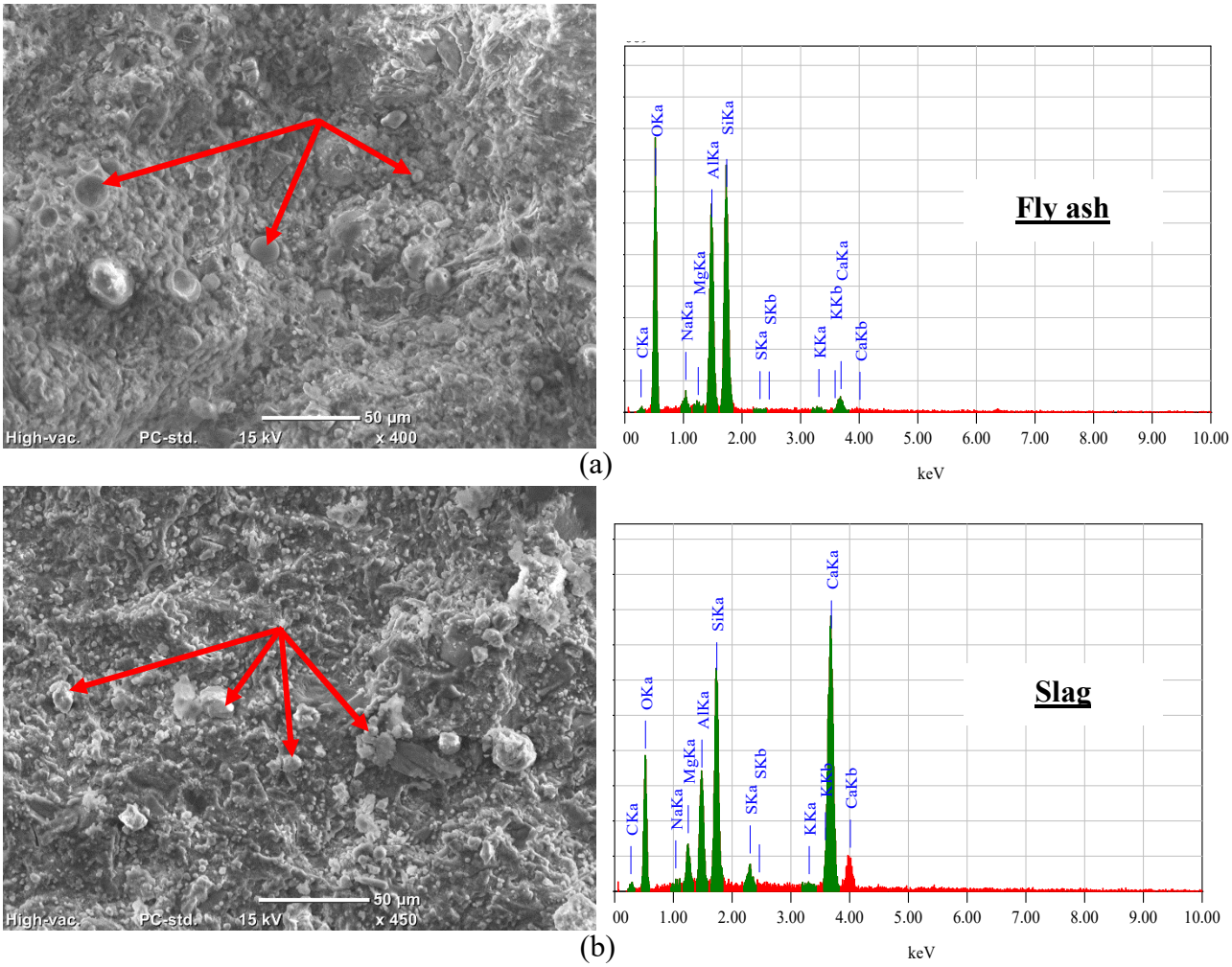

Figure 4.20: SEM and EDX analyses of (a) 0.5GUFA20, and (b) 0.5GUSG30 specimens after 56 days of curing.

On contrary, using high replacement ratios of cement with fly ash (40%) and slag (60%) escalated the mass loss of specimens relative to plain concrete. DSC analysis showed reduction of portlandite content in specimens containing 40% fly ash and 60% slag by only 14% and 19%, respectively, compared to that in specimens with moderate dosages (Fig. 4.17), alluding to high proportion of unreacted fly ash and slag particles at this age. This conforms to previous studies that reported large proportions of unreacted particles in

binders with high-volume fly ash or slag even after one year of curing (Bentz 2014; Wang 2014). This led to coarsened pore structure of concrete (Tables 4.4 and 4.6), especially in the drying portion of concrete experiencing unfavorable curing conditions, resulting in higher wicking factors throughout testing compared to that of reference concrete and specimens with moderate amounts of SCMs (Figs. 4.11b,c). Higher wicking factors indicated more solution uptake/evaporation leading to higher amounts of crystallizing salt, and consequently surface scaling of concrete. This trend may change for dissimilar exposure conditions that promote further curing during testing. For example, Zhutovsky and Hooton (2017a) reported that addition of 45 and 65% slag reduced the mass loss of mortar under full immersion in 30% Na_2SO_4 while cycling the temperature between 30 and 5°C. This full immersion test protocol likely promoted further curing and development of the hydration/pozzolanic processes due to the constantly high RH and intermittently high-temperature portion of the cycle. However, the latter exposure does not mimic partially embedded concrete elements (e.g. piers) or those in contact with wet soil from one side (e.g. tunnel linings).

Compared to the reference PSA exposure, the coexistence of carbonation with PSA increased the mass loss of all specimens incorporating SCMs compared to the reference 0.5GU specimens. Fig. 4.2 showed higher rates of carbonation in specimens containing SCMs relative to reference concrete, which increased with higher replacement ratios. Initial consumption of portlandite (Fig. 4.17) in the pozzolanic reaction of fly ash and slag decreased the resistance of concrete to carbonation and increased the vulnerability of C-S-H to decalcification, facilitating further ingress of carbon dioxide and sodium sulfate, which led to more damage. Hence, specimens containing SCMs exposed to dual damage had higher wicking factors than that of reference specimens, with larger values for

specimens comprising higher volumes of SCMs [i.e. less initial portlandite in the system, Fig. 4.17 and coarser pore structure, Table 4.6]. For example, the wicking factor of 0.5GUFA20 and 0.5GUFA40 specimens was mostly higher than that of 0.5GU specimens throughout testing with 5% and 15%, respectively higher final values (Fig. 4.11b). In addition, unreacted particles of fly ash and slag in the surface layer of concrete would negatively affect the resistance of concrete to combined damage in a manner similar to the reference PSA exposure being easily removed as surface scaling proceeded.

CHAPTER 5: EFFECT OF COATINGS ON CONCRETE RESISTANCE TO PHYSICAL SALT ATTACK

The preceding chapter has elucidated the damage mechanism of concrete exposed to single physical salt attack (PSA) and combined PSA with carbonation, considering the effect of mixture design parameters (e.g. water-to-binder ratio, cement type, and supplementary cementitious materials). In this chapter, different types of surface coatings are applied to concrete to assess their suitability for resisting PSA. Concretes with different water-to-binder ratios are tested and severe PSA conditions are implemented, using sodium sulfate, to obtain conclusive trends on the performance of coatings.

5.1 Introduction

ACI 201.2R (2016) (*Guide to Durable Concrete*) defines physical salt attack (PSA) as a damage mechanism caused by salt crystallization in pores near evaporative surfaces of concrete. PSA damage is mainly physical in nature (with no to limited chemical alteration of hydration products), leading to progressive surface scaling and flaking of concrete (Flat 2002; Haynes and Bassuoni 2011). In most field cases, PSA occurs where there is continuous supply of salt solution and simultaneous crystallization at the evaporative front (wicking action) such as in partially embedded foundations and tunnels (Scherer 2004). High evaporation rate with respect to solution uptake forms sub-florescence beneath the surface, causing significant crystallization pressure on the pore walls, reported to reach 10–20 MPa, which is far greater than concrete tensile strength, thus causing PSA damage (Flat 2002).

Conventional methods for protecting concrete against PSA are still uncertain. For instance, although decreasing the water-to-binder ratio (*w/b*) improves the resistance of

Sakr, M. R., Bassuoni, M. T., and Taha, M. R., "Effect of Coatings on Concrete Resistance to Physical Salt Attack," *ACI Materials Journal*, V. 11, No. 6, 2019, pp. 255-267.

concrete to PSA, the surface damage is not fully eliminated (Bassuoni and Rahman 2016). Moreover, there is discrepancy in the published literature on how supplementary cementitious materials (SCMs) affect concrete resistance to PSA. For instance, Zhutovsky and Hooton (2017a) reported that Class F fly ash (20% and 40%) significantly increased the mass loss of specimens under PSA exposure compared with the reference mixture such that mortars with 20% fly ash gave final mass loss higher than those with 40%. Conversely, the long-term studies of Portland Cement Association (PCA) reported inferior performance of field concrete containing 40% Class F fly ash compared with those made with 20% fly ash throughout 16 years of monitoring (Stark 2002). Irassar et al. (1996) reported that incorporating 20% Class F fly ash led to the least surface scaling compared with ordinary concrete mixtures after 5 years of field exposure. While Zhutovsky and Hooton (2017a) reported that mixtures comprising 45% and 65% slag had a final mass loss lower than that of the reference mixture, Irassar et al. (1996) found that mixtures made with 80% slag were more vulnerable to PSA in the field. Excessive pore structure refinement of concrete using very low *w/b* along with some types and combinations of SCMs was reported to make the concrete vulnerable to high crystallization pressure and scaling (Bassuoni and Nehdi 2009).

Prior to and during PSA, continuous supply of salt solutions into concrete occurs through the surface layer within the evaporative zone; also, salt solutions may migrate upwards onto the concrete surface and then diffuse into concrete. Accordingly, treatment of this layer with surface coatings may improve the performance of concrete elements vulnerable to PSA as they could discount the ingress of salt solutions and their rate of evaporation. Depending on the function, surface treatments can be categorized into four types (Pan et al. 2017): coatings forming a continuous film on surface, hydrophobic (water-repellent) agents, surface pore blockers, and multifunctional treatments. However, the

effectiveness of surface treatments/coatings on mitigating PSA on concrete has not been substantiated as there is dearth of information in the technical literature in this area. One study attempted to determine the suitability of four surface treatments to resist PSA of concrete (Suleiman et al. 2014). The coated cylinders were partially immersed in a 5% Na_2SO_4 solution and subjected to cyclic conditions (one week at 20ºC/82% relative humidity [RH] followed by one week at 40ºC/31% RH) for six months. Epoxy and silane were reported to be successful at resisting PSA due to their barrier and hydrophobic effects, respectively, while the bituminous and acrylic-based coatings were not adequate at resisting PSA. Nevertheless, the test conditions applied in that study (Suleiman et al. 2014) were not sufficiently severe to conclusively judge the performance of these coatings as the maximum reported mass loss for uncured and reference specimens was less than 3% at the end of exposure.

5.2 Research Significance

ACI 201.2R (2016) states that no specific measures can be given at this stage to prevent PSA on concrete; however, it suggests that the use of protective coatings may be beneficial. Yet, limited research exists on this aspect without general understanding of the characteristics necessary of coatings to successfully protect concrete against PSA. In this study, various types of surface coatings were tested to determine their effectiveness at protecting concrete under severe PSA conditions. Moreover, the coatings were applied on concrete with different qualities (variable *w/b* and inclusion of SCMs) to determine the effect of concrete quality on surface coatings' performance.

5.3 Experimental Program

5.3.1 Materials and Mixtures

5.3.1.1 Concrete mixtures

The materials used in this Chapter were similar to those used in Chapter 3 (refer to Section 3.3.2). Four base mixtures were developed to cover a wide range of pore structure characteristics/qualities with a total binder content of 400 kg/m^3. Three mixtures were prepared using general use (GU) cement with varying *w/b* (0.40, 0.50, and 0.60) representing fine, moderate, and coarse porosities (designated as GU0.4, GU0.5, and GU0.6, respectively). Moreover, silica fume (SF) (8% by mass of the total binder) was incorporated with GU in one mixture at *w/b* of 0.35 to represent the very fine pore structure (designated as GUSF0.35). All specimens were cured for 28 days. Table 5.1 presents the mixture proportions and compressive strength of the tested mixtures.

Table 5.1: Proportions of mixtures per cubic meter of concrete

Mixture ID.	Cement, kg	Silica fume, kg	Water, kg	Coarse aggregate, kg	Fine aggregate, kg	HRWRA, l/m^3	28 day Compressive strength, MPa*
GUSF0.35	368	32	140	1200	663	1.5	62 (1.30)
GU0.4	400	--	160	1200	621	0.5	53 (1.44)
GU0.5	400	--	200	1200	514	--	45 (0.43)
GU0.6	400	--	240	1200	409	--	36 (1.18)

* Values between brackets are the standard deviations for compressive strength results.

5.3.1.2 Coatings

Seven types of commercially available coatings [epoxy (EP), acrylic emulsion (AE), methyl methacrylate (MMA), high molecular weight methacrylate (HMMA), silane (S), sodium silicate (SS), and ethyl silicate (ES)] were applied in this study. Table 5.2 presents the properties of these coatings as specified by the manufacturers. At 28 days, triplicate (75×150 mm) cylinders of each mixture were treated with each coating, according to the manufacturers' recommendations. Specimens were air-dried at 20°C and 50% RH for 48 h

before coating, except for acrylic emulsion coated specimens where concrete was required to be in saturated surface dry condition. The bottom 20 mm of all specimens were left uncoated to allow for salt ingress simulating partially embedded elements.

Table 5.2: Properties of coatings

Coating	Density, kg/l	Viscosity, (cps)	Tensile strength, MPa	Tensile elongation, %	Pot life, min	Tack free time, min
Epoxy	1.37	2800	44	2.7	40	180-240
Acrylic emulsion	1.6	--	4.1	70	60	--
MMA	0.95	5-10	56	5	15-20	30-40
HMMA	1.03	15-25	11	1-5	35-40	240-420
Silane	0.88	5-10	N/A	N/A	N/A	N/A
Sodium silicate	1.39	--	N/A	N/A	N/A	N/A
Ethyl silicate	0.93	--	N/A	N/A	N/A	N/A

(--) values were not reported by the manufacturer.

Epoxy components (resin and hardener) were pre-stirred separately, then mixed together (1:1 mixing ratio by volume) with a low-speed drill until reaching uniform consistency. For the acrylic emulsion coating, the powder was mixed with liquid at a ratio of 5:3 by volume for 3-4 min. until achieving a lump-free creamy consistency. Two layers of epoxy and acrylic emulsion were applied by brushing separated by 24 h. MMA resin was mixed with powder initiator immediately before application until the powder was dissolved. Similarly, HMMA resin was first mixed with a promotor; then, an initiator was added and stirred for 2 min. MMA and HMMA were sprayed by a low-pressure sprayer at a rate of 0.0015 ml/mm^2 divided on two layers allowing the first layer to cure for 1 h and 16 h for MMA and HMMA, respectively.

Silane was sprayed in three successive layers (time interval of 30 min) until the surface was dampened by silane as specified by the manufacturer. Application of sodium silicate was performed directly such that two coatings were applied by brushing with 24 h time interval. Ethyl silicate was sprayed using a low-pressure sprayer in two cycles with each cycle consisting of three successive applications at 15 min time intervals and the

duration between the two cycles was 60 min. Treated specimens were air-cured in laboratory for 72 h to provide enough time for proper interaction/bonding with substrate before PSA exposure.

5.3.2 Physical Salt Attack Exposure

Uncoated (reference) and coated specimens were exposed to the accelerated PSA conditions described in Section 3.3.3.

5.3.3 Testing

Similar to Chapters 3 and 4, the features of pore structure for uncoated specimens were determined after 28 days by mercury intrusion porosimetry (MIP). An absorption and desorption experiment was performed to give an indication on the effect of coatings on the rates of solution supply and evaporation. Following drying of specimens, coatings were applied to the top surface of specimens (100×50 mm) with *w/b* of 0.60 (worst case scenario); after curing of coatings, remaining sides (except the bottom) were sealed by a rapid-setting epoxy. Subsequently, in the absorption test, specimens were dried at 50±2^{o}C and 40% RH until constant mass, while for desorption, specimens were fully immersed in 10% Na_2SO_4 as applied in the PSA exposure. Thus, the bottom face allowed for the drying and saturation of specimens, respectively, in the case of absorption and desorption procedures. Afterward, the bottom surface of specimens was sealed and the initial mass (m_i) was recorded. For absorption, dry specimens were immersed in 10% Na_2SO_4 for 48 h, where the solution was absorbed through the top coated face only. For desorption, saturated specimens were placed at the same PSA test drying conditions (40±2°C and 35±5% RH) for 48 h, where evaporation happened through the top coated face only. The absorption/desorption percentage at a certain time (t) was calculated as: $100\times (m_t - m_i)/m_i$, where m_t is the mass at time t.

Every 15 cycles, salt deposits on surface and debris were removed using a nylon brush. Also, every 30 cycles, debris were removed and the specimens were left to dry under laboratory conditions for 6 h, then the mass change of specimens was determined relative to the initial masses before exposure. At the end of exposure, specimens were visually assessed based on 0 (no scaling) to 5 (severe scaling) pictorial rating scale (Bassuoni and Rahman 2016). In addition, the underlying degradation mechanisms were studied by mineralogical and microstructural analyses (refer to Section 3.3.3).

5.4 Experimental Results

5.4.1 Penetrability

Table 5.3 shows the MIP results for uncoated concrete before exposure. The cumulative intrusion volume of mercury was linked to the *w/b* in the sense that lower intrusion corresponded to lower *w/b*, complying with the well-documented trend of *w/b* influence on concrete penetrability (Mehta and Monteiro 2014). For instance, reducing *w/b* from 0.60 to 0.40 led to significant decrease in total porosity from 19.5% to 13.2%, i.e. 32% reduction. Specimens showed distinctive trends in terms proportion of micro-pores (< 1 μm) due pore size refinement with *w/b* reduction and/or incorporation of silica fume. Correspondingly, the threshold pore diameters of GU0.6, GU0.5, GU0.4, and GUSF0.35 specimens were 1, 0.68, 0.35, and 0.05 μm, respectively.

Table 5.3: MIP results for uncoated specimens before exposure

Mixture ID.	Total porosity (%)	Proportion of micro-pores (%)	Threshold pore diameter (μm)
GUSF0.35	8.5	79.5	0.05
GU0.4	13.2	64.4	0.35
GU0.5	17.0	49.8	0.68
GU0.6	19.5	35.9	1.00

5.4.2 Absorption/desorption Tests

The mass gain (absorption) and loss (desorption) percentages for the GU0.6 specimens after 48 h are summarized in Table 5.4. Uncoated concrete gave the highest mass change for absorption (+7.32%) and desorption (-2.86%) followed by specimens coated with sodium silicate. Epoxy and ethyl silicate specimens showed slight mass gain (0.35% and 0.52%, respectively) and loss (-0.14% and -0.26%, respectively). Specimens with acrylic emulsion showed a relatively high absorption compared to other coatings, while the desorption value was much lower (30% of the absorption). Comparable trends were observed for MMA and HMMA specimens; the average absorption and desorption were +4% and -1.1%, respectively. Specimens coated with silane yielded a relatively low absorption (1.35%) compared to uncoated concrete, but the desorption was approximately 32% higher.

Table 5.4: Absorption and desorption values for GU0.6 specimens at 48 h

Specimen	Absorption, %	Desorption, %
Uncoated	7.32	2.86
Epoxy	0.35	0.14
Acrylic emulsion	5.56	1.65
MMA	3.67	1.25
HMMA	4.43	1.05
Silane	1.35	1.78
Sodium silicate	6.25	2.62
Ethyl silicate	0.52	0.26

5.4.3 Visual Assessment

Figures 5.1-5.4 show the state of uncoated and coated cylinders at different *w/b* after exposure along with a visual rating. During the drying stage, salt deposited on the evaporative surface of untreated concrete due to solution uptake and fast evaporation caused by the testing conditions. Time taken for salt efflorescence to appear depended on concrete quality (e.g. 3 and 8 days for GU0.6 and GU0.4, respectively). With time, efflorescence accumulated on the drying surfaces of specimens, and surface scaled just

above the solution level propagating upwards while the immersed part remained mostly intact. Progressive damage caused concrete spalling and reduction of cross section. For uncoated specimens, the height of scaling above the solution level depended on the *w/b*; for example, the scaling reached full height above solution level in GU0.6 cylinders after 45 cycles and they broke after 105 cycles (Fig. 5.1), but for GUSF0.35 specimens, the scaling height reached around 50 mm (half the height above solution level) with marginal reduction of cross-section (Fig. 5.4).

All epoxy coated specimens did not show any visual features of damage, and the coating remained intact, irrespective of the *w/b*. Ethyl silicate minimized the surface damage of concrete; only minor scaling occurred within 20 mm above the solution level for GU0.5 and GU0.6 specimens. The acrylic emulsion coating served as a sacrificial layer, which was vulnerable to minor scaling [maximum visual rating of 1] up to the top of specimens. MMA and HMMA coatings were effective at protecting higher quality concrete (GUSF0.35 and GU0.4), while for GU0.5 and GU0.6 specimens, they detached from surface after 60 cycles of exposure and scaling progressed to underlying concrete (Fig. 5.5)**.** Both silane and sodium silicate coatings protected the GUSF0.35 specimens from PSA, but the silane was more efficient for the GU0.4 and GU0.5 specimens. However, their GU0.6 counterparts were broken at 120 and 112 cycles, respectively. Similar to MMA and HMMA, silane specimens showed no scaling up to 50 cycles; subsequently, swelling and cracking appeared on the surface, which led to peeling of 2-3 mm surface layer (Fig. 5.5) followed by scaling of specimens at a rapid rate.

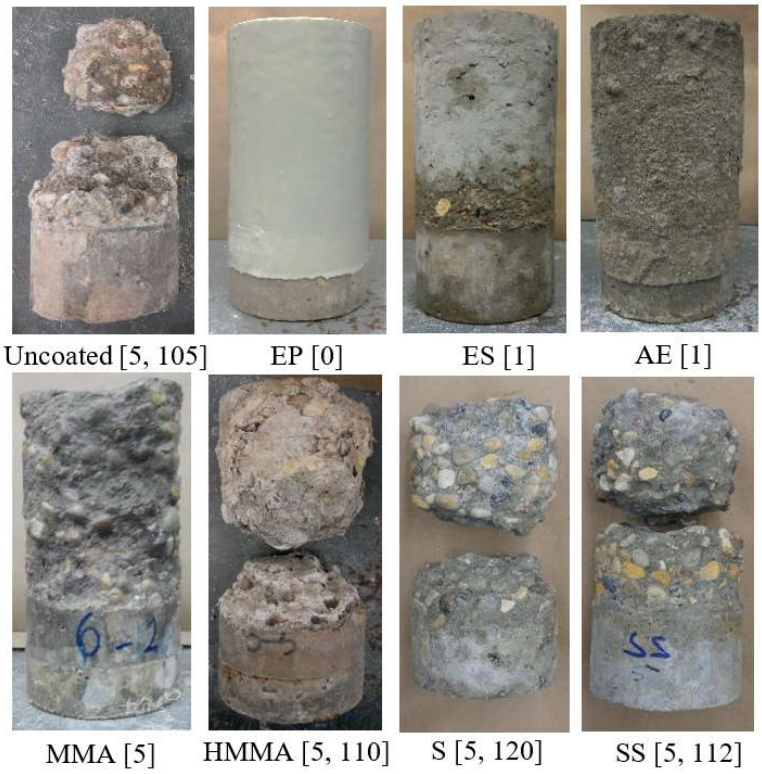

Figure 5.1: Uncoated and coated GU0.6 specimens at the end of PSA exposure. (Note: Numbers between brackets are the final visual ratings and the number of cycles at failure respectively if applicable)

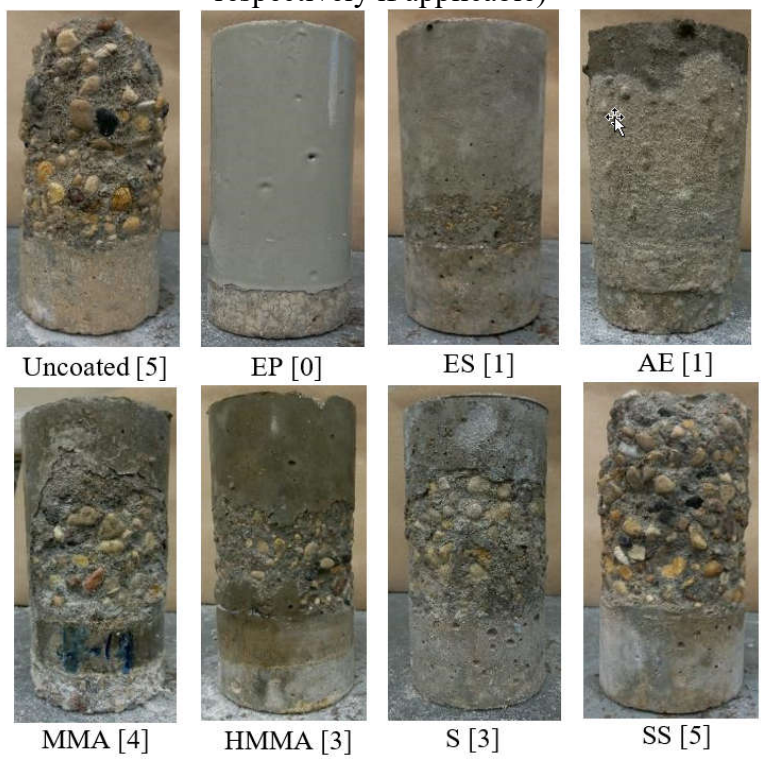

Figure 5.2: Uncoated and coated GU0.5 specimens at the end of PSA exposure. (Note: Numbers between brackets are the final visual ratings)

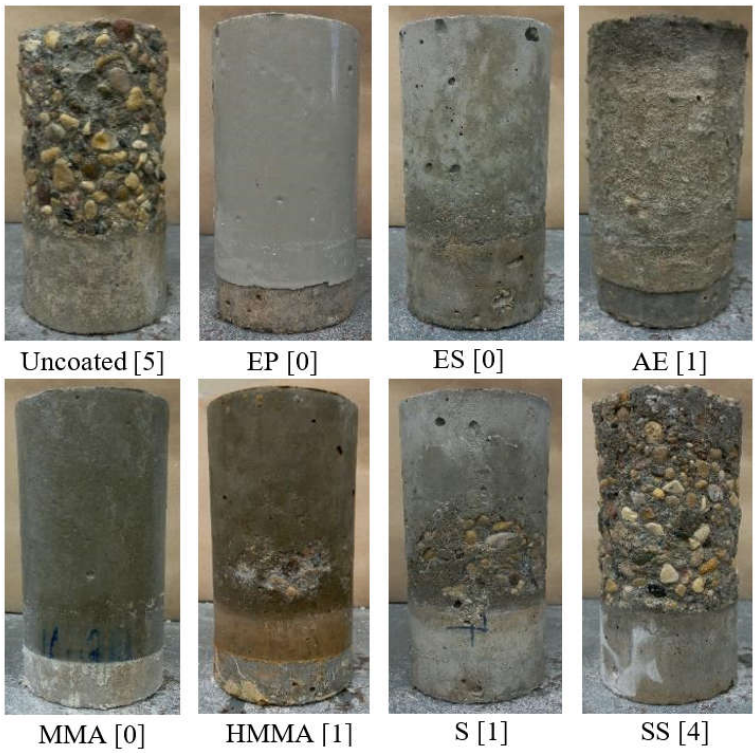

Figure 5.3: Uncoated and coated GU0.4 specimens at the end of PSA exposure. (Note: Numbers between brackets are the final visual ratings)

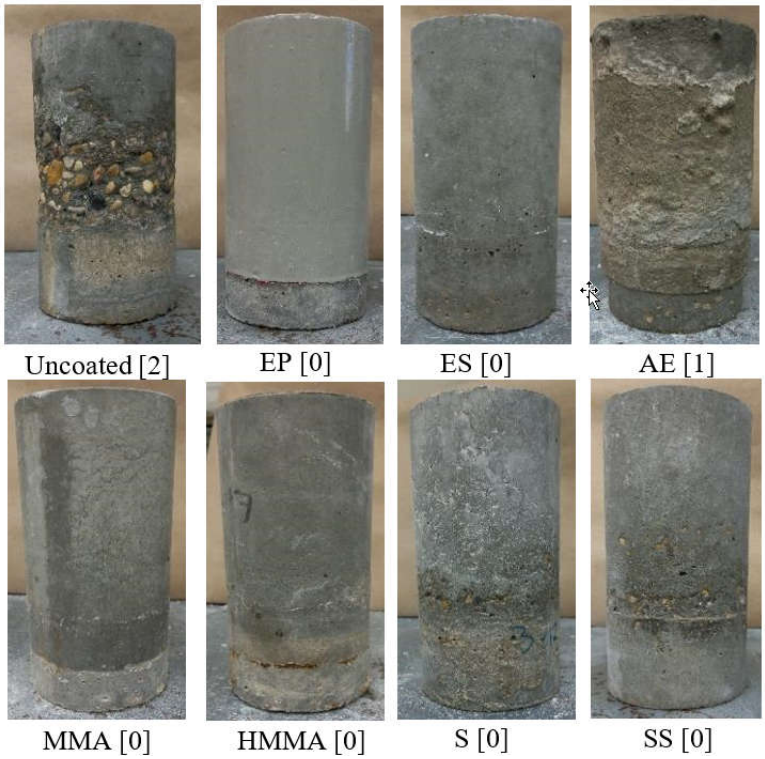

Figure 5.4: Uncoated and coated GUSF0.35 specimens at the end of PSA exposure. (Note: Numbers between brackets are the final visual ratings)

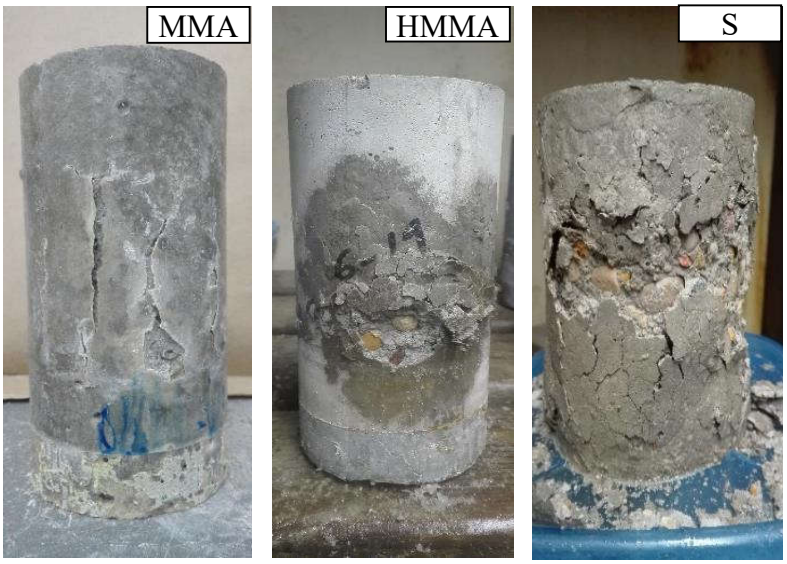

Figure 5.5: Examples for the crust detachment of MMA, HMMA and silane (S) coated specimens at *w/b* of 0.6 at 60, 60, and 55 cycles, respectively.

5.4.4 Mass Change

Mass change was determined every 30 cycles during exposure as shown in Table 5.5. During the first 30 cycles, most of the specimens gained little mass due to solution ingress from the bottom portion. However, uncoated GU0.6 specimens lost mass due to the faster rate of scaling relative to mass gained by solution absorption. Afterward, the trend of mass change varied significantly depending on *w/b* and coating type conforming to visual inspection results. Uncoated GU0.6, GU0.5, and GU0.4 specimens scaled rapidly after 60 cycles such that the final mass loss was directly proportional to *w/b* (27%, 15%, and 9%, respectively). Combining a low *w/b* with silica fume (GUSF0.35) considerably enhanced the resistance of uncoated concrete to PSA as indicated by only 1% final mass loss. Analysis of variance (ANOVA) at a significance level (α) of 0.05 for mass loss results of different mixtures gave an *F*-value of 143 compared to a critical threshold (F_{cr}) of 4.06 indicating a statistically significant effect of *w/b* on the average results (Montgomery 2014).

Table 5.5: Variation of mass of uncoated and coated specimens with time

Mixture ID.	Days/Cycles							
	30		60		90		120	
GU0.6	-1.25	[0.27]	-3.87	[0.91]	-16.38	[1.45]	-26.87[1]	[2.05]
GU0.6-EP	+0.60	[0.08]	+0.56	[0.13]	+0.70	[0.12]	+0.87	[0.15]
GU0.6-ES	+0.13	[0.19]	-0.17	[0.03]	-0.29	[0.03]	-0.45	[0.05]
GU0.6-AE	+0.22	[0.16]	-0.02	[0.10]	-0.86	[0.23]	-1.75	[0.58]
GU0.6-MMA	+0.34	[0.22]	-0.56	[0.30]	-5.20	[1.00]	-10.88	[1.57]
GU0.6-HMMA	+0.49	[0.21]	-0.34	[0.20]	-3.96	[0.57]	-11.27[2]	[2.07]
GU0.6-S	+0.47	[0.00]	-1.21	[0.08]	-5.70	[1.39]	-15.34[3]	[2.00]
GU0.6-SS	+0.12	[0.03]	-1.20	[0.37]	-8.86	[1.06]	-20.38[4]	[1.37]
GU0.5	+0.21	[0.08]	-1.27	[0.60]	-4.59	[0.85]	-14.75	[1.70]
GU0.5-EP	+0.38	[0.08]	+0.38	[0.05]	+0.52	[0.08]	+0.66	[0.22]
GU0.5-ES	+0.25	[0.05]	+0.21	[0.08]	-0.14	[0.08]	-0.20	[0.15]
GU0.5-AE	+0.34	[0.12]	-0.09	[0.10]	-0.44	[0.15]	-0.68	[0.10]
GU0.5-MMA	+0.51	[0.09]	-0.64	[0.24]	-1.19	[0.18]	-3.30	[0.76]
GU0.5-HMMA	+0.35	[0.15]	-0.02	[0.15]	-0.98	[0.37]	-1.58	[0.57]
GU0.5-S	+0.28	[0.16]	-0.24	[0.10]	-0.83	[0.41]	-1.77	[0.65]
GU0.5-SS	+0.20	[0.03]	-0.65	[0.38]	-1.98	[1.21]	-12.6	[2.10]
GU0.4	+0.30	[0.30]	-0.84	[0.15]	-4.28	[0.70]	-8.64	[1.63]
GU0.4-EP	+0.10	[0.10]	+0.27	[0.06]	+0.39	[0.07]	+0.45	[0.12]
GU0.4-ES	+0.12	[0.08]	+0.34	[0.18]	-0.02	[0.06]	-0.06	[0.08]
GU0.4-AE	+0.20	[0.09]	-0.04	[0.03]	-0.40	[0.08]	-0.61	[0.15]
GU0.4-MMA	+0.20	[0.03]	+0.32	[0.03]	+0.40	[0.07]	+0.50	[0.03]
GU0.4-HMMA	+0.18	[0.00]	+0.34	[0.12]	-0.08	[0.03]	-0.36	[0.05]
GU0.4-S	+0.20	[0.10]	+0.30	[0.43]	-0.22	[0.07]	-0.50	[0.15]
GU0.4-SS	+0.24	[0.13]	-0.49	[0.20]	-2.32	[0.38]	-5.85	[1.02]
GUSF0.35	+0.16	[0.18]	-0.04	[0.08]	-0.40	[0.13]	-0.97	[0.23]
GUSF0.35-EP	+0.12	[0.08]	+0.17	[0.10]	+0.12	[0.12]	+0.19	[0.05]
GUSF0.35-ES	+0.08	[0.07]	+0.27	[0.03]	+0.25	[0.10]	+0.23	[0.29]
GUSF0.35-AE	-0.09	[0.05]	+0.19	[0.19]	-0.35	[0.07]	-0.57	[0.11]
GUSF0.35-	+0.10	[0.07]	+0.21	[0.05]	+0.19	[0.05]	+0.18	[0.05]
GUSF0.35-	-0.04	[0.07]	+0.23	[0.13]	+0.23	[0.13]	+0.16	[0.17]
GUSF0.35-S	+0.16	[0.36]	+0.16	[0.43]	+0.20	[0.15]	+0.02	[0.20]
GUSF0.35-SS	+0.14	[0.05]	+0.23	[0.17]	-0.02	[0.06]	-0.08	[0.05]

*Note: values are in percentage (%); (-) refers to mass loss and (+) refers to mass gain.
**Values between brackets refer to standard deviation.
[1,2,3,4] refers to mass loss at 105, 110, 120, and 112 cycles, respectively when specimens were fractured.

All coated cylinders had lower final mass losses compared with uncoated concrete; some coatings were effective, while others failed to protect concrete from loss of mass due to PSA. ANOVA at α of 0.05 for mass loss results of coated concrete showed that the extent of *w/b* influence on damage level varied according to treatment type. Epoxy, acrylic emulsion and ethyl silicate had *F*-values of 7.6, 6.8 and 22.5, respectively relative to an F_{cr} of 4.06, while higher *F*-values of 71.65, 50, 96 and 64 were obtained for MMA, HMMA,

silane and sodium silicate, respectively indicating stronger dependence on *w/b*. Irrespective of the *w/b*, the entire set of epoxy coated cylinders did not show any mass loss; instead, there was a slight increase in mass. Moreover, ethyl silicate was a good candidate to minimize surface scaling such that the final mass change of cylinders ranged from -0.45%to +0.23% for the GU0.6-ES and GUSF0.35-ES specimens, respectively. All acrylic emulsion specimens showed an average mass loss of 0.6% after the exposure, except for the GU0.6-AE (2% mass loss). The reduction in mass was due to scaling of the acrylic emulsion layer, whereas the underlying concrete remained intact. GUSF0.35 specimens coated with MMA, HMMA, silane, and sodium silicate did not show any mass loss. GU0.4 and GU0.5 specimens coated with MMA, HMMA, and silane showed marginal mass loss (max. of 3%); comparatively, sodium silicate specimens had the worst performance, after uncoated specimens, with mass losses of 6% and 13%, respectively. These trends were replicated for the GU0.6 coated specimens, but the mass loss values were significantly higher than that of GU0.4 and GU0.5 specimens.

5.5 Discussion

5.5.1 Effect of Water-to-binder Ratio

Concrete exposed to PSA may exhibit limited formation of sulfate reaction products depending on the quality of concrete. For example, Figure 5.6 shows the XRD analysis on samples extracted from unexposed and exposed GU0.6 and GU0.35 specimens representing low- and high-quality concretes, respectively. For both unexposed concretes, some traces of hydration (primary) ettringite were found along with portlandite peaks. Immersed parts of these specimens showed small peaks of ettringite and gypsum, without damage manifestations of swelling and cracking, indicating limited chemical sulfate attack within this short period of exposure. In case of GU0.6, the drying portion of exposed GU0.6

specimens showed a prevailing occurrence of thenardite (Na_2SO_4) with some traces of sulfate reaction products (ettringite and gypsum). The traces of gypsum indicate an incipient stage of chemical sulfate attack due to the ingress (absorption) of larger quantity of sulfate ions. Comparatively, the drying portion of GUSF0.35 specimens did not show gypsum peaks; only ettringite was found in the surface with similar intensities to unexposed samples, implying primary ettringite from hydration reactions. This indicates that no chemical attack occurred in the GUSF0.35 specimens up to 120 days due to the incorporation of silica fume along with the low *w/b*, which significantly reduced the ingress of sulfate ions. These trends indicated that PSA was the primary cause of surface scaling and substantiated the positive effect of *w/b* reduction on improving the resistance of concrete to physical and chemical attacks.

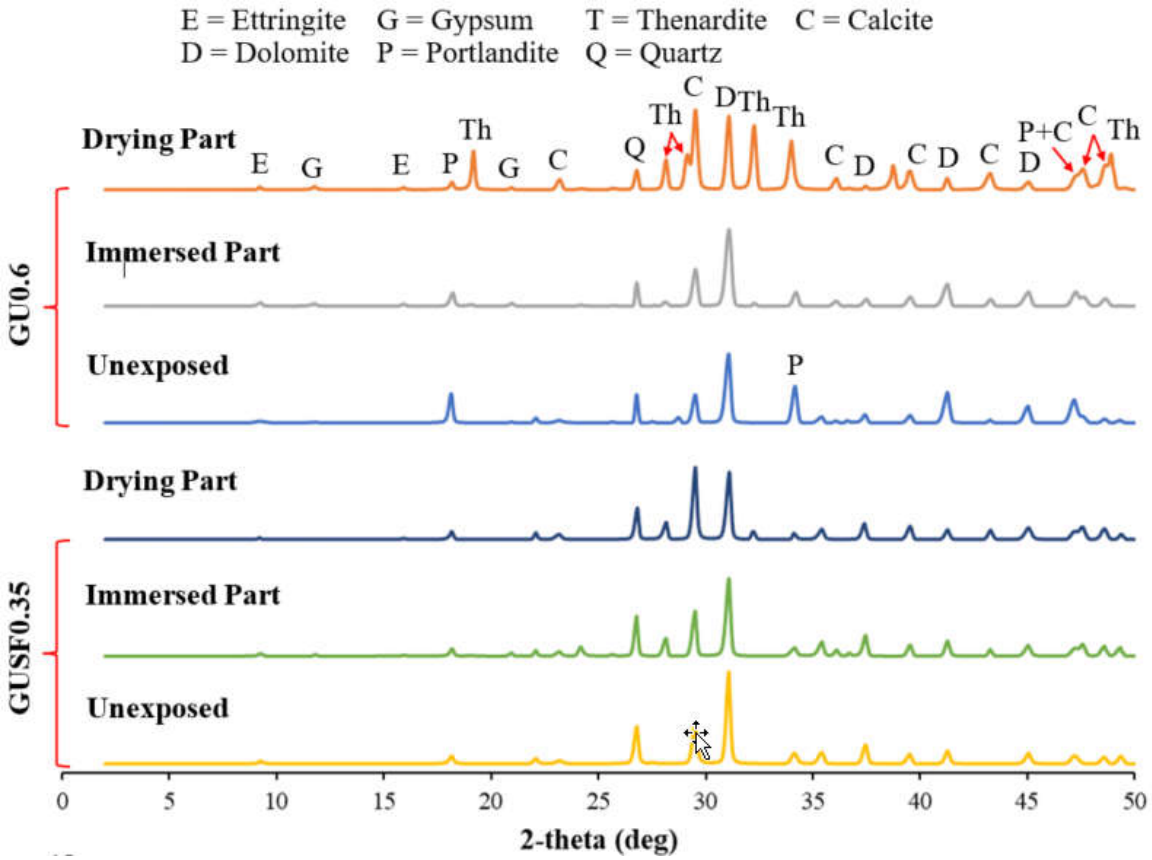

Figure 5.6: XRD analysis of unexposed and exposed GUSF0.35 and GU0.6 specimens.

The effect of varying the *w/b* on the visual and mass loss results differed depending on whether the specimens were coated. Uncoated GU0.6 specimens fractured before the end of exposure (after 105 cycles) with average mass loss of 27%, while GU0.5 and GU0.4 specimens did not break throughout the test with mass loss of 15% and 9%, respectively indicating a considerable improvement in performance. GUSF0.35 specimens showed only about 1% mass loss. According to the MIP trends, high *w/b* led to more porous and continuous pore structure of concrete, resulting in higher rate of solution uptake, increased volume of crystallizing salt, and consequently more surface scaling of concrete. Generally, the effect of *w/b* followed the results reported in previous studies (e.g. Bassuoni and Rahman 2016) and current recommendations of ACI 201.2R (2016) to reduce *w/b* for producing concretes with improved performance in environments conducive to PSA. The effect of *w/b* in case of different coatings is discussed in the subsequent section.

5.5.2 Effect of Surface Coatings

Visual ratings and mass loss results were found to be significantly influenced by the coating type at each *w/b*. Some coatings (e.g. epoxy, acrylic emulsion, MMA, and HMMA) form a membrane layer on surface that presumably minimizes detrimental effects from the surrounding environment (Pan et al. 2017). In this study, epoxy was superior at protecting concrete against PSA regardless of the *w/b*. The SEM analysis on samples extracted from the drying surface of specimens (e.g. Fig. 5.7) showed sound bond between the epoxy saturated layer and concrete surface towards the inner core with no sodium sulfate deposits. This was also confirmed by the XRD analysis at the highest *w/b* of 0.60 where traces of thenardite were formed within the surface (0-15 mm) of specimens (Fig. 5.8). Table 5.4 indicated minimal capillary rise and absorption of salt solution within the concrete surface coated with epoxy. Also, epoxy acted as an unbreathable layer (very low desorption) that

prevented the evaporation of solution diffusing upwards through the concrete core (by wicking), and thus minimizing the risk of forming a sub-florescence zone. In addition, the epoxy used had a high tensile strength of 44 MPa which may resist the crystallization pressure of sodium sulfate, if developed.

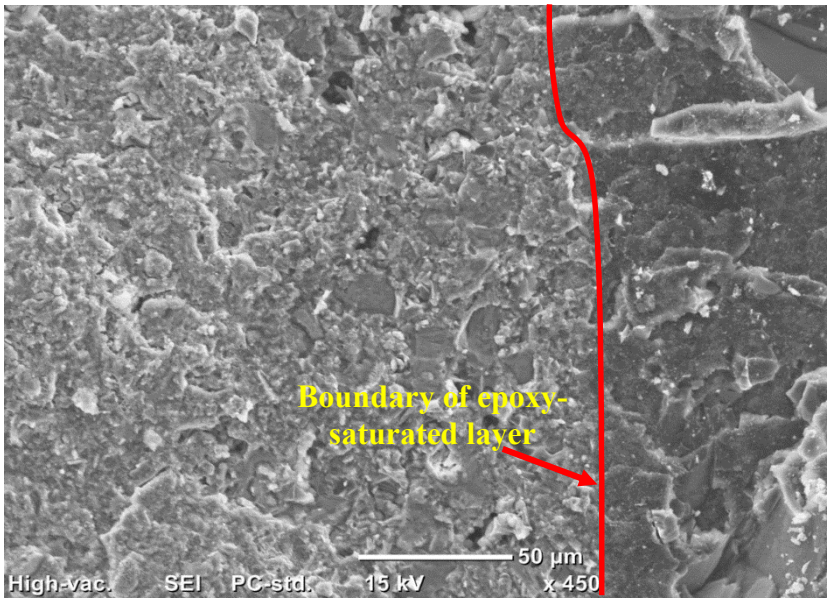

Figure 5.7: SEM of samples extracted from the drying portion (top) of epoxy-coated GU0.6 specimens.

The acrylic emulsion coating is a flexible, abrasion resistant, and waterproof mortar. Although it acted as a sacrificial layer that reduced in thickness with progression of PSA, it was effective at protecting the underlying concrete during the test period. It is a porous material that allowed absorption, evaporation (Table 5.4) and crystallization of sodium sulfate (Fig. 5.9), which led to the scaling of this coating. XRD analysis on concrete layer directly beneath the acrylic mortar coating at the highest *w/b* (Fig. 5.8) showed the existence of thenardite; however, its intensity was remarkably less than that in corresponding uncoated concrete. Moreover, some traces of gypsum and ettringite were detected. Although salt crystals were formed indicating the possibility of crystallization

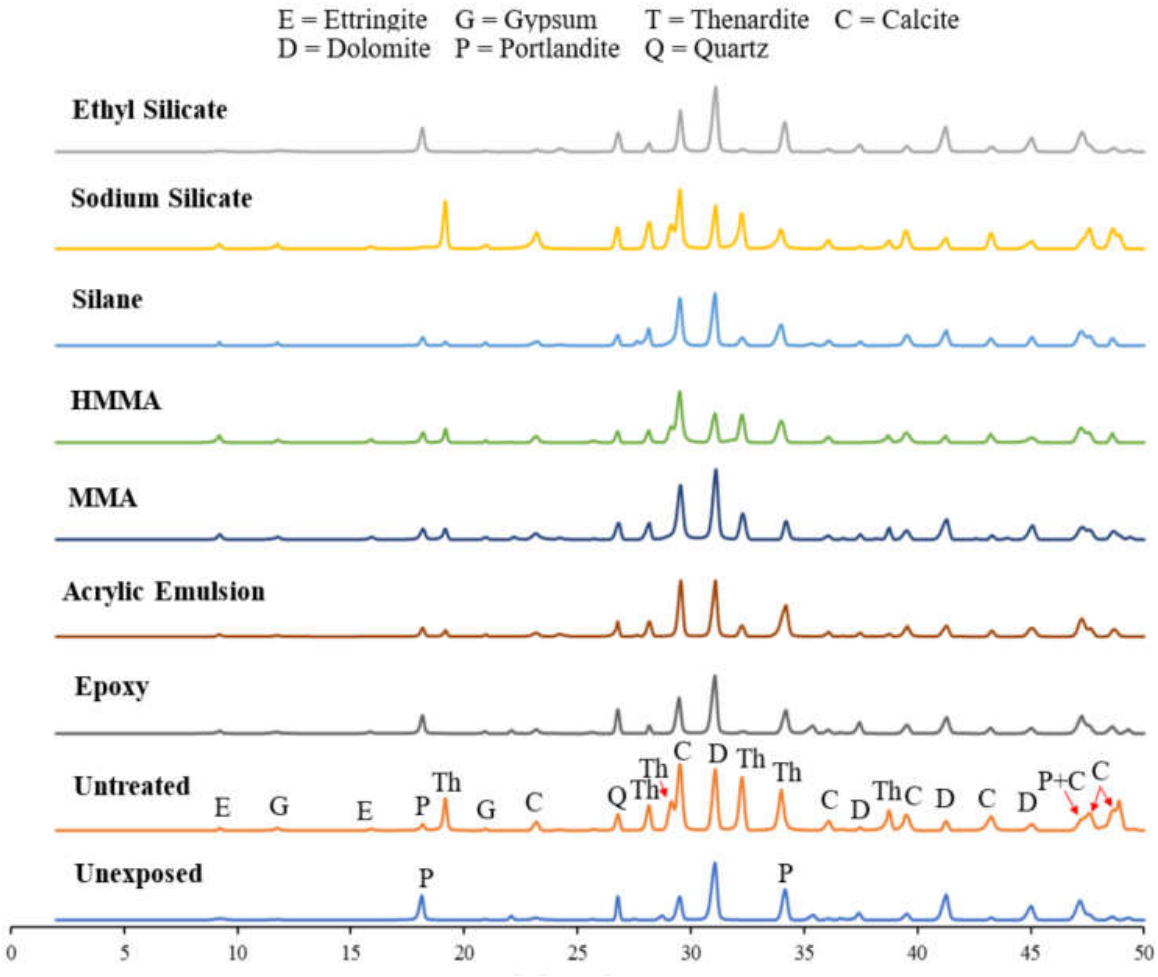

Figure 5.8: XRD of samples extracted from the drying portion (15 mm of surface) of unexposed, uncoated, and coated GU0.6 specimens.

pressure development, neither full detachment nor failure of the coating was observed which might be attributed to the high elongation capacity (up to 70%, Table 5.2) of this mortar allowing the material to accommodate volumetric expansion. However, the SEM analysis of this mortar showed a potential of swelling and debonding micro-cracks from precipitation of reaction products and salt crystals (Fig. 5.9). This may allude to the likelihood of failure in field applications involving high concentrations of sodium sulfate and/or long periods of exposure.

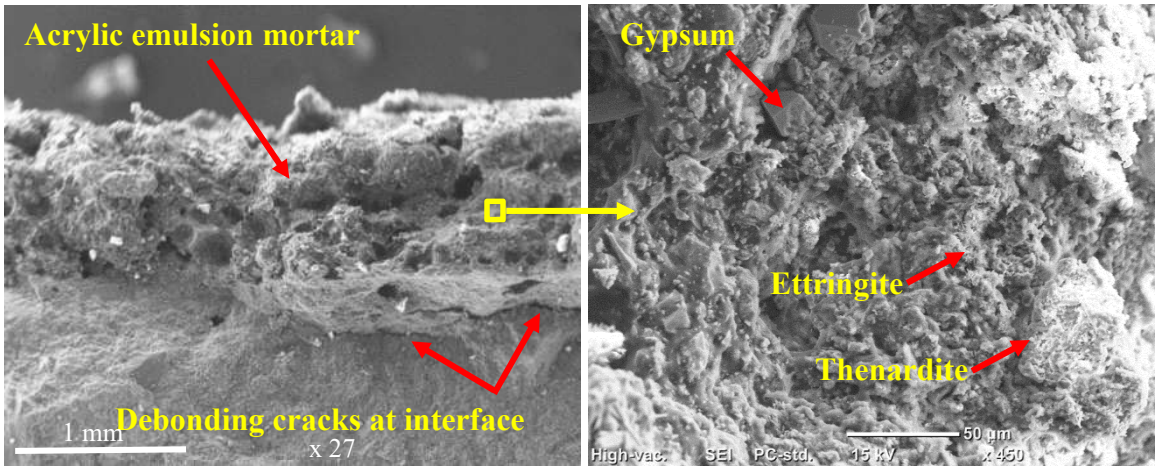

Figure 5.9: Degradation of acrylic emulsion mortar in the top part of GU0.6 specimen after the PSA exposure.

MMA and HMMA are based on low viscosity methacrylate acid; they provide protection to concrete by partially filling the surface pores and forming a thin membrane on the surface that acts as an isolating layer (McGill et al. 1990). In this study, MMA and HMMA coatings comparably failed to mitigate PSA when applied to GU0.6 and GU0.5 specimens while they were successful for GU0.4 and GUSF0.35 specimens indicating that the quality of concrete surface plays a dominant role in the performance of some coatings. Saraswathy and Rengaswamy (1998) reported that adhesion of MMA based coatings to concrete decreases at higher *w/b* due to higher moisture content in surface pores leading to reduction in the bond strength and subsequent detachment. Figure 5.5 shows the detachment of a surface crust of MMA and HMMA coated GU0.6 specimens at 60 cycles. Beneath the detached layer, white salt deposits were found along with scaled debris suggesting that the damage involved solution uptake through the immersed part (wicking) followed by salt crystallization and pressure build-up against the outer surface leading to its swelling and detachment.

Table 5.4 showed that MMA and HMMA reduced absorption/desorption of concrete; however, fluid transmission was not fully prevented resulting in evaporation of salt solution and crystallization. This explains the existence of salt deposits just below the detached surface. Once the outer crust failed, the damage proceeded at a fast rate in a similar manner to uncoated specimens. XRD analysis (Fig. 5.8) of samples extracted from top portions of damaged MMA and HMMA coated specimens (within 15 mm underneath the surface) showed the coexistence of thenardite and traces of gypsum and ettringite. Microstructural analysis (e.g. Fig. 5.10) on the inner side of detached crust comprising MMA or HMMA and concrete supported these findings by showing massive sodium sulfate crystals forming into planes were primarily depositing underneath the crust causing its detachment. Moreover, SEM analysis of samples extracted from the remaining surface (0-15 mm) of top parts showed dominant occurrence of sodium sulfate crystals at the outer zone (2-5 mm), signifying the role of PSA in the damage process by forming a sub-florescence zone. Proceeding inwards, incidental occurrence of ettringite and gypsum were observed (Fig. 5.10) indicating an incipient stage of chemical attack in concrete specimens with the highest *w/b*. Similar trends were observed for HMMA coated specimens.

Silane is normally applied as a water-repellent primer and hydrophobic impregnating agent for concrete members. It is capable of penetrating into concrete surface due to its small particle size (from 10 nm to few micrometers); subsequently, silane reacts with water and alkaline species present in concrete pore solution, generating an active hydrophobic ingredient that lowers the water absorbency of the treated concrete (Moon and Lee 2017). However, similar to MMA and HMMA, silane was ineffective as a surface coating in resisting the PSA exposure for the GU0.6 and GU0.5 specimens, which

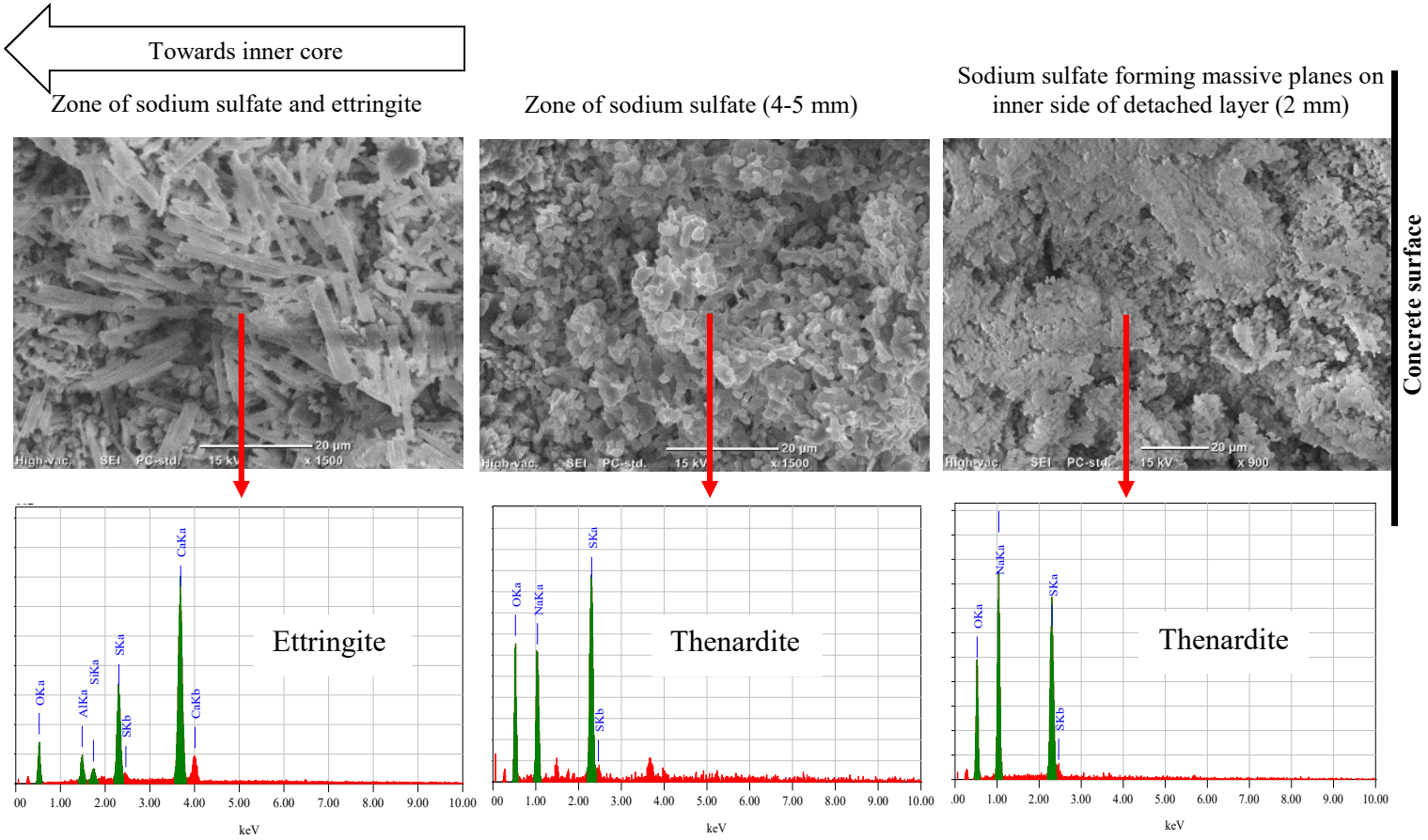

Figure 5.10: SEM and EDX analyses from top parts of MMA-coated GU0.6 specimen showing the zonation of formed compounds starting from the surface to inner core.

contradicts the findings reported by Suleiman et al. (2014), likely due to the milder exposure conditions adopted. For the silane-treated GU0.6 specimens, the damage pattern was similar to that of MMA and HMMA coated specimens where cracking formed on the surface resulting in detachment of a surface layer followed by rapid scaling **(**Fig. 5.5**)**. XRD analysis (Fig. 5.8) of powder samples extracted from damaged silane-treated concrete showed the coexistence of thenardite and traces of chemical sulfate attack products (gypsum and ettringite). Again, SEM images of the inner face of peeled layer showed massive and stacked planes of sodium sulfate crystals forming a sub-florescence zone (Fig. 5.11). This suggests that silane hydrophobicity prevented capillary rise onto outer surface leading to minor crystallization and efflorescence, while solution suctioned through the bottom core (wicking) led to formation of sub-florescence due to evaporation of sodium sulfate solution through the surface. According to Table 5.4, silane allowed slightly higher transmission from inside to outside of concrete (1.78%) than that of MMA (1.25%) and HMMA (1.05%), resulting in faster build-up of pressure that pushed against the surface layer causing its severe cracking and detachment at an early stage, after 50 cycles (Fig. 5.56). SEM analysis revealed a zonation of physical and chemical sulfate products beneath the detached crust (2-3 mm). After the salt crystals zone, a zone (3-4 mm) of combined ettringite and sodium sulfate crystals was found followed by a zone containing ettringite crystals (Fig. 5.11).

Sodium silicate was inadequate at protecting concrete against PSA, except for the GUSF0.35 specimens (due to the dominant effect of low *w/b*). Thus, it had the most inferior performance among the coatings tested in this study. XRD analysis on samples extracted from top parts of the sodium silicate-coated cylinders showed the abundant existence of

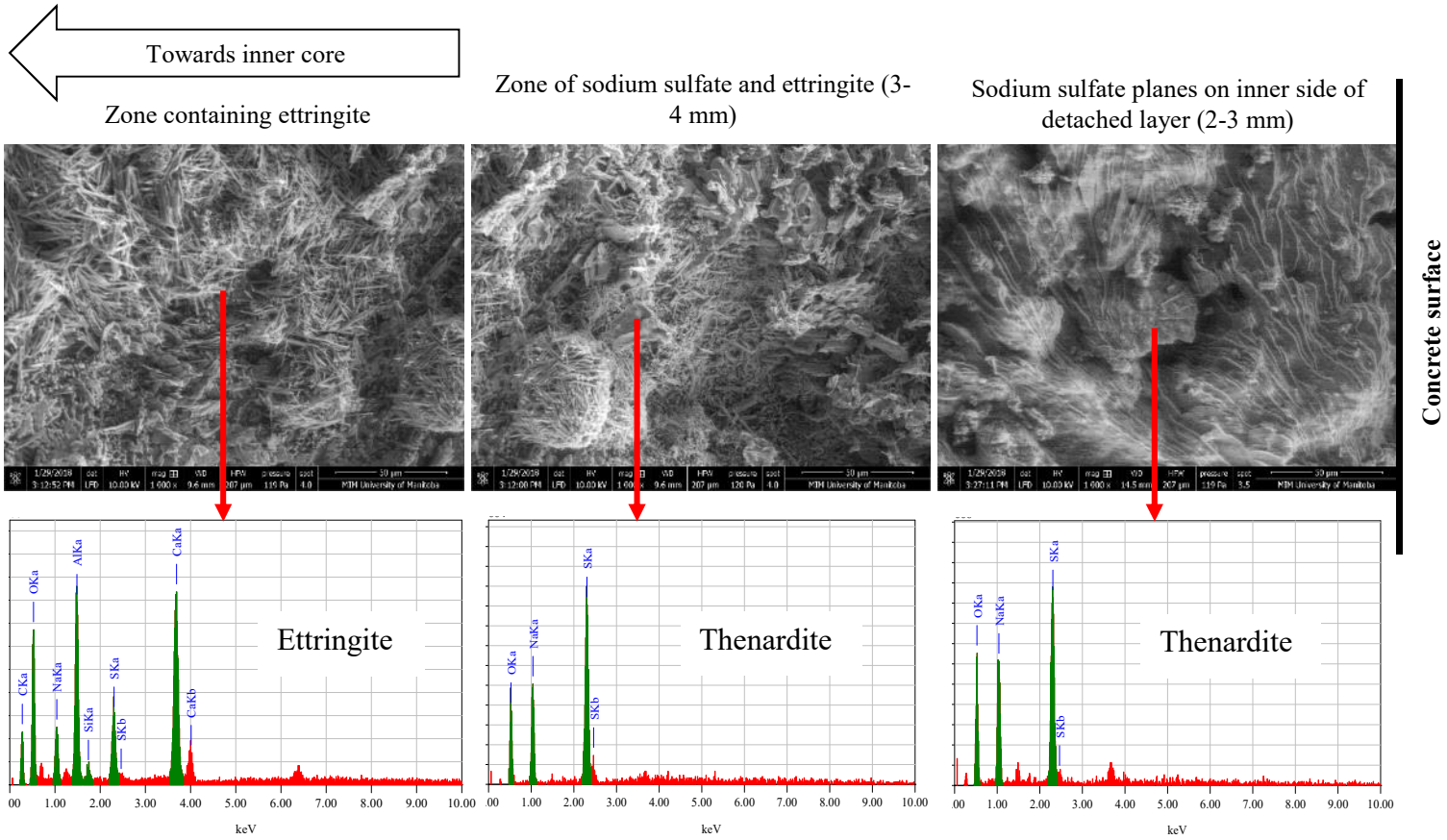

Figure 5.11: SEM and EDX analyses from top parts of silane-coated GU0.6 specimen showing the zonation of formed compounds starting from the surface to inner core.

thenardite with some traces of ettringite and gypsum (Fig. 5.8). Sodium silicate should act as a surface pore blocker such that it reacts with portlandite in concrete to form calcium silicate hydrate that precipitates and fill the pores (Baltazar et al. 2014). This process may lead to densification of the microstructure similar to the effect of *w/b* reduction. However, the latter was far more pronounced at improving the concrete resistance to PSA, as discussed earlier. Sodium silicate showed a slightly lower absorption and desorption values compared to untreated concrete (Table 5.4). Thus, the process of PSA progressed in a similar manner to untreated concrete, but at a relatively slower rate. The salt solution rose through the concrete core and onto surface (as shown by formation of efflorescence, Fig. 5.12a). Subsequent cycling and crystallization led to surface scaling due to formation of sub-florescence zone rich in sodium sulfate crystals (Fig. 5.12a), resulting in surface scaling and mass loss after approximately 45 cycles. Subsequently, PSA proceeded rapidly till fracture of GU0.6 specimens at 112 cycles. Applying additional layers of sodium silicate might have improved the performance of concrete in this exposure. However, this was not investigated in the present study, which closely followed the manufactures' recommendations for the rates and methods of application of all coatings tested.

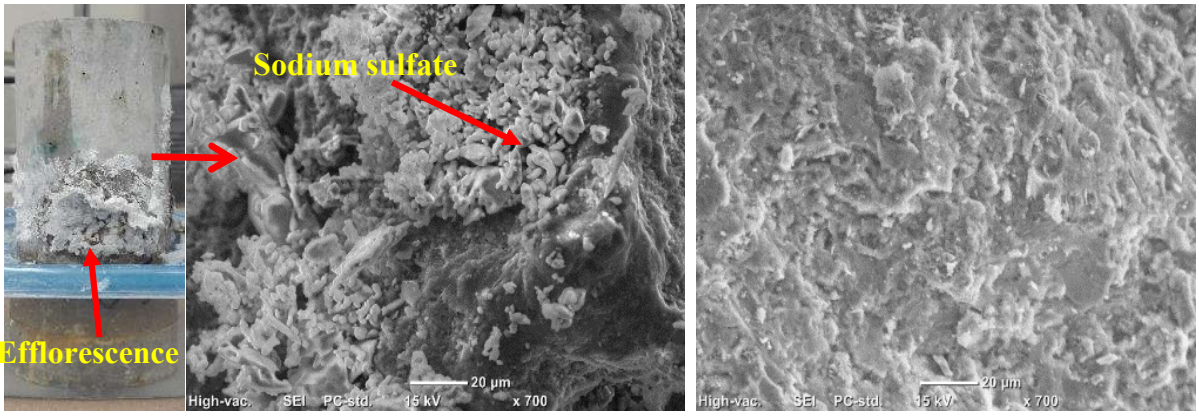

(a) (b)

Figure 5.12: (a) Eff- and sub-florescence in samples extracted from the top portion of sodium silicate coated GU0.6 specimens, and (b) Exemplar SEM micrograph of samples extracted from the drying portion of GU0.6 specimens coated with ethyl silicate.

Similar to epoxy, the application of ethyl silicate (or tetraethylorthosilicate, TEOS) to concrete led to improved performance under this PSA exposure, irrespective of the *w/b*. This coating has dual functions: pore-blocking and water-repelling. Silicates may react with calcium hydroxide in the cement paste, producing calcium silicate hydrate that acts as a micro-filler, generating a compact microstructure and dense surface layer of concrete. Moreover, similar to silane, TEOS is alkoxylsilane compound which hydrolyses into silanol groups after being applied to alkaline concrete, condensing into hydrophobic silica gel (Barberena-Fernández et al. 2015). Thus, ethyl silicate was notably effective at decreasing absorption and desorption of the solution (Table 5.4). These trends were verified by the SEM analysis of the surface layer which showed a dense matrix without any damage features (Fig. 5.12b). Correspondingly, the XRD analysis (Fig. 5.8) showed absence of thenardite and sulfate reaction products within this surface zone (0-15 mm). These trends substantiate that combining the hydrophobic function of silane and pore blocking ability of sodium silicate (i.e. in case of ethyl silicate) led to significantly improving the durability of concrete to PSA.

The above testing program indicates that protecting concrete against PSA might require classifying concrete porosity to select a suitable coating that can prevent fluid transport behind the concrete surface and thus interrupting PSA process. It is also apparent that the absorption and desorption behavior of the coating material and its bond to the concrete surface are critical criteria that might govern the effectiveness of the coating to protect concrete.

CHAPTER 6: EFFECT OF NANO-BASED COATINGS ON CONCRETE UNDER AGGRAVATED EXPOSURES

Chapter 5 evaluated the ability of various commercial surface treatments to resist conditions provoking physical salt attack (PSA). In the current chapter, a synthesized water-based nano-silica (5 to 50%) solution and silane/nano-clay (5 to 50%) composite were used as superficial treatments for concrete and assessed under severe PSA exposure. In addition, the developed coatings were evaluated against salt-frost scaling to provide a generalized conclusion on their applicability in field-like environments.

6.1 Introduction

Reducing the transport properties of the surface layer of concrete is crucial for extended service life of concrete structures, as in most cases ingress of detrimental substances from the surrounding environment into concrete is the primary cause of durability issues. Surface treatments can be applied to new or existing concrete elements to provide efficient protection of the surface layer by enhancing barrier properties. Depending on the function, surface treatments of concrete can be categorized into four types (Pan et al. 2017): coatings forming a continuous film on the surface (e.g. epoxy and methyl methacrylate), hydrophobic/water-repellent agents (e.g. silane and siloxane), surface pore blockers (e.g. sodium silicate), and multifunctional treatments (e.g. ethyl silicate). Application of surface treatments may improve the durability of concrete elements exposed to aggressive environments, for example involving salts combined with cyclic conditions (wetting/drying [W/D], freezing/thawing [F/T]).

Nanoparticles (e.g. nano-silica and nano-clay) have been introduced in the field of surface treatments being applied either directly on concrete or mixed into other compounds.

Specifically, nano-silica has been used as a direct treatment for concrete likely due to its high reactivity and deposition within the surface layer. For example, Hou et al. (2015) soaked hardened cement paste specimens with water-to-cement ratios (*w/c*) of 0.26, 0.38, 0.60 and 1 in colloidal nano-silica (mean particle size of 20 nm and solids content of 30%) for 1 h followed by curing for 7 days. This treatment effectively decreased the water absorption ratio and water vapor transmission coefficient especially at higher *w/c*. Ardalan et al. (2017) cured fresh concrete specimens by immersion for 28 days in colloidal nano-silica (mean particle size of 50 nm and concentrations of 4%, 8%, and 12%) compared with another group of specimens sprayed by nano-silica (25% and 50%) three times within 4 h after casting. Relative to uncoated concrete, treated concrete showed reduction in permeability which varied between 5% and 31% for concrete cured by immersion compared to 14% for sprayed specimens. Nano-silica can be considered as a surface pore blocker, as it may react with the portlandite in the cementitious matrix and precipitate phases that block the pathway for external substances into the host material (Jalal et al. 2015). Nano-silica also possesses some characteristics that could be beneficial when applied as a surface treatment e.g. acting as nuclei to promote cement hydration, nano-filling and limiting the growth of calcium hydroxide (Madani et al. 2012; Khaloo et al. 2016).

Regarding nanocomposites (nanoparticles mixed into inorganic or organic compounds), few studies were performed using nano-clay into neat compounds to improve their barrier properties. For instance, Scarfato et al. (2012) mixed organo-modified montmorillonite (2%, 4%, and 6%) into two resins: Fluoline CP (a blend of an acrylic polymer and a vinylidenefluoride based polymer in acetone solution) and Antipluviol S (a solution based on siloxane resins in isooctane/orthoxylene). The nanocomposites were

applied by brushing to concrete made with water-to-binder ratio (*w/b*) of 0.53, and they showed significant enhancement in protection of concrete with respect to plain resins in terms of barrier effects to water vapor and capillary sorption. Woo et al. (2007) mixed two montmorillonite-based clays, namely Cloisite 20A and I.30P into silane at 1%, 3% and 5%. Neat silane and silane/nano-clay (5%) composite significantly reduced the moisture permeability of concrete. The salt spray test indicated that neat silane and nanocomposite coatings reduced the chloride content by 92% and 69%, respectively, compared to uncoated concrete arguably due to deeper penetration of silane into concrete than the nanocomposite. Yet, the previous studies in this area mainly focused on characterizing the transport properties of treated concrete, without assessing its performance under severe durability exposures frequently encountered in the field. For example, physical salt attack (PSA) is a key deterioration mechanism of concrete exposed to salt-rich sources under certain environmental conditions (e.g. hot-arid regions, W/D cycles). PSA involves no or limited chemical alteration of hydration products; instead, salt compounds crystallize in the near-surface pores of concrete producing excessive crystallization pressure (10–20 MPa) acting on the pore walls with tensile stresses that are far greater than the concrete tensile strength (Haynes et al. 2008). There is dearth of information in the technical literature on the effectiveness of surface treatments on mitigating PSA on concrete. In the previous chapter, epoxy, ethyl silicate, and acrylic emulsion were effective at protecting concrete against PSA, irrespective of the *w/b*. Comparatively, the performance of silane, sodium silicate, methyl methacrylate, and high-molecular weight methyl methacrylate was inefficient, especially with high *w/b*. Further research is still required in this direction to provide innovative measures for mitigating PSA on concrete, for example using nano-based coatings.

Freezing/thawing (F/T) exposure is a key durability concern for concrete in cold regions, especially for transportation infrastructure where de-icing chemicals are applied. Combination of F/T cycles and de-icing salts can negatively affect concrete physically (scaling and cracking) and/or chemically (alteration/decomposition of hydration products). Yet, there is scarce data on evaluating the performance of various surface treatments to protect concrete against frost damage or salt-frost scaling. For instance, Mamaghani et al. (2009) reported that an ultralow-viscosity epoxy sealer was efficient at improving concrete resistance to salt-frost scaling. Dang et al. (2014) reported the benefit of silane to improve the concrete durability exposed to salt-frost scaling. Nevertheless, there have been no studies on the effect of surface treatments comprising nanoparticles on the salt-frost scaling resistance of concrete.

6.2 Research Significance

Given the aforementioned research gaps, the efficacy of nano-based coatings for enhancing the durability of concrete to severe conditions is still uncertain. The current study aimed at applying water-based nano-silica sol and silane/nano-clay composite with different dosages of nanoparticles to concrete surface to assess the improvement in performance, if any. The durability of treated concrete was evaluated under aggravated field-like exposures conductive to PSA and salt-frost scaling. Moreover, the coatings were applied on concrete with different qualities (variable *w/b* and inclusion of SCMs) to determine the effect of this key parameter on the performance of nano-based coatings developed herein. Results from this study should contribute essential knowledge on optimum types and loading ratios of nano-based surface coatings for concrete under aggressive exposures involving salt-laden and environmental cycling (W/D and F/T).

6.3 Experimental Program

6.3.1 Materials and Mixtures

6.3.1.1 Concrete mixtures

The materials used in this Chapter were similar to those used in Chapter 3 (refer to Section 3.3.2). In addition, a fresh air content of 6±1% was achieved by an air-entraining admixture for specimens exposed to F/T. Concrete mixtures were similar to those used in Chapter 5 (refer to Section 5.3.1.1) and cured for 28 days.

6.3.1.2 Coatings

In this chapter, two types of coatings were applied as surface coatings for concrete: a water-based coating (nano-silica [NS] sol) and a silane-based coating (silane/nano-clay [SNC] composite). Nano-silica was obtained from the manufacturer in a colloidal form at a solid concentration of 50%. The nano-silica particles have purity of 99.5%, average particle size of 50 nm, and fineness of 80,000 m^2/kg. Silane, a hydrophobic impregnating agent for concrete, was used as the base compound for mixing with montmorillonite nano-clay (purity 99%) which has MT2EtOH (methyl, tallow, bis-2-hydroxyethyl, quaternary ammonium) organic modifier with 90 meq/100 g concentration. Nano-clay has an average density of 2.8 g/cm^3 and particle sizes range from 40 to 80 nm.

Various contents of solid particles (nano-silica and nano-clay) in each coating (5%, 10%, 15%, 25%, and 50% by mass) were tested. Nano-silica of concentration 50% was diluted by distilled water to reach the required concentrations. Regarding silane/nano-clay composite, the amount of nano-clay powder required to obtain a specific concentration was mixed with silane. The preliminary mixture was stirred using a drill mixer (300-450 rpm) until the powder was uniformly dispersed in the solvent without visible agglomerates. Ultrasonication was subsequently performed to ensure homogenous dispersion of the

nanoparticles for each coating. Ultrasonication was done for 1 h in an ultrasonic bath at 200 W and 60 kHz at lab ambient conditions. After 28 days of curing, triplicate concrete specimens were air-dried for 48 h, and then coated with the corresponding coating type and loading ratio. Concrete surface was treated by brushing three successive layers at a time-interval of 30 min. The specimens were then cured at 22±2ºC and > 95% RH for 7 days to allow for the reaction of nanoparticles with calcium hydroxide in concrete pores. Afterward, the coated surfaces were abraded with a wire brush to remove the remaining excess debris deposited on surface after drying to restore the aesthetics of the surface and simulate wearing (e.g. induced by traffic on concrete pavements).

6.3.2 Testing

6.3.2.1 Characterization of coatings and concrete surface

After ultrasonication, analysis by transmission electron microscopy (TEM) was conducted on ultrathin film samples prepared from each coating to investigate the dispersion quality. Also, the nano-indentation technique was used to determine the variation in hardness of paste due to surface treatment and possible penetration depth of each coating. Hysitron Triboindenter TI 750 fitted with Berkovitch probe (radius of 150 nm, angle of 142.35º) was used. For tested points, a trapezoidal loading was applied such that the load was increased to 1000 mN in 10 seconds, kept at 1000 mN for 10 seconds, and then decreased to zero in 10 seconds.

To evaluate the penetrability of the untreated and treated concrete, rapid chloride penetration test (RCPT) was performed on duplicate specimens from all mixtures at various loading ratios, according to ASTM C1202 (2019); noting that for treated concrete, only the side facing the cathodic compartment was coated to study the effect of coating on penetration through that surface. To alleviate the electrolysis bias of the pore solution, the

penetration depth of chloride ions into concrete was determined which better correlates to the physical characteristics of the pore structure and gives an indication on the ease of ingress of external fluids. After the RCPT, the specimens were axially split and sprayed with 0.1 M silver nitrate solution, which forms a white precipitate of silver chloride, to measure the physical penetration depth of chlorides (Bassuoni et al. 2006).

Since durability issues of concrete involving W/D cycles (e.g. PSA) depend on the solution supply and evaporation rates, an absorption/desorption experiment was designed to indicate the effect of coating on those rates similar to Chapter 5 (Section 5.3.3).

6.3.2.2 Durability exposures

The PSA exposure implemented in this chapter was the same as that conducted in Chapter 3 (Section 3.3.3). In addition, the influence of coatings on the scaling resistance of concrete exposed to F/T cycles in the presence of de-icing chemicals was evaluated according to ASTM C672 (2012) using concrete slabs (250×250×100 mm) and 4% calcium chloride solution ponded on the top surface of specimens. The test continued for 50 cycles, and each cycle comprised 16 h at freezing environment (-18^{o}C) followed by thawing at 23±2^{o}C/50±5% RH for 8 h. Cumulative scaled mass was used as a measure of deterioration and the final visual condition of specimens was assessed based on ASTM C672/C672M rating scale (ASTM C672 2012). The underlying degradation mechanisms were studied by mineralogical, thermal, and microstructural analyses (refer to Section 3.3.3).

6.4 Results

6.4.1 Transmission Electron Microscopy (TEM)

The dispersion of the prepared coatings was characterized by TEM. For example, Figure 6.1 shows the images of nano-silica and silane/nano-clay coatings at a dosage of 25%. It was observed that the spherical SiO_2 particles were evenly distributed, and the particle size

of nano-silica varied between 20 to 70 nm (Fig. 6.1a). Nano-clay particles (appearing as dark gray lines in Fig. 6.1b) were homogeneously distributed in the silane matrix and dispersed at a nanoscale. The obtained morphology of silane/nano-clay showed the presence of exfoliated nano-clay as indicated by the evenly dispersed sheets; also, intercalated structures were found which were shown as small stacks of the silicate particles in the matrix. This morphology of silane/nano-clay which appeared like a fishnet maybe a key factor for the improvement of composite properties (e.g. barrier properties).

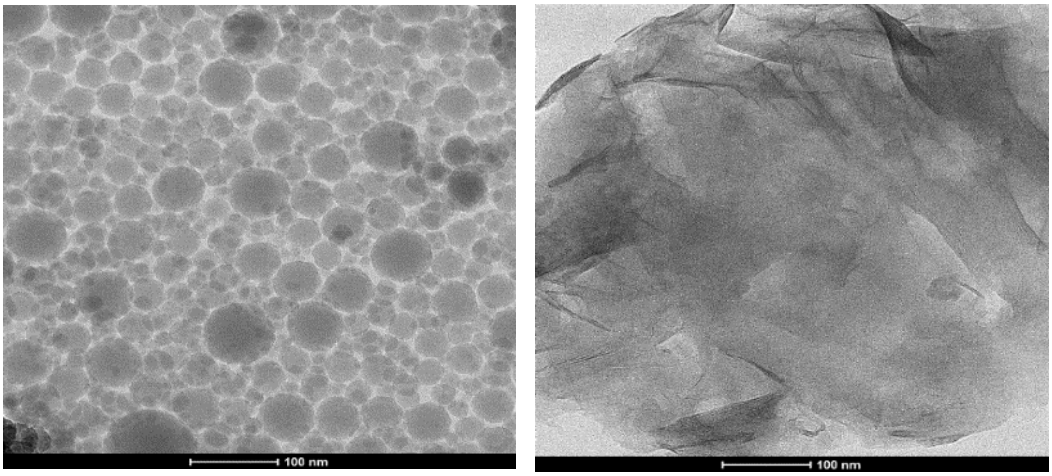

(a) (b)

Figure 6.1: TEM images of: (a) nano-silica and (c) silane/nano-clay composite at a loading ratio of 25%.

6.4.2 Transport Properties

6.4.2.1 Rapid chloride penetrability test (RCPT)

Table 6.1 presents the average passing charges and penetration depths of all specimens. In addition, the chloride migration coefficient of concrete was calculated on the basis of the penetration depth as described in NT BUILD 492 (1999), to account for the specimens that reached the maximum temperature (due to the Joule effect) allowed by the apparatus and thus did not complete the required 6 hours of testing. The penetration depths and migration coefficients were directly proportional to the values of passing charges. Irrespective of coating type, higher *w/b* led to higher penetration depth/migration coefficient of concrete

and vice versa, which conforms to the well-documented trend of the effect of *w/b* on the penetrability of concrete (Mehta and Monteiro 2014). For example, the average penetration depth for the GU0.6 and GU0.4 specimens ranged from 6 to 50 mm and from 4 to 23 mm, respectively corresponding to migration coefficients ranging from 4.86 to 97.28×10^{-12} m^2/s and from 3.12 to 20.93×10^{-12} m^2/s, respectively.

Specimens coated with nano-silica showed significant reduction of the penetration depth with increasing the dosage of particles beyond 5% in the colloid at all *w/b*. For instance, the reduction in penetration depth of GU0.6 specimens coated with 10%, 15%, 25%, and 50% nano-silica was 28%, 42%, 62%, and 68%, respectively relative to the uncoated specimens. Analysis of variance [ANOVA] (Montgomery 2014) at a significance level (α) of 0.05 showed that the coating with NS50% relative to uncoated concrete gave an *F*-value of 1229.45 compared to a critical threshold (F_{cr}) of 18.51 (Table 6.2). Comparatively, the silane/nano-clay composite showed more reduction in the penetrability of concrete at all *w/b*, especially at lower dosages of nano-clay. For example, GU0.6 specimens coated with 5 to 10% SNC had a penetration depth of 6 mm (88% reduction relative to uncoated specimens), whereas conjugate specimens coated with 50% SNC had a penetration depth of 15 mm (70% reduction). The effect of silane/nano-clay was also confirmed by ANOVA where an *F*-value of 1561.18 was obtained for specimens coated with SNC5% relative to the reference concrete. Regarding the coating type, using silane with dosages from 5 to 25% nano-clay led to much better results especially at lower dosages while at 50%, both coatings gave comparable results (Table 6.2).

Table 6.1: RCPT results of uncoated and coated specimens

	Mixtures											
	GU0.6			**GU0.5**			**GU0.4**			**GUSF0.35**		
Coating ID.	Passing Charges (coulombs)	Penetration Depth (mm)	Migration Coefficient ($\times 10^{-12}$ m^2/s)	Passing Charges (coulombs)	Penetration Depth (mm)	Migration Coefficient ($\times 10^{-12}$ m^2/s)	Passing Charges (coulombs)	Penetration Depth (mm)	Migration Coefficient ($\times 10^{-12}$ m^2/s)	Passing Charges (coulombs)	Penetration Depth (mm)	Migration Coefficient ($\times 10^{-12}$ m^2/s)
Uncoated	OVF*	50	97.28	6575	32	29.94	4015	23	20.93	1345	9	7.60
NS5%	OVF*	50	73.08	4903	31	28.93	3143	20	18.00	1296	8.1	6.78
NS10%	5803	36	34.05	3865	24.5	22.41	2785	19	17.03	1264	7.9	6.60
NS15%	4693	29	26.91	3457	22	19.95	2442	16	14.15	1200	7.5	6.23
NS25%	2989	19	17.03	2671	17	15.11	1885	12	10.38	992	6.2	5.06
NS50%	2572	16	14.15	2298	14.5	12.73	1711	9	7.60	768	4.8	3.82
SNC5%	832	6	4.88	656	5.5	4.44	425	4	3.12	255	2.4	1.74
SNC10%	785	6	4.86	647	5	3.99	488	4.6	3.64	393	3.7	2.85
SNC15%	1100	7	5.78	765	7	5.78	658	6.2	5.06	457	4.3	3.38
SNC25%	1162	6.5	5.33	699	7.5	6.23	762	7	5.78	595	5.6	4.53
SNC50%	1907	15	13.20	1624	11.5	9.91	882	8.3	6.96	722	7	5.78

*OVF stands for "over-flow" which led to the termination of the RCPT cell before 6 h.

Table 6.2: Analysis of variance (ANOVA) for the results of GU0.6 specimens

Parameter	Migration coefficient		Absorption		Desorption		PSA mass loss		Frost scaling mass loss	
	F	***F_{cr}***	***F***	***F_{cr}***	***F***	***F_{cr}***	***F***	***F_{cr}***	***F***	***F_{cr}***
Coating type										
NS5% vs. SNC5%	476.72*	18.51	246.34*	18.51	220.04*	18.51	41.22*	7.70	1322.80*	18.51
NS10% vs. SNC10%	691.55*	18.51	553.84*	18.51	154.38*	18.51	38.09*	7.70	417.98*	18.51
NS15% vs. SNC15%	115.12*	18.51	270.4*	18.51	13.27	18.51	16.9*	7.70	1910.94*	18.51
NS25% vs. SNC25%	98.5*	18.51	32.33*	18.51	0	18.51	7.05	7.70	7.20	18.51
NS50% vs. SNC50%	1.15	18.51	1.95	18.51	20.51*	18.51	4.80	7.70	43.56*	18.51
Dosage										
Uncoated vs. NS5%	39.88*	18.51	0.65	18.51	0.88	18.51	43.27*	7.70	19.06*	18.51
NS5% vs. NS10%	143.86*	18.51	17.02	18.51	8.25	18.51	1.01	7.70	29.88*	18.51
NS10% vs. NS15%	10.73	18.51	42.61*	18.51	31.37*	18.51	5.6	7.70	10.31	18.51
NS15% vs. NS25%	21.27*	18.51	21.16*	18.51	0.09	18.51	0.78	7.70	1554.13*	18.51
NS25% vs. NS50%	6.08	18.51	3.77	18.51	5	18.51	3.56	7.70	27.04*	18.51
Uncoated vs. NS50%	1229.45*	18.51	82.5*	18.51	136.34*	18.51	150.06*	7.70	1096.10*	18.51
Uncoated vs. SNC5%	1561.18*	18.51	143.63*	18.51	184.69*	18.51	164.7*	7.70	1127.04*	18.51
SNC5% vs. SNC10%	0	18.51	1.20	18.51	8	18.51	0.19	7.70	--	18.51
SNC10% vs. SNC15%	2.35	18.51	0.22	18.51	16	18.51	0.19	7.70	--	18.51
SNC15% vs. SNC25%	0.3	18.51	26.47*	18.51	5.06	18.51	0.01	7.70	169*	18.51
SNC25% vs. SNC50%	76.57*	18.51	0.07	18.51	0.80	18.51	0.03	7.70	15.08	18.51

*Denotes statistical significance

6.4.2.2 Absorption/desorption tests

In addition to RCPT, the performance of coatings in controlling the transport of fluids into and outside of concrete specimens was evaluated by absorption and desorption (evaporation) tests (Table 6.3). The GU0.6 specimens were selected for this purpose as they represented coarse and continuous pore structure as indicated by the RCPT results (Table 6.1). Uncoated concrete had the highest absorption and desorption ratios of +7.03% and -3.22%, respectively. Similar to the results of RCPT, the specimens coated with nano-silica had better performance in terms of controlling the transport of fluids compared with uncoated specimens. Increasing the dosage of nano-silica beyond 5% proportionally reduced the absorption and desorption percentages of concrete, with NS50% resulting in a significantly low values of +1.50% and -0.92%, respectively (79% and 71% enhancement relative to uncoated specimens). Table 6.2 showed that using nano-silica had a statistically significant effect on the absorption and desorption results.

Table 6.3: Absorption and desorption values for GU0.6 specimens at 48 h

Specimen	Absorption (%)		Desorption (%)	
Uncoated	7.03	[0.53]	-3.22	[0.18]
NS5%	6.51	[0.37]	-3.00	[0.15]
NS10%	4.83	[0.17]	-2.43	[0.13]
NS15%	3.35	[0.15]	-1.36	[0.14]
NS25%	2.20	[0.20]	-1.30	[0.15]
NS50%	1.50	[0.30]	-0.92	[0.08]
SNC5%	0.65	[0.05]	-0.77	[0.01]
SNC10%	0.72	[0.04]	-0.81	[0.01]
SNC15%	0.75	[0.05]	-0.85	[0.00]
SNC25%	1.05	[0.03]	-1.30	[0.20]
SNC50%	1.07	[0.07]	-1.50	[0.10]

*Values between brackets are standard deviations

The silane/nano-clay composite further reduced the transport properties of concrete compared to nano-silica, especially at lower dosages of nano-clay (5 to 15%). specimens coated with SNC5% showed the least absorption and desorption values of +0.65% and -0.77%, respectively. These values corresponded to 91% and 76% improvement, respectively, compared to uncoated concrete and 50 and 48% improvement, respectively, compared to specimens coated with neat silane (reported in Chapter 5). Increasing nano-clay dosage beyond 15% markedly increased the absorption/desorption values with the maximum values in the silane/nano-clay group were +1.07% and -1.50%, respectively for SNC50%. These values were marginally lower than that of the corresponding specimens coated with neat silane, which highlighted the inefficiency of larger dosages of nano-clay at improving the surface properties of concrete (Table 6.2), similar to the trends obtained from RCPT.

6.4.3 Exposure Results

6.4.3.1 Physical salt attack (PSA)

The visual conditions of uncoated concrete cylinders after 120 cycles of the PSA exposure are shown in Fig. 6.2. Also, Table 6.4 shows the variation of mass with exposure. Surface scaling of specimens occurred above the solution level proceeding upwards while the immersed part remained intact in all specimens. Initially, most specimens slightly gained mass due to ingress of solution, except for uncoated and nano-silica (5-15%) GU0.6 specimens, as their rates of scaling were higher than that of solution absorption. For deteriorating specimens, the rate of mass loss increased rapidly after 60 cycles of exposure. Lower quality concrete (GU0.6 and GU0.5) suffered severe scaling and cross-sectional reduction due to PSA. For instance, compared to uncoated GUSF0.35 specimens (low *w/b*) that scaled up to the mid-height of the upper part with minimal mass loss (1%) up to 120

cycles, scaling propagated to the top of GU0.6 specimens after only 45 cycles and they fractured after 105 cycles (mass loss of 27%) [Fig. 6.2].

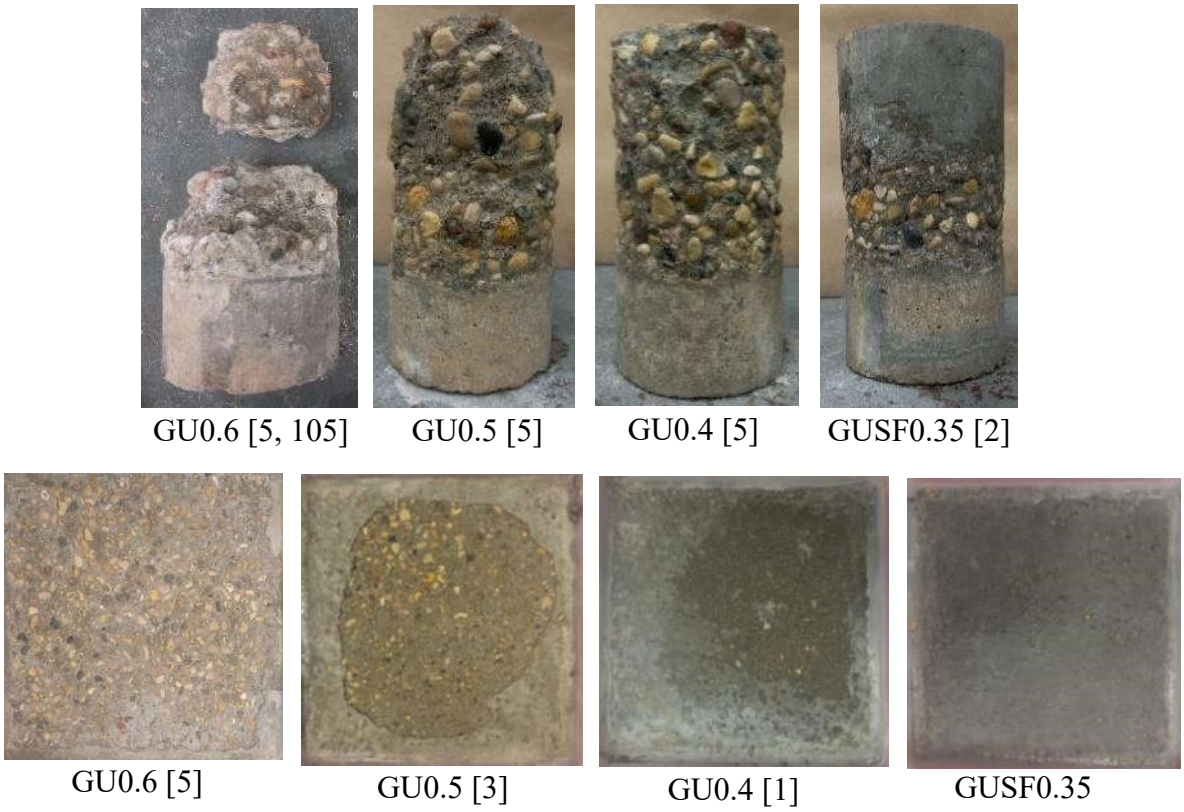

Figure 6.2: Condition of uncoated specimens at the end of PSA (top) and salt-frost scaling (bottom) exposures. (Note: Numbers between brackets are the final visual ratings and number of cycles at failure, respectively if applicable).

Specimens coated with nano-silica showed enhanced resistance to PSA with increasing the dosage up to 50%. For example, compared to severely deteriorated uncoated specimens, GU0.6 specimens coated with NS50% showed a scaling height of 40 mm and visual rating of 2 at 120 cycles (mass loss 1%) [Fig. 6.3] (the visual condition at other *w/b* are in Appendix B, Figs. B.1-B.3). ANOVA at a significance level (α) of 0.05 for the mass loss results of different coatings at *w/b* of 0.60 showed that coating specimens with NS50% compared to uncoated concrete had a statistically significant effect on the average results [*F*-value of 150.06 compared to a critical threshold (F_{cr}) of 7.70] (Table 6.2). However, within the nano-silica group, the significance of higher dosage of nano-silica decreased as

Table 6.4: Variation of mass of uncoated and coated specimens in the PSA exposure

Mixture ID.	Days/Cycles							
	30		60		90		120	
GU0.6	-1.25	[0.27]	-3.87	[0.91]	-16.38	[1.45]	-26.87[1]	[2.05]
NS5%	-1.10	[0.18]	-3.12	[0.61]	-5.97	[1.15]	-10.16[2]	[1.50]
NS10%	-1.02	[0.15]	-2.87	[0.44]	-4.56	[0.79]	-8.23	[1.22]
NS15%	-0.85	[0.20]	-1.66	[0.30]	-3.24	[0.75]	-4.56	[0.95]
NS25%	+0.05	[0.22]	-0.69	[0.25]	-1.78	[0.27]	-3.37	[0.95]
NS50%	+0.38	[0.06]	-0.22	[0.08]	-1.02	[0.11]	-1.49	[0.30]
SNC5%	+0.30	[0.08]	+0.11	[0.05]	-0.24	[0.10]	-0.45	[0.18]
SNC10%	+0.24	[0.19]	+0.15	[0.10]	-0.33	[0.10]	-0.58	[0.21]
SNC15%	+0.26	[0.22]	-0.05	[0.00]	-0.48	[0.20]	-0.60	[0.16]
SNC25%	+0.40	[0.11]	-0.30	[0.11]	-0.56	[0.16]	-0.82	[0.14]
SNC50%	+0.33	[0.20]	-0.10	[0.06]	-0.48	[0.08]	-0.78	[0.11]
GU0.5	+0.21	[0.08]	-1.27	[0.60]	-4.59	[0.85]	-14.75	[1.70]
NS5%	+0.25	[0.06]	-1.00	[0.50]	-1.43	[0.67]	-2.15	[0.88]
NS10%	+0.11	[0.12]	+0.15	[0.20]	-0.06	[0.15]	-0.80	[0.52]
NS15%	+0.33	[0.08]	+0.28	[0.19]	+0.36	[0.22]	+0.44	[0.26]
NS25%	+0.40	[0.20]	+0.43	[0.25]	+0.60	[0.30]	+0.62	[0.33]
NS50%	+0.20	[0.10]	+0.20	[0.10]	+0.34	[0.15]	+0.58	[0.28]
SNC5%	+0.26	[0.03]	+0.10	[0.08]	+0.12	[0.05]	-0.09	[0.13]
SNC10%	+0.17	[0.10]	+0.21	[0.11]	0.00	[0.10]	-0.12	[0.11]
SNC15%	+0.20	[0.15]	+0.11	[0.09]	-0.04	[0.11]	-0.12	[0.15]
SNC25%	+0.25	[0.13]	0.00	[0.24]	-0.06	[0.20]	-0.15	[0.09]
SNC50%	+0.22	[0.21]	+0.04	[0.12]	-0.03	[0.15]	-0.13	[0.20]
GU0.4	+0.30	[0.30]	-0.84	[0.15]	-4.28	[0.70]	-8.64	[1.63]
NS5%	+0.08	[0.10]	+0.30	[0.12]	-0.40	[0.25]	-0.68	[0.30]
NS10%	+0.0	[0.15]	+0.15	[0.09]	-0.05	[0.13]	-0.36	[0.17]
NS15%	+0.20	[0.13]	+0.18	[0.11]	+0.41	[0.14]	+0.58	[0.33]
NS25%	+0.16	[0.20]	+0.30	[0.21]	+0.30	[0.21]	+0.40	[0.25]
NS50%	+0.22	[0.19]	+0.40	[0.13]	+0.36	[0.23]	+0.42	[0.27]
SNC5%	+0.20	[0.05]	+0.23	[0.08]	+0.42	[0.15]	+0.40	[0.11]
SNC10%	+0.15	[0.10]	+0.32	[0.03]	+0.32	[0.09]	+0.38	[0.16]
SNC15%	+0.05	[0.00]	+0.10	[0.11]	+0.24	[0.15]	+0.29	[0.09]
SNC25%	+0.10	[0.20]	+0.12	[0.20]	+0.22	[0.13]	+0.29	[0.20]
SNC50%	+0.09	[0.16]	+0.14	[0.15]	+0.20	[0.20]	+0.25	[0.26]
GUSF0.35	+0.16	[0.18]	-0.04	[0.08]	-0.40	[0.13]	-0.97	[0.23]
NS5%	+0.16	[0.20]	+0.14	[0.19]	0.00	[0.18]	-0.05	[0.23]
NS10%	+0.12	[0.22]	+0.12	[0.15]	+0.20	[0.17]	+0.18	[0.20]
NS15%	+0.09	[0.16]	+0.11	[0.20]	+0.15	[0.20]	+0.16	[0.25]
NS25%	+0.20	[0.09]	+0.25	[0.11]	+0.26	[0.10]	+0.24	[0.16]
NS50%	+0.04	[0.11]	+0.06	[0.16]	+0.13	[0.20]	+0.20	[0.18]
SNC5%	+0.05	[0.00]	0.00	[0.09]	+0.02	[0.08]	+0.02	[0.06]
SNC10%	+0.10	[0.06]	+0.12	[0.10]	+0.08	[0.19]	+0.06	[0.14]
SNC15%	+0.04	[0.10]	+0.10	[0.15]	+0.07	[0.19]	+0.07	[0.13]
SNC25%	+0.04	[0.13]	+0.10	[0.20]	+0.22	[0.13]	+0.10	[0.24]
SNC50%	+0.10	[0.02]	+0.13	[0.22]	+0.20	[0.28]	+0.10	[0.26]

Values are in percentage (%); (-) refers to mass loss and (+) refers to mass gain
Values between brackets refer to standard deviation
[1,2]Refers to mass loss at 105 and 117 cycles when specimens were fractured

the concentration increased such that ANOVA between NS25%and NS50% gave an insignificant effect (Table 6.2). For other *w/b*, NS5% and NS10% resulted in a marginal mass loss (max. of -2% in case of GU0.5), while higher loading ratios did not show any mass loss (Table 6.4).

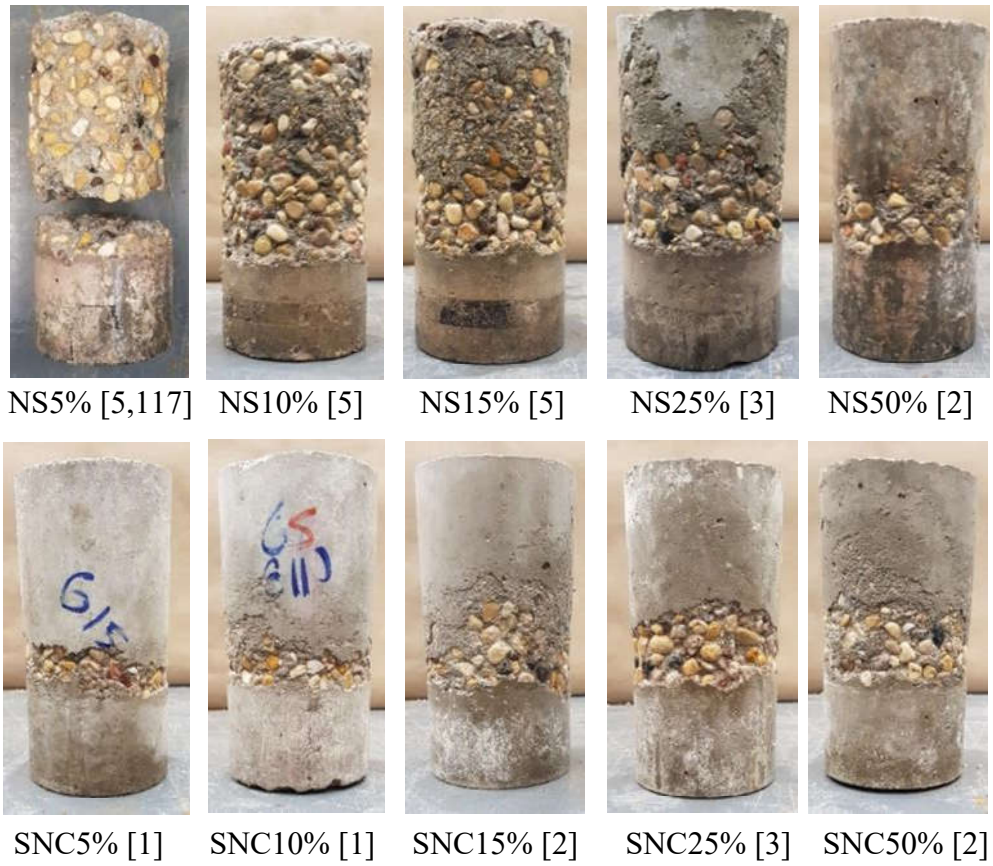

Figure 6.3: Exemplar coated specimens (GU0.6) at the end of PSA exposure. (Note: Numbers between brackets are the final visual ratings and the number of cycles at failure respectively, if applicable; NS: nano-silica, SNC: silane/nano-clay composite).

Specimens coated with the silane/nano-clay composite showed enhanced resistance to PSA compared to uncoated and nano-silica coated specimens, with optimum nano-clay loading ratios of 5 and 10%, even for GU0.6 specimens (minor scaling occurred within 20 mm above the solution level with visual rating of 1, Fig. 6.3). For the GU0.6 specimens, the final mass losses of cylinders were less than 1%, with 5% loading ratio being sufficient to impart enhanced resistance to PSA. The GU0.5 specimens experienced a slight mass

loss, and the entire set of GU0.4 and GUSF0.35 specimens did not show any mass loss. There was no significant variation in the mass loss results with changing the loading ratio of nano-clay in the composite (Table 6.4). Considering a fixed dosage of nanoparticles (nano-silica or nano-clay), ANOVA (Table 6.4**)** showed that changing the type of coating had a statistically significant effect on the mass loss results of GU0.6 specimens at low dosages (5 to 15%) with the *F*-value decreasing with concentration, and the effect became insignificant at higher dosages (25 and 50%).

6.4.3.2 Salt-frost scaling

The salt-frost scaling exposure was conducted for 50 cycles considering the combined action of de-icing salt and F/T cycling. Table 6.5 lists the final mass of scaled material (mass loss) per unit surface area, and Figure 6.2 shows the final conditions for uncoated specimens along with the visual ratings. Decreasing the *w/b* led to improved concrete performance such that the visual rating decreased from 5 for GU0.6 specimens to 0 for GUSF0.35 specimens, conforming to the cumulative mass loss results. The cumulative mass losses from the surface for uncoated GU0.6, GU0.5, GU0.4, and GUSF0.35 specimens were 1175, 528, 98, and 0 g/m^2, respectively.

Similar to the trends observed in the PSA exposure, the nano-silica coating resulted in enhancing the resistance of concrete to salt-frost scaling, particularly as the dosage increased at higher *w/b* (Figure 6.4). Small dosages of nano-silica (5%, 10%, 15%) led to higher mass losses (982, 736, 612 g/m^2, respectively) in GU0.6 specimens while treating the surface with NS25% and NS50% led to minimal (less than 50 g/m^2) surface deterioration. ANOVA for the mass loss results showed that varying the dosage of nano-silica within the range of 5 to 15% had minimal effect on the average results, while increasing the dosage from 15% to 25% caused significant improvement in the average

results (F-value of 1554.13 compared to a critical threshold (F_{cr}) of 18.51) [Table 6.2]. However, increasing the dosage from 25% to 50% had an insignificant effect on the results. The performance of nano-silica coatings markedly improved with reducing the *w/b* such that specimens made with 0.50, 0.40, and 0.35 *w/b* had low (maximum of 136 g/m^2) to nil surface scaling at all loading ratios of nano-silica (Table 6.5). Comparatively, all specimens coated with the silane/nano-clay composite had superior resistance to salt-frost scaling, i.e. minimal or no scaling, regardless of the *w/b* and the dosage of nano-clay (e.g. Fig. 6.4); a dosage of 5% nano-clay dispersed in silane was sufficient to eliminate the surface damage of specimens. ANOVA (Table 6.2) showed that using SNC5% had a significant effect on the scaled mass results compared to untreated concrete (F-value of 1127 compared to F_{cr} of 18.51). The F-value could not be obtained in the range of 5 to15% as the mass loss was nil for these ratios, while changing the dosage beyond 15% gave an F-values indicating the negative effect of increasing the dosage beyond 15%.

Table 6.5: Final salt-frost scaling results of uncoated and coated specimens

Coating ID	**Scaled Mass (g/m^2)**							
	GU0.6		**GU0.5**		**GU0.4**		**GUSF0.35**	
Uncoated	1175	[35]	528	[18]	98	[8]	0	[0]
NS5%	982	[27]	136	[6]	25	[5]	0	[0]
NS10%	736	[36]	75	[5]	12	[2]	0	[0]
NS15%	612	[14]	62	[8]	0	[0]	0	[0]
NS25%	38	[4]	10	[2]	0	[0]	0	[0]
NS50%	12	[3]	0	[0]	0	[0]	0	[0]
SNC5%	0	[0]	0	[0]	0	[0]	0	[0]
SNC10%	0	[0]	0	[0]	0	[0]	0	[0]
SNC15%	0	[0]	0	[0]	0	[0]	0	[0]
SNC25%	26	[2]	0	[0]	0	[0]	0	[0]
SNC50%	40	[3]	0	[0]	0	[0]	0	[0]

Values between brackets refer to standard deviation

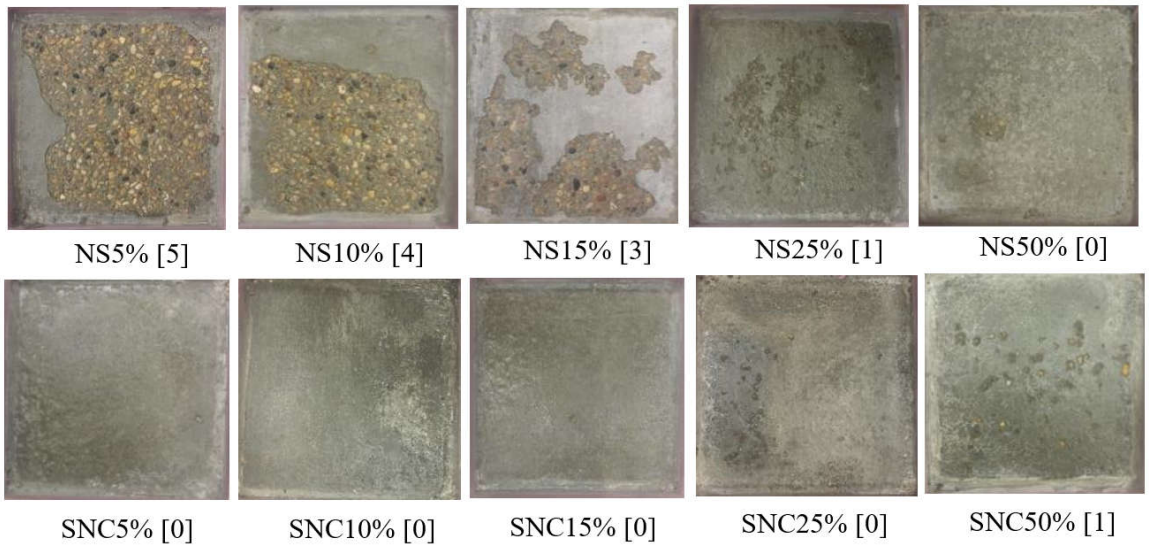

Figure 6.4: Exemplar coated specimens (GU0.6) at the end of the salt-frost scaling exposure. (Note: Numbers between brackets are the final visual ratings; NS: nano-silica, SNC: silane/nano-clay composite).

At fixed dosage of nanoparticles, changing the type of coatings had a statistically significant effect on the mass loss results, especially at lower dosages (5 to 15% nano-silica and nano-clay). Table 6.2 shows that using silane/nano-clay instead of nano-silica is statistically significant with *F*-values of 1322.8, 417.98, and 1910.94 for dosages of 5%, 10, and 15% respectively. Above 15%, using either type of coatings led to comparable performance. Ministry of Transportation of Ontario (MTO) (2018) and Bureau du normalization du Quebec (BNQ) (2002) specify a failure limit for the salt-frost scaling test of 800 and 500 g/m^2, respectively using a less aggressive solution of 3% sodium chloride. Hence, all coated specimens herein can be considered resistant to salt-frost scaling, except for the GU0.6 specimens coated with 5 to 15% nano-silica.

6.5 Discussion

6.5.1 Effect of Water-to-Binder Ratio

Water-to-binder ratio had a significant effect on the results of uncoated and coated concrete in both exposures. Figure 6.5 shows the XRD analysis on samples extracted from uncoated

and unexposed (reference) GU0.6 and GUSF0.35 specimens compared with corresponding uncoated specimens after the PSA and F/T exposures. In case of PSA, analysis of the drying portion of specimens showed a prevailing occurrence of thenardite (Na_2SO_4) peaks in the GU0.6 specimens with traces of sulfate reaction products (ettringite and gypsum). Comparatively, the drying portion of GUSF0.35 specimens showed minimal intensity of thenardite compared to GU0.6 specimens indicating the positive effect of *w/b* reduction on enhancing the performance of concrete under PSA. SEM images (Fig. 6.6a) on the inner side of detached crust from uncoated GU0.6 specimens showed that massive sodium sulfate crystals were depositing beneath the surface layer (sub-florescence) causing its detachment.

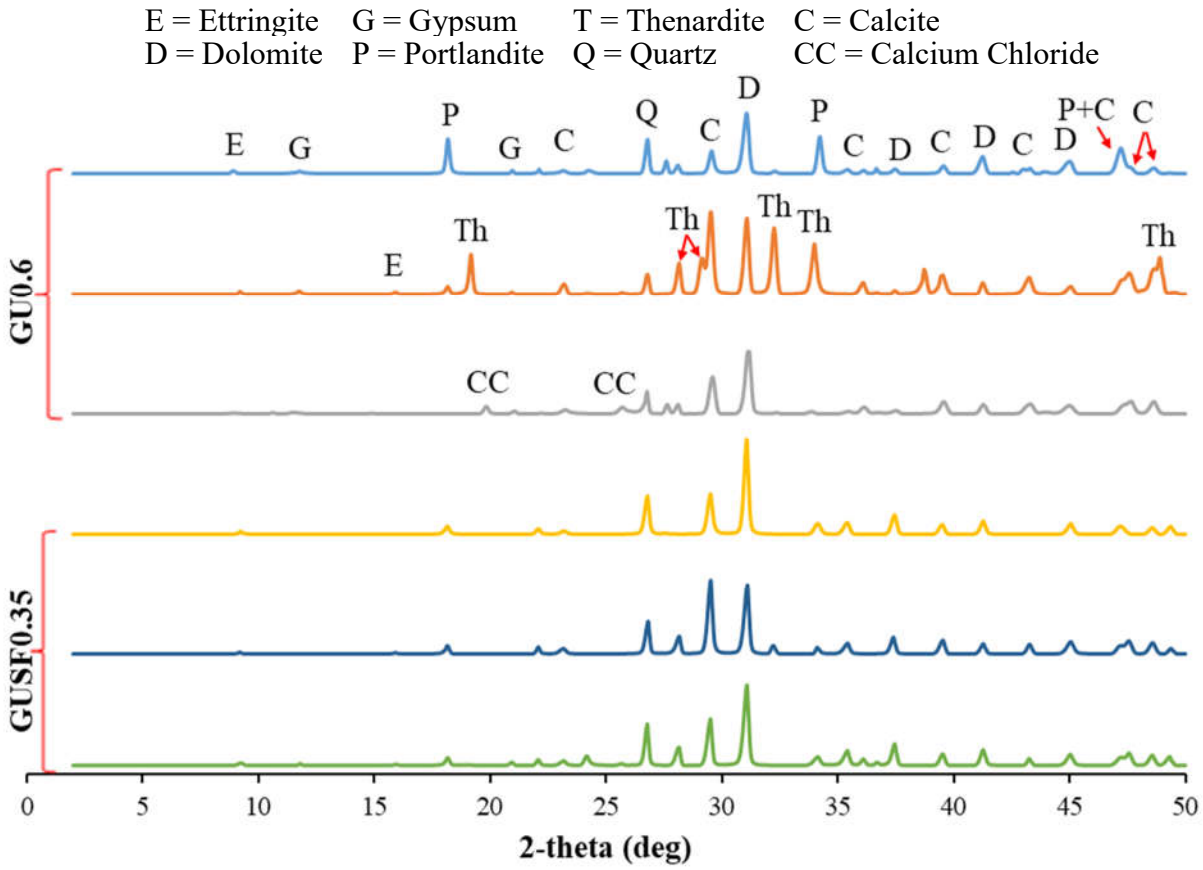

Figure 6.5: XRD analysis on samples extracted from unexposed and exposed GU0.6 and GUSF0.35 specimens.

In case of the F/T with de-icing salt exposure, XRD of GU0.6 specimens (Fig. 6.5) showed the existence of calcium chloride peaks; also, Figure 6.6b shows the existence of $CaCl_2$ crystals beneath the scaled layer in these specimens. The peaks of $CaCl_2$ were almost absent in the surface of GUSF0.35 specimens. Crystallization of de-icing salts just below the surface of concrete, where saturation is achieved by progressive infiltration of solution within this layer has been considered among the key mechanisms of salt-frost scaling (Scherer 2004).

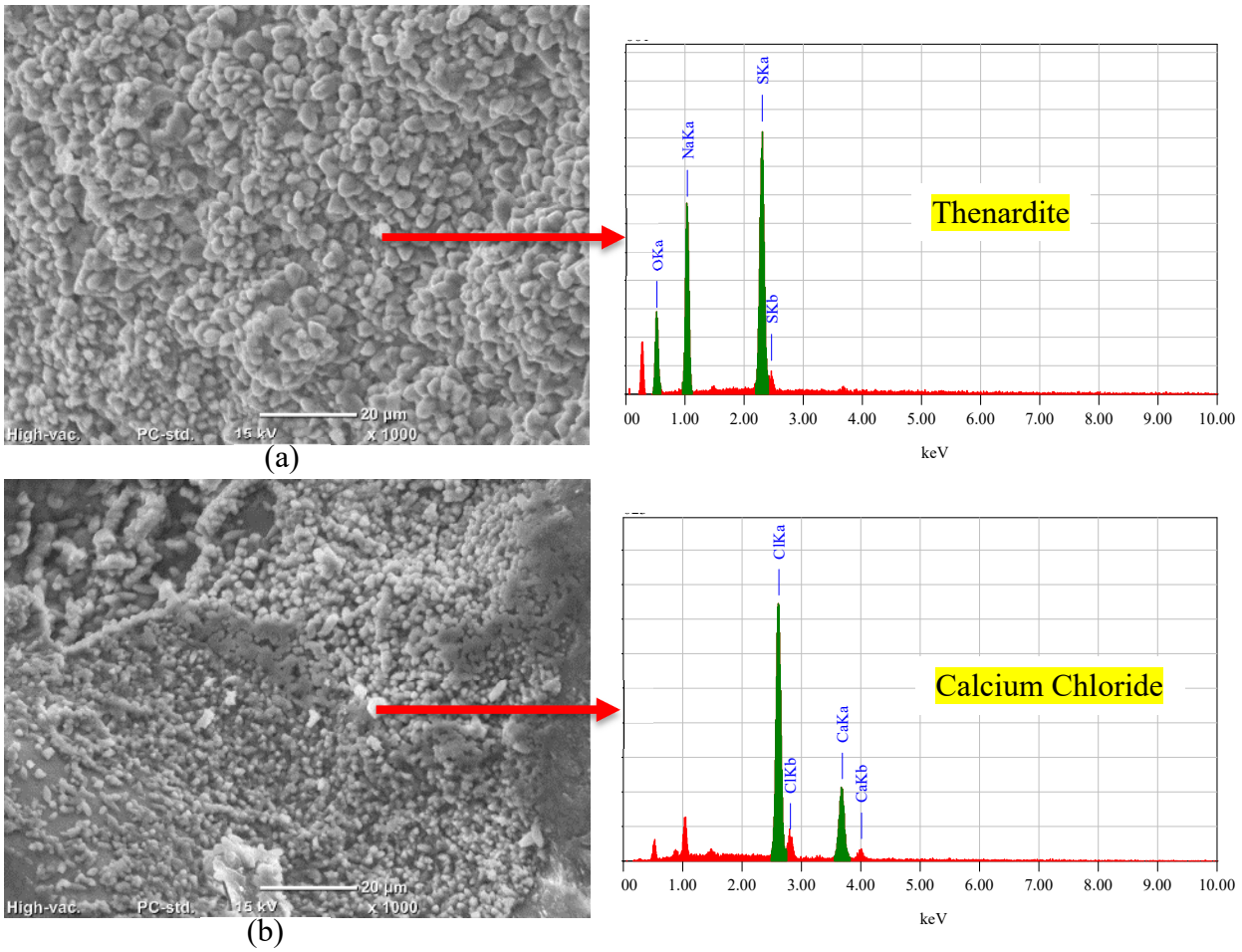

Figure 6.6: SEM and EDX analyses of scaled concrete layer from GU0.6 specimen exposed to: (a) PSA and (b) F/T with de-icing salt.

As expected, decreasing the *w/b* of concrete refined the microstructure of the hardened paste, especially in the case of silica fume (pozzolanic and filler effects), and in

turn reduced its penetrability as indicated by the results of fluid transport tests. In the case of PSA exposure, this led to discounting the rates of absorption/desorption of the sodium sulfate solution, which decelerated or impeded the process of salt crystallization in the drying portion of specimens, and thus improving the resistance of concrete to PSA. In the case of the F/T exposure, reducing the *w/b* of concrete produced dense microstructure, as indicated by the reduction of the physical penetration depth of chloride ions in the RCPT. In addition to the adequate air content (6±1%), this discounted the ingress of calcium chloride solution into the exposed surface of concrete, making specimens less vulnerable to critical saturation and subsequent salt crystallization and frost-scaling. The effect of *w/b* in case of different coatings is discussed in the subsequent sections.

6.5.2 Effect of Nano-silica Coating

The application of high dosages of nano-silica coating to concrete surface led to improving the performance of concrete under the PSA and F/T exposures. The effective depth of nanoparticles into concrete can indicate the extent of their influence on modifying the surface properties. This depth was determined by means of nano-indentation through profiling the variation in concrete hardness with depth starting from the coated surface proceeding inwards. Indentation was performed on a series of horizontal rows separated at 1 mm; for each row, five points spaced at 30 μm were tested. The effect of nano-silica improved with reduction of *w/b*; for example, NS10% could minimize the damage of GU0.4 specimens but it failed in the case of GU0.6 specimens, due to the dominant effect of *w/b* as discussed earlier. Therefore, the analysis was performed on GU0.6 specimens (lowest quality microstructure) coated with NS50% which was the dosage resulting in the best performance in terms of reducing the transport properties and enhancing the resistance of high porosity concrete to both exposures. Figure 6.7a shows the load-depth curves for

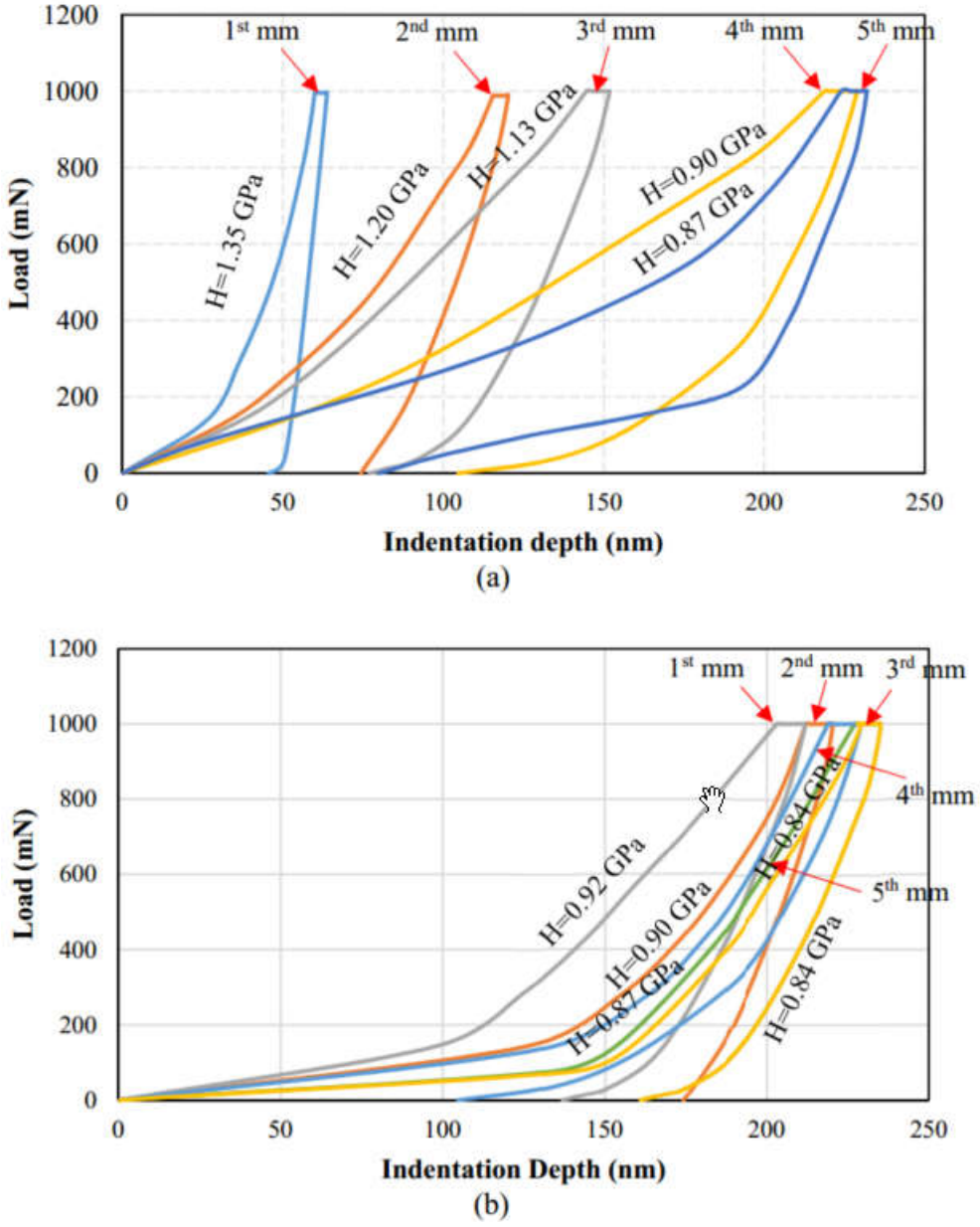

Figure 6.7: Load-depth curves obtained from GU0.6 specimens coated with (a) NS50% and (b) SNC5%.

the first five rows (5 mm) tested; the corresponding average hardness values were 1.35, 1.20, 1.13, 0.90, and 0.87 GPa, respectively. The treatment with 50% nano-silica led to increasing the hardness of the hydrated paste; the improvement was maximum close to the coated surface and it decreased until almost a constant value at the fourth and fifth millimeter, as the hardness corresponded to that of uncoated concrete (0.87 GPa). This

suggests that the zone affected by nano-silica was up to three millimeters from the coated surface, where the hardness of paste increased by 29% to 53% relative to that of uncoated paste. This includes the sub-florescence zone (around 2 mm) where salts tend to crystallize and exert pressure on concrete surface (Chapter 5). The penetration depth achieved conforms to reported values in previous studies for coatings that act as pore blockers. For example, ethyl silicate and sodium silicate were reported to penetrate 3 to 6 mm into concrete/mortar surface after three times of applications by brushing (Moon and Lee 2017).

The hydration products in the effective zone were studied to determine the mechanisms by which the nano-silica coating improved the resistance of concrete to aggressive exposures. DSC analysis was performed on powder samples extracted from the surface (0 to 3 mm) of unexposed GU0.6 specimens and coated with various dosages of nano-silica (Fig. 6.8). Semi-quantitative analysis based on the enthalpy concept (integration of heat flow peaks over the temperature range of 400-450^{o}C) was used to assess the content of portlandite (calcium hydroxide) in the cementitious matrix, as the enthalpy of a certain phase is directly related to its content. The results showed pozzolanic effect for the low dosages of nano-silica (5-10%) as specimens coated with NS5% and NS10% had an average reduction of the initial portlandite content by 20% and 32%, respectively, compared to uncoated concrete. Increasing the dosage of nano-silica led to progressive reduction in the amount of portlandite such that the enthalpy of portlandite was 70% lower for NS50% than that of the uncoated concrete, indicating highly efficient pozzolanic reactivity. This produced more compact and densified microstructure due to the deposition of secondary calcium silicate hydrate (C-S-H). Also, EDX analysis was performed at multiple points in the first 3 mm from surface on fracture pieces extracted from uncoated and coated specimens to calculate the calcium-to-silicate ratio (*Ca/Si*) (Fig.

6.9); the average value of *Ca/Si* was 0.86 for GU0.6 specimens coated with NS50% compared to 2.05 for reference concrete, indicating efficient pozzolanic reactivity of this coating within the effective zone which conforms to the typical *Ca/Si* for the secondary (average of 1.1) and primary (average of 1.7) C-S-H, respectively (Detwiler et al. 1996).

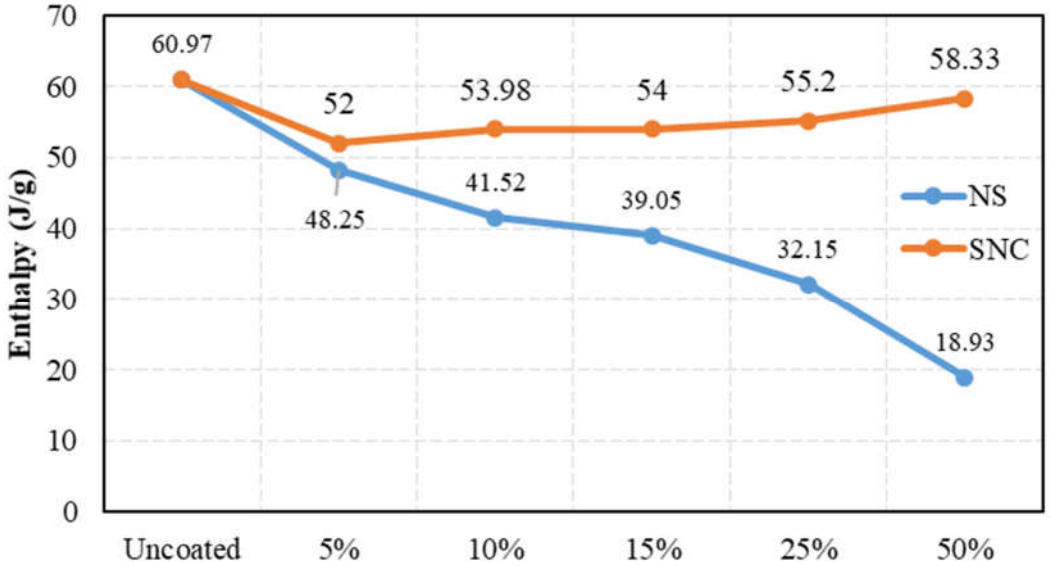

Figure 6.8: Enthalpy of portlandite in uncoated and coated GU0.6 specimens with nano-silica and silane/nano-clay composite

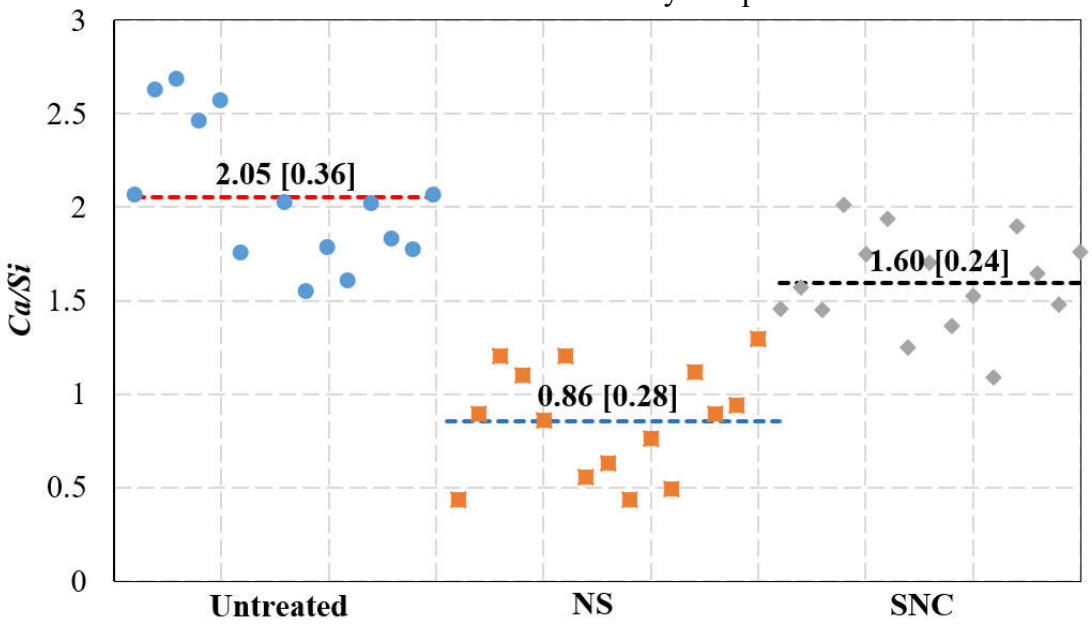

Figure 6.9: *Ca/Si* at multiple points in fracture pieces extracted from the effective zone of GU0.6 specimens: uncoated and coated with NS50% and SNC5%. (Note: horizontal lines represent the average of points with standard deviations between brackets)y SEM.

Figure 6.10 shows the morphology of the surface of GU0.6 concrete specimens coated with NS50%. It was observed that the outer surface was covered by a condensed layer of nano-silica. The average value of *Ca/Si* was 0.14 indicating the abundance of silica compared to calcium, which suggested that the source of silica in the spectrum is not from the primary or secondary C-S-H phases. Thus, the filler effect of nano-silica was another improvement mechanism, where the deposition of high dosages of condensed nano-silica on the surface of concrete acted as a barrier. The denser microstructure of concrete surface combined with the filler/barrier effect of condensed nano-silica discounted the rates of salt solutions ingress (in case of PSA and F/T) and rate of evaporation to the surrounding environment (in case of PSA), as indicated by the lower values of the chloride penetration depth and the absorption/desorption percentages of coated specimens. This explains the marked delay in the initial damage for specimens coated with 25% and 50% nano-silica and their lower visual damage ratings and mass loss after PSA and F/T compared to the uncoated specimens. Compared to Fig. 6.6 that shows the formation of massive sodium sulfate and calcium chloride crystals beneath the detached surface layer of concrete in the uncoated GU0.6 specimens, Figure 6.11 shows the SEM image of GU0.6 specimens coated with NS50% after both exposures. The images indicated the absence of thenardite crystals in the sub-florescence zone (2-5 mm from the outer surface), reflecting the high resistance of specimens to PSA; also, there were no calcium chloride crystals which led to improved salt-frost scaling resistance, even at a high *w/b* of 0.60.

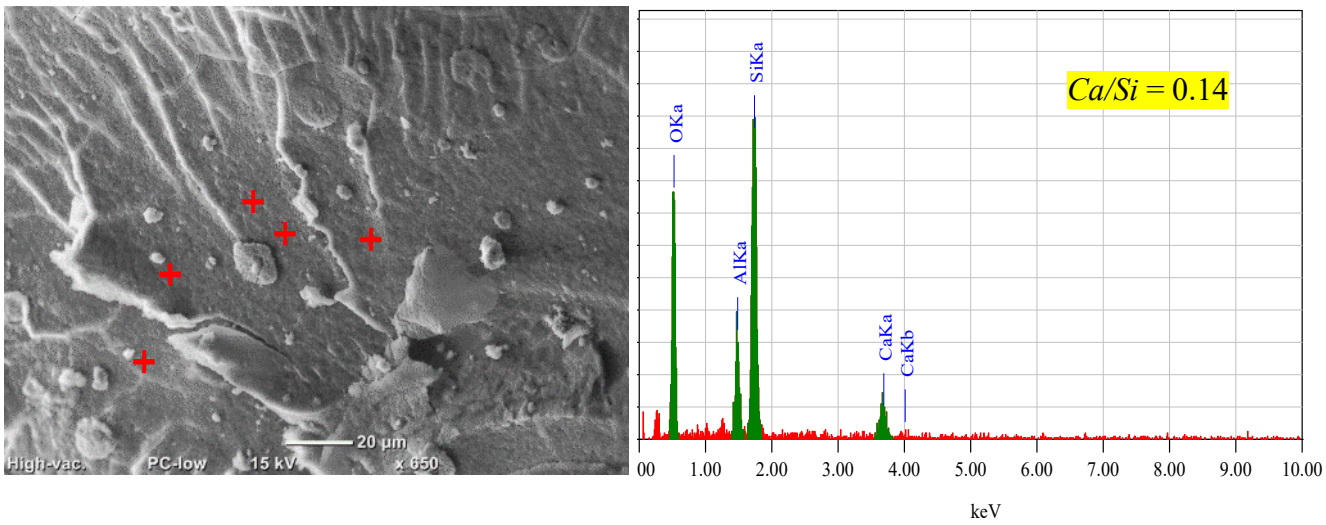

Figure 6.10: SEM and EDX of the surface of GU0.6 concrete coated with NS50% showing condensed nano-silica.

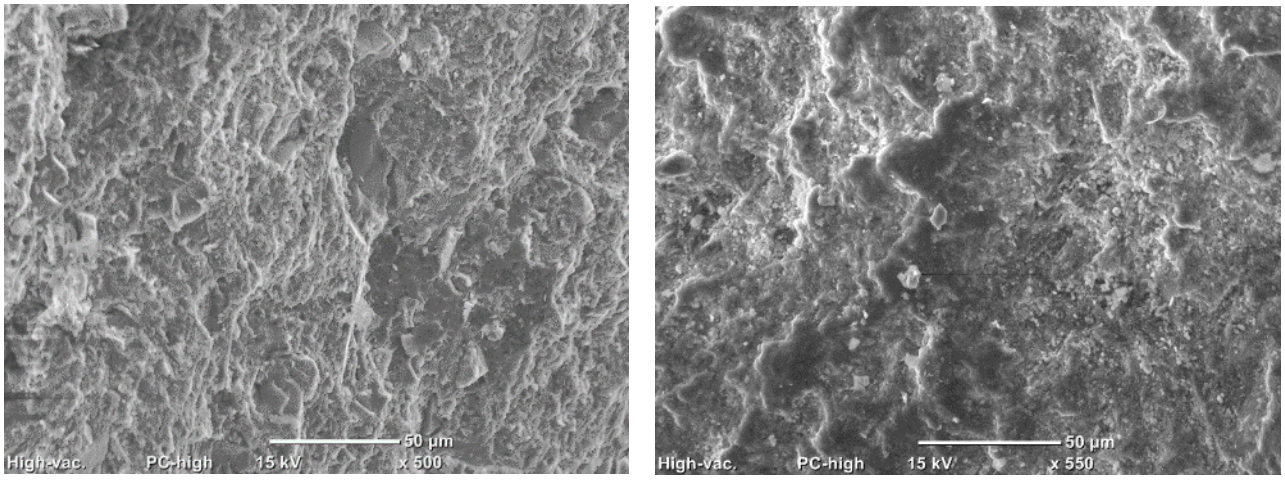

(a) (b)

Figure 6.11: SEM images of coated GU0.6 concrete with NS50% after: (a) PSA, and (b) F/T exposures.

6.5.3 Effect of Silane/nano-clay Coating

The silane/nano-clay composite was efficient at protecting concrete exposed to PSA and F/T, especially at lower dosages of nano-clay. The effect of silane/nano-clay on the performance of concrete, in terms of reducing transport properties and mass loss, depended on the dosage of nano-clay and *w/b*. At constant *w/b*, reducing the dosage of nano-clay below 10% resulted in improving the performance of concrete. Using higher dosages of nano-clay in silane did not result in homogenous dispersion of the nanoparticles within the

matrix; the nanocomposite tended to form lumpy masses at higher dosages resulting in difficulty for the nanoparticles to evenly distribute over and diffuse through the concrete surface. This was not the case at lower dosages, as the composite formed a much flowable liquid, without lumps. The dependence of silane/nano-clay performance on *w/b* varied according to the range of *w/b*; at constant dosage of nano-clay, decreasing the *w/b* in the range of 0.60 to 0.50 led to marginal reduction in transport properties and mass loss, while for the range of 0.40 to 0.35, the performance of silane/nano-clay was independent of the *w/b* (i.e. all dosages led to equivalent performance).

Similar to the nano-silica coating, nano-indentation was performed using the same methodology described earlier on GU0.6 specimens (lowest quality microstructure) coated with SNC5%, which led to the best performance in terms of reducing the transport properties and improving concrete resistance to both exposures. Compared to nano-silica, the SNC led to marginal increase (average of 5%) in the hardness value of the cement paste (0.92 and 0.90 GPa in the first two millimeters) relative to uncoated concrete (0.87 GPa) (Fig. 6.7b). This indicated that the SNC did not modify the mechanical characteristics of the concrete surface.

DSC analysis was performed on powder samples extracted from the surface (0 to 3 mm) of unexposed GU0.6 specimens and coated with various dosages of SNC to determine the extent of pozzolanic activity that could be achieved by nano-clay. The enthalpies corresponding to portlandite were in the range of 52 J/g (SNC5%) to 58 J/g (SNC50%) [Fig. 6.8]. Increasing the dosage of nano-clay resulted in a slight increase in enthalpy; the lowest dosage of nano-clay led to better pozzolanic reactivity (15% reduction of portlandite relative to reference concrete), due to the better distribution of nano-clay particles within the concrete surface as discussed earlier. Compared to nano-silica, SNC showed limited

pozzolanic activity as only 5% nano-silica led to higher consumption of portlandite, which significantly increased with dosage. This could be attributed to the smaller particle size and highly amorphous nature of nano-silica compared to nano-clay that led to enhanced pozzolanic reactivity and faster growth of secondary C–S–H. The nano-clay used comprised platy particulates, resulting in harder penetration into concrete surface. In addition, it comprises 47% SiO_2 compared to 99.5% in nano-silica, which significantly reduced its pozzolanic reactivity; while nano-silica is highly amorphous, nano-clay has limited amorphousness that depends on the calcination process (Hakamy et al. 2015). Correspondingly, the average *Ca/Si* obtained from EDX analysis on fracture pieces extracted from GU0.6 specimens coated with SNC5% was 1.6 (Fig. 6.9), which is closer to the ratio of conventional C-S-H (1.7). This conformed to the low hardness values obtained from the specimens coated with SNC5%, which were comparable to that of uncoated concrete. These trends exclude the pozzolanic reactivity of nano-clay as a primary mechanism for improving the superficial properties of concrete coated with this composite.

The SNC functionality could be linked to its base matrix. Silane has water-repelling effect, and it is capable of penetrating into concrete due to its small particle size; it could penetrate to a depth of 2 to 4 mm into concrete surface, which covers the depth where sub-florescence zone forms. Silane then reacts with alkaline elements in the pore solution to produce a hydrophobic ingredient that reduces the water absorbency of concrete (Moon and Lee 2017). For example, silane was reported to provide adequate resistance to coated concrete exposed to potassium acetate as a de-icer (Mamaghani et al. 2009), and 15 F/T and W/D cycles (Dang et al. 2014). However, in Chapter 5, silane-coated specimens failed to protect concrete as cracking/detachment of the surface crust happened after 50-60 cycles. The breathability of neat silane led to high rates of evaporation with time, and thus

formation of sub-florescence zone and considerable crystallization pressure that damaged the surface of concrete. However, the combination of nano-clay into silane matrix herein led to enhanced barrier properties due to the formation of an interwoven structure as shown by TEM (Fig. 6.1). Figure 6.12 shows the surface morphology of GU0.6 concrete coated with SNC5% indicting the deposition of nano-clay particulates on and in parts of the surface including micro-cracks which in-turn improved the barrier properties of concrete against salt solutions in case of PSA (reduced absorption/desorption rates) and F/T (reduced penetrability). Figure 6.13 shows that no salt crystallites were formed in the surface of coated specimens with SNC5% after both exposures. These trends substantiate that combining the hydrophobic function of silane and barrier/filling effect of nano-clay particles was effective at significantly improving the durability of concrete to these aggravated exposures.

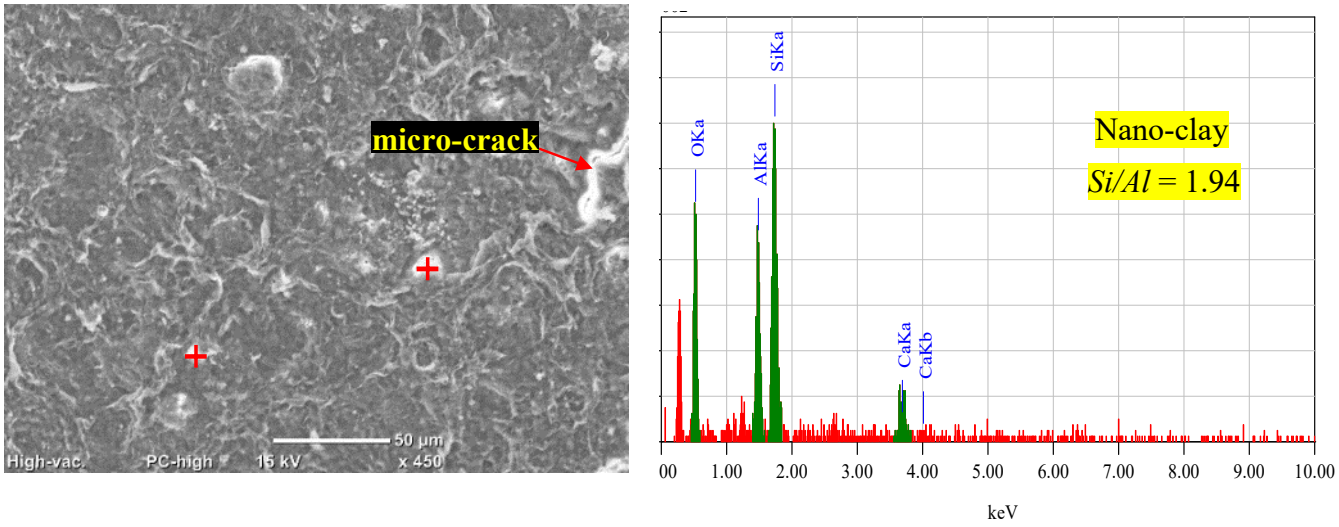

Figure 6.12: SEM and EDX of GU0.6 concrete surface coated with SNC5% showing deposition of nano-clay.

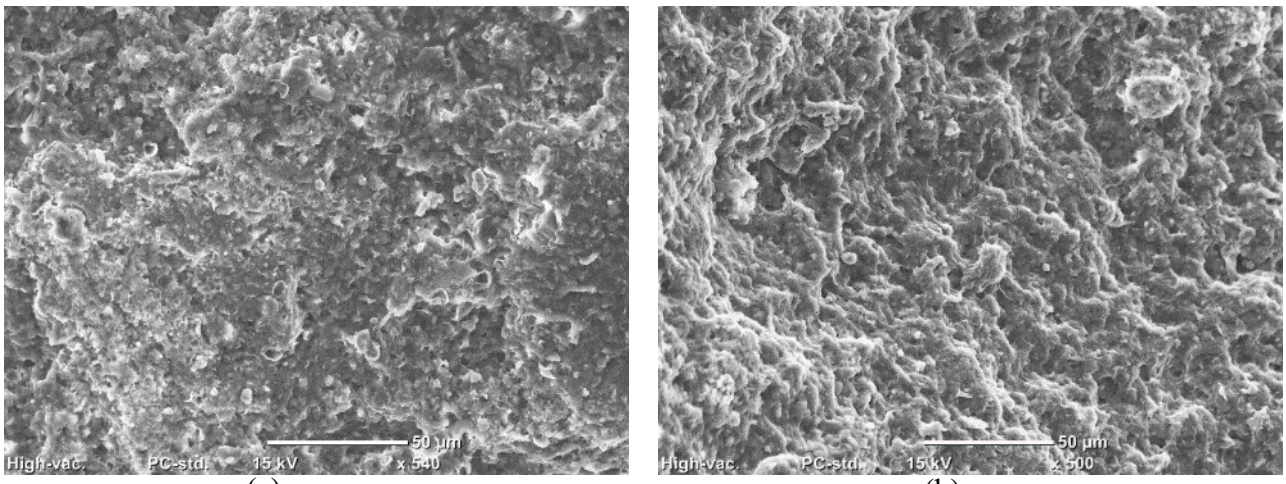

(a) (b)

Figure 6.13: SEM images of GU0.6 concrete coated with SNC5% after (a) PSA, and (b) F/T exposures.

CHAPTER 7: SILANE AND METHYL-METHACRYLATE BASED NANOCOMPOSITES AS COATINGS FOR CONCRETE EXPOSED TO PSA AND SALT-FROST SCALING

This chapter expands on the previous chapter and aims at investigating the efficiency of polymeric nanocomposites as superficial treatments for concrete subjected to aggravated exposures. Silane and methyl-methacrylate are used as base resins, in which nano-clay and nano-silica particles are mixed at 0, 5, and 10%. The durability of coated concrete is assessed under severe conditions: physical salt attack (PSA) and salt-frost scaling to provide a generalized conclusion on their applicability in field-like environments.

7.1 Introduction

Poor quality of the surface layer of concrete can lead to severe deterioration of concrete infrastructure due to ingress of moisture and deleterious substances from surrounding environment. Accordingly, costly repairs are expected during the designed service life of structures due to disruption of concrete durability (Lindvall 2001). Surface treatments that provide efficient protection against intrusive media are considered a viable strategy for cutting down future maintenance and repair costs when applied to new or existing concrete elements. Pan et al. (2017) categorized treatments into four groups according to their function: coatings/sealers providing a barrier film on concrete surface (e.g. epoxy), hydrophobic impregnations that line concrete pores and repel diffusing moisture (e.g. silane), pore blockers that react with paste constituents and precipitate compounds that fill the pores (e.g. sodium silicate), and multifunctional treatments (e.g. ethyl silicate which acts as a hydrophobic agent and pore blocker). For example, Almusallam et al. (2003) reported the ability of surface coatings (e.g. epoxy, polyurethane,

and acrylic coatings) to minimize water absorption of mortar compared to uncoated mortars. Also, silane, polymer-modified cementitious coatings, and polyurethane sealers could reduce the chloride diffusion coefficients of concrete by three orders of magnitude (Buenfeld and Zhang 1998).

Few studies incorporated nanoparticles into surface treatments as additives to neat polymer resins before application on concrete. Polymeric nanocomposites showed enhanced mechanical and barrier properties, thermal stability, and wear resistance compared to that of neat polymers (Choudalakis and Gotsis 2009). Ammar et al. (2016) found that incorporating nano-silica into an acrylic-silicone polymeric resin increased the hydrophobicity of the composite and showed potential for corrosion protection, due to efficient barrier effects. Also, Li et al. (2018) reported that adding nano-silica and nano-titania to polyurethane, epoxy, and chlorinated rubber resins increased the contact angles of concrete with fluids and reduced its water absorption, by increasing the degree of surface roughness of coatings, with nano-silica being more efficient. Scarfato et al. (2012) reinforced two polymeric resins: Fluoline CP (a mixture of acrylic and vinylidenefluoride polymers) and Antipluviol S (a solution based on siloxane) with nano-montmorillonite clay. The polymeric nanocomposites were applied to concrete made with water-to-binder ratio (*w/b*) of 0.53, and they significantly reduced the water vapor and capillary sorption of concrete compared to concrete coated with neat resins. Moreover, Woo et al. (2007) reported that silane mixed with 5% nano-clay considerably reduced the chloride diffusivity (as determined by a salt spray test) into concrete by 69% compared to that of uncoated concrete. Similarly, Leung et al. (2008) reported that adding nano-clay (1 to 5%) to epoxy and silane notably improved their barrier efficacy against the ingress of detrimental substances, as expressed by water vapor transmission and salt spray tests.

Yet, previous studies on polymeric nanocomposites mainly focused on assessing the barrier and transport properties of concrete; however, the mechanisms of enhancement imparted by nanoparticles were not fully addressed. In addition, these studies did not assess the functionality of the developed polymeric nanocomposites under aggressive environments that involve salt solutions and cyclic environments that may be encountered in the field. Therefore, the current study focused on evaluating polymeric nanocomposites under two key durability exposures: physical salt attack (PSA) and salt-frost scaling. PSA is a wetting/drying (W/D) damage mechanism occurring in hot-arid regions with salt-rich media. The deterioration results from the formation of high tensile stresses (10–20 MPa) due to salt crystallization in the near-surface pores of concrete (Haynes et al. 2008). Yet, the mitigation/protection methods of this phenomenon have not been adequately addressed in the literature. In the work of Chapter 5 on neat resins, epoxy, ethyl silicate, and acrylic emulsion were found successful at eliminating/minimizing PSA damage of concrete. Comparatively, silane, sodium silicate, methyl-methacrylate, and high-molecular-weight methacrylate, which comprise a wide sector of the commercially applied treatments, were insufficient to protect concrete against PSA. This warrants further research to introduce innovative measures, for example by using nano-modified coatings, to improve the performance of such treatments, and consequently mitigate PSA of concrete.

In addition, salt-frost scaling is a major concern for transportation agencies in cold climate regions, due to the application of de-icing chemicals on concrete pavements and bridges. De-icers combined with freezing/thawing (F/T) cycles can cause severe scaling and cracking of concrete surface, which disrupt the function of vital transportation, associated with significant rehabilitation costs. However, scarce data is available on the suitability of surface coatings to improve the salt-frost scaling resistance of concrete. For

example, ultralow viscosity epoxy was found beneficial at improving concrete durability to salt-frost scaling (Mamaghani et al. 2009). Basheer and Cleland (2011) reported that pore liners (silane and siloxane) reduced the cumulative scaled material due to salt-frost scaling when initially applied on dry concrete surface. Similarly, epoxy and silane were found to substantially reduce the mass loss by 90% relative to reference concrete after 15 freeze/thaw and wet/dry cycles (Dang et al. 2014). Liu and Hansen (2016) reported that the hydrophobic function rendered by silane application was the main reason for this improvement. Other sealers such as high-molecular-weight methacrylate were reported to have the ability to restore functionality of cracked bridge decks, but the performance maybe compromised with exposure to de-icing chemicals (Rahim et al. 2010). However, there is dearth of information on the potential of polymeric nanocomposites to resist salt-frost scaling of concrete.

7.2 Research Significance

Given the aforementioned research gaps and needs, the functionality of polymeric nanocomposites to protect concrete exposed to aggravated exposures remains uncertain. In this chapter, silane (pore liner and waterproofing agent) and methyl-methacrylate (pore filler/sealer), which were inadequate alone at protecting concrete against PSA (Chapter 3), were used as dispersants for nanoparticles (nano-clay and nano-silica) in an attempt to produce polymeric nanocomposites for concrete with improved performance under field-like exposures. The coatings were applied to low- and high-quality concretes made with *w/b* of 0.60 and 0.40, respectively. Moreover, the efficiency of such coatings was verified through application on an additional set of pre-cracked specimens to simulate restoration of damaged concrete. Results from this study should contribute essential knowledge on the underlying role of nanoparticles in shifting the behavior of polymers and applicability of

polymeric nanocomposites as surface treatments for concrete under severe exposures involving salt-media and cyclic environments.

7.3 Experimental Program

7.3.1 Materials and Mixtures

7.3.1.1 Concrete mixtures

The materials used in this Chapter were similar to those used in Chapter 3 (refer to Section 3.3.2). In addition, a fresh air content of 6±1% was achieved by an air-entraining admixture for specimens exposed to F/T. Two concrete mixtures were prepared and cured for 28 days: GU0.6 and GU0.4 to represent fine and coarse pore structure. Details of these mixtures can be found in Chapters 5 and 6 (refer to Section 5.3.1.1).

7.3.1.2 Coatings

Two types of polymeric resins were used as the base media for dispersing nanoparticles: silane (S) and methyl-methacrylate (MMA). Nano-clay and nano-silica were used to synthesize the following nanocomposites: silane/nano-clay (denoted as SNC), silane/nano-silica (denoted as SNS), MMA/nano-clay (denoted as MNC), and MMA/nano-silica (denoted as MNS). The nano-silica powder has purity of 99.5%, average particle size of 20-30 nm, average specific surface area of 160 m^2/g, and density of 2.21 g/cm^3. Montmorillonite nano-clay (99% purity, particle sizes of 40-80 nm, average specific surface area of 70 m^2/g, and density of 1.98 g/cm^3), which has MT2EtOH (methyl, tallow, bis-2-hydroxyethyl, quaternary ammonium) organic modifier with 90 meq/100 g concentration, was used.

Two contents of solid particles (nano-clay or nano-silica) in each nanocomposite (5% and 10% by mass) were used. Initially, the amount of powder required to obtain a specific concentration was mixed with the corresponding neat resin. A drill mixer (300 to

450 rpm) was used for 3 min to uniformly disperse the powder in the primary mixture without visible agglomerates. This mixture was then ultrasonicated for an hour in an ultrasonic bath at 200 W and 60 kHz at lab ambient conditions to further disperse nanoparticles homogeneously in each coating. After curing of concrete, specimens from each mixture were air-dried for 48 h, and then coated with each nanocomposite. For silane/nanocomposites, concrete surface was brushed by three successive layers at a time-interval of 30 min, whereas for MMA/nanocomposites, two layers separated by 45 min were applied, as recommended by the respective manufacturers for neat resins. The performance of concrete coated with polymeric nanocomposites was compared to uncoated concrete and corresponding specimens coated with neat resins. After setting of coatings, coated specimens were cured for 7 days at 22±2ºC and RH ≥ 95% to allow for proper interaction of nanoparticles with substrate before exposure as most pozzolanic reactivity of nanoparticles has been found to occur within 7 days (Madani et al. 2012). Subsequently, the remaining excess coating on the surface after drying was abraded using a wire brush to simulate wearing induced by various sources such as traffic on concrete pavements/bridges.

7.3.2 Testing

7.3.2.1 Characterization of nanocomposites and concrete surface

Transmission electron microscopy (TEM) was performed on ultrathin film samples prepared from each ultrasonicated composite to investigate the dispersion quality. Also, a hardness tester fitted with Berkovitch probe (radius of 150 nm, angle of 142.35º) was used as means of nano-indentation and measuring the variation of paste hardness due to treatment. For tested points, a trapezoidal loading was applied such that load was increased to 1000 mN in 10 seconds, kept at 1000 mN for 10 seconds, and then decreased to zero in

10 seconds. Static contact angle measurements were performed on concrete samples using contact angle goniometer to evaluate the effect of coatings on the wettability of concrete surface. An angle (Θ) of 90^{o} is considered a threshold below which, a material is considered hydrophilic and above which, the material tends to hydrophobicity (Law and Zhao 2016). For each sample, five water drops were placed on separate spots over the surface at different *w/b* and the average contact angle was calculated.

Similar to Chapter 6, the penetrability of uncoated and coated concrete was assessed using rapid chloride penetration test (RCPT) as per ASTM C1202 (2019). In addition, absorption and desorption percentages were calculated for GU0.6 [worst quality] specimens to evaluate the effect of coatings on the rates of solution supply and evaporation.

7.3.2.2 Durability exposures

Exposure conditions for PSA and salt frost scaling were similar to those applied in Chapter 6 (refer to Section 6.3.2.2). In addition, another series of specimens were cracked before coating to simulate rehabilitation of existing/deteriorated concrete elements and verify performance of coatings. However, in the case of PSA, the procedure of repairing a damaged element starts with cleaning/removing the surface layer contaminated with salt followed by restoring the surface using a sound repair mortar, which is subsequently coated (Haynes 2012). This scenario resembles the application of coating on sound concrete surface; thus, for PSA, no cracked specimens were used as their performance is expected to be similar to that of sound specimens. Elements exposed to de-icing salts and salt-frost scaling (e.g. bridge decks) maybe regularly maintained through direct application of waterproofing liners (e.g. silane) and crack sealers (e.g. MMA), if existing scaling/wear is not significant (Oman 2014). Therefore, only this exposure was used for verification. For pre-cracked specimens, three parallel cracks were induced using a 0.5 mm saw blade at

approximately equal distance (62 mm). The middle crack extended to the mid-thickness of slabs (50 mm) to simulate deep cracks in concrete, while the other two cracks had a depth of 10 mm to represent shallower cracks. The crack thickness and depths were selected based on an analysis performed by the authors on cracked cores extracted from bridge decks in Winnipeg, Manitoba, which receive direct application of MMA coatings as a regular method of maintenance.

7.3.2.3 Microstructural analysis

The modification of concrete surface due to coatings and degradation mechanisms of specimens due to exposures were studied by mineralogical, thermal, and microscopy analyses (refer to Section 3.3.3).

7.4 Results

7.4.1 Transmission Electron Microscopy (TEM)

TEM observations were used to qualitatively evaluate dispersion of nanoparticles in the base polymers. Figure 7.1 shows exemplar TEM images of the nanocomposites at 5% loading ratio. Nano-clay particles appeared as meshing lines and were homogeneously dispersed in silane and MMA [Figs. 7.1a,b]. The resulting morphology of nano-clay based composites indicated the formation of exfoliated sheets in addition to some intercalated stacks of nanoparticles; also, it appeared that nano-clay tended to be more intercalated in case of MMA. The formed interwoven structure might contribute to enhanced barrier properties of the nano-clay composites. Regarding nano-silica, Figure 1c shows that spherical SiO_2 particles were well distributed in silane with an average particle size of 20 nm. In MMA, nano-silica did not retain its spherical morphology; the particles tended to

disperse into MMA appearing like an irregularly shaped, but a coherent component of the matrix [Fig 7.1d].

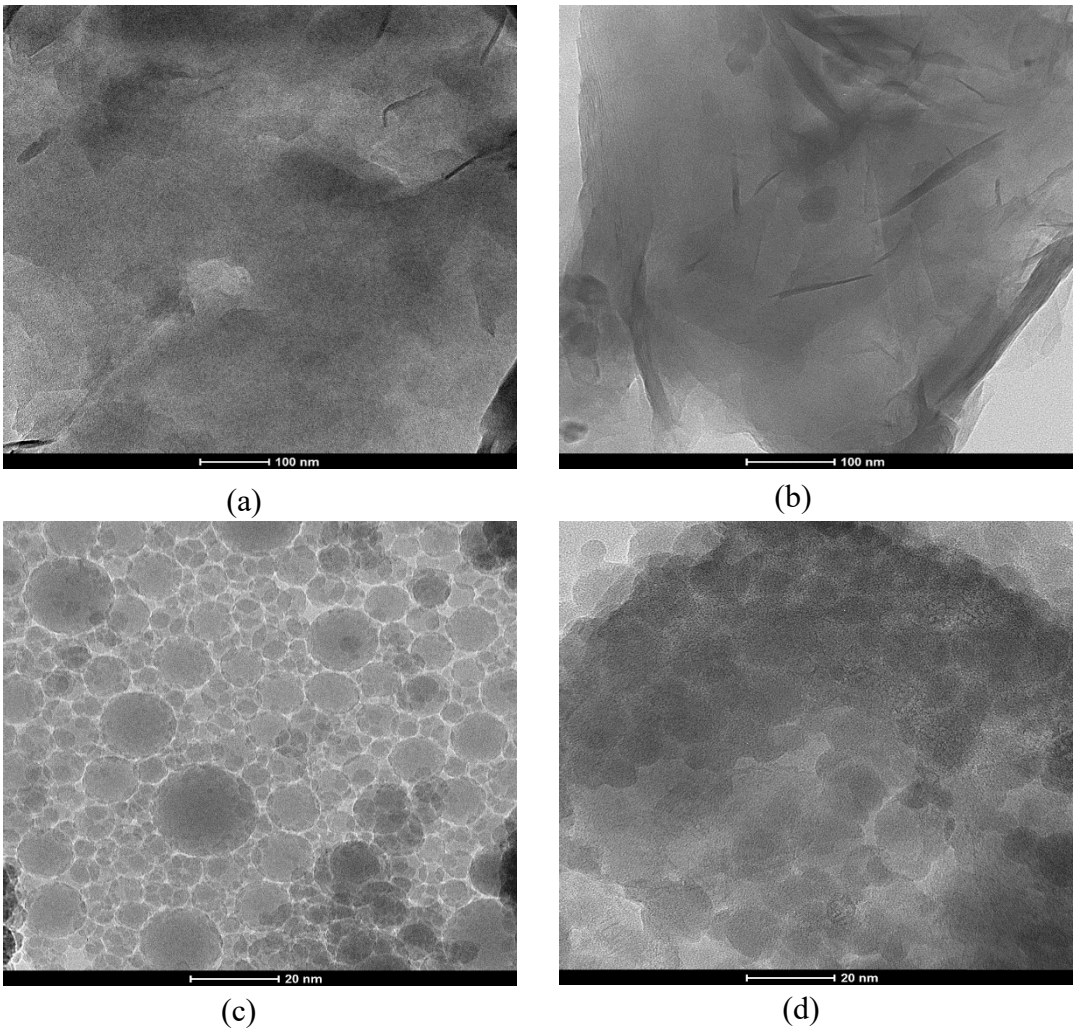

(a) (b)

(c) (d)

Figure 7.1: Exemplar TEM images of: (a) silane/nano-clay, (b) MMA/nano-clay, (c) silane/nano-silica, and (d) MMA/nano-silica composites at 5% concentration.

7.4.2 Contact Angle Measurements

Contact angle is a function of the surface tension of liquid and surface energy of the contact surface (determined by its roughness and heterogeneity); a stronger interface between liquid and solid than surface tension produces low contact angle, and vice versa (Chau et al. 2009). Contact angles were measured to determine the effect of surface treatment on hydrophobicity (ability to repel water) of concrete surface. Water droplets roll easily on hydrophobic surfaces, retaining their spherical shape. In contrast, on hydrophilic surfaces,

the water droplets tend to spread out. Uncoated concrete made with *w/b* of 0.60 and 0.40 had zero contact angle indicating a highly hydrophilic tendency. The application of coatings increased the contact angle of concrete and caused the droplets to become more rounded on the surface, as depicted in Fig. 7.2.

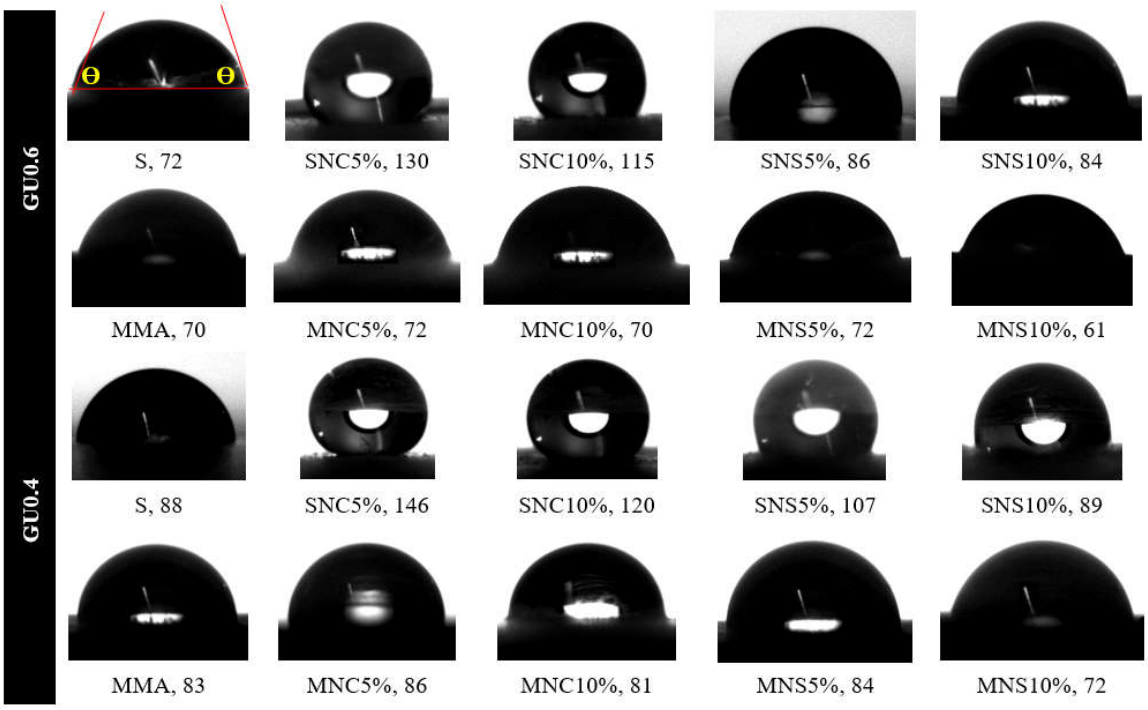

Figure 7.2: Contact angles (degrees) of concrete coated with various nanocomposites at different *w/b*.

Regardless of the type of base resin and nanoparticles, decreasing the *w/b* from 0.60 to 0.40 enhanced the water repellency of a coated surface, i.e. higher contact angles; accordingly, the ranges of contact angles were 61 to 130° and 72 to 46° for concrete with *w/b* of 0.60 and 0.40, respectively. Concrete coated with silane (hydrophobic agent) showed capability for water repellency compared to uncoated concrete; GU0.6 and GU0.4 specimens coated with neat silane had contact angles of 72° and 88°, respectively. However, the application of silane did not change the condition of surface to fully hydrophobic as Θ was less than 90°. Addition of nanoparticles to silane significantly

enhanced the hydrophobic nature of concrete surface. For instance, at *w/b* of 0.60, mixing 5% nano-clay with silane remarkably increased the contact angle to 130^{o} (81% higher than that of neat silane). Comparatively, 5% nano-silica (SNS5%) moderately increased the contact angle of that same concrete by 20% compared to plain silane. For both types of nanoparticles, increasing the dosage in silane to 10% led to reduction of contact angle, possibly due to the tendency of nanoparticles to agglomerate at higher dosages, and thus not homogeneously covering the surface of concrete; yet, the values were still higher than that of neat silane.

MMA is not a hydrophobic agent; it rather acts as pore filler/sealer for concrete surface. Correspondingly, GU0.6 and GU0.4 specimens coated with neat MMA had contact angles less than 90^{o}. The incorporation of nanoparticles into MMA was not as effective as silane at increasing the hydrophobicity of concrete as contact angles obtained for MMA/nanocomposites were comparable to that of neat MMA. For example, GU0.6 specimens coated with MNC5% and MNC10% had a contact angle of 72^{o}, which is 3% higher than the angle for MMA. For GU0.6 specimens, the use of 5% nano-silica with MMA showed similar hydrophobic nature to MMA; however, using MNS10% led to 13% lower contact angle relative to neat MMA. It should be noted that the contact angle is indicative of the surface nature (hydrophobic vs. hydrophilic), and whether a droplet would be retained on or readily penetrate into the surface depends on its absorption capacity (Weisheit et al. 2016). Thus, the fluid transport properties of a coated surface need to be determined.

7.4.3 Transport Properties

7.4.3.1 Rapid chloride penetrability test (RCPT)

The passing charges from RCPT are listed in Table 7.2 with corresponding penetration depths in uncoated and coated specimens. Also, the chloride migration coefficients were calculated based on the penetration depths according to NT BUILD 492 (1999) to provide a uniform basis of comparison considering cells that stopped before the completion of testing due to overheating caused by the Joule effect. The penetration depths and migration coefficients were directly proportional to passing charges. For uncoated and coated concrete, decreasing the *w/b* resulted in lower penetration depths/migration coefficients regardless of the type of polymer and nanoparticles, which complies with the well-known effect of *w/b* on the penetrability of concrete (Mehta and Monteiro 2014).

Table 7.1: RCPT results for uncoated and coated specimens

Coating ID	Mixtures					
	GU0.6			GU0.4		
	Passing Charges (coulombs)	**Penetration Depth (mm)**	**Migration Coefficient ($\times 10^{-12}$ m^2/s)**	**Passing Charges (coulombs)**	**Penetration Depth (mm)**	**Migration Coefficient ($\times 10^{-12}$ m^2/s)**
Uncoated	OVF*	50	97.28	4015	23	20.93
S	1788	13.2	11.50	963	6.5	5.33
MMA	2981	19.5	17.50	1785	13.6	11.87
SNC5%	832	6	4.88	425	4	3.12
SNC10%	785	6	4.86	488	4.6	3.64
SNS5%	1012	8.5	7.14	466	4.2	3.29
SNS10%	1530	13	11.30	609	5.5	4.44
MNC5%	993	8	6.68	569	5	4.00
MNC10%	1025	8	6.70	826	7	5.78
MNS5%	1168	10	8.50	761	5.8	4.70
MNS10%	2661	17	15.10	1542	12	10.38

*OVF stands for "overflow" which led to termination of the RCPT cell before 6 h

Coating specimens with neat silane significantly reduced the penetrability of concrete compared to untreated specimens (Table 7.1). For example, GU0.6 specimens

coated with silane had a migration coefficient of 11.50×10^{-12} m^2/s, compared to 97.28×10^{-12} m^2/s for uncoated concrete (i.e. 88% reduction). The addition of nanoparticles to silane further reduced the transport properties of concrete. For example, GU0.6 specimens coated with SNC5% had passing charges of 832 coulombs and low migration coefficient of 4.88×10^{-12} m^2/s which correspond to 53% and 58% reduction, respectively, relative to that of neat silane. This was substantiated by the analysis of variance (ANOVA) [Table 7.2] at a significance level (α) of 0.05 which showed that coating with SNC5% relative to neat silane gave an *F*-value of 63.25 compared to a critical threshold (F_{cr}) of 18.51, indicating a statistically significant effect on the migration coefficients (Montgomery 2014). Conjugate specimens coated with higher dosage of nano-clay (10%) showed comparable results to that obtained for SNC5% specimens, without statistical significance (Table 7.2). The use of nano-silica with silane led to more reduction in penetrability compared to neat resin, yet to a lesser degree than nano-clay. For example, GU0.6 specimens coated with SNS5% gave 22% and 46% higher passing charges and migration coefficient, respectively, than that of SNC5%. However, the effect of nanoparticles type at dosage of 5% was statistically insignificant [*F*-value of 12.77 relative to F_{cr} of 18.51 (Table 7.2)]. SNS10% resulted in insignificant reduction in penetrability compared to silane as the migration coefficient for GU0.6 concrete coated with this nanocomposite was only 2% lower than that of specimens coated with neat silane.

The MMA-based coatings reduced the penetrability of concrete; however, the degree enhancement was lower than that imparted by silane-based coatings. Specimens coated with plain MMA had a migration coefficient of 17.50×10^{-12} m^2/s, compared to 97.28×10^{-12} m^2/s for uncoated specimens (82% reduction). Similar to silane/nanocomposites, adding nanoparticles to MMA enhanced the resistance of concrete

Table 7.2: Example of analysis of variance (ANOVA) for the results of GU0.6 specimens

Parameter	Migration coefficient		Absorption		Desorption		PSA mass loss		Frost scaling mass loss	
	F	F_{cr}	***F***	F_{cr}	***F***	F_{cr}	***F***	F_{cr}	***F***	F_{cr}
Type of coating										
Uncoated vs. S	1309*	18.51	105.26*	18.51	60.29*	18.51	16.21*	7.70	331.63*	18.51
Uncoated vs. MMA	1168*	18.51	33.35*	18.51	111.20*	18.51	38.17*	7.70	147.58*	18.51
S vs. MMA	53.53*	18.51	64.69*	18.51	0.36	18.51	3.06	7.70	34.74*	18.51
Type of nanoparticles										
SNC5% vs. SNS5%	12.77	18.51	2.59	18.51	13.88	18.51	2.49	7.70	--	18.51
SNC10% vs. SNS10%	70*	18.51	5.89	18.51	29.78*	18.51	4.55	7.70	13	18.51
MNC5% vs. MNS5%	9.40	18.51	2.84	18.51	0.45	18.51	1.05	7.70	0.31	18.51
MNC10% vs. MNS10%	256.30*	18.51	10.68	18.51	0.46	18.51	24.32*	7.70	39*	18.51
Dosage										
S vs. SNC5%	63.25*	18.51	17.44	18.51	13.09	18.51	54.91*	7.70	214.74*	18.51
SNC5% vs. SNC10%	0.001	18.51	1.20	18.51	8	18.51	0.19	7.70	--	18.51
S vs. SNS5%	34.43*	18.51	7.60	18.51	5.40	18.51	52.23*	7.70	214.74*	18.51
SNS5% vs. SNS10%	29.23*	18.51	1.80	18.51	9.45	18.51	2.12	7.70	13	18.51
MMA vs. MNC5%	333.21*	18.51	60.32*	18.51	70.62*	18.51	41.71*	7.70	11.45	18.51
MNC5% vs. MNC10%	0.003	18.51	1.48	18.51	3.38	18.51	1.48	7.70	1.97	18.51
MMA vs. MNS5%	162*	18.51	66.01*	18.51	14.11	18.51	161.54*	7.70	5.54	18.51
MNS5% vs. MNS10%	100.16*	18.51	13.36	18.51	0.89	18.51	17.26*	7.70	42.14*	18.51

*Denotes statistical significance

to penetration of fluids compared to neat MMA, with nano-clay performing better than nano-silica. For instance, GU0.6 specimens coated with MNC5% had passing charges and migration coefficient of 993 coulombs and 6.68×10^{-12} m^2/s, respectively (i.e. reduction of 67% and 62%, respectively, relative to that of neat MMA). Conjugate specimens coated with MNC10% yielded similar results to MNC5%, without statistical significance (Table 7.2). The use of nano-silica resulted in higher penetrability compared to nano-clay. For example, application of MNS5% on concrete with *w/b* of 0.60 had 18% and 27% higher passing charge and migration coefficient, respectively, relative to that of MNC5%. Nevertheless, ANOVA showed that the type of nanoparticles mixed with MMA at 5% dosage had insignificant effect on the migration coefficient results (F-value of 9.40 compared to F_{cr} of 18.51, Table 7.2). Using nano-silica at 10% in MMA caused significantly higher penetrability compared to MNS5%, which was also confirmed by ANOVA (Table 7.2).

7.4.3.2 Absorption/desorption

Absorption and desorption (evaporation) tests were performed to assess the ability of coatings to control the transport of fluids into and out of concrete (Table 7.3). The test was conducted on GU0.6 specimens as they represent the worst-quality (coarse microstructure) concrete as indicated by the RCPT results (Table 7.1). Uncoated concrete exhibited the highest ratios of absorption and desorption (+7.03% and -3.22%, respectively). Conforming to the results of RCPT, the application of neat silane to concrete gave considerably low absorption and desorption ratios of +1.35% and -1.78%, respectively (reduction of 81% and 45%, respectively, compared to that of reference concrete). For the silane/nanocomposites, mixing silane with 5% nano-clay showed the lowest absorption and desorption values of +0.65% and -0.77%, respectively. Using nano-silica at the same

dosage (5%) with silane led to slightly higher transport properties than that of nano-clay with absorption and desorption values of +0.83% and -0.96%, respectively. Thus, the effect of changing the type of nanoparticles at a dosage of 5% was insignificant as shown by ANOVA (F-values of 2.59 and 13.88, compared to F_{cr} of 18.51, for absorption and desorption, respectively, Table 7.2). For both nano-clay and nano-silica, higher dosages (10%) slightly increased the absorption and desorption ratios of concrete, without statistical significance.

Table 7.3: Absorption and desorption of GU0.6 specimens

Specimen	Absorption* (%)		Desorption* (%)	
Uncoated	7.03	[0.53]	-3.22	[0.18]
S	1.35	[0.16]	-1.78	[0.07]
MMA	3.67	[0.24]	-1.25	[0.05]
SNC5%	0.65	[0.05]	-0.77	[0.01]
SNC10%	0.75	[0.05]	-0.81	[0.01]
SNS5%	0.83	[0.10]	-0.96	[0.05]
SNS10%	1.05	[0.13]	-1.25	[0.08]
MNC5%	1.34	[0.18]	-0.77	[0.03]
MNC10%	1.65	[0.18]	-0.90	[0.07]
MNS5%	1.66	[0.06]	-0.83	[0.10]
MNS10%	2.85	[0.32]	-1.05	[0.21]

*Values between brackets are standard deviations

Similar to silane, specimens coated with MMA significantly decreased the absorption and desorption ratios of concrete to +3.67% and -1.25%, respectively (reduction of 48% and 61%, respectively, compared to that of uncoated concrete). Compared to the corresponding silane/nanocomposite, MMA/nanocomposites led to relatively higher absorption of fluids into concrete, but lower desorption in most cases. However, ANOVA showed a significant effect for changing the type of coating in only the case of absorption (Table 7.2). Incorporating nano-clay with MMA at a dosage of 5% further decreased the absorption and desorption ratios of concrete by 63% and 39%, respectively, compared to that of specimens coated with MMA. In comparison, coatings synthesized with MMA and

nano-silica led to higher absorption/desorption values; for instance, the ratios for MNS5% were +1.66% (24% more absorption than MNC5%) and -0.83% (10% more desorption than MNC5%), respectively, without statistical significance. Similar to silane/composites, higher dosages of nanoparticles (10%) with MMA increased the absorption and desorption of concrete, without statistical significance (Table 7.2).

7.4.4 Exposure Results

7.4.4.1 Physical salt attack (PSA)

Figures 7.3 and 7.4 show examples of the condition of uncoated and coated concrete cylinders made with *w/b* of 0.60 along with visual ratings. Also, the variation in mass during exposure is shown in Table 7.4. For uncoated concrete, salt deposits accumulated on the evaporative surfaces of specimens followed by progressive surface scaling just above the solution level propagating upwards causing concrete spalling and reduction of cross-section. The extent of damage depended on the *w/b* such that higher *w/b* led to severe scaling; GU0.6 specimens fractured after 105 cycles with a mass loss of 27%, while GU0.4 specimens had a final mass loss of 9% after 120 cycles. For all coatings, their application on higher quality concrete (*w/b* of 0.40) resulted in highly resistant specimens to PSA, which highlights the key effect of *w/b* on the performance of concrete.

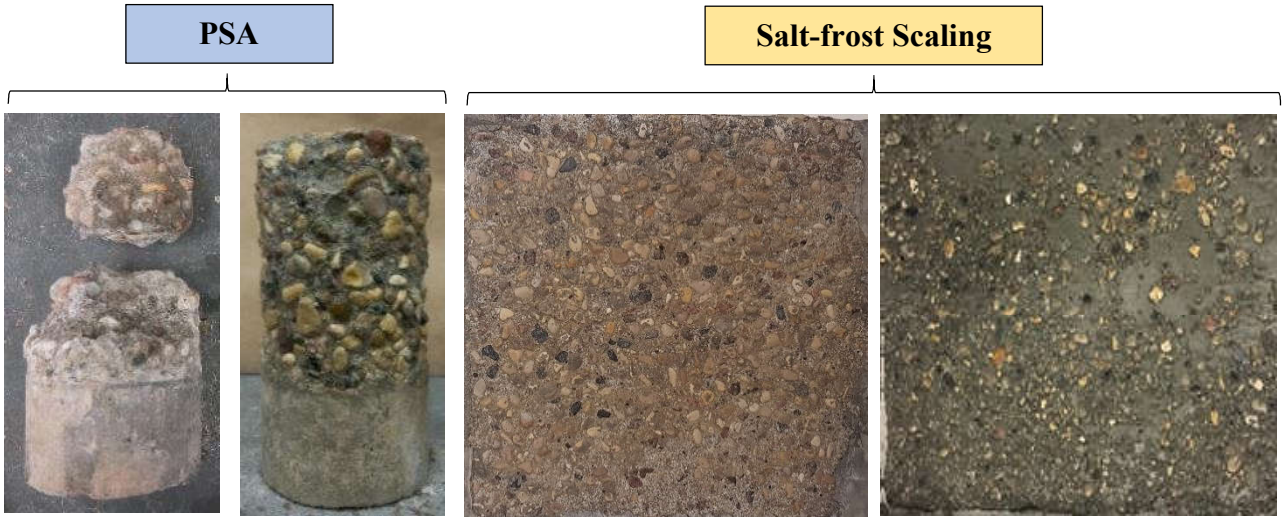

Figure 7.3: Uncoated specimens at the end of the PSA and salt-frost scaling exposures. (Note: numbers between brackets are the final visual ratings and number of cycles at failure, respectively, if applicable)

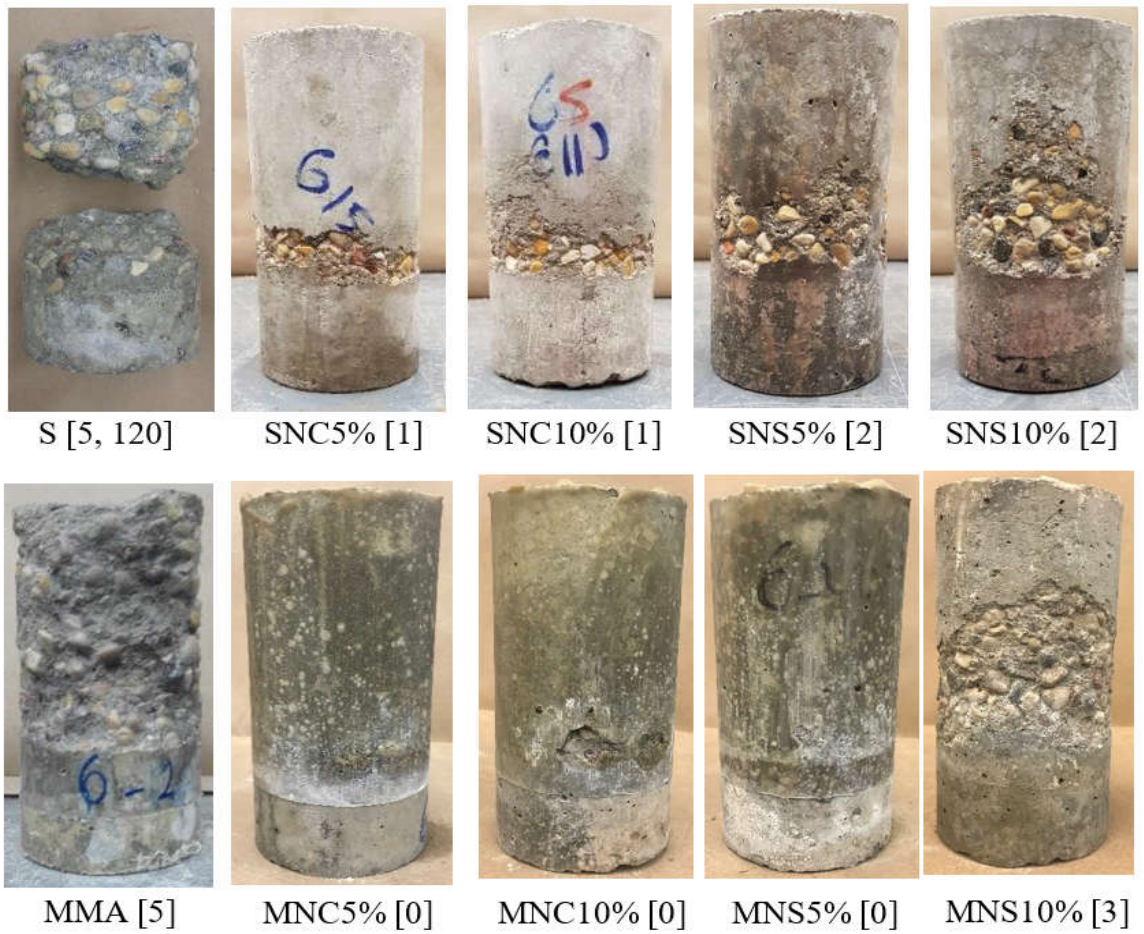

Figure 7.4: GU0.6 coated specimens at the end of PSA exposure. (Note: numbers between brackets are the final visual ratings and number of cycles at failure, respectively, if applicable)

GU0.6 specimens coated with neat silane, although had lower final mass losses compared with that of uncoated concrete, were inadequate to protect concrete as specimens severely deteriorated (mass loss of 15%) and fractured due to PSA. Silane/nano-clay composites substantially improved the concrete resistance to PSA. GU0.6 specimens coated with SNC5% and SNC10% experienced minor scaling within 20 mm above the solution level (visual rating of 1); their mass losses were 0.4% and 0.6%, respectively. Comparatively, incorporating nano-silica with silane resulted in slightly higher surface scaling (visual rating of 2) and mass losses (0.8% and 1.3% for SNS5% and SNS10%, respectively) compared to SNC composites at similar nanoparticles dosage. ANOVA for the mass loss results confirmed that coating specimens with SNC5% and SNS5% had a statistically significant effect on the average results compared with silane [F-values of 54.9 and 52, respectively, relative to F_{cr} of 7.70] (Table 7.2). However, the F-values for changing the type or increasing the dosage of nanoparticles were insignificant (Table 7.2).

Regarding MMA-based coatings, the neat resin failed to protect concrete against PSA as the coated crust detached from surface during exposure causing scaling to progress to underlying concrete (final mass loss of 11%). On contrary, GU0.6 specimens coated with MMA mixed with nano-clay (5% and 10%) showed superior resistance to PSA with no visual damage or mass loss; specimens gained slight mass at the end of exposure due to absorption of salt solution. Table 7.2 shows the significant effect of using MNC compared to neat MMA. Using 5% nano-silica showed the same high resistance to PSA as MNC5%; however, specimens coated with MNS10% had a final mass loss of 3% suggesting the adverse effect of higher dosages of nano-silica on the resistance of concrete to PSA.

Table 7.4: Variation of mass (%) of uncoated and coated specimens in the PSA exposure

Mixture ID.	Days/Cycles							
	30		60		90		120	
	GU0.6							
Uncoated	-1.25	[0.27]	-3.87	[0.91]	-16.38	[1.45]	-26.87[1]	[2.05]
S	+0.47	[0]	-1.21	[0.08]	-5.70	[1.39]	-15.34[2]	[2.00]
MMA	+0.34	[0.22]	-0.56	[0.30]	-5.20	[1.00]	-10.88	[1.57]
SNC5%	+0.30	[0.08]	+0.11	[0.05]	-0.24	[0.10]	-0.45	[0.18]
SNC10%	+0.24	[0.19]	+0.15	[0.10]	-0.33	[0.10]	-0.58	[0.21]
SNS5%	+0.35	[0.10]	+0.06	[0]	-0.50	[0.19]	-0.84	[0.16]
SNS10%	+0.26	[0.07]	-0.48	[0.20]	-1.03	[0.16]	-1.26	[0.24]
MNC5%	+0.19	[0.13]	+0.44	[0.06]	+0.48	[0.05]	+0.63	[0.15]
MNC10%	+0.22	[0.11]	+0.20	[0.08]	+0.23	[0.30]	+0.38	[0.14]
MNS5%	+0.32	[0.11]	+0.60	[0.32]	+0.72	[0.15]	+0.80	[0.07]
MNS10%	+0.40	[0.19]	-1.23	[0.34]	-2.19	[0.39]	-2.61	[0.43]
	GU0.4							
Uncoated	+0.30	[0.30]	-0.84	[0.15]	-4.28	[0.70]	-8.64	[1.63]
S	+0.20	[0.10]	+0.30	[0.43]	-0.22	[0.07]	-0.50	[0.15]
MMA	+0.20	[0.03]	+0.32	[0.03]	+0.40	[0.07]	+0.50	[0.03]
SNC5%	+0.20	[0.05]	+0.23	[0.08]	+0.42	[0.15]	+0.40	[0.11]
SNC10%	+0.15	[0.10]	+0.32	[0.03]	+0.32	[0.09]	+0.38	[0.16]
SNS5%	+0.35	[0.08]	+0.40	[0.03]	+0.40	[0.20]	+0.43	[0.20]
SNS10%	+0.16	[0.10]	+0.16	[0.16]	+0.41	[0.10]	+0.58	[0.20]
MNC5%	+0.32	[0.05]	+0.30	[0.09]	+0.19	[0.10]	+0.26	[0.12]
MNC10%	+0.14	[0]	+0.28	[0.16]	+0.30	[0.04]	+0.30	[0]
MNS5%	+0.20	[0.15]	+0.28	[0.05]	+0.23	[0.16]	+0.48	[0.08]
MNS10%	+0.19	[0.15]	+0.34	[0.14]	+0.50	[0.22]	+0.50	[0.11]

(-) refers to mass loss and (+) refers to mass gain
Values between brackets refer to standard deviations
[1,2] Refers to mass loss at 105 and 120 cycles, respectively when specimens were fractured

7.4.4.2 Salt-frost scaling of uncracked and pre-cracked concrete

The visual conditions/ratings of uncoated and coated sound concrete after 50 cycles of freezing/thawing combined with de-icing salts are shown in Figures 7.3 and 7.5. Also, variation of cumulative mass of scaled material is given in Table 7.5. All specimens (coated or uncoated) made with lower *w/b* had better visual condition and less cumulative mass loss. For example, uncoated GU0.6 and GU0.4 specimens had a visual rating of 5 and 2, with corresponding final mass losses of 1175 and 192 g/m^2, respectively. The application of neat silane on GU0.6 specimens significantly reduced the mass loss of GU0.6 specimens

by 67% relative to reference concrete. Conforming to PSA results, the application of silane/nano-clay composites resulted in excellent resistance of concrete to salt-frost scaling; nil mass loss was obtained for GU0.6 specimens coated with SNC5% and SNC10%. Using nano-silica at 5% dosage resulted in the same superior performance as nano-clay; however, increasing the dosage of nano-silica to 10% resulted in slightly increasing the visual rating to 1 with a final mass loss of 65 g/m^2. ANOVA (Table 7.2) showed that using SNC5% and SNS5% had a significant effect on the scaled mass results compared to neat silane (F-value of 214.7 compared to F_{cr} of 7.70). Also, the increase in dosage of nano-clay and nano-silica did not yield a significant difference in results (Table 7.2).

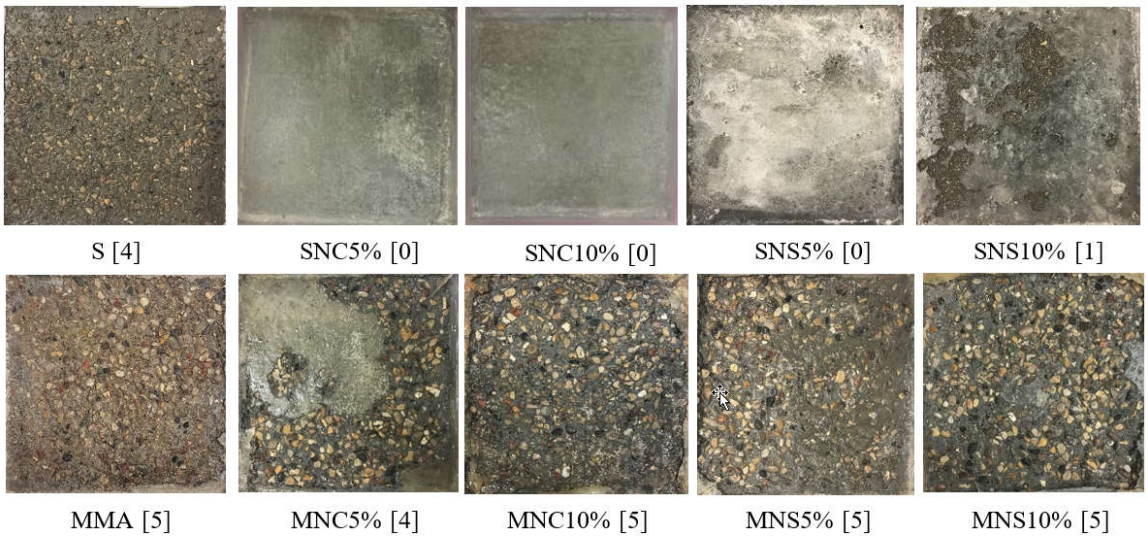

Figure 7.5: Exemplar coated specimens (GU0.6) at the end of the salt-frost scaling exposure. (Note: numbers between brackets are the final visual ratings)

On contrary to the PSA exposure, MMA-based coatings (neat or mixed with nanoparticles) failed to protect concrete with high *w/b* in this exposure. GU0.6 specimens coated with MMA had a final visual rating of 5 and experienced a mass loss of 615 g/m^2. The addition of nano-clay to MMA moderately enhanced the resistance to salt-frost scaling. The cumulative masses of MNC5% and MNC10% specimens were 503 and 542 g/m^2,

respectively (visual ratings of 4 and 5, respectively), indicating 18% and 12% less mass loss, compared to neat MMA. Similarly, using 5% nano-silica led to a reduction of scaled mass by 16% compared to plain MMA; thus, ANOVA showed insignificant effect for changing the type of nanoparticles at 5% concentration. MNS10% increased the final mass loss to 782 g/m^2 compared to 615 g/m^2 for MMA, but the effect of nanoparticles addition to MMA was still statistically insignificant as shown in Table 7.2. Ministry of Transportation of Ontario (MTO) (2018) and Bureau du normalization du Quebec (BNQ) (2002) specify a failure limit for the salt-frost scaling test of 800 and 500 g/m^2, respectively,

Table 7.5: Variation of cumulative scaled mass (g/m^2) of specimens during the salt-frost scaling exposure

Mixture ID.	**Days/Cycles**							
	10		**25**		**35**		**50**	
	GU0.6							
Uncoated	292	[7]	725	[21]	945	[16]	1175	[35]
S	25	[3]	185	[9]	256	[9]	381	[26]
MMA	60	[3]	290	[12]	421	[15]	615	[30]
SNC5%	0	[0]	0	[0]	0	[0]	0	[0]
SNC10%	0	[0]	0	[0]	0	[0]	0	[0]
SNS5%	0	[0]	0	[0]	0	[0]	0	[0]
SNS10%	0	[0]	15	[4]	43	[8]	65	[18]
MNC5%	0	[0]	250	[10]	392	[10]	503	[14]
MNC10%	0	[0]	280	[8]	402	[15]	542	[24]
MNS5%	0	[0]	261	[13]	390	[20]	520	[27]
MNS10%	90	[5]	350	[14]	533	[22]	782	[30]
	GU0.4							
Uncoated	24	[3]	54	[3]	106	[8]	192	[13]
S	0	[0]	0	[0]	0	[0]	0	[0]
MMA	0	[0]	22	[1]	39	[5]	64	[7]
SNC5%	0	[0]	0	[0]	0	[0]	0	[0]
SNC10%	0	[0]	0	[0]	0	[0]	0	[0]
SNS5%	0	[0]	0	[0]	0	[0]	0	[0]
SNS10%	0	[0]	0	[0]	0	[0]	0	[0]
MNC5%	0	[0]	0	[0]	0	[0]	0	[0]
MNC10%	0	[0]	0	[0]	0	[0]	0	[0]
MNS5%	0	[0]	0	[0]	0	[0]	0	[0]
MNS10%	0	[0]	0	[0]	23	[4]	40	[6]

Values between brackets refer to standard deviations

using a less aggressive solution of 3% sodium chloride. Accordingly, all specimens coated with silane-based coatings can be considered resistant to salt-frost scaling, whereas for MMA composites, all coatings failed only the BNQ criterion.

Figure 7.6 shows the conditions of uncoated and coated pre-cracked GU0.6 specimens after exposure to salt-frost scaling to verify the performance of nanocomposites. Also, Figure 7.7 summarizes the corresponding mass loss of pre-cracked specimens. Similar to the trends obtained for sound/uncracked concrete, silane/nanocomposites (SNC and SNS) were effective at eliminating the surface scaling caused by F/T cycles and de-icing salt as indicated by the nil mass loss in most cases. On contrary, MMA/nanocomposites were ineffective at protecting pre-cracked concrete in this exposure, which conforms to the trends for uncracked concrete.

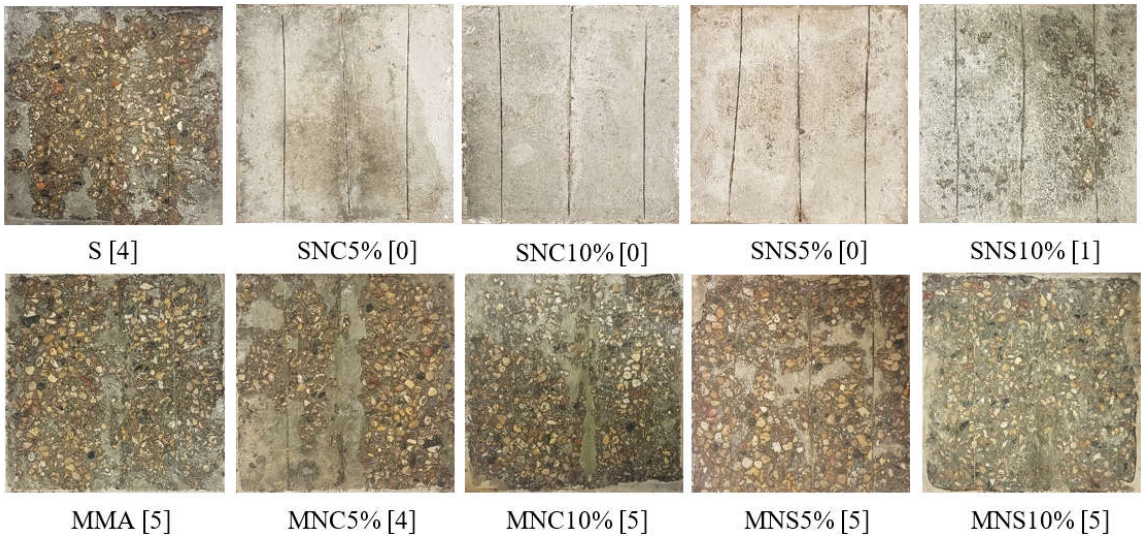

Figure 7.6: Pre-cracked GU0.6 specimens at the end of the salt-frost scaling exposure. (Note: numbers between brackets are the final visual ratings)

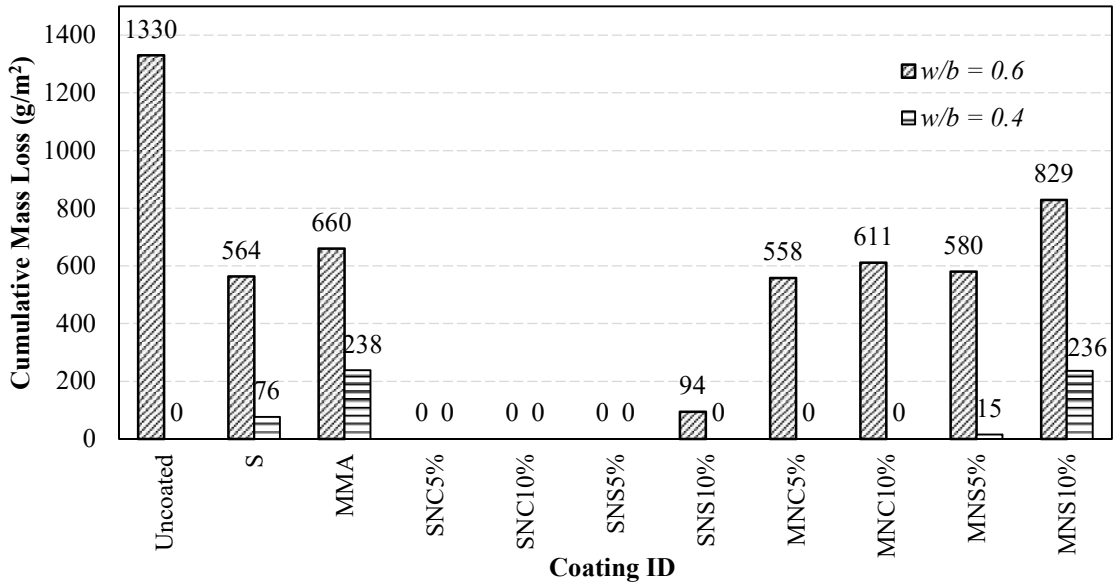

Figure 7.7: Final cumulative mass of pre-cracked specimens after the salt-frost scaling exposure. (Note: "0" refers to nil mass loss)

7.5 Discussion

7.5.1 Effect of Water-to-binder Ratio

Generally, the effect of *w/b* complied with the results reported in previous studies for the positive effect of *w/b* reduction on concrete durability (ACI 201.2R 2016; Bassuoni and Rahman 2016). The *w/b* was a key factor at improving the resistance of uncoated and coated concrete to the applied exposures. In case of PSA, XRD analysis on samples obtained from the evaporative front of uncoated specimens showed more intense peaks of thenardite (Na_2SO_4) in GU0.6 specimens compared to that in the GU0.4 specimens (Fig 7.8), highlighting the improved performance of concrete under PSA as *w/b* is reduced. The massive deposition of sodium sulfate crystals beneath the surface layer (sub-florescence) was responsible for its detachment as shown by the SEM images of the inner side of detached crust from uncoated GU0.6 specimens (Fig 7.9a). Similarly, in case of salt-frost scaling, XRD analysis (Fig 7.8) showed frequent occurrence of calcium chloride ($CaCl_2$)

crystals beneath the scaled layer of uncoated GU0.6 specimens, which was also confirmed by SEM (Fig 7.9b). In comparison, the peaks of $CaCl_2$ were less intense in the surface of GU0.4 specimens. The crystallization process of de-icing salts within the surface layer of concrete after its saturation with a salt solution is considered a primary process of salt-frost scaling of concrete (Scherer 2004).

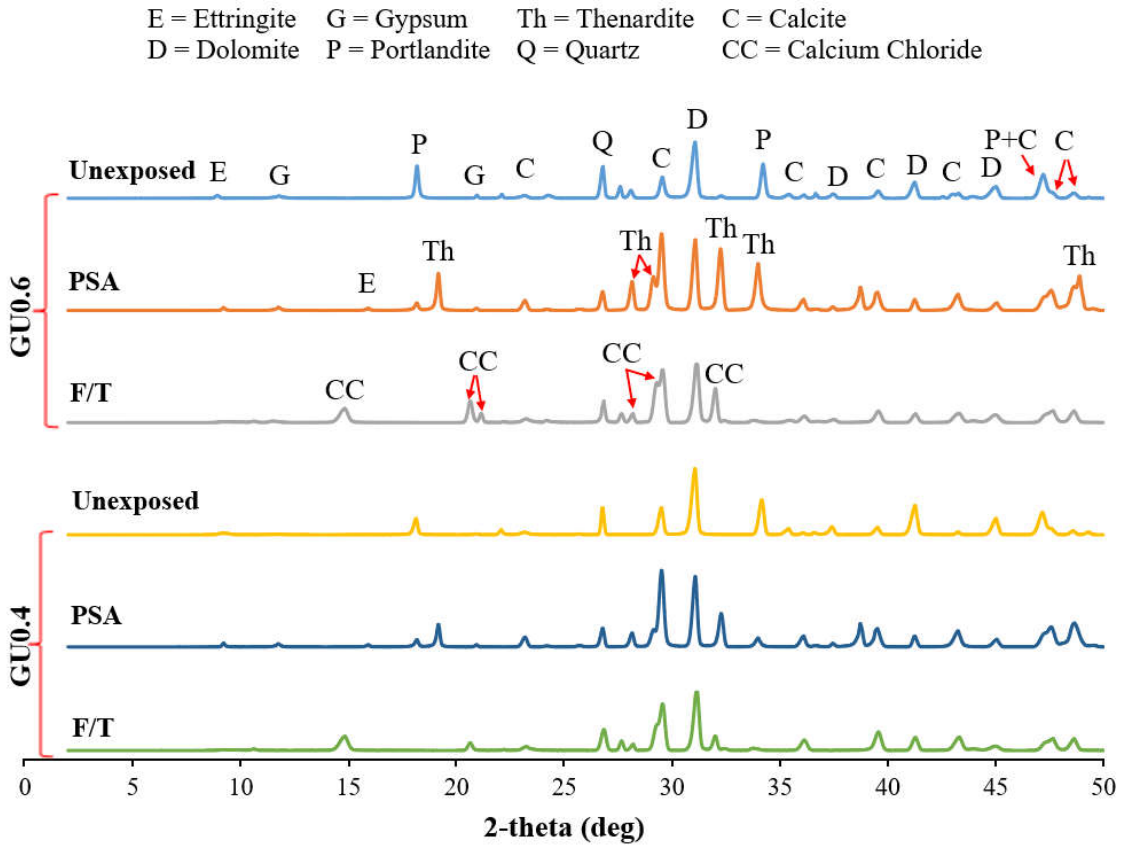

Figure 7.8: XRD of samples extracted from uncoated GU0.6 and GU0.4 specimens.

According to the results of fluid transport tests, high *w/b* led to concrete with more porosity and continuous pore structure, which would affect the process of damage. For PSA, *w/b* reduction led to discounting the rates of absorption/desorption of sodium sulfate solution, which caused lower rate of solution uptake and evaporation, decreased amount of crystallizing salt, and consequently less surface scaling of concrete. Regarding salt-frost scaling, the denser microstructure obtained for lower *w/b* (as shown by the reduced

penetration depth of chloride ions) decreased the ingress of calcium chloride into concrete making specimens less susceptible to critical saturation and subsequent crystallization and scaling. In addition, the densification of microstructure caused by reducing *w/b* improved the performance of applied coatings, likely due to harder absorption of coatings into the pore network, i.e. precipitation of higher proportion of coatings on concrete surface and retention within surface pores, and consequently better sealing, as shown by contact angle, RCPT and absorption/desorption tests (Bader et al. 2017). The influence of *w/b* in case of different coatings is discussed in the subsequent sections.

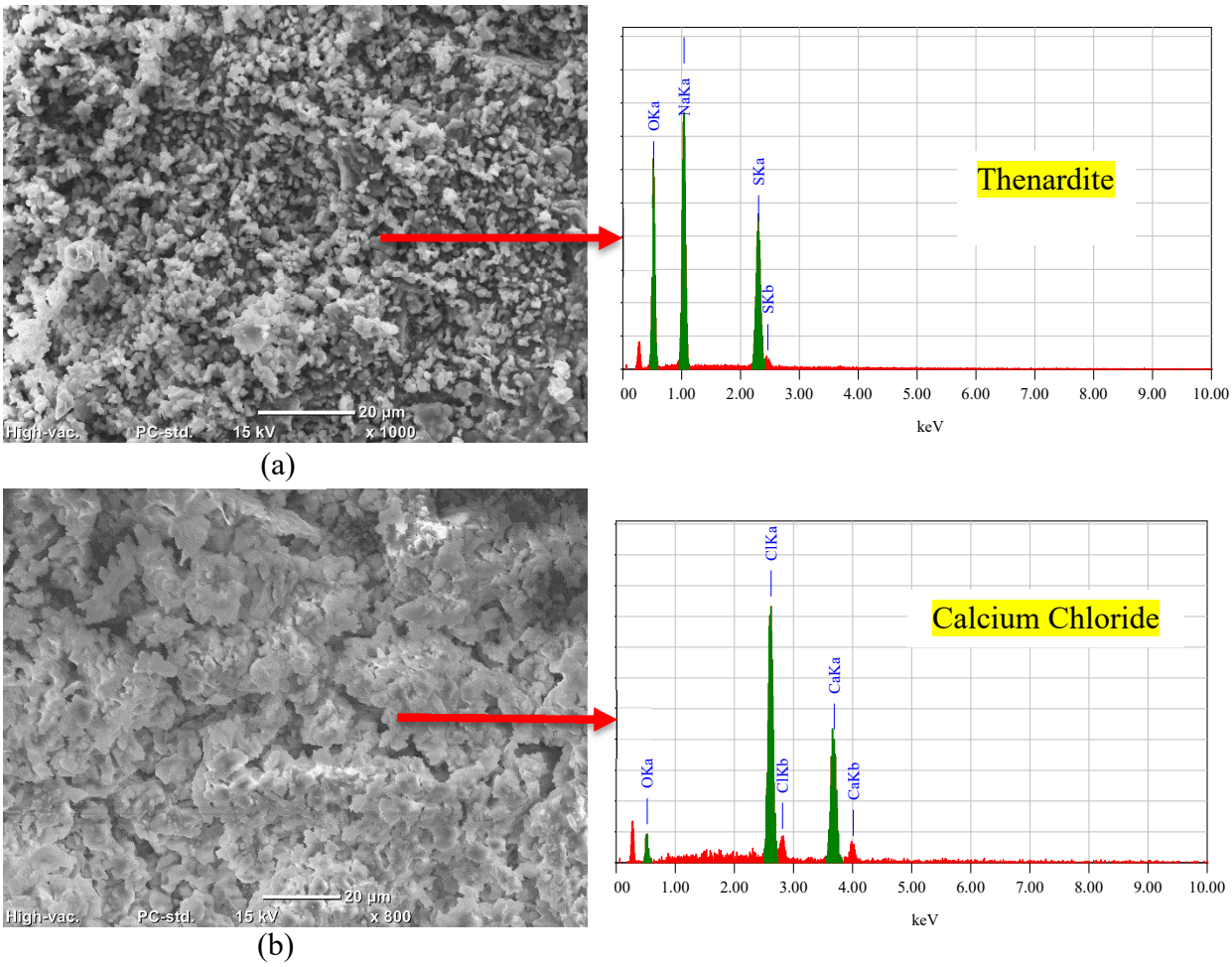

Figure 7.9: SEM and EDX of scaled concrete layer from GU0.6 specimens exposed to: (a) PSA, and (b) salt-frost scaling.

7.5.2 Silane/nanocomposites

Although neat silane showed some improvement to the resistance of concrete to PSA and salt-frost scaling, it did not fully protect concrete from distress induced by these damage mechanisms. In Chapter 5, the inadequacy of silane for application in case of PSA was attributed to its breathability, which allowed for higher evaporation rate than that of absorption (continuous wicking of salt solution into concrete surface); thus, progressive salt crystallization pressure disrupted the surface of concrete. Regarding salt-frost scaling, RCPT and absorption results implicated that silane coated concrete could still allow sufficient amount of salt solution to cumulatively build up in the surface, followed by subsequent crystallization and scaling. While the mass losses of silane-coated specimens were below the failure limits of MTO and BNQ in uncracked specimens, they failed the BNQ limit in the case of GU0.6 pre-cracked specimens (Fig 7.7). Comparatively, all silane/nanocomposites were more successful to protect concrete subjected to conditions stimulating PSA and salt-frost scaling (uncracked and pre-cracked) regardless of the *w/b* as similar trends were obtained for the GU0.6 and GU0.4 specimens in terms of reduced transport properties and mass loss of concrete in these exposures. For both nano-clay and nano-silica, the lower dosage (5%) of nanoparticles was more effective at enhancing the performance of concrete surface because of the higher tendency of both nanoparticles to agglomerate with increasing the loading ratio in the resin. Nano-silica was less efficient than nano-clay due to its smaller particle size (average of 20-30 nm) relative to nano-clay (average of 40-80 nm) that led to significantly higher number of particles mixed with the polymer to reach a constant filler concentration (Ashraf et al. 2018). Smaller nanoparticles possess larger surface area to volume ratio and surface energy, which cause stronger attractive interaction among nanoparticles by van der Waals, electrostatic and covalent

bonds, resulting in more aggregation/agglomeration (Zare 2016). This resulted in composites with more lumpy masses for nano-silica than nano-clay, which might have led to inefficient and heterogeneous distribution of the nanocomposite through the surface of concrete.

Nano-indentation was performed to determine the effective depth of coatings into concrete by evaluating the variation in its surface hardness. As most coatings could minimize the damage at a *w/b* of 0.40, the test was conducted on GU0.6 specimens (lowest quality microstructure) coated with the optimum dosage of nanoparticles (i.e. SNC5% and SNS5%). For each sample, three rows separated at 1 mm (starting from the coated surface) were tested; in each row, five points spaced at 30 μm were indented and averaged to give a hardness value representing the row. Figure 7.10a shows the load-depth curves for the first three rows (3 mm) of samples coated with SNC5%, with corresponding hardness values of 0.92, 0.90, and 0.84 GPa, respectively. This- indicated marginal improvement (maximum of 6%) in surface hardness of concrete by SNC compared to uncoated concrete (surface hardness of 0.87 GPa). Comparatively, samples coated with SNS5% (Fig 7.10b) showed relatively higher hardness values of 1.02, 0.98, and 0.89, respectively for the first 3 mm (3 to 18% increase relative to uncoated concrete). This showed that maximum improvement occurred closer to the coated surface and the effective zone affected by nanoparticles was within 2 mm from that surface, which covers the critical zone, in case of PSA and salt-frost scaling, where salts crystallize and exert pressure against concrete surface (Chapters 5, 6).

The alteration of hydration products caused by silane/nanocomposites in the effective zone was studied by DSC on powder samples extracted from the surface layer (0-3 mm) of GU0.6 specimens (Fig 7.11). The quantification of portlandite was based on

enthalpy [integration of heat flow peaks over the temperature range of 400-450ºC], which is proportional to its content. Nano-clay showed some pozzolanic activity as the enthalpy of portlandite was 52 J/g for SNC5% (i.e. 15% reduction compared to that of uncoated

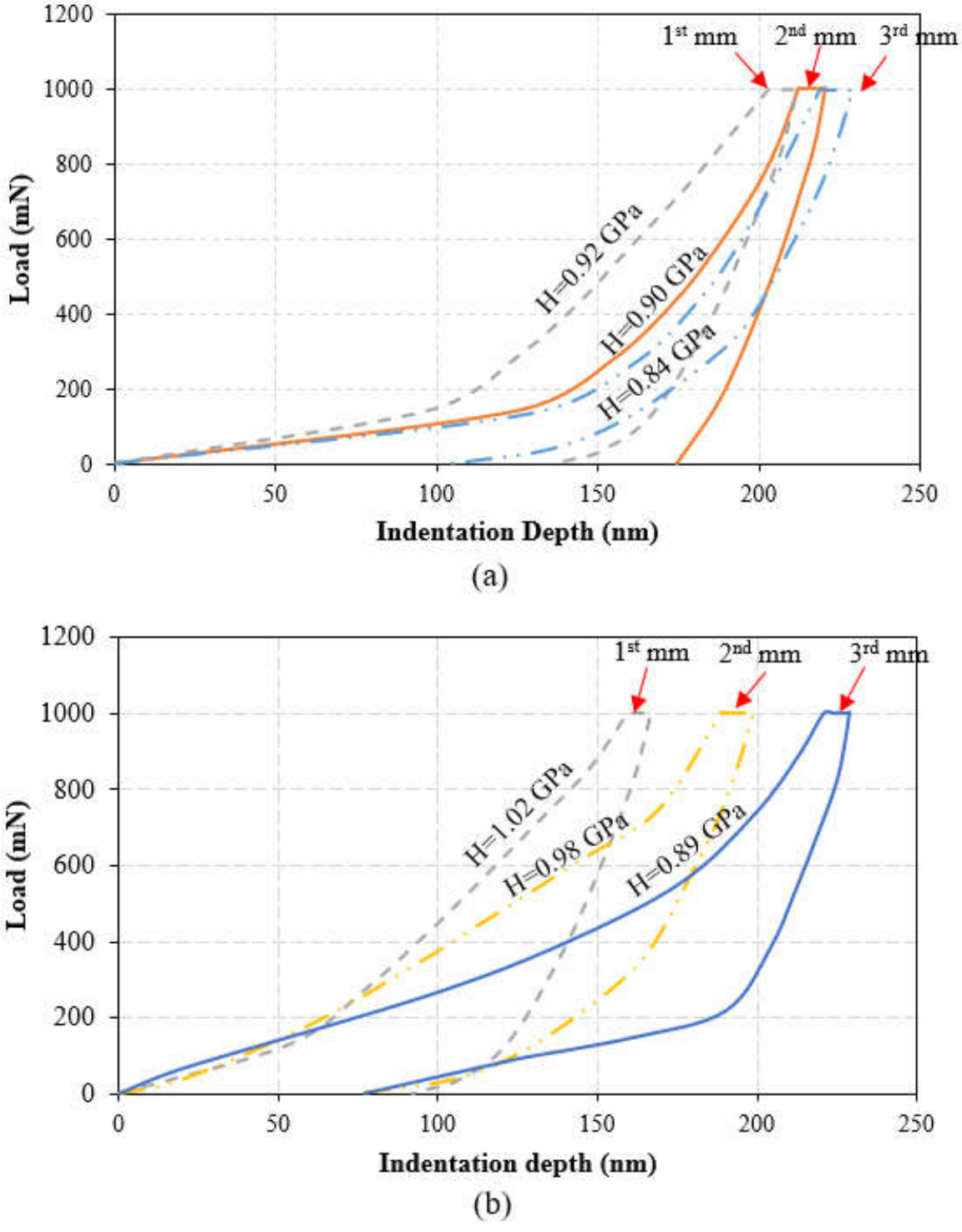

Figure 7.10: Load-depth curves of GU0.6 samples coated with: (a) SNC5%, and (b) SNS5%.

concrete). Comparatively, lesser amount of portlandite was obtained for nano-silica at a concentration of 5% [enthalpy of 47 J/g; 23% less than reference concrete)] indicating relatively better pozzolanic reactivity within the coated surface. This could be attributed to the higher silica (SiO_2) content in nano-silica (99.5%) compared to nano-clay (47%). Also, the rounded morphology and smaller particle size of nano-silica may ease its penetration into concrete, relative to the platy nano-clay particulates.

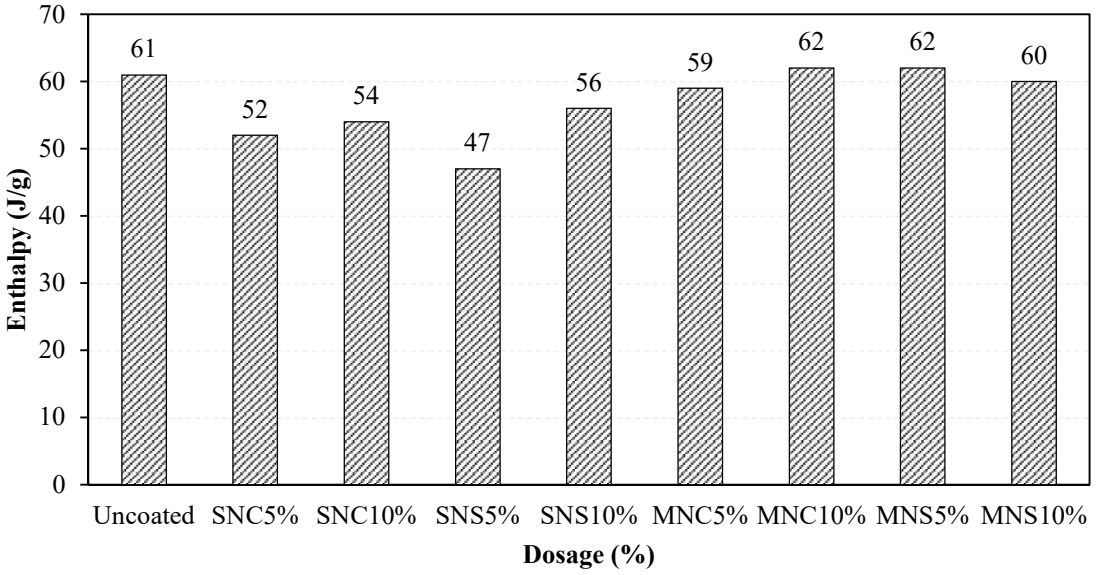

Figure 7.11: Enthalpy of portlandite in uncoated and coated GU0.6 specimens.

Additionally, elemental analysis was performed using EDX on several points in the surface layer (0-3 mm) to calculate the calcium-to-silicate ratio (*Ca/Si*) (Fig 7.12) to augment the trends obtained from nano-indentation and DSC. The average *Ca/Si* of the paste of GU0.6 specimens coated with SNC5% and SNS5% was 1.6 and 1.46, respectively, compared to 2.05 for reference concrete. This substantiated the lesser pozzolanic reactivity of nano-clay within the surface of concrete and alluded to the physical (barrier) effect as being mainly responsible for the improved properties of concrete coated with SNC. In comparison, nano-silica had higher reactivity to consume portlandite within the surface layer of concrete leading to denser microstructure by precipitating pozzolanic C-S-H with less *Ca/Si*

(chemical mechanism) contributing to discounting the rates of salt solutions ingress and evaporation. These trends explain the higher hardness values obtained for SNS5% relative to that of SNC5% specimens.

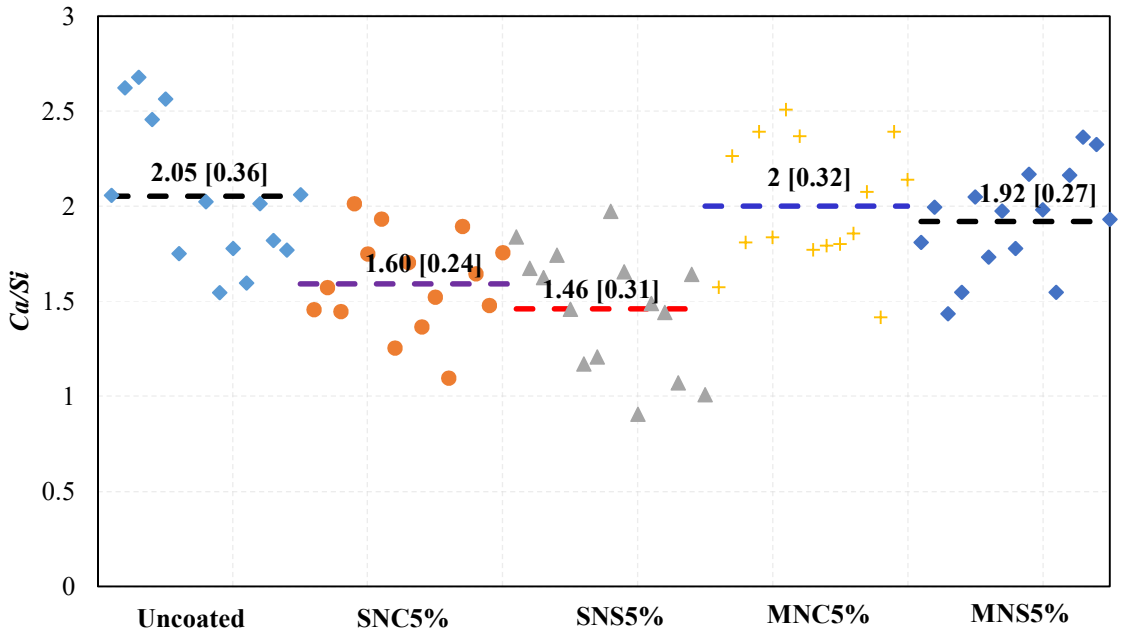

Figure 7.12: *Ca/Si* at multiple points in fracture pieces extracted from the effective zone in GU0.6 specimens. (Note: horizontal lines represent the average of points with standard deviations between brackets)

The basic functionality of silane/nanocomposites is attributed to silane, which is a water-repellent agent that could penetrate through the surface zone (within a depth of 2-4 mm) where salt crystals form and push against concrete surface. It reacts with alkaline elements in the pore solution producing a hydrophobic ingredient that lines the surface pores and reduces the wettability of concrete as shown by the higher contact angle measurements and lower absorption values, compared to that of uncoated concrete. Nevertheless, neat silane was insufficient at protecting concrete against aggravated exposures. The combination of 5% nanoparticles with silane much improved the barrier properties of concrete surface, with nano-clay providing relatively better performance than that of nano-silica. TEM (Fig 7.1) showed that the SNC composite tended to have an

interwoven structure, which efficiently enhanced the resistance of concrete to fluid transport compared with the morphology of SNS composite. Figure 7.13 shows SEM images of the surface of coated GU0.6 specimens with SNC5% and SNS5%. Particulates of nano-clay were observed to continuously deposit on the outer surface of concrete, reflecting dimensional stability of the physically blocking barrier (Fig 7.13a). Comparatively, for SNS, a remaining layer of condensed silica covered the surface of concrete (physical barrier), but with discontinuities and shrinkage micro-cracks (Fig 7.13b), likely due to ingress of silane, coagulation of remaining nano-silica and drying, rendering its physical blocking nature less effective than that of SNC. Compared to uncoated concrete where excessive salt crystals formed, salt deposits were absent in concrete specimens coated with SNC5% and SNS5% after exposures (Fig 7.14).

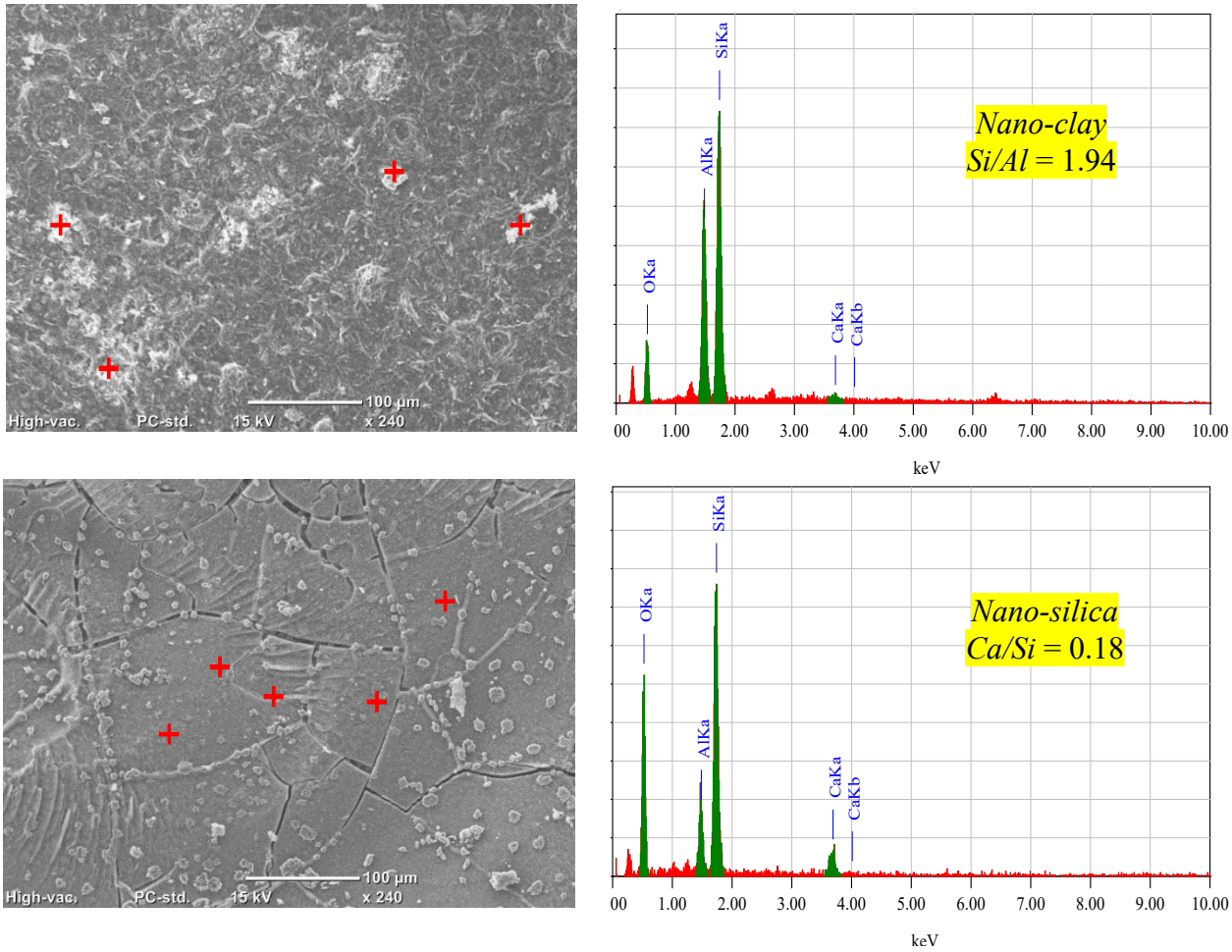

Figure 7.13: SEM and EDX of the surface of GU0.6 concrete coated with: (a) SNC5%, and (b) SNS5%.

These trends substantiate that combining the basic function of silane and pozzolanic and/or barrier effects of nanoparticles was effective at enhancing concrete durability to aggravated exposures due to discounting the rate of salt solutions ingress (in case of PSA and F/T) and rate of evaporation to the surrounding environment (in case of PSA).

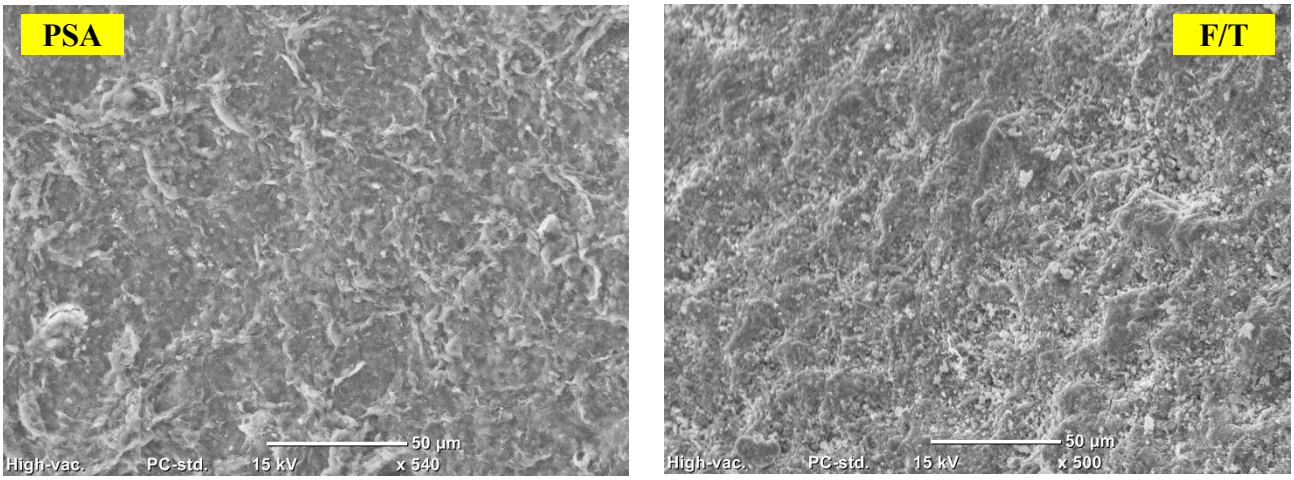

(a)

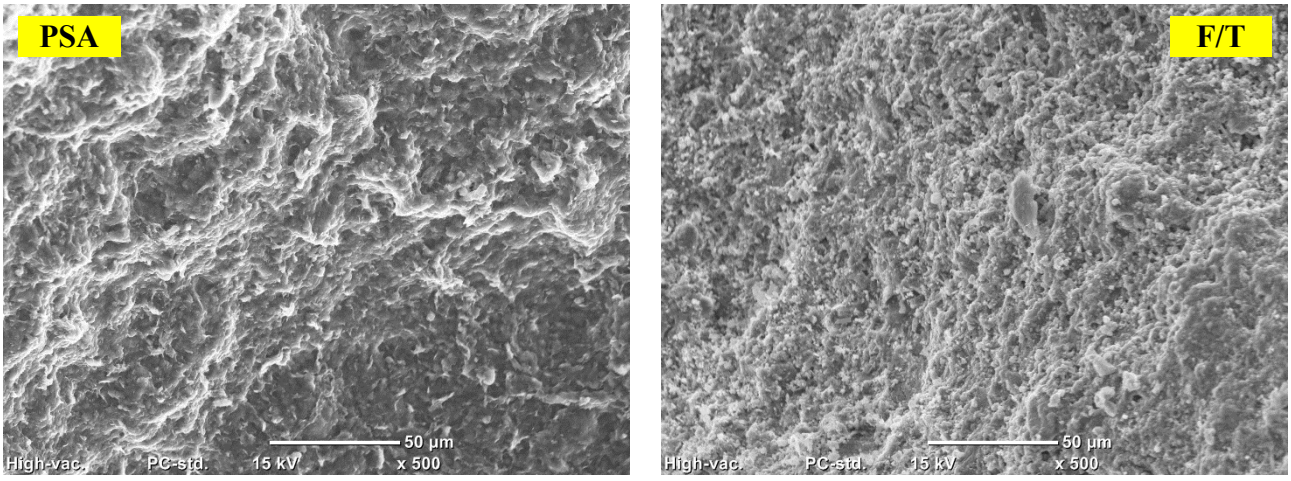

(b)

Figure 7.14 : SEM images of GU0.6 concrete specimens coated with: (a) SNC5%, and (b) SNS5% after both exposures.

7.5.3 MMA/nanocomposites

MMA is characterized by its low viscosity that enables the resin to partially fill out the surface pores and form a thin membrane (sealer) on the concrete surface, hence the lower

contact angles below 90°. However, it was inadequate herein to protect concrete under PSA and salt-frost scaling at *w/b* of 0.60. Saraswathy and Rengaswamy (1998) reported the reduction of adhesion of MMA-based coatings to concrete and ease of detachment as the *w/b* increases due to the higher moisture content in surface pores, which was also confirmed in Chapter 5 where MMA failed to mitigate PSA on concretes with $w/b \geq 0.50$, while succeeded for concretes with $w/b \leq 0.40$. The performance of MMA/nanocomposites varied depending on the exposure conditions and type of nanoparticles. In case of PSA, MMA/nano-clay composites at dosages of 5% and 10% were successful to protect concrete regardless of the *w/b*. For nano-silica, MNS5% eliminated PSA damage, while MNS10% did not fully protect concrete due to the formation of lumpy masses within the resin resulting in uneven distribution of nano-silica on the coated surface and exfoliation of the particles after drying of coatings. For the salt-frost scaling exposure, MMA/nanocomposites were inadequate to resist the surface scaling of GU0.6 concrete, while they eliminated the damage when the *w/b* was reduced to 0.40, because of the better isolation/sealing effect of coatings caused by the densification of microstructure as explained earlier.

Nano-indentation was applied, using the same methodology for silane/nanocomposites, to GU0.6 samples coated with MMA containing the optimum dosage of nanoparticles (5%) that led to improved performance in terms of reduced transport properties and mass loss. The average hardness values (Fig 7.15) obtained in the first 3 mm were [0.87, 0.84, 0.85 GPa] and [0.9, 0.85, 0.85 GPa] for MNC5% and MNS5%, respectively, indicating almost no change in hardness of paste compared to that of reference concrete (0.87 GPa). DSC tests on powder samples combined with EDX analysis on fracture pieces extracted from the surface region (0-3 mm) of specimens coated with

MMA/nanocomposites showed limited involvement of nanoparticles in reaction with calcium hydroxide as the enthalpies corresponding to portlandite [59 J/g to 62 J/g] were comparable to that of uncoated concrete [61 J/g] (Fig 7.11). Correspondingly, the average *Ca/Si* of paste was 2 and 1.92 for MNC5% and MNS5%, respectively (Fig 7.2), which is approximately equivalent to the paste ratio (2.05) in the reference concrete. Hence, the pozzolanic reactivity (chemical effect) of nanoparticles as a potential mechanism for shifting the superficial properties of concrete coated with MMA/nanocomposites was excluded. MMA-based coatings were reported to retain nanoparticles in synthesized composites due to strong adhesion with the resin (Soni et al. 2018). This might have caused the irregular morphology of nano-silica particles as observed by TEM (Fig 7.1d). In addition, smaller molecules of MMA may attach to nanoparticles when mixed together causing surface modification (Lin and Zheng 2013; Mallakpour and Naghdi 2018). Hence, these particles would not be readily available for chemical reactions, which impeded their pozzolanic reactivity as shown by the nano-indentation and DSC results.

Incorporation of nanoparticles with low viscosity MMA resins was reported to increase the adhesion strength of the composite with calcium phosphate-based materials (Atai et al. 2009). This was analogously shown herein with calcium-silicate matrices under the PSA exposure for MMA mixed with 5% and 10% nano-clay and 5% nano-silica as no detachment of concrete surface occurred throughout the entire exposure. However, at higher filler content of nano-silica, MNS10% did not perform similar to MNC10% due to the higher aggregation/agglomeration of nano-silica caused by its increased fineness, as discussed in the silane/nanocomposites section. Thus, MNS10% led heterogeneous distribution and peeling of the nanocomposite at some areas on the concrete surface causing higher transport properties and mass loss than that of MNC10%.

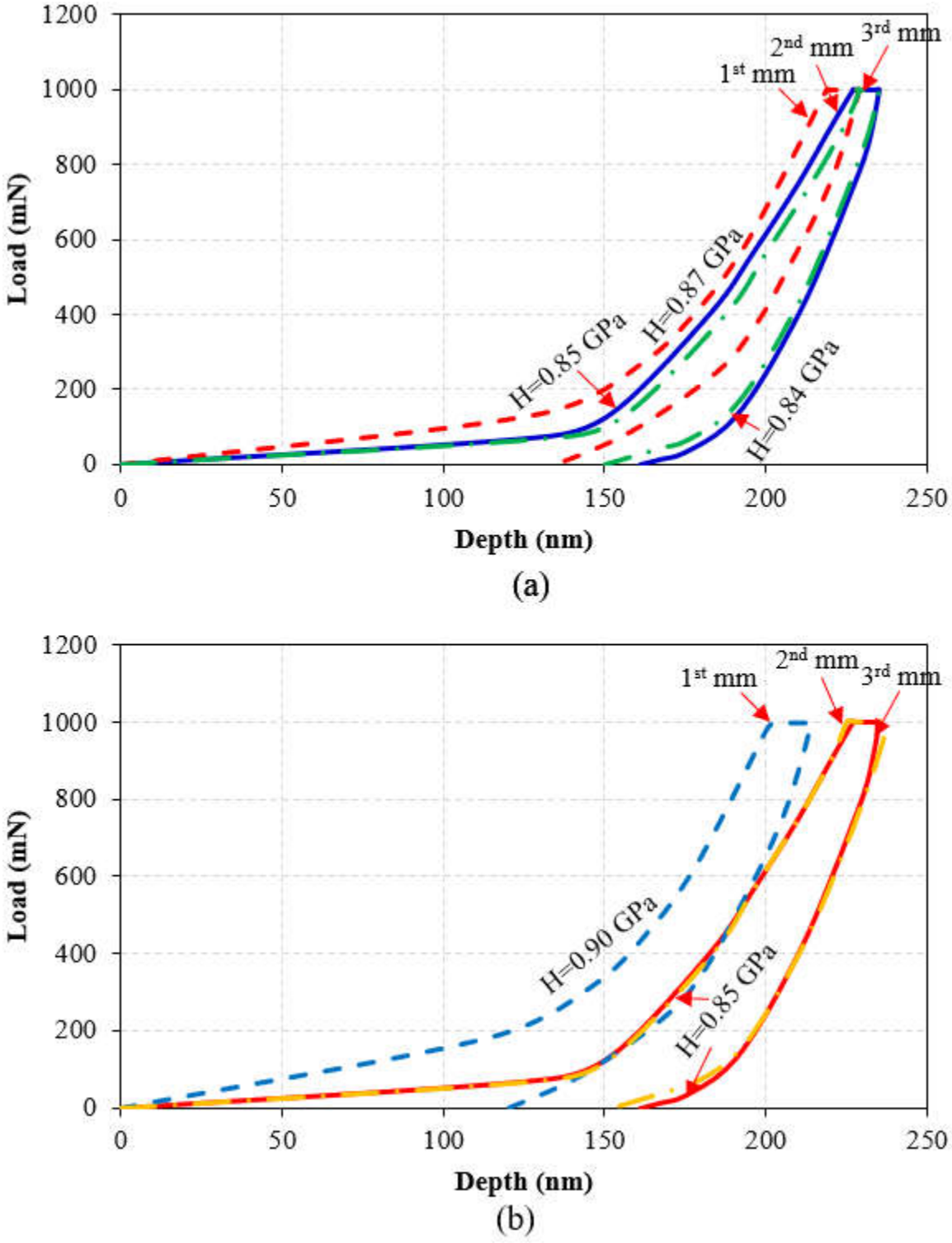

Figure 7.15: Load-depth curves of GU0.6 samples coated with: (a) MNC5%, and (b) MNS5%.

Improved barrier properties of concrete were generally achieved as a result of mixing nanoparticles with MMA as indicated by the reduction in transport parameters (Tables 7.1, 7.3). However, in the case of chloride penetration and absorption, the extent of this improvement was less compared to respective silane/nanocomposites because of the additional hydrophobic contribution of silane to the filler/barrier role of nanoparticles. Figure 7.16 showed that application of MNC5% and MNS5% resulted in formation of a continuous layer of MMA/nanocomposites on the surface of concrete substantiating the integration of nanoparticles into MMA resin, as also shown by the TEM images (Fig 7.1),

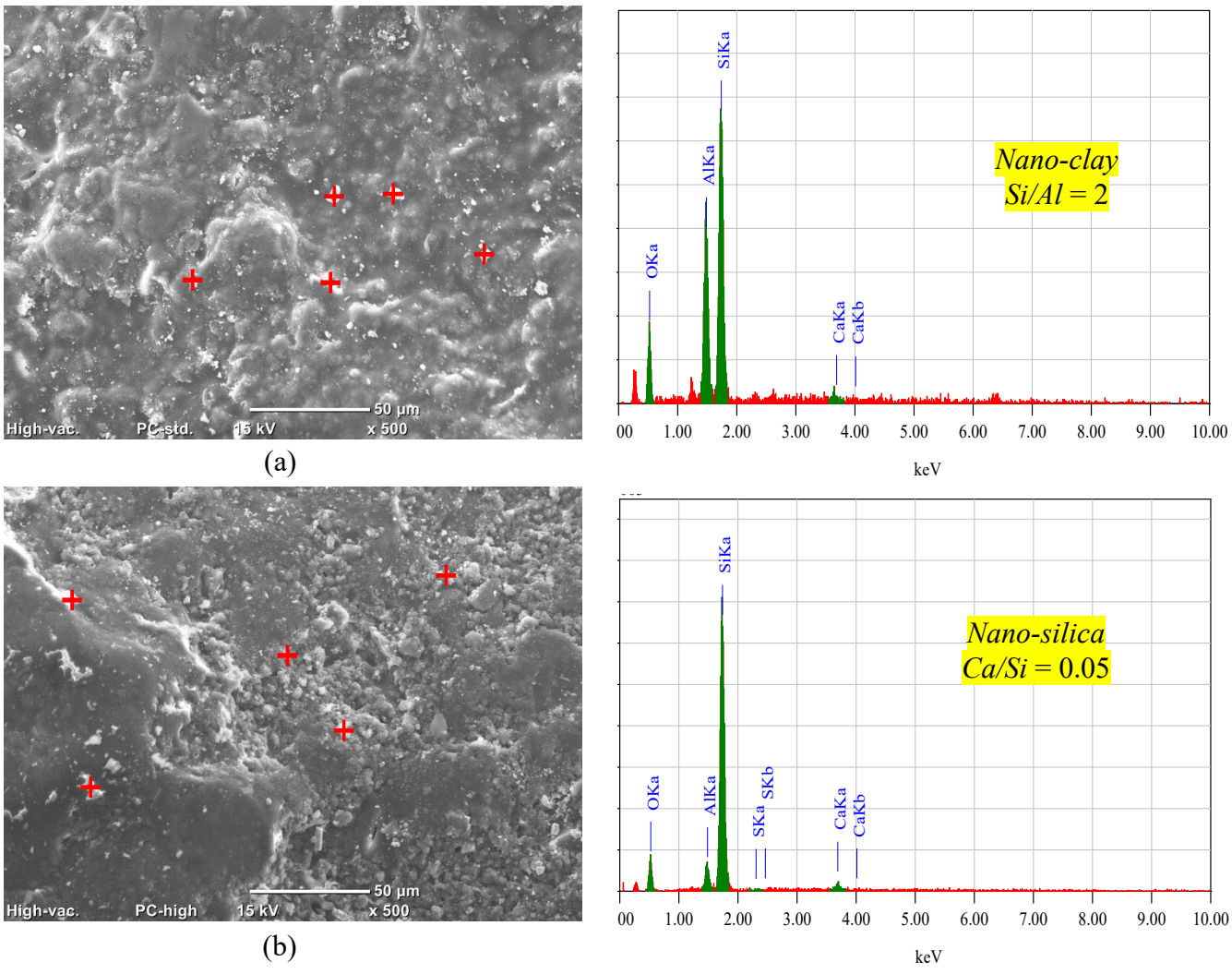

Figure 7.16: SEM and EDX of the surface of GU0.6 concrete coated with: (a) MNC5%, and (b) MNS5%.

which formed a barrier discounting the pathway of fluid exchange within the surface of concrete. Hence, in case of MMA/nanocomposites, the improved adhesion with the substrate and enhanced barrier properties (reduction of the rates of absorption/evaporation to prevent excessive crystallization pressures) were responsible for improving the resistance of concrete to PSA. Accordingly, Figure 7.17 shows the absence of thenardite crystals in the surface layer of GU0.6 specimens coated with MNC5% and MNS5% after the PSA exposure.

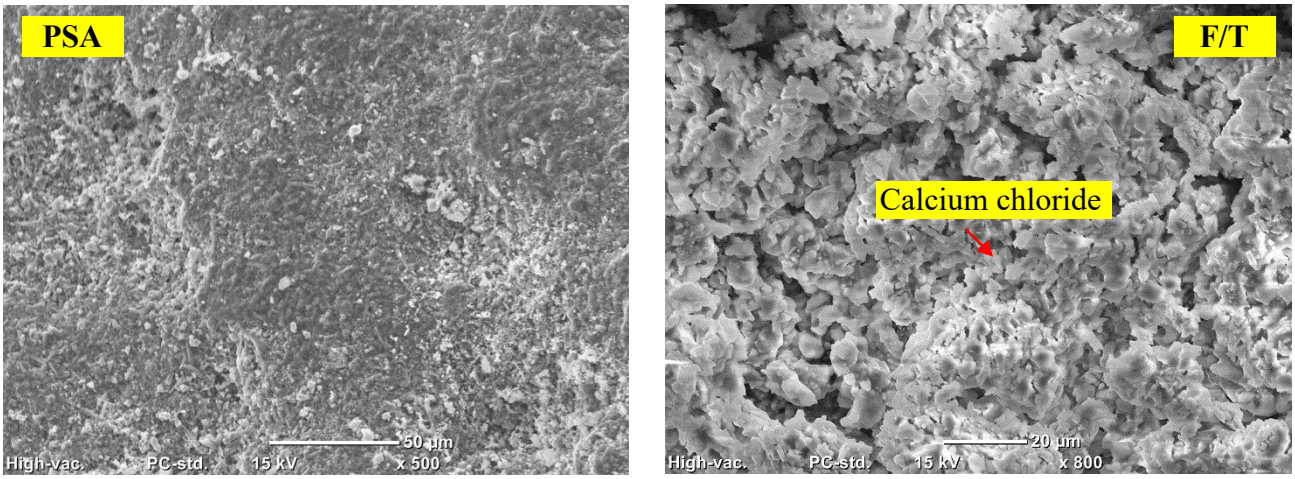

(a)

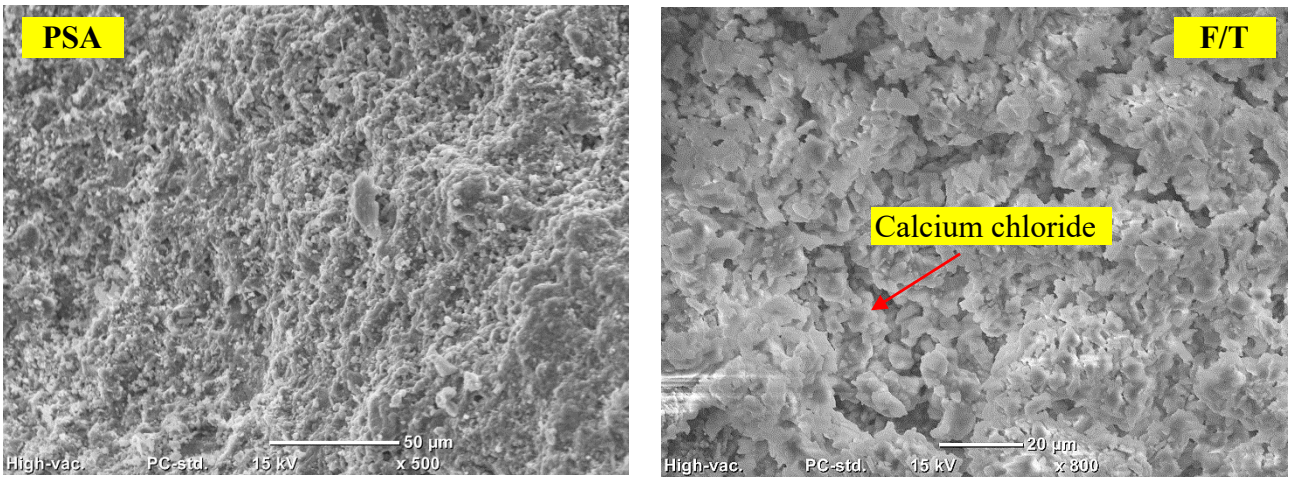

(b)

Figure 7.17: SEM images of GU0.6 concrete specimens coated with: (a) MNC5%, and (b) MNS5% after both exposures

Although MMA-based coatings relatively improved the resistance to salt-frost scaling of GU0.6 specimens compared to uncoated specimens, they failed during the exposure and allowed for increased rate of scaling after detachment of crust (between 20 to 25 cycles). In the case of PSA, the efficiency of a coating depends on the extent of balanced reduction it achieves in the absorption and desorption (evaporation) of concrete surface to interrupt the wicking processes, and consequently formation of the sub-florescence zone. Comparatively, the resistance of concrete to salt-frost scaling depends mainly on the absorption (initially) and continual migration/diffusion of salt solution within the surface, which were decreased as a result of MMA coatings. However, the achieved reductions were insufficient to eliminate the damage, compared with the silane-based (hydrophobic pore liner) coatings. Migration coefficients and absorption results, especially at higher *w/b* (0.60), showed higher tendency of concrete treated with MMA-based coatings to allow ingress of external fluids. With addition of nanoparticles (especially at the 5% dosage), such properties were improved leading to slower rate of damage compared to neat MMA (Table 7.5); however, the obtained initial transport properties were not adequate to prevent moisture saturation and cumulative build-up of calcium chloride, followed by crystallization, detachment/peeling of the crust comprising coatings, and progression of damage at a fast rate in a similar manner to uncoated specimens. Correspondingly, Figure 7.17 shows the formation of massive salt crystals beneath the detached layer of specimens coated with MMA/nanocomposites and exposed to salt-frost scaling.

CHAPTER 8: SUMMARY, CONCLUSIONS, AND RECOMMENDATIONS

8.1 Summary

Physical salt attack (PSA) is a key deterioration mechanism for concrete in contact with salt-rich media. In this thesis, experimental work and statistical modeling were conducted in order to comprehend the mechanisms of PSA damage, and factors affecting the degradation level, as well as identifying efficient surface treatments to protect concrete against PSA.

The response surface method, a statistical modeling approach, was used to assess the influence of water-to-binder ratio (*w/b*), binder content, and dosages of supplementary cementitious materials (SCMs) on the performance of 52 mixtures under accelerated PSA. Also, the PSA damage of concrete was mapped by regression analysis based on combination of prescriptive and performance-based parameters. Multi-objective optimization was then performed to determine optimal combinations of parameters producing mixtures resistant to PSA. In addition, a classification for the resistance of concrete to PSA based on performance indicators (mechanical capacity and wicking factor) was proposed.

This program adopted a holistic testing approach to consider additional parameters that may exist in service and alter the traditional mechanisms and kinetics of PSA (e.g. carbonation). Concrete was concurrently investigated under PSA and carbonation, simulating elements serving in heavy traffic and industrial zones, while implementing realistic ambient conditions in geographic locations with previous cases of PSA. Based on the tested mixture design parameters [*w/b*, cement type, SCMs], potential performance

risks that maybe encountered in field were identified.

Regarding the protection of concrete against PSA, seven types (epoxy, acrylic emulsion, methyl methacrylate, high-molecular weight methacrylate, silane, sodium silicate, and ethyl silicate) of surface coatings were initially applied to concrete to assess their suitability for resisting PSA. Concretes with different *w/b* (0.35 to 0.60) were tested and severe PSA conditions were implemented, using sodium sulfate, to obtain conclusive trends on the performance of coatings. To implement the innovative nano-based coatings in the protection of PSA, a nano-silica (5 to 50%) water-based solution and silane/nano-clay (5 to 50%) composite were used as superficial treatments for concrete. The coatings were applied on concretes with different *w/b* (0.35 to 0.60) and evaluated under severe durability exposures: PSA and salt-frost scaling. In addition, the efficiency of polymeric nanocomposites as superficial treatments for concrete was evaluated. Silane and methyl-methacrylate were used as base resins, in which nano-clay and nano-silica particles were mixed at different concentrations (0, 5, and 10%). The nanocomposites were applied to inferior and good quality [*w/b* of 0.60 and 0.40, respectively] concretes and assessed under severe PSA and salt-frost scaling conditions. The transport properties of treated concrete were evaluated by the rapid chloride penetrability test and absorption/desorption percentages. Deterioration of the concrete surface was visually assessed and quantified by mass loss; in addition, mineralogical, thermal, and microscopy analyses were performed on concrete specimens to elucidate the mechanisms of enhancement imparted by surface treatments.

8.2 Conclusions

8.2.1 Factors affecting PSA (Chapter 3)

- For portland cement concrete exposed to PSA, mixtures with *w/b* of 0.40 and binder

content (*B)* of 400 kg/m^3, consistently performed better (lower band) than other combinations, irrespective of the type of binder (single or blended), due to increased mechanical capacity and reduced wicking factor.

- Binary binders with fly ash or slag relatively provided improved resistance to PSA as long as their dosages were limited to 25 and 30%, respectively, and a total of 35% in case of ternary blends combining both. With extended curing, the pozzolanic reactivity in such binders is promoted, without large proportions of unreacted particles in the matrix that make concrete vulnerable to scaling under PSA.
- Binary and ternary/quaternary (28 to 35% SCMs) binders comprising silica fume (≥ 8%) were capable of resisting severe conditions conductive to PSA by significantly discounting the wicking factor of concrete.
- The optimum blended binder combinations, especially the ones comprising silica fume, would dually protect concrete against PSA and chemical sulfate attack, if they occur together in the field.
- The proposed performance classification based on combined performance parameters (mechanical capacity and wicking factor) can be used in the pre-qualification process of construction projects for designing various concrete mixtures resistant to PSA.
- Key findings from this study (e.g. dosages/combinations of SCMs, performance-based classification) can be used for updating the current guidance in ACI 201.2R on PSA.

8.2.2 Combined Damage by PSA and Carbonation (Chapter 4)

- Damage of concrete specimens exposed to the reference (single) PSA exposure evolved at a slow rate up to 32 cycles, followed by accelerated surface scaling till the end of exposure. Continual scaling of the drying portions of specimens occurred due to progressive deposition of sodium sulfate crystals beneath the surface layer of

concrete (sub-florescence).

- Specimens in the combined exposure showed a bimodal trend of damage. On contrary to the reference PSA exposure, the damage progressed rapidly up to mid of exposure due to the decalcification of C-S-H in the surface zone by carbonation and consequent increase in the wicking factor. Subsequently, the rate of scaling of specimens diminished/stabilized till the end of testing since a layer of calcite crystals was formed beneath the sub-florescence zone, which diminished wicking process.
- The combined exposure to PSA and carbonation had coupled and possibly synergistic effects on concrete, causing the co-occurrence of multiple-complex deterioration mechanisms (salt crystallization, decalcification of C-S-H, natrite and thaumasite formation) depending on the mixture constituents. This is fundamentally different from investigating a single degradation mechanism (salt crystallization) acting on concrete in the reference PSA tests.
- Under the reference PSA and combined exposures, decreasing the water-to-binder ratio (*w/b*) notably reduced the mass loss of concrete, regardless of cement type, due to densified microstructure of hardened paste, discounted ingress/evaporation rates of salt solution (wicking factor), and/or carbonation and subsequently less damage of concrete surface.
- The role of PLC (higher fineness and filler effect) at reducing the wicking factor of concrete were effective at decreasing its vulnerability to the reference PSA exposure. However, in the combined exposure, the dilution and nucleation effects of PLC led to reducing the portlandite in the matrix, thus facilitating decalcification of C-S-H causing higher wicking factors and further ingress of fluids. Also, limestone materials contributed to formation of natrite and thaumasite in the matrix.

- While the pozzolanic reactivity of moderate dosages of SCMs (20% fly ash or 30% slag) slightly enhanced the resistance of concrete to reference PSA, using high dosages (40% fly ash or 60% slag) notably increased the mass loss of concrete due to significant proportions of unreacted particles in concrete surface that were readily dislodged by PSA.
- In case of combined PSA and carbonation, the use of SCMs at all dosages worsened the resistance of concrete to surface scaling due to the initial consumption of portlandite that accelerated decalcification of C-S-H by carbonation, which led to increased wicking factors, and thus more cumulative mass loss of specimens.
- The synoptic outcomes from this study may be used for updating current guidelines/recommendations on PSA of concrete such as limiting *w/b* at or below 0.40 and cautioning against the use of limestone materials (if the intruding salt is sodium sulfate) and SCMs for elements exposed to dual PSA and carbonation.

8.2.3 Mitigation of PSA by Surface Treatments (Chapters 5, 6, and 7)

- The exposure regime implemented was suitable to conclusively evaluate the effectiveness of the coatings against PSA, as indicated by the severe significant damage of uncoated specimens.
- Reducing the water-to-binder ratio (*w/b*) markedly improved the concrete resistance to PSA due to decreased penetrability and less volume of crystallizing salt within the sub-florescence zone, complying with the information reported in ACI201.2R (2016).
- Epoxy, ethyl silicate, and acrylic emulsion were found effective at protecting concrete against PSA, irrespective of the *w/b*, whereas the performance of silane, methyl methacrylate (MMA), high molecular weight methacrylate (HMMA) and sodium silicate was adversely affected at high *w/b*.

- Epoxy and ethyl silicate were efficient due to the minimal absorption and evaporation of salt solution caused by their membrane action and pore blocking plus hydrophobic effects, respectively. Also, the acrylic emulsion mortar acted as a sacrificial layer protecting the substrate concrete; however, it may be vulnerable to debonding in long-term exposures.
- At high *w/b*, MMA, HMMA, and silane coated specimens comprised distinctive zones within the concrete surface. Because of their breathability, microstructural analysis indicated that sub-florescence formation and crystallization pressure were the primary cause of cracking and detachment of the surface crust after 50-60 cycles, which was succeeded by rapid rates of surface scaling.
- Sodium silicate was unsuitable for protecting concrete against PSA, as specimens showed significant surface scaling due to the formation of a considerable sub-florescence zone beneath the surface, resulting from its high rate of evaporation.
- The absorption and desorption behavior through a specific coating played a significant role in determining the level of damage in concrete due to PSA. Therefore, this criterion might be used for selecting or developing effective surface treatments for concrete vulnerable to PSA.
- The performance of uncoated concrete under severe PSA and salt-frost scaling can be drastically improved by decreasing the water-to-binder ratio (*w/b*), which in turn densified the microstructure of concrete and discounted the ingress/evaporation of salt brines and subsequent crystallization of salts in the surface layer.
- It is inadequate to only assess the performance of polymeric nanocomposites for concrete based on transport properties of the surface; these tests need to be supplemented by durability exposures expected in the field to reliably reach decisive

conclusions on the applicability of coatings under different field conditions.

- The performance of water-based nano-silica coating was adversely affected at higher *w/b*. Coatings with 25% and 50% nano-silica had a pronounced effect at improving the resistance of concrete to PSA and salt-frost scaling due to the reduced salt solutions ingress in both exposures and evaporation to the surrounding environment in the PSA exposure. The efficient pozzolanic and filler/blocking effects imparted by nano-silica at these dosages resulted in densified microstructure and a condensed outer layer that significantly improved the barrier features of concrete surface.
- The performance of silane/nanocomposites was marginally dependent on the *w/b*, while the efficiency of MMA/nanocomposites diminished at higher *w/b*. For both cases, the higher dosage of nanoparticles in the resins increased fluids transport properties, and consequently mass loss of concrete surface, due to the tendency for agglomeration of nanoparticles and heterogeneous dispersion, especially in the case of nano-silica (smaller particle size and higher fineness).
- Silane mixed with 5% nano-clay or nano-silica mitigated the PSA and salt-frost scaling damage of sound and pre-cracked concrete, even with inferior quality, with relatively better performance for nano-clay due to its unique morphology (interwoven barrier). The combination of the water-repellent action of silane with the barrier/filling/pozzolanic effects of nanoparticles on the concrete surface was the primary mechanism for its enhanced durability under aggravated exposures.
- MMA/nanocomposites were successful at protecting concrete, irrespective of the *w/b*, against PSA due to enhanced bonding with the substrate complemented with a robust barrier effect that was adequate to disrupt the wicking action of salt solution within the concrete surface. However, for high *w/b* concrete, MMA composites failed to

maintain their functionality up to the end of the salt-frost scaling exposure due to progressive ingress of salt solution, crystallization of salt built-up and detachment of coated surface which was aggravated by the cyclic frost action.

- The synoptic results of this study indicate that while MMA/nanocomposites are suitable for specific conditions conducive to PSA, silane/nanocomposites (especially at 5% loading ratio) have more promising potential and wider applicability for concrete, with variable quality, vulnerable to severe conditions involving salt-solutions and cyclic environments (W/D and F/T).

8.3 Recommendations for Future Work

- Based on the results obtained herein, supplemental research is required to further verify the model predictions with other mixture formulations and/or field data.
- The mechanism of damage by combined salts (e.g. sodium sulfate/sodium carbonate and sodium sulfate/sodium chloride) needs to be investigated.
- In addition to the current standards and specifications for concrete, much research is still needed to develop performance standards and specifications that consider the synergistic effects of chemical and physical processes existing in the field. This should lead to producing more reliable data on the durability of concrete with expected improvements in the durability-based design of concrete structures.
- Currently, there is no standardized test for PSA of concrete. A systematic research program is still needed to standardize a partial immersion test that can be used to reliably predict field performance. Thus, it is recommended that standardization agencies such as CSA and ASTM motivate research programs with this approach in the near future.
- Field studies need to be conducted to substantiate the laboratory trends of successful

surface treatments. Also, other important aspects, which were not examined in this thesis, such as the effects of concrete surface preparation and surface condition on the performance of coatings need to be explored.

REFERENCES

Aguayo, F., 2016. External sulfate attack of concrete: an accelerated test method, mechanisms, and mitigation techniques. Ph.D. Thesis, University of Texas at Austin, USA.

Almusallam, A. A., Khan, F. M., Dulaijan, S. U. and Al-Amoudi, O., 2003. Effectiveness of surface coatings in improving concrete durability. *Cement and Concrete Composites, 25*(4), pp. 473-481.

American Concrete Institute, 2006. ACI 350-06 Code requirements for environmental engineering concrete structures. Farmington Hills, Michigan, USA, 488 p.

American Concrete Institute, 2008. ACI 201.2R-08 Guide to durable concrete. Farmington Hills, Michigan, USA, 49 p.

American Concrete Institute, 2016. ACI 201.2R-16 Guide to durable concrete. Farmington Hills, Michigan, USA, 84 p.

American Concrete Institute, 2016. ACI 301-16 Specifications for structural concrete. Farmington Hills, Michigan, USA, 64 p.

American Concrete Institute, 2019. ACI 318-19 Building code requirements for structural concrete. Farmington Hills, Michigan, USA, 628 p.

Ammar, S., Ramesh, K., Vengadaesvaran, B., Ramesh, S. and Arof, A. K., 2016. A novel coating material that uses nano-sized SiO_2 particles to intensify hydrophobicity and corrosion protection properties. *Electrochimica Acta, 220*, pp. 417-426.

Arandigoyen, M., Bicer-Simsir, B., Alvarez, J. I. and Lange D. A., 2006. Variation of microstructure with carbonation in lime and blended pastes. *Applied Surface Science, 252*(20), pp. 7562-7571.

Ardalan, R. B., Jamshidi, N., Arabameri, H., Joshaghani, A., Mehrinejad, M. and

Sharafi, P., 2017. Enhancing the permeability and abrasion resistance of concrete using colloidal nano-SiO_2 oxide and spraying nanosilicon practices. *Construction and Building Materials, 146*, pp. 128-135.

Ashraf, M. A., Peng, W., Zare, Y. and Rhee, K. Y., 2018. Effects of size and aggregation/agglomeration of nanoparticles on the interfacial/interphase properties and tensile strength of polymer nanocomposites. *Nanoscale Research Letters, 13*(214).

ASTM C1202, 2019. Standard test method for electrical indication of concrete's ability to resist chloride ion penetration. *ASTM International*, *04.02*, West Conshohocken, Pennsylvania, USA, 8 p.

ASTM C192, 2019. Standard practice for making and curing concrete test specimens in the laboratory. *ASTM International*, *04.02*, West Conshohocken, Pennsylvania, USA, 8 p.

ASTM C215, 2019. Standard test method for fundamental transverse, longitudinal, and torsional resonant frequencies of concrete specimens. *ASTM International*, *04.02*, West Conshohocken, Pennsylvania, USA, 7 p.

ASTM C39, 2018. Standard test method for compressive strength of cylindrical concrete specimens. *ASTM International*, *04.02*, West Conshohocken, Pennsylvania, USA, 8 p.

ASTM C494, 2019. Standard specification for chemical admixtures for concrete. *ASTM International*, *04.02*, West Conshohocken, Pennsylvania, USA, 15 p.

ASTM C496, 2017. Standard test method for splitting tensile strength of cylindrical concrete specimens. *ASTM International*, *04.02*, West Conshohocken, Pennsylvania, USA, 5 p.

ASTM C672, 2012. Standard test method for scaling resistance of concrete surfaces exposed to de-icing chemicals. *ASTM International*, *04.02*, West Conshohocken, Pennsylvania, USA, 3 p.

ASTM C88, 2013. Standard test method for soundness of aggregates by use of sodium sulfate or magnesium sulfate. *ASTM International*, *04.02*, West Conshohocken, Pennsylvania, USA, 5 p.

Atahan, H. N. and Arslan, K. M., 2016. Improved durability of cement mortars exposed to external sulfate attack: the role of nano and micro additives. *Sustainable Cities and Society, 22*, pp. 40-48.

Atai, M., Solhi, L., Nodehi, A., Mirabedini, S. M., Kasraei, S., Akbari, K. and Babanzadeh, S., 2009. PMMA-grafted nanoclay as novel filler for dental adhesives. *Dental Materials, 25*(3), pp. 339-347.

Aye, T. and Oguchi, C. T., 2011. Resistance of plain and blended cement mortars exposed to severe sulfate attacks. *Construction and Building Materials, 25*(6), pp. 2988-2996.

Bader, T., Unterberger, S. H. and Lackner, R., 2017. Effect of substrate moisture on the weatherability of surface treatment for high-performance concrete (HPC). *Cement and Concrete Composites, 83*, pp. 57-65.

Baltazar, L., Santana, J., Lopes, B., Rodrigues, M. P. and Correia, J. R., 2014. Surface skin protection of concrete with silicate-based impregnations: influence of the substrate roughness and moisture. *Construction and Building Materials, 70*, pp. 191-200.

Barberena-Fernández, A. M., Carmona-Quiroga, P. M. and Blanco-Varela, M. T., 2015. Interaction of TEOS with cementitious materials: chemical and physical effects. *Cement and Concrete Composites, 55*, pp. 145-152.

Basheer, L. and Cleland, D. J., 2011. Durability and water absorption properties of surface treated concretes. *Materials and Structures, 44*(5), pp. 957-967.

Basheer, P. A. M., Basheer, L., Cleland, D. J. and Long, A. E., 1997. Surface treatments for concrete: assessment methods and reported performance. *Construction and Building Materials, 11*(7-8), pp. 413-429.

Bassuoni, M. T. and Nehdi, M. L., 2009. Durability of self-consolidating concrete to different exposure regimes of sodium sulfate attack. *Materials and Structures, 42*(8), pp. 1039-1057.

Bassuoni, M. T. and Rahman, M. M., 2016. Response of concrete to accelerated physical salt attack exposure. *Cement and Concrete Research, 79*, pp. 395-408.

Bassuoni, M.T., Nehdi, M.L. and Greenough, T.R., 2006. Enhancing the reliability of evaluating chloride ingress in concrete using the ASTM C 1202 rapid chloride penetrability test. *Journal of ASTM International*, *3*(3), pp.1-13.

Bates, S. J., 2010. A critical evaluation of salt weathering impacts on building materials at Jazirat Al Hamra, UAE. *Geoverse,* Available at: http://geoverse.brookes.ac.uk/article_resources/batesSJ/batesSJ.htm.

Benavente, D., Cueto, N., Martínez-Martínez, J., Del Cura, M. G. and Cañaveras, J. C., 2007. The influence of petrophysical properties on the salt weathering of porous building rocks. *Environmental Geology, 52*(2), pp. 215-224.

Benavente, D., Garcia del Cura, M., Bemabeu, A. and Ordonez, S., 2001. Quantification of salt weathering in porous stones using an experimental continuous partial immersion method. *Engineering Geology, 59*(3-4), pp. 313-325.

Bentz, D. P., 2014. Activation energies of high-volume fly ash ternary blends: hydration and setting. *Cement and Concrete Composites, 53*, pp. 214-223.

Bland, W. and Rolls, D., 1998. Weathering: an introduction to the scientific principles. Oxford University Press, New York, USA.

British Standards Institution, 2013. BS EN 206 Concrete: specification, performance, production and conformity. UK.

Buenfeld, N. R. and Zhang, J., 1998. Chloride diffusion through surface-treated mortar specimens. *Cement and. Concrete Research, 28*(5), pp. 665-674.

Building Research Establishment, 2005. BRE Special Digest 1 Concrete in aggressive ground. Watford, UK.

Bureau de Normalisation du Québec, 2002. BNQ NQ 2621-900 Determination of the scaling resistance of concrete surfaces exposed to freezing and thawing cycles in the presence of deicing chemicals, Annex A, pp.19-22.

Canadian Standards Association, 1942. CSA A23.1/A23.2 Concrete materials and methods of concrete construction/test methods and standard practices for concrete. Mississauga, Ontario, Canada.

Canadian Standards Association, 2018. CAN/CSA-A3001 Cementitious materials for use in concrete. Mississauga, Ontario, Canada, 691 p.

Canadian Standards Association, 2019. CSA A23.1/A23.2 Concrete materials and methods of concrete construction/test methods and standard practices for concrete. Mississauga, Ontario, Canada, 882 p.

Chau, T. T., Bruckard, W. J., Koh, P. T. L. and Nguyen, A.V., 2009. A review of factors that affect contact angle and implications for flotation practice. *Advances in Colloid and Interface Science, 150*(2), pp. 106-115.

Chen, F., Gao, J., Qi, B. and Shen, D., 2017. Deterioration mechanism of plain and blended cement mortars partially exposed to sulfate attack. *Construction and Building Materials, 154*, pp. 849-856.

Choudalakis, G. and Gotsis, A.D., 2009. Permeability of polymer/clay nanocomposites: a review. *European Polymer Journal, 5*(4), pp. 967-984.

Clement, J. C., 2009. Laboratory and field evaluations of external sulfate attack, Phase II. MSc Thesis, University of Texas at Austin, USA.

Correns, C.W., 1949. Growth and dissolution of crystals under linear pressure. *Discussions of the Faraday Society*, pp. 267-271.

Dang, Y., Xie, N., Kessel, A., McVey, E., Pace, A. and Shi, X., 2014. Accelerated laboratory evaluation of surface treatments for protecting concrete bridge decks from salt scaling. *Construction and Building Materials, 55*, pp. 128-135.

Davis, D. S. and Kulwiec, R. A., 1969. Chemical processing nomographs. Chemical Publishing Company Inc., New York, USA, 346 p.

Detwiler, R., Bhatty, J. and Bhattacharja, S., 1996. Supplementary cementing materials for use in blended cements. Portland Cement Association, Skokie, IL, 103 p.

Dhole, R., Thomas, M. D., Folliard, K. J. and Drimalas, T., 2019. Chemical and physical sulfate attack on fly ash concrete mixtures. *ACI Materials Journal, 116*, pp. 31-42.

Diamond, S., 2000. Mercury porosimetry: an inappropriate method for the measurement of pore size distributions in cement-based materials. *Cement and Concrete Research, 30*(10), pp. 1517-1525.

Doehne, E., 2002. Salt weathering: a selective review. *Geological Society, 205*, pp. 51-64.

Drimalas, T., 2007. Laboratory and field evaluations of external sulfate attack. PhD Thesis, University of Texas at Austin, USA.

Ferraris, C. F., Stutzman, P. E. and Snyder, K. A., 2006. Sulfate resistance of concrete: a new approach. R&D Bulletin 2486, Portland Cement Association, Skokie, Illinois, USA.

Flatt, R. J., 2002. Salt damage in porous materials: how high supersaturations are generated. *Journal of Crystal Growth, 242*(3-4), pp. 435-454.

Florinsky, I. V., Eilers, R. G. and Lelyk, G. W., 2000. Prediction of soil salinity risk by digital terrain modeling in the Canadian prairies. *Canadian Journal of Soil Science, 80*(3), pp. 455-463.

Folliard K. J. and Sandberg, P., 1994. Mechanisms of concrete deterioration by sodium sulfate crystallization. *ACI Special Publication, 145*, pp. 933-945.

Gaze, M. E. and Crammond, N. J., 2000. Formation of thaumasite in a cement:lime:sand mortar exposed to cold magnesium and potassium sulfate solutions. *Cement and Concrete Composites, 22*, pp. 209-222.

Goudie, A. and Viles, H., 1997. Salt weathering hazards. John Wiley & Sons, Chichester, West Sussex, UK, 241 pp.

Goudie, A. S. and Viles, H. A., 1995. The nature and pattern of debris liberation by salt weathering: a laboratory study. *Earth Surface Processes and Landforms, 20*, pp. 437-449.

Goudie, A. S., 1986. Laboratory simulation of 'the wick effect' in salt weathering of rock. *Earth Surface Processes and Landforms, 11*(3), pp. 275-285.

Goudie. A. S., 1993. Salt weathering simulation using a single-immersion technique. *Earth Surface Processes and Landforms, 18*, pp. 369-376.

Hakamy, A., Shaikh, F. U. A. and Low, I. M., 2015. Effect of calcined nanoclay on microstructural and mechanical properties of chemically treated hemp fabric-reinforced cement nanocomposites. *Construction and Building Materials, 95*, pp. 882-891.

Hamilton, J. J. and Handegord, G. O., 1968. The performance of ordinary portland cement concrete in prairie soils of high sulfate content. In *Performance of Concrete: Resistance of Concrete to Sulphate and Other Environmental Conditions; A Symposium in Honour of T. Thorvaldson,* edited by Swenson, E. G., University of Toronto Press, Toronto, pp. 135-158.

Hansen, W. C., 1968. The chemistry of sulphate-resisting portland cements. In *Performance of Concrete: Resistance of Concrete to Sulphate and Other Environmental Conditions; A Symposium in Honour of T. Thorvaldson,* edited by Swenson E. G., University of Toronto Press, Toronto, pp. 18-55.

Hartell, J. A., Boyd, A. J. and Ferraro, C. C., 2011. Sulfate attack on concrete: effect of partial immersion. *Journal of Materials in Civil Engineering, 23*(5), pp. 572-579.

Hasholt, M. T., Christensen, K. U. and Pade, C., 2019. Frost resistance of concrete with high contents of fly ash-a study on how hollow fly ash particles distort the air void analysis. *Cement and Concrete Research, 119*, pp. 102-112.

Haynes, B., 2012. Preliminary tests of repair material for physical sulfate attack. Technical Session on Physical Salt Attack of Concrete Parts I & II, ACI Committee 201, ACI Spring 2012 Convention – The Art of Concrete, Dallas, Texas, USA.

Haynes, H. and Bassuoni, M. T., 2011. Physical salt attack on concrete. *Concrete International, 33*(11), pp. 38-42.

Haynes, H., 2002. Sulfate attack on concrete: laboratory vs. field experience. *Concrete International, 24*(7), pp. 64-70.

Haynes, H., 2005. ASTM C 88 test on soundness of aggregate using sodium sulfate or magnesium sulfate: a study of the mechanisms of damage. *Journal of ASTM International, 2*(1), pp. 1-17.

Haynes, H., O'Neill, R. and Mehta, P. K., 1996. Concrete deterioration from physical attack by salts. *Concrete International, 18*(1), pp. 63-68.

Haynes, H., O'Neill, R., Neff, M. and Mehta, P. K., 2008. Salt weathering distress on concrete exposed to sodium sulfate environment. *ACI Materials Journal, 105(1)*, pp. 35-43.

Haynes, H., O'Neill, R., Neff, M. and Mehta, P. K., 2010. Salt weathering of concrete by sodium carbonate and sodium chloride. *ACI Materials Journal, 107*(3), pp. 258-266.

Hekal, E. E., Kishar, E. and Mostafa, H., 2002. Magnesium sulfate attack on hardened blended cement pastes under different circumstances. *Cement and Concrete Research, 32*(9), pp. 1421-1427.

Holland, R. B., Kurtis, K. E. and Kahn, L. F., 2017. Sulfate resistance of ternary blend concretes: influence of binder composition on performance. in *ACI Special Publication, 317*: Sulfate Attack on Concrete: A Holistic Perspective, edited by Bassuoni, M. T., Hooton, R. D. and Drimalas, T., 2017, 172 p.

Hou, P., Cheng, X., Qian, J., Zhang, R., Cao, W. and Shah, S. P., 2015. Characteristics of surface-treatment of nano-SiO_2 on the transport properties of hardened cement pastes with different water-to-cement ratios. *Cement and Concrete Composites, 55*, pp. 26-33.

Irassar, E., Di Maio, A. and Batic, O., 1996. Sulfate attack on concrete with mineral admixtures. *Cement and Concrete Research, 26*(1), pp. 113-123.

Jalal, M., Pouladkhan, A., Harandi, O. F. and Jafari, D., 2015. Comparative study on effects of Class F fly ash, nano silica and silica fume on properties of high performance self compacting concrete. *Construction and Building Materials, 94*, pp. 90-104.

Johannessen, C. L., Feiereisen, J. J. and Wells, A. K., 1982. Weathering of ocean cliffs by salt expansion in mid-atitude coastal environment. *Shore Beach, 50*, pp. 26-34.

Kandasamy, S. and Shehata, M. H., 2014. Durability of ternary blends containing high calcium fly ash and slag against sodium sulphate attack. *Construction and Building Materials, 53*, pp. 267-272.

Khaloo, A., Mobini, M. H. and Hosseini, P., 2016. Influence of different types of nano-SiO_2 particles on properties of high-performance concrete. *Construction and Building Materials, 113*, pp. 188-201.

Law, K. Y. and Zhao, H., 2016. Surface wetting: characterization, contact angle, and fundamentals. Springer, Switzerland, 162 p.

Lee, B. Y. and Kurtis, K. E., 2017. Effect of pore structure on salt crystallization damage of cement-based materials: consideration of *w/b* and nanoparticle use. *Cement and Concrete Research, 98*, pp. 61-70.

Leung, C. K., Zhu, H. G., Kim, J. K. and Woo, R. S., 2008. Use of polymer/organoclay nanocomposite surface treatment as water/ion barrier for concrete. *Journal of Materials in Civil Engineering, 20*(7), pp. 484-492.

Li, G., Yue, J., Guo, C. and Ji, Y., 2018. Influences of modified nanoparticles on hydrophobicity of concrete with organic film coating. *Construction and Building Materials, 169*, pp. 1-7.

Lin, T. and Zheng, Y., 2013. Synthesis and characterisation of polymethyl-methacrylate/nanosilica and nanosilica/polymethylmethacrylate core-shell structure composite microspheres. *Micro & Nano Letters, 8*(5), pp. 217-220.

Lindvall, A., 2001. Environmental actions and response - reinforced concrete structures exposed in road and marine environments. Publication P-01:3, Department of Building Materials, Chalmers University of Technology, Sweden.

Liu, Z. and Hansen, W., 2016. Effect of hydrophobic surface treatment on freeze-thaw durability of concrete. *Cement and Concrete Composites, 69*, pp. 49-60.

Liu, Z., Hu, W., Hou, L. and Deng, D., 2018. Effect of carbonation on physical sulfate attack on concrete by Na_2SO_4. *Construction and Building Materials, 193*, pp. 211-220.

Liu, Z., Zhang, F., Deng, D., Xie, Y., Long, G. and Tang, X., 2017. Physical sulfate attack on concrete lining-a field case analysis. *Case Studies in Construction Materials, 6*, pp. 206-212.

Long, G. C., Xie, Y. J., Deng, D. H. and Li, X. K., 2011. Deterioration of concrete in railway tunnel suffering from sulfate attack. *Journal of Central South University of Technology, 18*(3), pp. 881-888.

Lowe, T. E., 2011. An investigative study on physical sulfate attack and alkali-silica reaction test methods. M.Sc. Thesis, University of Texas at Austin, USA.

Madani, H., Bagheri, A. and Parhizkar, T., 2012. The pozzolanic reactivity of monodispersed nanosilica hydrosols and their influence on the hydration characteristics of portland cement. *Cement and Concrete Research, 42*(12), pp. 1563-1570.

Mallakpour, S. and Naghdi, M., 2018. Polymer/SiO_2 nanocomposites: production and applications. *Progress in Materials Science, 97*, pp. 409-447.

Mamaghani, I. H., Moretti, C., Dockter, B. A., Falken, L. and Tonnenson, J., 2009. Evaluation of penetrating sealers for reinforced concrete bridge decks. *Journal of the Transportation Research Board, 2108*(1), pp. 86-96.

Marzouki, A., Lecomte, A., Beddey, A., Diliberto, C. and Ouezdou, M. B., 2013. The effects of grinding on the properties of Portland-limestone cement. *Construction and Building Materials, 48*, pp. 1145-1155.

McGill, L. P., Humpage, M. and Chemicals, F. C., 1990. Prolonging the life of reinforced concrete structures by surface treatment. In *Protection of Concrete: Proceedings of the International Conference, University of Dundee*, CRC Press, pp. 191-200.

Mehta, P. K. and Monteiro, P. J. M., 2014. Concrete: microstructure, properties and materials. McGraw Hill Education, USA, 675 p.

Ministry of Transportation Ontario, 2018. MTO special provisions manual, Ontario, Canada.

Mittermayr, F., Baldermann, A., Kurta, C., Rinder, T., Klammer, D., Leis, A., Tritthart, J. and Dietzel, M., 2013. Evaporation - a key mechanism for the thaumasite form of sulfate attack. *Cement and Concrete Research, 49*, pp. 55-64.

Montgomery, D. C., 2014. Design and analysis of experiments. John Wiley and Sons, Arizona, USA, 326 p.

Moon, S. and Lee, K. J., 2017. Simultaneous control of size and surface functionality of silica particle via growing method. *Advanced Powder Technology, 28*(11), pp. 2914-2920.

Moreira, P. M., Aguiar, J. B. and Camoes, A., 2006. Systems for superficial protection of concretes. In *International Symposium Polymers in Concrete*, University of Minho, Portugal, pp. 225-236.

Nadelman, E. I. and Kurtis, K. E., 2019. Durability of Portland-limestone cement-based materials to physical salt attack. *Cement and Concrete Research,125*, 105859.

Nadelman, E. I., 2016. Hydration and microstructural development of portland limestone cement-based materials. PhD Dissertation, Georgia Institute of Technology, USA.

Najjar, M. F., Nehdi, M. L., Soliman, A. M. and Azabi, T. M., 2017. Damage mechanisms of two-stage concrete exposed to chemical and physical sulfate attack. *Construction and Building Materials, 137*, pp. 141-152.

Nehdi, M. L., Suleiman, A. R. and Soliman, A. M., 2014. Investigation of concrete exposed to dual sulfate attack. *Cement and Concrete Research, 64*, pp. 42-53.

Neville, A., 2004. The confused world of sulfate attack on concrete. *Cement and Concrete Research, 34*(8), pp. 1276-1296.

Ngala, V. and Page, C., 1997. Effects of carbonation on pore structure and diffusional properties of hydrated cement pastes. *Cement and Concrete Research, 27*(7), pp. 995-1007.

Nordtest, 1999. NT BUILD 492 Concrete, mortar and cement-based repair materials, chloride migration coefficient from non-steady-state migration experiments. Denmark.

Novak, G. A. and Colville, A. A., 1989. Efflorescent mineral assemblages associated with cracked and degraded residential concrete foundations in southern California. *Cement and Concrete Research, 19*(1), pp. 1-6.

Obla, K. and O'Neill, R., 2017. Criteria for selecting mixtures resistant to physical salt attack. in *ACI Special Publication, 317*: Sulfate Attack on Concrete: A Holistic Perspective, edited by Bassuoni, M. T., Hooton, R. D. and Drimalas, T., 20 p.

Obla, K. H. and Lobo, C. L., 2017. Criteria for concrete mixtures resistant to chemical sulfate attack. in *ACI Special Publication, 317*: Sulfate Attack on Concrete: A Holistic Perspective, edited by Bassuoni, M. T., Hooton, R. D. and Drimalas, T., 16 p.

Oman, M.S., 2014. Concrete bridge deck crack sealant evaluation and implementation. Report No. MN/RC 2014-34, Minnesota Department of Transportation, St. Paul, Minnesota, USA.

Pan, X., Shi, Z., Shi, C., Ling, T. C. and Li, N., 2017. A review on concrete surface treatment Part I: types and mechanisms. *Construction and Building Materials, 132*, pp. 578-590.

Price, A. R., 1989. A field trial of waterproofing systems for concrete bridge decks. In *proceedings of the International Conference*, UK, pp. 333-346.

Price, G. C. and Peterson, R., 1968. Experience with Concrete in Sulphate Environments in Western Canada. In *Performance of Concrete: Resistance of Concrete to Sulphate and Other Environmental Conditions; A Symposium in Honour of T. Thorvaldson,* edited by Swenson E. G., University of Toronto Press, Toronto, pp. 93-112.

Rahim, A., Jansen, D., Abo-Shadi, N. and Simek, J., 2010. Overview of high-molecular-weight methacrylate for sealing cracks in concrete bridge decks, *Transportation Research Record, 2202*(1), pp. 77-81.

Rahman, M. M. and Bassuoni, M. T., 2014. Thaumasite sulfate attack on concrete: mechanisms, influential factors and mitigation. *Construction and Building Materials, 73*, pp. 652-662.

Rasheeduzzafar, D., Dakhil, H. and Bader, M. A., 1986. Toward solving the concrete deterioration problem in the gulf region. *Arabian Journal for Science and Engineering*, *11*(2), pp. 129-146.

Reading, T. J., 1982. Physical aspects of sodium sulfate attack on concrete. *ACI Special Publication, 77*, pp. 75-81.

Rimmelé, G., Barlet-Gouédard, V., Porcherie, O., Goffé, B. and Brunet, F., 2008. Heterogeneous porosity distribution in Portland cement exposed to CO_2- rich fluids. *Cement and Concrete Research, 38*(8), pp. 1038-1048.

Rodriguez-Navarro, C. and Doehne, E., 1999. Salt weathering: influence of evaporation rate, supersaturation and crystallization pattern. *Earth Surface Processes and Landforms, 24*(2-3), pp. 191-209.

Rodriguez-Navarro, C., Doehne, E. and Sebastian, E., 2000. How does sodium sulfate crystallize? implications for the decay and testing of building materials. *Cement and Concrete Research, 30*(10), pp. 1527-1534.

Rodriguez-Navarro, C., Doehne, E., Ginell, W. S. and Sebastian, E., 1996. Salt growth in capillary and porous media. In *Rehabilitation of Buildings and Architectural Heritage* edited by Sebastian, E., Valverde, I. and Zezza, U., Universidad de Granada, Spain, pp. 509-514.

Sakr, M. R., Bassuoni, M. T. and Taha, M. R., 2019. Effect of coatings on concrete resistance to physical salt attack. *ACI Materials Journal, 116*(6), pp. 255-267.

Saraswathy, V. and Rengaswamy, N. S., 1998. Adhesion of an acrylic paint coating to a concrete substrate. *Journal of Adhesion Science and Technology, 12*(7), pp. 681-694.

Saudi Building Code, 2018. SBC 304 Concrete structures. Saudi Buildings Code National Committee, KSA.

Scarfato, P., Di Maio, L., Fariello, M. L., Russo, P. and Incarnato, L., 2012. Preparation and evaluation of polymer/clay nanocomposite surface treatments for concrete durability enhancement. *Cement and Concrete Composites, 34*(3), pp. 297-305.

Scherer, G. W., 1999. Crystallization in pores. *Cement and Concrete Research, 29*(8), pp. 1347-1358.

Scherer, G. W., 2004. Stress from crystallization of salt. *Cement and Concrete Research, 34*(9), pp. 1613-1624.

Sevelsted, T. F. and Skibsted J., 2015. Carbonation of C–S–H and C–A–S–H samples studied by 13C, 27Al and 29Si MAS NMR spectroscopy. *Cement and Concrete Research, 71*, pp. 56-65.

Soni, G., Srivastava, S., Soni, P., Kalotra, P. and Vijay, Y. K., 2018. Optical, mechanical and structural properties of PMMA/SiO_2 nanocomposite thin films. *Materials Research Express, 5*(1).

Sperling, C. B. and Cooke, R. V., 1985. Laboratory simulation of rock weathering by salt crystallization and hydration processes in hot, arid environment. *Earth Surface Processes and Landforms, 10*, pp. 541-555.

St John, D. A., 1982. An unusual case of ground water sulphate attack on concrete. *Cement and Concrete Research, 12*(5), pp. 633-639.

Standards Association of Australia, 2018. AS 3600 Concrete structures. Sydney, Australia, 259 p.

Stark, D., 1989. Durability of concrete in sulfate-rich soils. R&D Bulletin O97, Portland Cement Association, Skokie, Illinois, USA, 14 p.

Stark, D., 2002. Performance of concrete in sulfate environments. R&D Bulletin RD129, Portland Cement Association, Skokie, Illinois, USA, 23 p.

Steiger, M., 2005. Crystal growth in porous materials-II: influence of crystal size on the crystallization pressure. *Journal of Crystal Growth, 282*, pp. 470-481.

Suleiman, A. R. and Nehdi M. L., 2017. Exploring effects of supplementary cementitious materials in concrete exposed to physical salt attack. *Magazine of Concrete Research, 69*(11), pp. 576-585.

Suleiman, A. R., Soliman, A. M. and Nehdi, M. L., 2014. Effect of surface treatment materials on durability of concrete exposed to physical sulfate attack. *Constructions and Building Materials, 73*, pp. 674-681.

Swenson, E. G. and Sereda, P. J., 1969. Mechanism of the carbonatation shrinkage of lime and hydrated cement. *Journal of Applied Chemistry, 18*(4), pp. 111-117.

Thaulow, N. and Sahu, S., 2004. Mechanism of concrete deterioration due to salt crystallization. *Materials Characterization, 53*(2-4), pp. 123-127.

Tiburzi, N. B., 2018. Mechanisms of deterioration of portland-limestone cement blended systems exposed to external sulfates. Ph.D. Dissertation, University of Texas at Austin, USA.

Tuthill, L. H., 1978. Resistance to chemical attack. In *Significance of Tests and Properties of Concrete and Concrete-Making Materials*, American Society for Testing and Materials STP-169-A, pp. 369-387.

Wang, L., Quan, H. and Li, Q., 2014. Evaluation of slag reaction efficiency in slag-cement mortars under different curing temperature. *Materials, 12*(18), 17 p.

Weisheit, S., Unterberger, S. H., Bader, T. and Lackner, R., 2016. Assessment of test methods for characterizing the hydrophobic nature of surface-treated high performance concrete. *Construction and Building Materials, 110*, pp. 145-153.

Wilson. R. and Cleve, A., 1928. Brief summary of tests of the effect of sulfate soils and waters on concrete," Report of the Director of Research, Portland Cement Association, Skokie, Illinois, USA.

Wolf, A. V., 1966. Aqueous solutions and body fluids: their concentrative properties and conversion tables. Hoeber Medical Division, Harper & Row, New York, USA.

Woo, R. S., Zhu, H., Chow, M. M., Leung, C. K. and Kim, J. K., 2007. Barrier performance of silane-clay nanocomposite coatings on concrete structure. *Composites Science and Technology, 68*, pp. 2828-2836.

Yang, J., Wang, P., Li, H. and Yang, X., 2016. Sulfate attack resistance of air-entrained silica fume concrete under dry-wet cycle condition. *Journal of Wuhan University of Technology-Materials Science, 31*(4), pp. 857-864.

Yoshida, N., Matsunami, Y., Nagayama, M. and Sakai, E., 2010. Salt weathering in residential concrete foundations exposed to sulfate-bearing ground. *Journal of Advanced Concrete Technology, 8*(2), pp. 121-134.

Zare, Y., 2016. Study of nanoparticles aggregation/agglomeration in polymer particulate nanocomposites by mechanical properties. *Composites Part A*, *84*, pp. 158-164.

Zeidan, M., Bassuoni, M. T. and Said, A., 2016. Physical salt attack on concrete incorporating nano-silica. *Journal of Sustainable Cement-Based Materials, 6*(3), pp. 195-216.

Zhutovsky, S. and Hooton, R. D., 2017a. Experimental study on physical sulfate salt attack. *Materials and Structures, 50*(54), 10 p.

Zhutovsky, S. and Hooton, R. D., 2017b. Accelerated testing of cementitious materials for resistance to physical sulfate attack. *Construction and Building Materials, 145*, pp. 98-106.

APPENDIX A: SUPPLEMENTAL RESULTS FOR CHAPTER 3

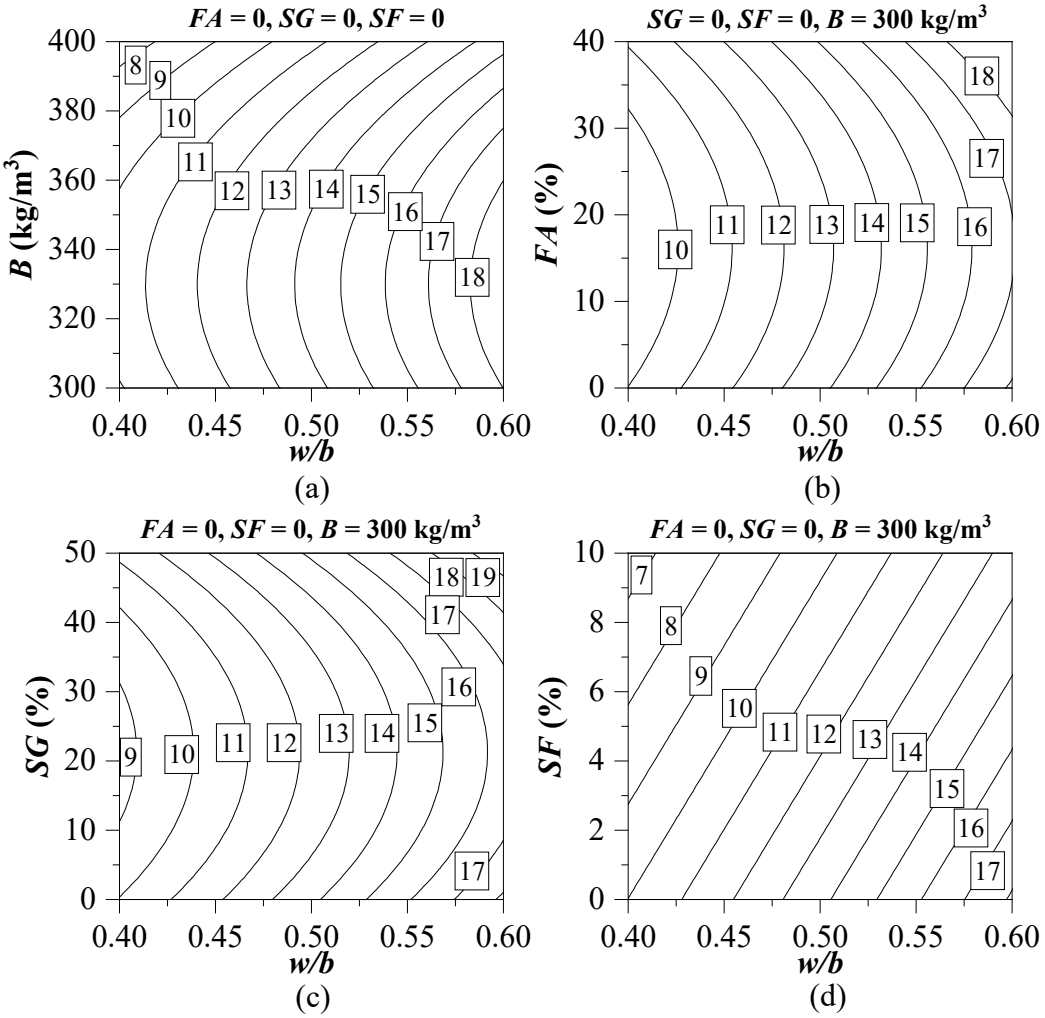

Figure A.1: Exemplar isoresponse plots showing the effect of *w/b* and: (a) *B*, (b) *FA*, (c) *SG*, and (d) *SF* on mass loss (%) of concrete under PSA. (B = 300 kg/m^3)

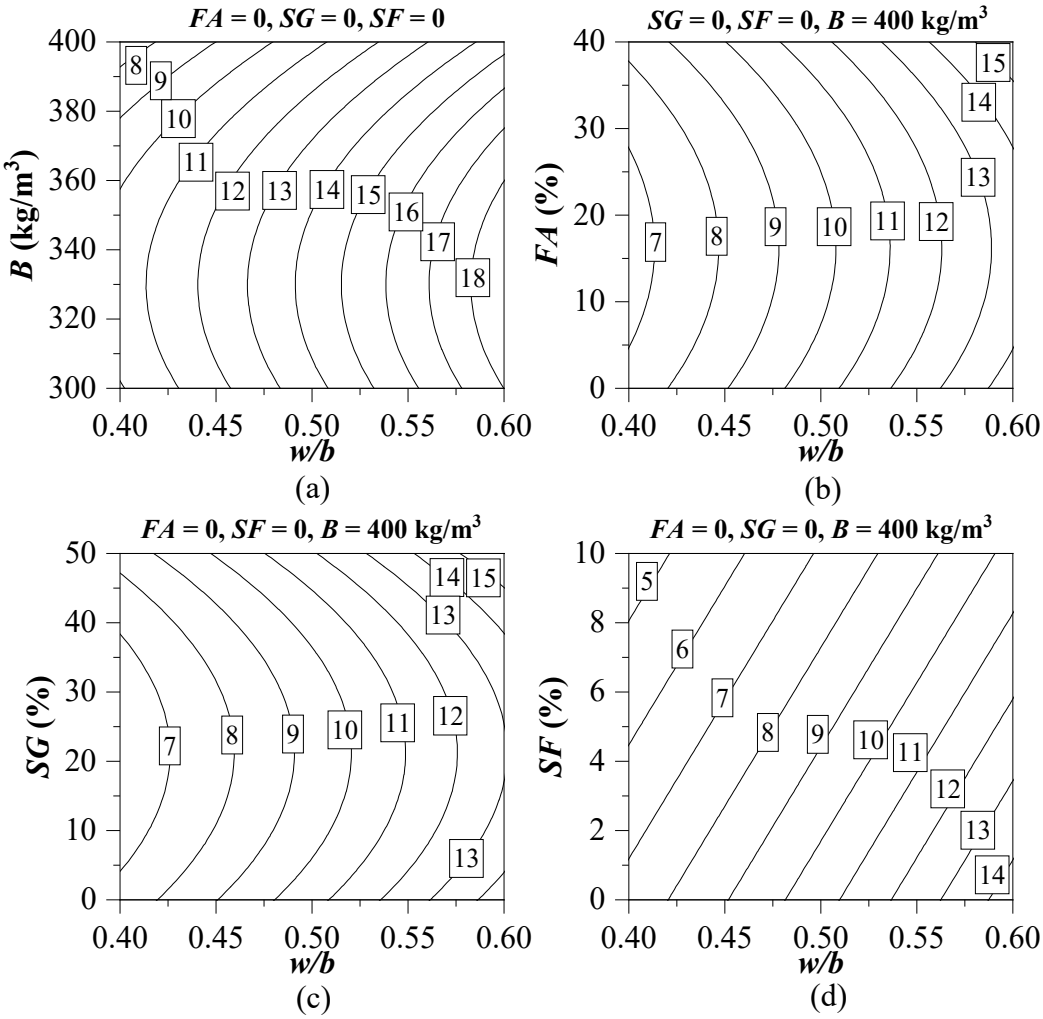

Figure A.2: Exemplar isoresponse plots showing the effect of *w/b* and: (a) *B*, (b) *FA*, (c) *SG*, and (d) *SF* on mass loss (%) of concrete under PSA (B = 400 kg/m^3).

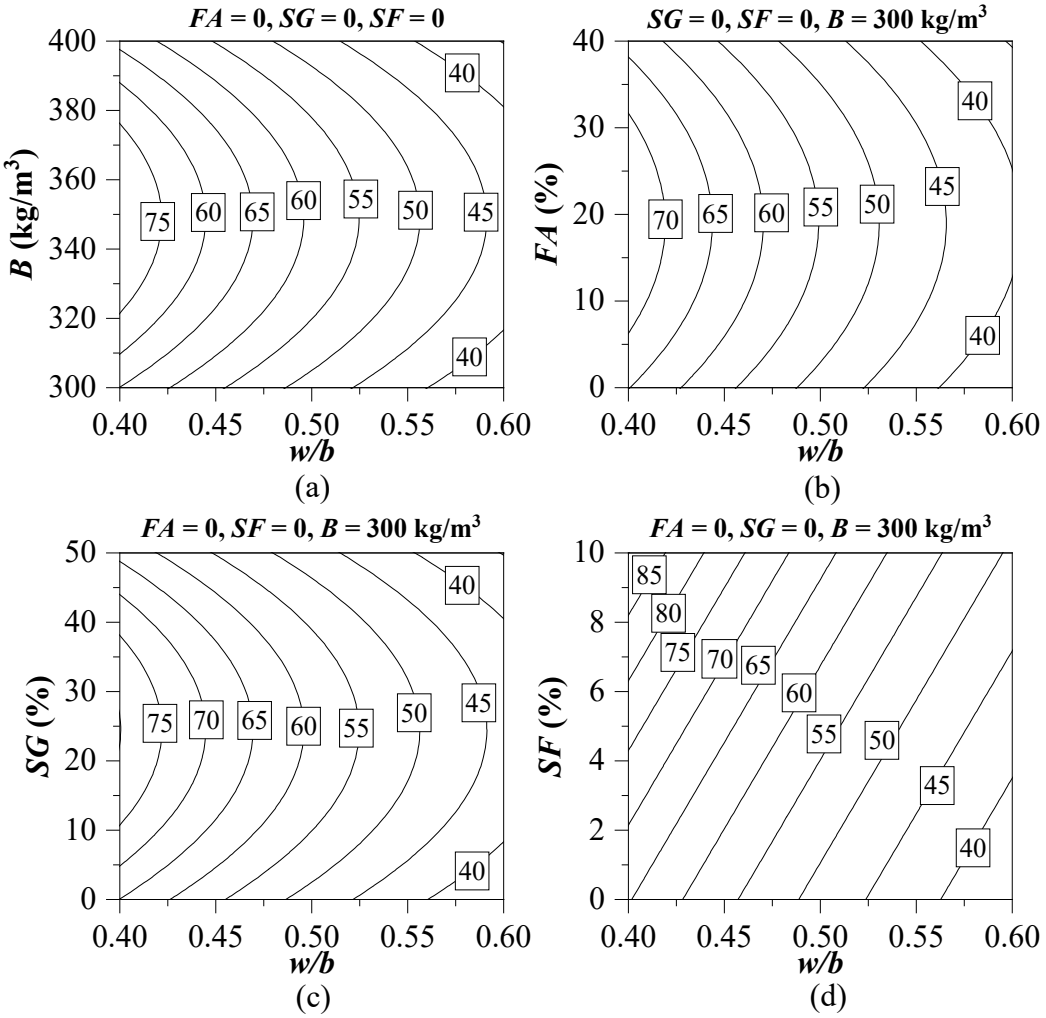

Figure A.3: Exemplar isoresponse plots showing the effect of *w/b* and: (a) *B*, (b) *FA*, (c) *SG*, and (d) *SF* on time to notable scaling (d) of concrete under PSA (B = 300 kg/m^3).

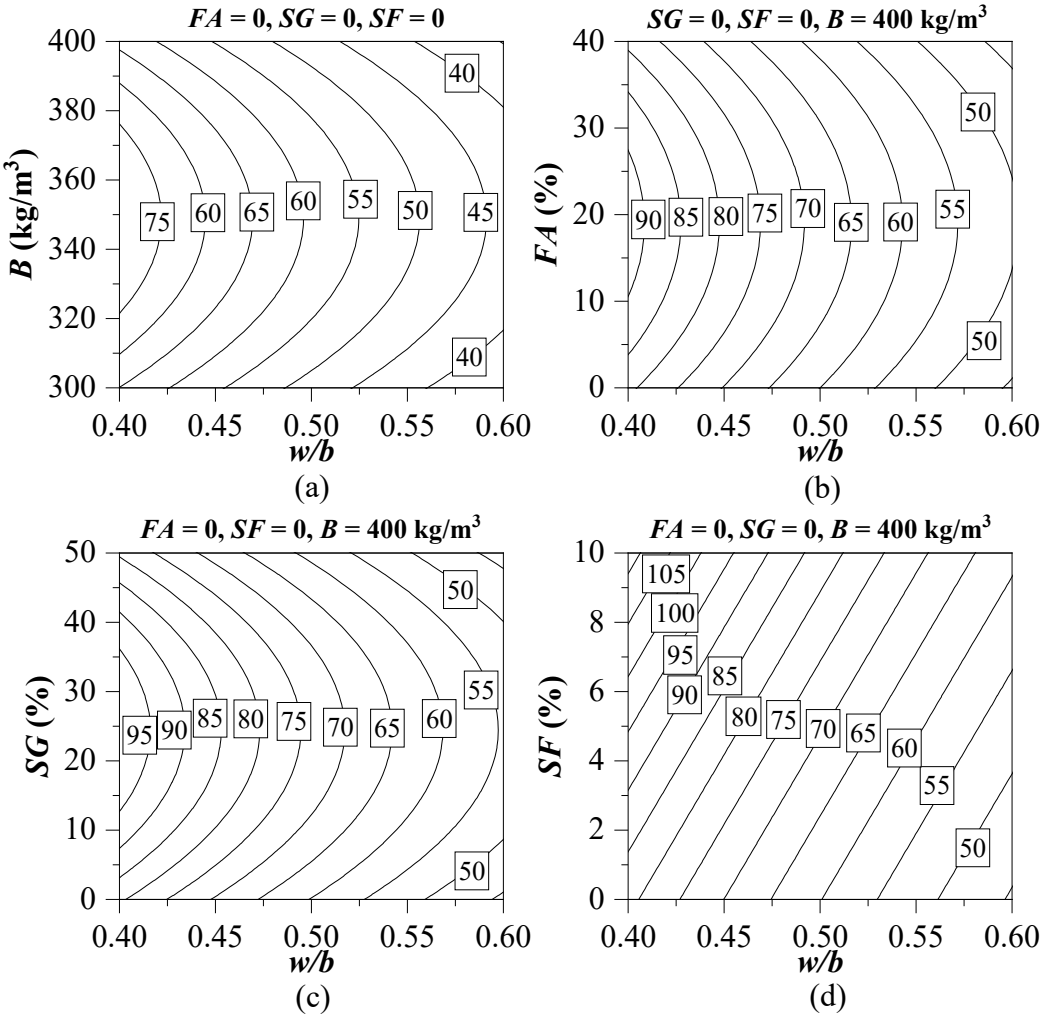

Figure A.4: Exemplar isoresponse plots showing the effect of *w/b* and: (a) *B*, (b) *FA*, (c) *SG*, and (d) *SF* on time to notable scaling (d) of concrete under PSA (B = 400 kg/m^3).

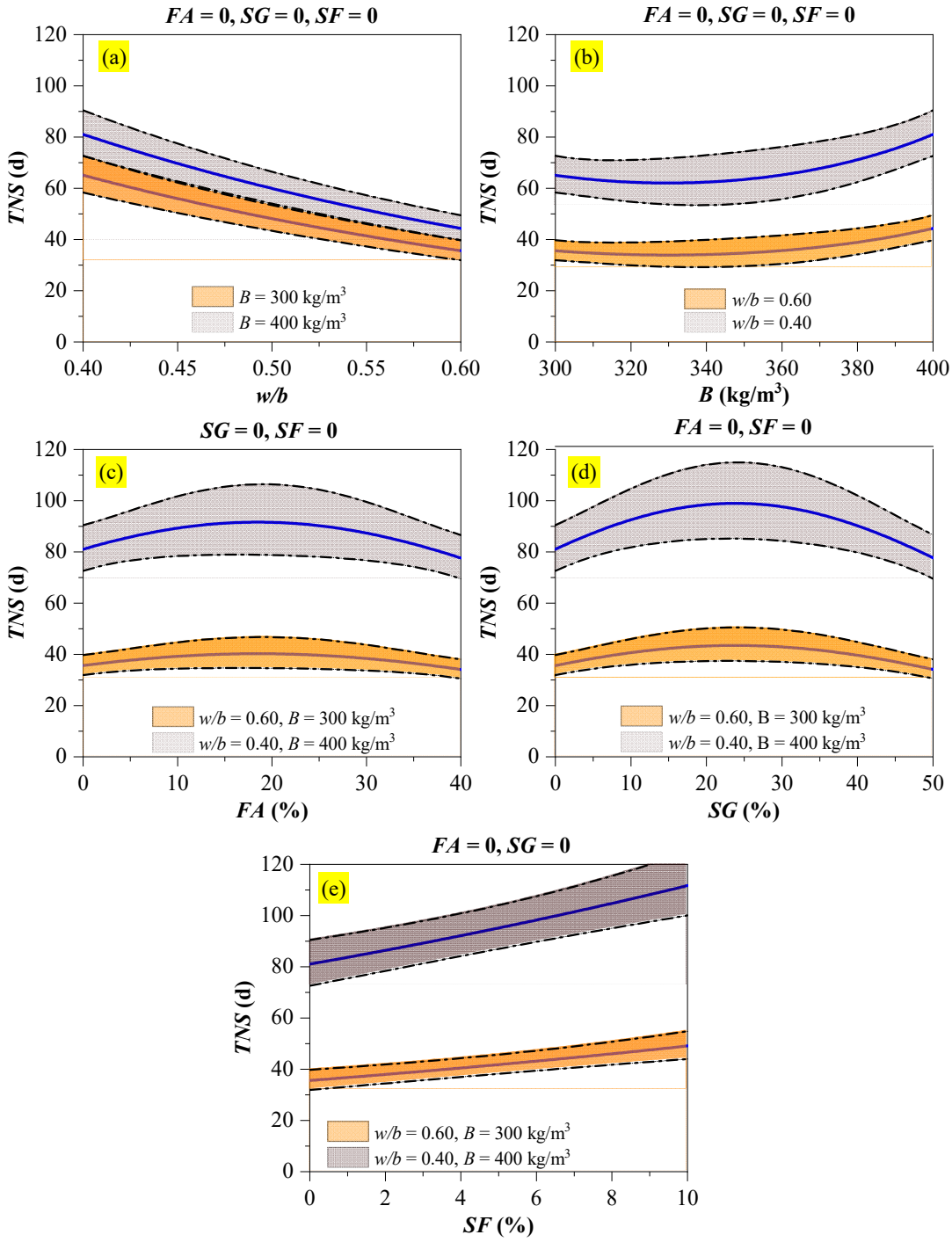

Figure A.5: Upper and lower bands for the effect of: (a) *w/b*, (b) *B*, (c) *FA*, (d) *SG*, and (e) *SF* on time to notable scaling (d) of concrete under PSA.

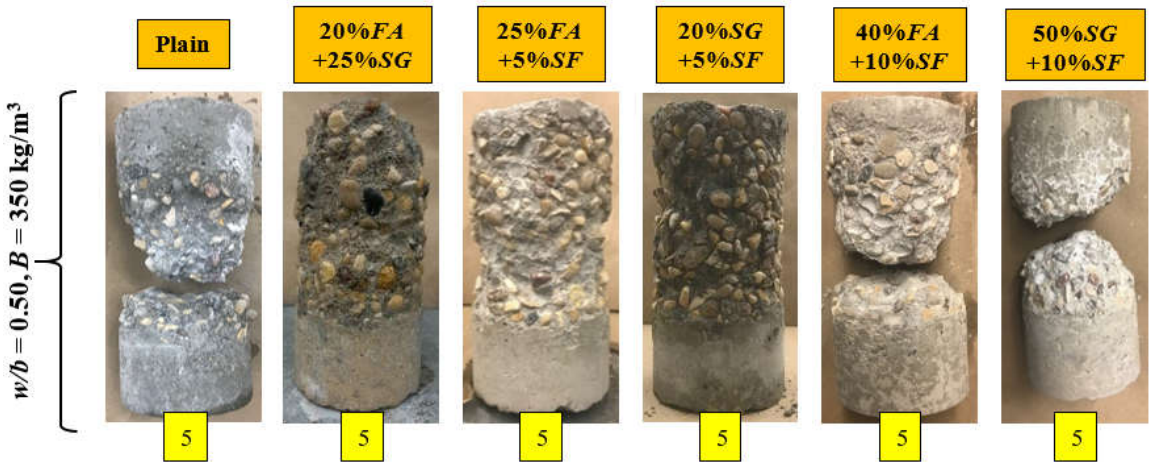

Figure A.6: Final condition of ternary binder specimens at the end of PSA exposure along with visual ratings.

APPENDIX B: SUPPLEMENTAL RESULTS FOR CHAPTER 6

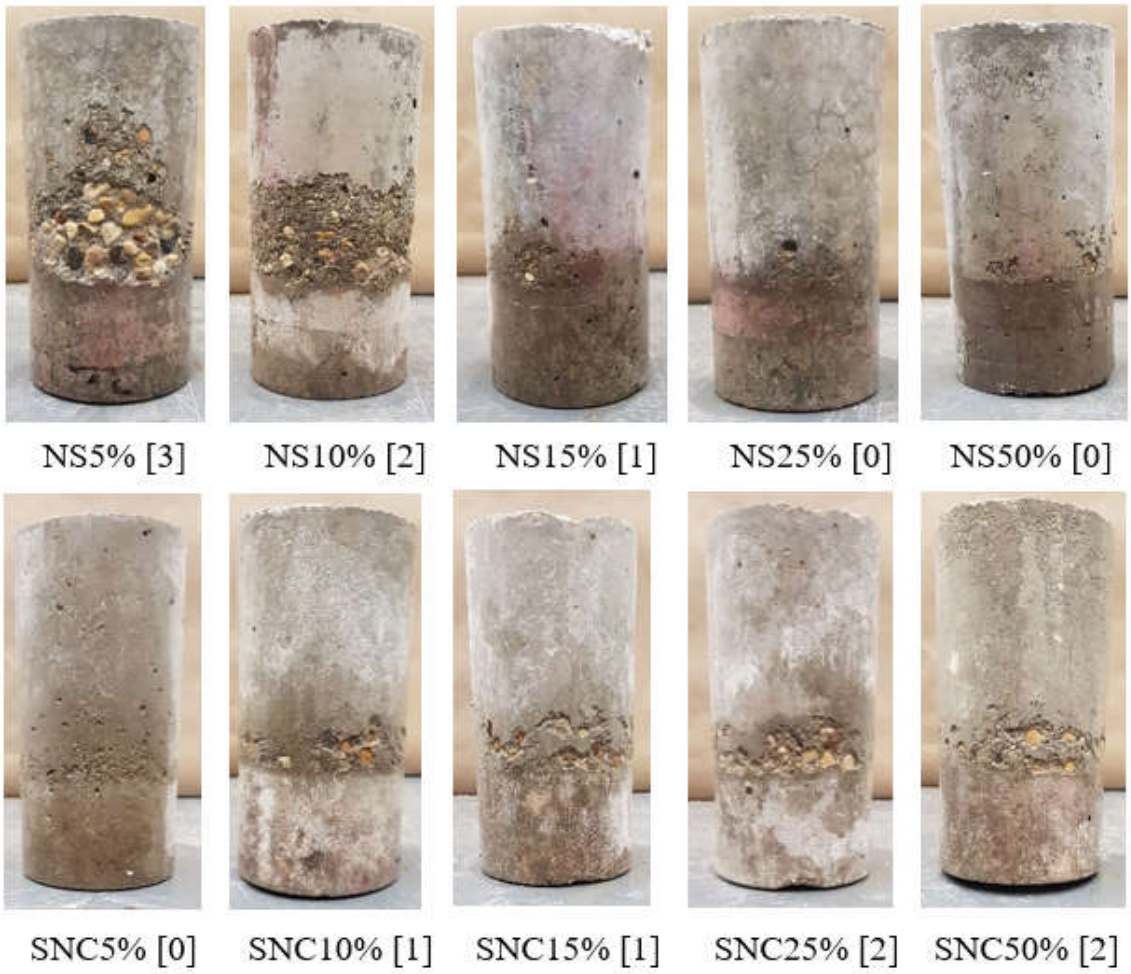

Figure B.1: Coated GU0.5 specimens at the end of PSA exposure. (Note: Numbers between brackets are the final visual ratings and the number of cycles at failure respectively, if applicable; NS: nano-silica, SNC: silane/nano-clay composite).

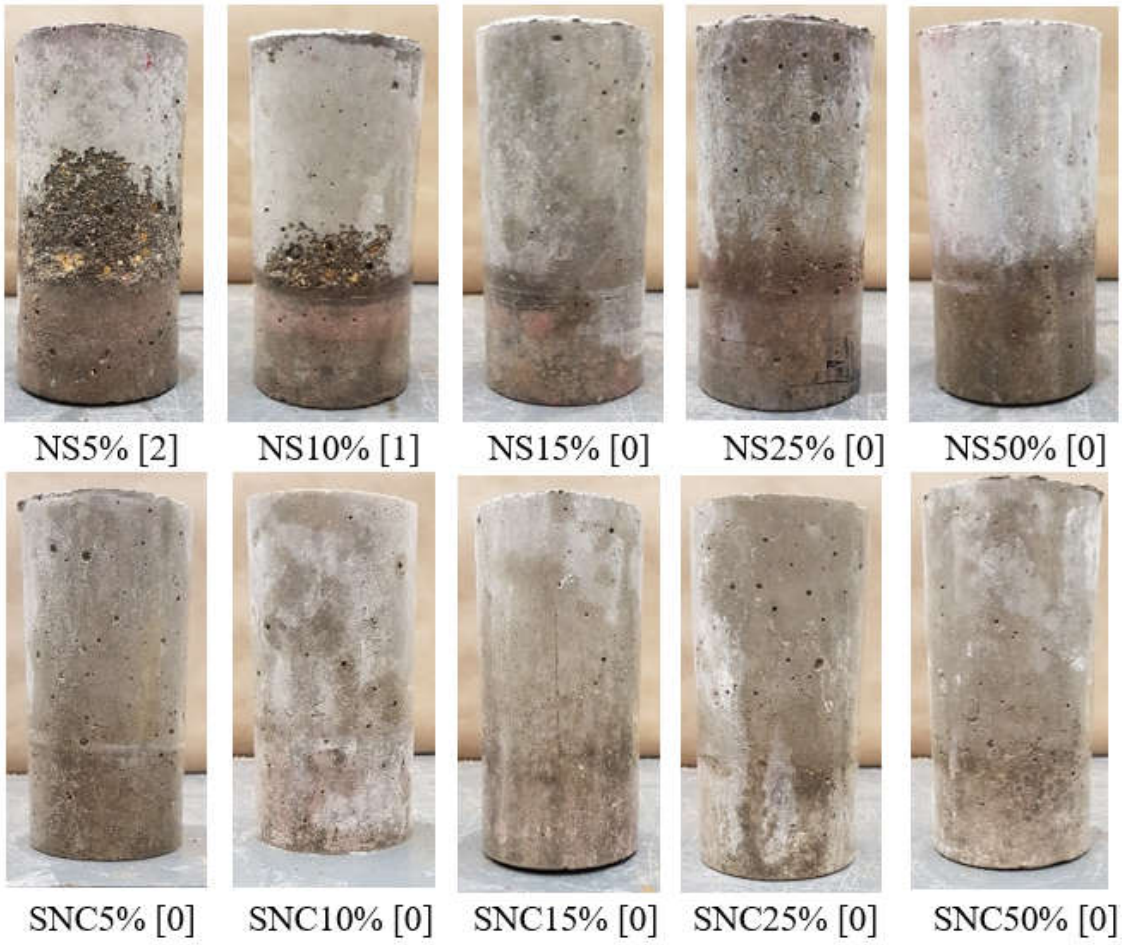

Figure B.2: Coated GU0.4 specimens at the end of PSA exposure. (Note: Numbers between brackets are the final visual ratings and the number of cycles at failure respectively, if applicable; NS: nano-silica, SNC: silane/nano-clay composite).

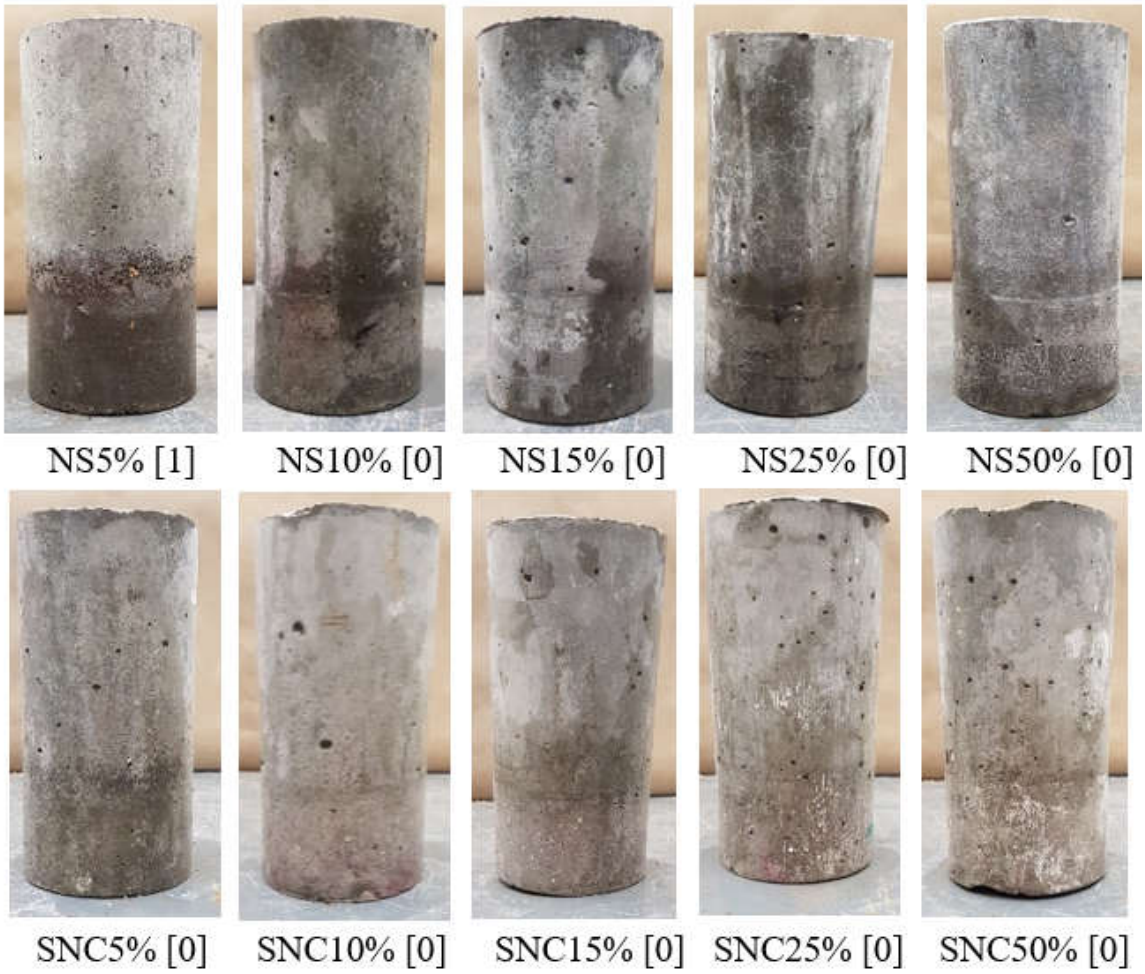

Figure B.3: Coated GUSF0.35 specimens at the end of PSA exposure. (Note: Numbers between brackets are the final visual ratings and the number of cycles at failure respectively, if applicable; NS: nano-silica, SNC: silane/nano-clay composite).